OBSERVATOIRE DE PARIS

INSTITUTE OF PHYSICS
HANOI, VIETNAM

Do Thi Hoai

Study at radio wavelengths of circumstellar envelopes around red giants

Supervisors:
Thibaut Le Bertre, LERMA/Observatoire de Paris
Pierre Darriulat, Vietnam National Satellite Centre, Hanoi

Defend on December 11th, 2015

Jury:

Daniel Rouan	Chairman
Dao Tien Khoa	Co-chairman
Stéphane Guilloteau	Referee
Dinh Van Trung	Referee
Pham Thi Tuyet Nhung	Member
Pham Ngoc Diep	Member

OBSERVATOIRE DE PARIS

ECOLE DOCTORALE
ASTRONOMIE ET ASTROPHYSIQUE D'ILE-DE-FRANCE

Doctorat
ASTRONOMIE ET ASTROPHYSIQUE

AUTEUR:
Do Thi Hoai

Etude en radio des enveloppes circumstellaires d'étoiles géantes rouges

Thèse dirigée par
Thibaut Le Bertre, LERMA/Observatoire de Paris
Pierre Darriulat, Vietnam National Satellite Centre, Hanoi

Soutenue le 11 décembre 2015

Jury:

Daniel Rouan	Président
Dao Tien Khoa	Co-président
Stéphane Guilloteau	Rapporteur
Dinh Van Trung	Rapporteur
Pham Thi Tuyet Nhung	Examinateur
Pham Ngoc Diep	Examinateur

VIỆN HÀN LÂM KHOA HỌC VÀ CÔNG NGHỆ VIỆT NAM

VIỆN VẬT LÝ

ĐỖ THỊ HOÀI

NGHIÊN CỨU LỚP VỎ CỦA CÁC SAO KHỔNG LỒ ĐỎ Ở BƯỚC SÓNG VÔ TUYẾN

Chuyên ngành:Vật lý nguyên tử
Mã số chuyên ngành: 62 44 01 06

NGƯỜI HƯỚNG DẪN KHOA HỌC

1. GS. Thibaut Le Bertre, Đài thiên văn Paris
2. GS. Pierre Darriulat, Trung tâm vệ tinh quốc gia, Hà Nội

HÀ NỘI –2015

Acknowledgements

This thesis was made under a joint supervision "cotutelle" agreement between Observatoire de Paris and Institute of Physics in Hanoi. I spent four months each of three successive years in Paris working with Pr. Thibaut Le Bertre and the rest of the time in Hanoi with Pr. Pierre Darriulat. I would like to thank all people and organizations in Vietnam and in France who helped me with my thesis work and made it possible for me to complete it under as good conditions as possible.

From the bottom of my heart, I would like to thank my supervisors, Pr. Thibaut Le Bertre and Pr. Pierre Darriulat for their guidance, their continuous support and their encouragements. I would like to thank Pr. Thibaut Le Bertre who taught me basic radio astronomy and introduced me to the physics of evolved stars. I highly appreciate his kindness, carefulness and patience. I am very grateful for his having introduced me to foreign colleagues and for having made it possible for me to attend schools and conferences during my stays in Europe. I would like to thank Pr. Pierre Darriulat who encourages me and protects me in all cases and is always ready to solve any problem I may meet in my research work. I am very lucky to be a student of such wonderful professors.

I thank Pr. Dao Tien Khoa and Pr. Daniel Rouan for having accepted to chair the jury and Pr. Stéphane Guilloteau and Dinh Van Trung for their referee work.

I particularly thank Dr. Pham Tuyet Nhung, who spent most of her time working with me during these years and contributed a large part of the results obtained in my thesis. I am grateful for her sharing her life with me, in particular during our stays in France. Her rigor, experience and good judgment helped me a lot in improving the quality of the thesis work. I thank Dr. Jan Martin Winters for helping me with the reduction of the IRAM data, spending time discussing about my studies and commenting and correcting the manuscript. I thank Arancha Castro-Carrizo and her colleagues for having kindly given me X Her and RX Boo data. The Red Rectangle data were observed, calibrated and cleaned by the ALMA staff whom I am deeply grateful for. I thank Dr. Pham Tuan Anh for his efforts in answering my questions on the technique and method of interferometry.

I am grateful to Dr. Pham Ngoc Diep and the members of the VATLY team who have been working with me for many years, for having shared with me their stories, their complaints and for the happy and enjoyable environment they create in the lab. I would like to thank our friends Nguyen Quang Rieu, Michèle Gerbaldi, Eric Gérard, Lynn Matthews, Pierre Lesaffre and Alain Maestrini for their moral support and help.

I am indebted to the Institute for Nuclear Science and Technology and the Vietnam Satellite Centre for their support. Financial support from the French Embassy in Hanoi, Campus France in Paris, the Rencontres du Vietnam and the Odon Vallet foundation, the World Laboratory and NAFOSTED is gratefully acknowledged.

Finally, I wish to thank my husband and my family who are always besides me, encouraging and supporting me in my research work.

Abstract

The thesis studies mass losing AGB stars and their circumstellar environments, with focus on the development of stellar outflows and their interaction with the surrounding medium. It uses emission from two tracers: carbon monoxide (CO), through its rotational lines in the millimeter range, probes the inner regions of the circumstellar shells out to photodissociation distances, while atomic hydrogen (H I, 21 cm) is better suited to the study of the external regions. The high spectral and spatial resolutions achieved in radio observations allow for a detailed exploration of the kinematics of the relatively slow outflows of red giants.

After having introduced the subject, I discuss the case of an S-type star (RS Cnc) that has been observed in CO with the IRAM telescopes, as well as in H I with the VLA, concentrating on the modelling of the spatially resolved CO line profiles and illustrating the complementarity between H I and CO. Results of the CO modelling of other AGB stars observed at IRAM (EP Aqr, X Her and RX Boo) and of a post-AGB star observed with ALMA, the Red Rectangle, are also presented.

The formation of the H I line profile in various cases of mass losing AGB stars, in particular Y CVn for which a model is presented, is studied next, exploring several effects that might explain the lack of detected emission from stars with high mass loss rates.

Similarities between the bipolar outflows of the AGB stars that have been studied, all having mass loss rates in the region of 10^{-7} solar masses per year and displaying nearly spherical morphologies are discussed together with the information on the gas temperature obtained from the simultaneous observation of two CO lines.

Résumé

La thèse étudie des étoiles de la branche AGB et leur environnement, particulièrement le développement de vents polaires et leur interaction avec le milieu environnant. Elle utilise l'émission radio de deux traceurs: les raies de rotation millimétriques du monoxyde de carbone (CO) sondent les couches internes de l'enveloppe circumstellaire tandis que la raie H I de l'atome d'hydrogène à 21 cm est mieux adaptée à l'étude des régions externes. Les bonnes résolutions spectrales et spatiales des observations radio permettent une exploration détaillée de la cinématique des vents relativement lents de ces géantes rouges.

Après avoir introduit le sujet, je discute le cas d'une étoile S (RS Cnc) observée en CO à l'aide des télescopes de l'IRAM et en H I avec le VLA, mettant l'accent sur la modélisation des raies CO résolues spectralement et spatialement et illustrant la complémentarité entre les observations CO et H I. Les résultats obtenus en appliquant la même approche à d'autres étoiles AGB observées en CO à l'IRAM (EP Aqr, X Her et RX Boo) et à une étoile post-AGB observée par ALMA, le Rectangle Rouge, sont également présentés.

J'étudie ensuite la formation des raies H I dans différents cas d'étoiles AGB, en particulier Y CVn dont je présente un modèle, explorant un certain nombre d'effets susceptibles d'expliquer l'absence d'émission détectable de la part des étoiles à forte perte de masse.

Je discute ensuite les similarités observées entre les vents polaires des étoiles AGB étudiées dans la thèse, toutes ayant des pertes de masse de l'ordre de 10^{-7} masses solaires par an qui ont peu affecté leur sphéricité, ainsi que les renseignements que l'observation simultanée de deux raies CO permet d'obtenir sur la température de l'enveloppe gazeuse.

Tóm tắt

Luận án này nghiên cứu các sao AGB đang trong giai đoạn mất khối lượng và môi trường vật chất bao quanh chúng, đặc biệt tập trung vào sự phát triển của gió sao và tương tác của chúng với môi trường xung quanh. Nghiên cứu sử dụng phát xạ từ carbon monoxide (CO), thông qua vạch quay của nó ở vùng bước sóng milimet, để tìm hiểu khu vực bên trong cho đến khoảng cách mà CO bị phân ly bởi trường bức xạ đến từ môi trường giữa các sao, và nguyên tử hidro trung hòa (vạch H I, 21 cm) để nghiên cứu khu vực bên ngoài. Độ phân giải cao về tần số và không gian đạt được trong thiên văn vô tuyến cho phép chúng ta nghiên cứu chi tiết tính chất động học của gió sao của các sao khổng lồ đỏ.

Sau khi giới thiệu tổng quan về nội dung nghiên cứu, tôi thảo luận về trường hợp của một sao loại S (RS Cnc) đã được quan sát thông qua phát xạ CO bởi các kính thiên văn của IRAM cũng như phát xạ H I bởi VLA. Tôi tập trung vào việc mô hình hóa phổ phát xạ CO và minh chứng cho sự bổ sung giữa các quan sát H I và CO. Tôi cũng trình bày các kết quả của mô hình phát xạ CO cho các sao AGB khác đã được quan sát bởi IRAM (EP Aqr, X Her và RX Boo) và một sao hậu AGB, Red Rectangle, được quan sát bởi ALMA.

Tiếp theo, tôi trình bày sự hình thành phổ vận tốc của H I trong một số trường hợp sao AGB, đặc biệt là trường hợp Y CVn. Một vài hiệu ứng cũng được xem xét giúp giải thích sự thiếu hụt thông lượng phát xạ đo được từ các sao có tốc độ mất khối lượng lớn.

Từ các sao AGB có tốc độ mất khối lượng vào khoảng 10^{-7} khối lượng mặt trời một năm và có hình dạng tương đối cầu đã được nghiên cứu, tôi cũng thảo luận về các tính chất tương đồng của các gió sao có cấu trúc lưỡng cực cùng những thông tin về nhiệt độ khí được tính toán từ phát xạ của hai vạch CO.

Substantial summary

From the end of their lifetime on the Main Sequence to their death as White Dwarfs, most stars evolve from a perfectly spherically symmetric morphology to the often very irregular shapes of Planetary Nebulae dissolving into the Interstellar Medium (ISM). The transition, with Red Giant and Asymptotic Giant Branch (AGB) as main intermediate states, is the object of intense study. The first departure from spherical symmetry is often observed to be the appearance of a bipolar outflow, axial symmetry replacing spherical symmetry. Many observations, whether of the dust from infrared, middle infrared and far infrared or of the gas from molecular radio emission, in particular carbon monoxide, are interpreted in terms of such symmetry. Namely they aim at giving a model of the star envelope displaying invariance with respect to rotation about a well-defined star axis, averaging over deviations from it, assumed to be small. The physics mechanisms at play in such symmetry breaking are not well understood and many observations aim at their clarification. The presence of a companion accreting gas from the dying star is very often invoked, but the roles of rotation and of magnetic field – how the angular momentum and magnetic flux of the original star are distributed between the degenerate core and the circumstellar envelope (CSE) – are still unclear. The availability of radio interferometers that offer excellent resolution, both spatial and spectral, in particular the Atacama Large Millemettre/submillimetre Array (ALMA), is currently giving a boost to this field of research. The present thesis addresses issues related to this topic.

The first two chapters introduce the subject.

Chapter 1 reviews the current knowledge of AGB stars and sets the scene: it describes the morphology of their gigantic circumstellar envelopes, the chemistry that they host, the mechanism of gas expansion via the go-between role of dust grains, the alternance between hydrogen burning and helium burning causing thermal pulses, the convection mixing different species between layers of different depths, the particular role of carbon monoxide in essentially exhausting the minority population of oxygen or carbon, leaving the excess majority population define the identity of the star as a carbon or oxygen star, the phenomenon of variability, etc. The mass loss mechanism that results, when gas molecules reach distances from the star where their mean velocity exceeds the escape velocity, occurs at a rate that varies between 10^{-8} to 10^{-4} solar masses per year, typically of the order of 10^{-7} at the entrance on the AGB and of the order of 10^{-5}, in the form of what is called a superwind, at the end of the branch. The present thesis studies stars having a rather low mass-loss rate, of the order of 10^{-7} solar masses per year, at various stages of their evolution: EP Aqr is a young AGB star, RS Cnc has already experienced several dredge up episodes and the Red Rectangle has left the AGB and is in the process of becoming a Planetary Nebula after having hosted one or more superwind outflows. This selection implies that the sample of stars that have been studied, although representative of a significant number of evolved stars, is not representative of the whole population, a caveat that must be kept in mind. The times spent by a typical star in various epochs of their life span a very broad spectrum: a star like our Sun spends ten billion years on the Main Sequence, a fraction of a billion years as a red giant, a few million years as an AGB star, some hundred thousand years in the transition to a Planetary Nebula and nearly infinite time as a slowly cooling down white dwarf.

Chapter 1 dedicates a full section to considerations on mechanisms of particular relevance to the thesis: transition from sphericity to axial-symmetry and interaction with the ISM. Different possible

processes have been invoked to describe the former, the most popular being binarity, which, however cannot explain all cases: the roles of angular momentum and magnetic flux conservation in a slowly expanding gas envelope are difficult to model precisely but cannot be ignored. Concerning the interaction with the ISM, the complementarity between CO and H I as respective tracers of the density, temperature and kinematics of the circumstellar gas is introduced, the latter taking over the former at large distances where UV-dissociations from the ISM becomes important.

Chapter 2 summarizes the main features of the instruments, observations and analysis methods relevant to the present study. It briefly recalls the bases of radio astronomy, both single dish and interferometry, and describes the IRAM telescopes, Pico Veleta and Plateau de Bure, and the Nançay telescope, from which much of the observations presented in the thesis have been taken. It also recalls the bases of atomic and molecular quantum physics, which govern the emission and absorption of radio photons, the population of quantum states and the propagation of radio waves through the CSE.

Chapter 3 is the first of four chapters that address the cases of specific evolved stars and attempt at modelling the morphology and kinematics of their CSE. It studies RS Cnc, a variable S star that has already experienced several dredge up episodes and has a mass loss rate of a few 10^{-7} solar masses per year. It uses CO(1-0) and CO(2-1) observations from the IRAM telescopes. After a brief review of earlier observations, it constructs a simple model of the gas envelope based on a stationary axial symmetric wind. The model uses a ray-tracing method for solving the radiative transfer. It can handle any kind of morpho-kinematics. However for RS Cnc, the density and the velocity are taken to vary smoothly from an equatorial plane to the corresponding polar axis. Good evidence is obtained for the presence of a bipolar outflow that causes the two-component nature of the global Doppler velocity distribution. The simultaneous observation of two molecular lines makes it possible to make significant statements on the radial distribution of the temperature. The distribution of the gas density departs only slightly from its original spherical shape in spite of the axi-symmetric kinematics. The existence of inhomogeneities limits the quantity and quality of the conclusions that can be reliably drawn from the available observations. A detailed understanding of the physics mechanisms at play, in particular of the validity of the stationarity hypothesis and of the reality of the positive velocity gradients implied by the model best fit, requires observations of improved spatial resolution (a proposal to IRAM has been made to this aim, RS Cnc being out of reach of ALMA. Figure 1 displays the spectral maps measured on the CO(1-0) and CO(2-1) lines and the results of the model best fits.

Chapter 4 studies EP Aqr, an M star that is believed to be at the beginning of its evolution on the AGB from the absence of technetium in its spectrum. It has a similar mass loss rate as RS Cnc and displays a similar two-component distribution of its Doppler velocity. However, at variance with RS Cnc, the Doppler velocity is uniformly distributed on the sky, which motivated an earlier study that invoked the presence of nearly spherical winds of different radial velocities to explain the presence of two components in the global Doppler distribution. The analysis presented here assumes instead the presence of a bipolar outflow similar to that observed in the case of RS Cnc but directed along an axis close to the line of sight, mimicking spherical winds when projected on the sky map. The peculiar geometry makes it possible, in particular under the strong but somewhat arbitrary hypotheses of radial stationary winds in thermal equilibrium, to reconstruct the density and temperature of the CSE in space. While being an interesting and successful exercise producing good fits to the observations, it should not be taken

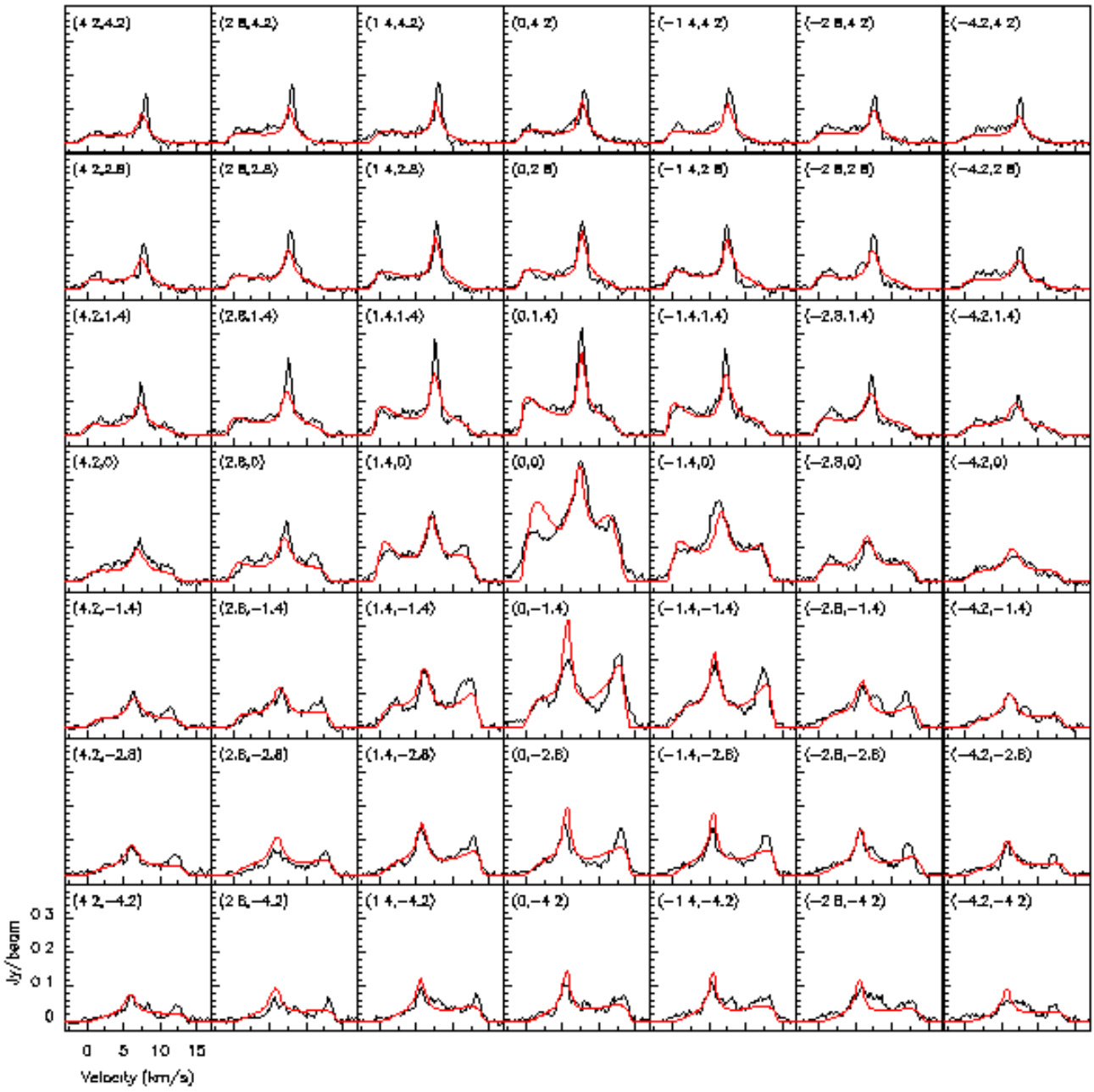

Figure 1a: RS Cnc: Spectral map of the CO(1-0) data (black) and best fit (red)

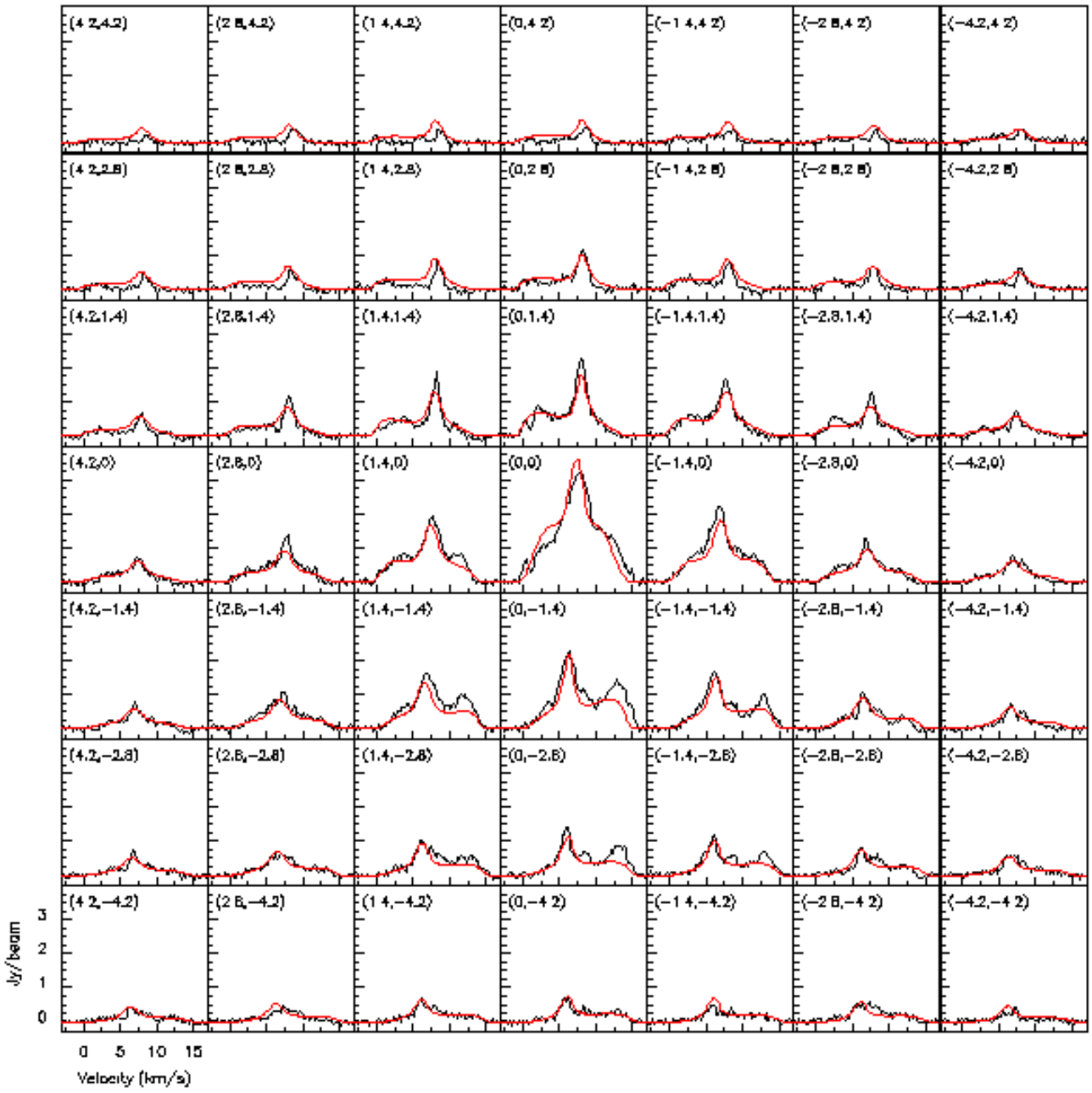

Figure 1b: RS Cnc: Spectral map of the CO(2-1) data (black) and best fit (red)

as evidence for the unicity of the model but rather serve as a caveat on the possibility to interpret the observations in different ways. The presence of very important inhomogeneities, significantly stronger than in the case of RS Cnc, makes the need for observations of better spatial resolution even more obvious than for RS Cnc in order to be able to draw more reliable conclusions. In this case ALMA observations with a higher spatial resolution over a large field of view are badly needed.

Figure 2 displays the distribution of the effective density reconstructed in space in the meridian plane of the star. The concept of effective density, such that its integral over the line of sight be equal to the integral of the flux density over Doppler velocity, is extensively used in the present work and found very useful.

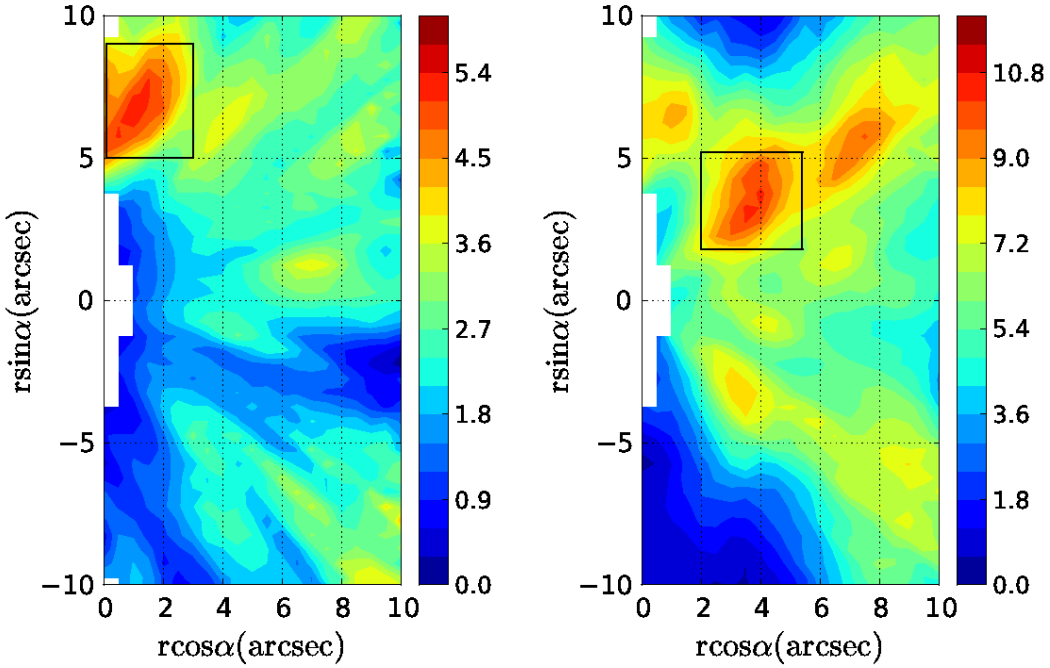

Figure 2: EP Aqr: Reconstructed maps of the effective density, multiplied by r^2, in the star meridian plane. Units of colour bars are Jy beam^{-1}km s^{-1} arcsec. The rectangle identify significant inhomogeneities.

Chapter 5 studies a star in a much more evolved state than the two preceding stars, the Red Rectangle, a famous and extensively studied post-AGB star, an archetype of a proto planetary nebula. Yet, it displays surprisingly slow winds, with a two-component velocity distribution reminiscent of those of RS Cnc and EP Aqr. The commonly accepted explanation is that the Red Rectangle has already gone through one or several successive superwind episodes that have shaped the CSE in its current strongly non-spherical but axi-symmetric form. A peculiarity of the Red Rectangle is to have its axis nearly perpendicular to the line of sight. While preventing a check of the validity of the hypothesis of rotational invariance about the star axis, it allows, when this is assumed, for a reconstruction in space of the effective density. Observations are made of two lines, CO(3-2) and CO(6-5), allowing for making statements on the temperature distribution of the gas envelope. An outstanding feature is the strong evidence, requiring the use of no model whatsoever, for an equatorial volume in rotation about the star axis (Figure 3) with sharp boundaries with respect to the rest of the gas envelope that displays a bipolar outflow similar to that

observed in the cases of RS Cnc and EP Aqr. It should be remarked that while the presence of rotation has been questioned and answered negatively in the case of RS Cnc, it could not be detected in EP Aqr because of its special geometry. Evidence for expansion in the equatorial region of the Red Rectangle causes outward spiraling of the gas flow as shown in Figure 3. Finally, Figure 4 displays evidence for a temperature enhancement at the boundary between the rotating equatorial volume and the expanding conical winds, the former displaying a lower temperature than the latter.

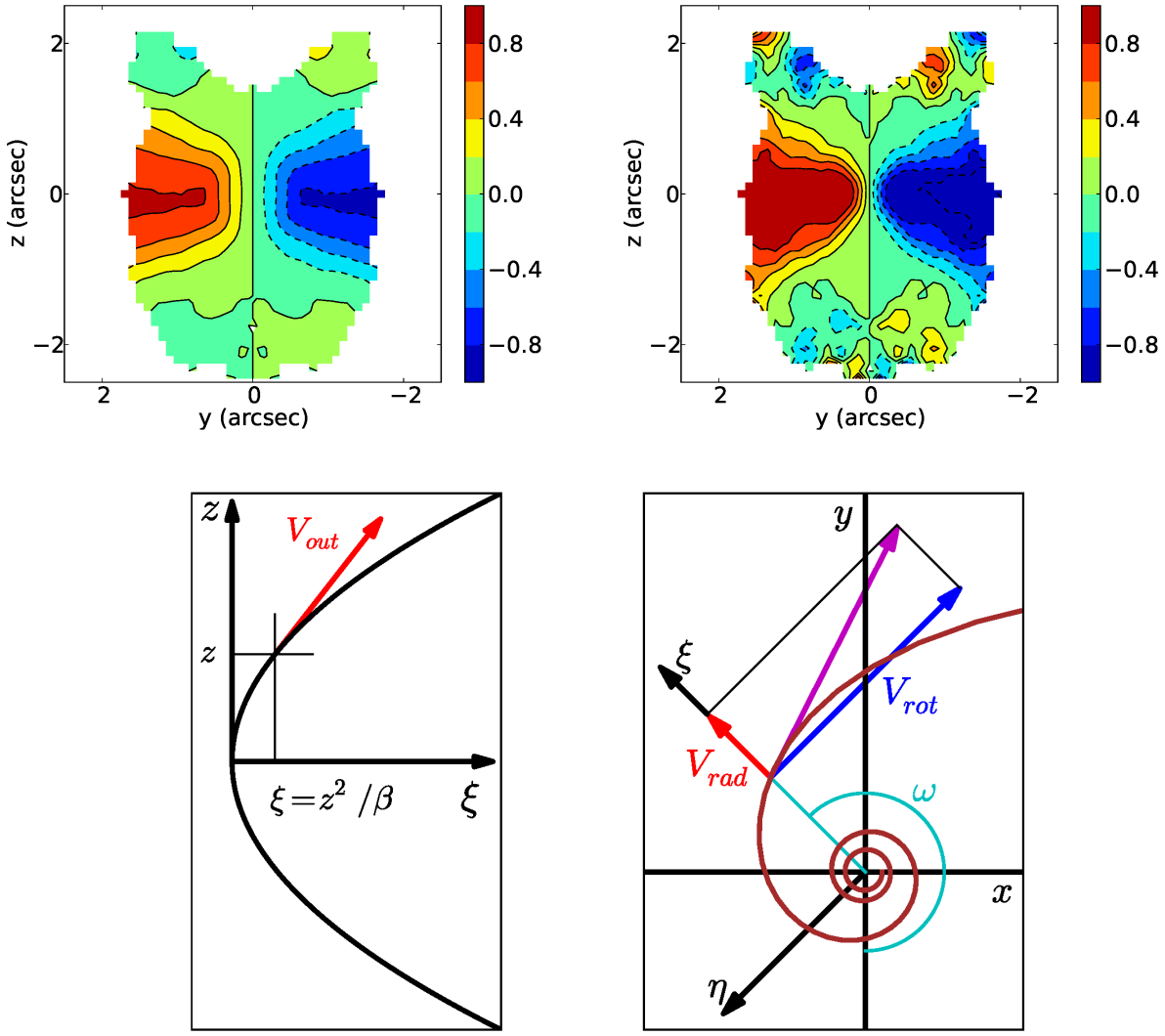

Figure 3: Red Rectangle. Upper panels: Sky maps of the east-west asymmetry of the Doppler velocity for CO(3-2) (left) and CO(6-5) (right). Lower panels: Gas velocity. Left: in the polar region (in the meridian plane of the star); Right: in the equatorial region (in the equatorial plane of the star).

Chapter 6 extends the previous analyses to the cases of two additional AGB stars observed in CO using the IRAM telescopes, X Her and RX Boo, providing again evidence for a bipolar outflow responsible for the two-component structure of the global Doppler velocity distribution. It then sums up by taking stock of the considerations developed in the preceding chapters. In particular, it remarks

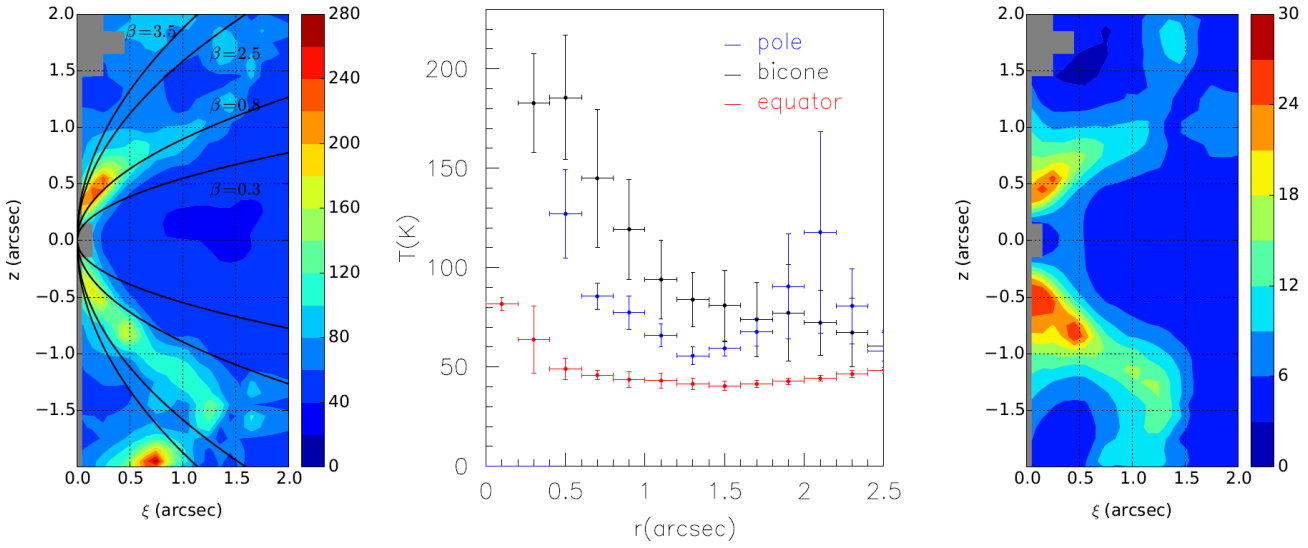

Figure 4: Red Rectangle. Left: Map of temperatures in the half-meridian plane of the star obtained from the effective densities. Middle: r-distribution of the gas temperature averaged over the three angular sectors: the red points are for the equatorial region, the black points are on the bicone and the blue points are for the polar regions. Error bars show the dispersion within each r bin. Right: CO density (in molecules/cm^3) multiplied by r^2 (in arcsec^2).

that while the quality of the data in terms of spectral resolution was usually sufficient, the need for as good as possible spatial resolution and high sensitivity is overwhelming. In this sense, ALMA opens a new era in terms of reliability and precision being now at hand. It marks a transition from a phase where many analyses were based on the visual inspection of channel and spectral maps and of position-velocity diagrams to a phase where more quantitative evaluations become possible. The origin of the observed bipolar outflow remains unclear and revealing its physical nature will remain a major source of investigations in the short range future.

Chapter 7 studies H I observations of wind-ISM interactions. Far away from the star, molecules are photo-dissociated: observations at large distances, in particular of the wind-ISM interaction region, require other tracers, such as dust or atomic species. Dust emits in the infrared at low temperatures and is indeed an excellent such tracer; however, being associated with continuous frequency distributions, it does not provide information on kinematics. For this we need velocity measurements, such as provided by the detection of the H I line. However, practical observations are difficult because the H I signal is weak and often coincident, both in position and in frequency, with strong galactic background and/or foreground emission. Indeed, initial efforts to detect H I associated with evolved stars were unsuccessful. It is only a decade ago that observations of H I emission using the upgraded Nançay telescope have been reported, soon followed by an extensive survey covering AGB stars and Planetary Nebulae showing that a significant fraction of the gas content of CSEs is in atomic form. Observations at distances of the order of 2 pc from the star display line profiles narrower than observed at closer distances, an effect of the slowing down of the outflow interacting with the ISM, also revealed by the presence of a systematic velocity gradient clearly observed in VLA data.

H I emissions from the stars studied in the previous chapters are reviewed, confirming the general

picture. However, H I emission from post-AGB and high mass-loss rate AGB stars remains undetected, which is puzzling as molecular hydrogen must be dissociated at large distances and produce a population of atomic hydrogen. One of the reasons invoked is that radiative transfer effects would weaken H I emission. As a contribution to the understanding of this issue, a simple model has been constructed with the aim of understanding the effects of background absorption and optical thickness. It considers three different possible scenarios, in line with suggestions made by various authors in the available literature, such as accounting for the possible presence of detached shells. Freely expanding winds have been detected in the H I line of only two red giants, Y CVn and Betelgeuse, making a free wind scenario best suited for the description of sources in their early phase of mass loss. In the case of Y CVn, the presence of a detached shell around a freely expanding wind, that is abruptly slowed down at a termination shock, provides a good model of the line profile as shown in Figure 5. However, several sources with high mass-loss rates, such as WX Psc, NML Tau and IZ Peg, which are observed at high galactic latitudes with an expected low interstellar H I background, remain undetected. The simulations presented in the thesis cannot account for such a result, suggesting that in such sources molecular hydrogen may dominate the composition of circumstellar shells, even at large distances from the central star.

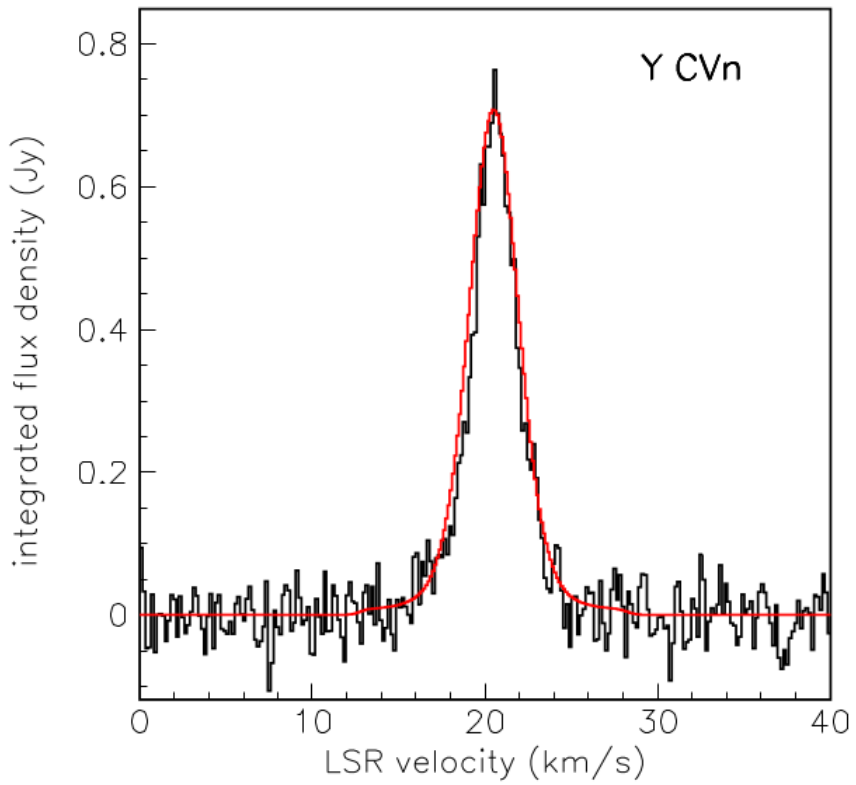

Figure 5: Y CVn integrated velocity spectrum observed (black) and best fit result using a mass loss rate of 1.3 10^{-7} solar masses per year and a freely expanding central wind surrounded by a detached shell covering radii between 2.8″ and 4.0″ (red).

Finally, Chapter 8 offers some conclusions and comments on future prospects. After having recalled the limitations of the proposed model, which have been amply discussed in the body of the main

text, it comments on the similarity of the observed outflow velocities at different stages of the star evolution, arguing that in the case of the Red Rectangle such similarity is likely to be accidental. The persistance of low velocity polar winds over much of the lifetime of the star on the AGB and the presence of important inhomogeneities already at the begining of the AGB phase are important features for which we do not have satisfactory explanations. The importance of observing at least two lines of the emission of a same molecule is underlined as providing a rich source of information on the temperature distribution of the gas envelope.

While data obtained at the PdBI or VLA, as used in the present thesis, have made it possible to make spectacular progress in our understanding of evolved stars, the reliability and accuracy of the conclusions that can be drawn are still essentially limited by the available sensitivity and resolution. In the near future, NOEMA and ALMA observations at molecular wavelengths and JVLA and FAST on the hydrogen line will allow for another major step forward.

Résumé substantiel

Depuis la fin de leur séjour sur la séquence principale jusqu'à leur mort sous la forme de naines blanches, la plupart des étoiles évoluent d'une forme parfaitement sphérique vers les morphologies souvent très irrégulières qui caractérisent les nébuleuses planétaires en passe de se dissoudre dans le milieu interstellaire. La transition entre ces deux états, avec pour phases intermédiaires les géantes rouges et celles de la branche asymptotique, fait l'objet d'études intenses. La première violation de la symétrie sphérique est souvent observée sous la forme d'un vent bipolaire, la symétrie sphérique faisant alors place à une symétrie axiale. De nombreuses observations ont fait l'objet d'interprétations en de tels termes, qu'il s'agisse de la poussière observée en infrarouge, proche, moyen ou lointain, ou du gaz observé en émission radio des molécules, en particulier grâce aux raies de rotation du monoxyde de carbone. En pratique, il s'agit de concevoir des modèles de l'enveloppe gazeuse de l'étoile invariants par rotation autour d'un axe bien défini, impliquant de moyenner les irrégularités de la densité, de la température et du champ de vitesses qu'on suppose faibles. Les mécanismes physiques en jeu dans la brisure de la symétrie sphérique ne sont pas bien compris et de nombreuses observations ont pour objet de les clarifier. La présence d'un compagnon accrétant le gaz de l'étoile en fin de vie est très souvent invoquée, mais les rôles joués par la rotation et par le champ magnétique restent mal compris: comment le moment cinétique et le flux magnétique de l'étoile originelle se distribuent-ils entre le cœur dégénéré et l'enveloppe circumstellaire? L'existence de nouveaux interféromètres radio offrant une excellent résolution, tant spatiale que spectrale, en particulier l'Atacama Large Millimeter/submillimeter Array (ALMA), donne un nouvel essor à ce champ de recherches. La thèse présentée ici traite de sujets relatifs à ces questions.

Les deux premiers chapitres introduisent le sujet.

Le premier chapitre passe en revue nos connaissances actuelles des géantes de la branche asymptotique et plante le décor: il décrit la morphologie de leurs gigantesques enveloppes circumstellaires; la chimie qu'elles abritent; le mécanisme d'expansion gazeuse et le rôle joué par les grains de poussière; l'alternance entre phases de fusion de l'hydrogène et phases de fusion de l'hélium, source de pulsations thermiques; le rôle de la convection dans le mélange d'espèces atomiques différentes entre couches de profondeurs différentes; le rôle particulier du monoxyde de carbone dont la formation épuise le moins peuplé des réservoirs d'oxygène et de carbone, laissant le plus peuplé définir le type de l'étoile – M, S ou C; le phénomène de variabilité; etc. Le mécanisme de perte de masse qui en découle, lorsque les molécules gazeuses atteignent des distances où leur vitesse moyenne dépasse la vitesse d'échappement, donne lieu à des taux qui varient entre 10^{-8} et 10^{-4} masses solaires par an, typiquement de l'ordre de 10^{-7} à l'entrée dans la branche asymptotique et de l'ordre de 10^{-5}, sous la forme de ce qu'on appelle un super-vent, à la sortie de la branche. La thèse étudie des étoiles géantes de la branche asymptotique dont le taux de perte de masse est modéré, à l'échelle de 10^{-7} masses solaires par an, à différentes phases de leur évolution: EP Aqr est jeune, RS Cnc a déjà connu plusieurs épisodes de dragage ("dredge-up") et le Rectangle Rouge a quitté la branche asymptotique et est en train de devenir une nébuleuse planétaire après avoir été le siège d'un ou plusieurs super-vents. Ce choix implique que l'échantillon d'étoiles étudiées, bien que représentatif d'un nombre important d'étoiles évoluées, ne l'est pas de l'ensemble de la population, une remarque qu'il conviendra de garder à l'esprit. Les temps passés par une étoile typique dans les différentes phases de son existence couvrent un très large spectre: une étoile telle que notre soleil

passe dix milliards d'année sur la séquence principale, quelques centaines de millions d'années sous la forme d'une géante rouge, quelques millions d'années sur la branche asymptotique, quelques centaines de milliers d'années en une étoile centrale de nébuleuse planétaire et un temps pratiquement infini sous la forme d'une naine blanche dont la température décroit lentement.

Le premier chapitre consacre une section entière à des considérations portant sur des mécanismes particulièrement pertinents au sujet de la thèse: la transition de la symétrie sphérique à la symétrie axiale et l'interaction avec le milieu interstellaire. Des possibilités diverses ont été invoquées pour rendre compte de la première, la plus courante étant la binarité qui, toutefois, ne saurait expliquer tous les cas de figure: les rôles joués par la conservation du moment cinétique et du flux magnétique dans une enveloppe gazeuse en lente expansion sont difficiles à modéliser avec précision mais ne peuvent pas être ignorés. En ce qui concerne l'interaction avec le milieu interstellaire, il faut souligner la complémentarité entre CO et H I dans leur rôle de traceurs de la densité, de la température et de la cinématique de la masse gazeuse circumstellaire, le second prenant le relais du premier à grande distance, quand la dissociation des molécules par le rayonnement ultra-violet interstellaire devient important.

Le chapitre 2 résume les propriétés les plus importantes des instruments et des méthodes d'observation et d'analyse des données utilisées dans la thèse. Il présente un bref rappel des bases de la radio astronomie, tant en antenne simple qu'en interférométrie, et décrit les télescopes de l'IRAM, Pico Veleta et Plateau de Bure, le Very Large Array, ainsi que le radio télescope de Nançay, les quatre instruments principaux utilisés dans les observations analysées dans la thèse. Il rappelle brièvement les bases de la physique quantique atomique et moléculaire qui gouverne l'émission et l'absorption de photons radio, la population des états quantiques et la propagation des ondes radio à travers l'enveloppe circumstellaire.

Le chapitre 3 est le premier de quatre chapitres consacrés à l'étude de cas particuliers d'étoiles évoluées, tentant de construire un modèle de la morphologie et de la cinématique de leurs enveloppes circumstellaires. On y étudie RS Cnc, une étoile variable de type S qui a déjà connu plusieurs épisodes de "dredge-up" et dont le taux de perte de masse est de quelques 10^{-7} masses solaires par an. Il utilise des observations en CO(1-0) et CO(2-1) obtenues avec les télescopes de l'IRAM. Après un bref rappel des observations antérieures, on construit un modèle simple de l'enveloppe gazeuse, basé sur les hypothèses de stationnarité et de symétrie axiale du vent stellaire. Le modèle intègre la densité de flux le long de la ligne de vue associée à chaque point du ciel pour tenir compte du phénomène de transfert radiatif. Il permet de traiter toutes les configurations morpho-cinématiques possibles. Toutefois, dans le cas de RS Cnc, la densité du gaz et la vitesse du vent sont supposées varier de façon continue de l'équateur aux pôles. La présence d'un vent bipolaire, cause de l'existence de deux composantes de la distribution de la vitesse Doppler globale, est mise en évidence. L'observation simultanée de deux raies moléculaires permet de faire des remarques pertinentes sur la distribution radiale de la température. La distribution de la densité en fonction de la latitude stellaire ne diffère que peu de la forme sphérique originelle malgré l'élongation axiale du champ de vitesses. L'existence d'inhomogénéités limite la qualité et la quantité des conclusions qu'on peut tirer avec confiance des observations dont on dispose. Pour comprendre les détails des mécanismes physiques en jeu, en particulier la validité de l'hypothèse de stationnarité et la réalité des gradients de vitesse positifs demandés par l'ajustement du modèle aux données, on aurait besoin d'observations de meilleures résolution spatiale que présentement disponibles. Une proposition d'observation a été soumise à l'IRAM, RS Cnc étant hors de portée d'ALMA. La figure 1 montre les

cartes spectrales mesurées sur les raies CO(1-0) et CO(2-1) et le résultat de l'ajustement des paramètres du modèle.

Le chapitre 4 étudie EP Aqr, une étoile de type M qu'on pense être au début de son séjour sur la branche asymptotique à cause de l'absence de technetium dans son spectre. Elle a un taux de perte de masse proche de celui de RS Cnc et son spectre de vitesse Doppler contient lui aussi deux composantes. Cependant, au contraire de RS Cnc, la vitesse Doppler est uniformément distribuée sur le ciel, ce qui a justifié une interprétation antérieure de ces observations faisant l'hypothèse de vents isotropes de vitesses radiales différentes permettant de rendre compte des deux composantes du spectre de vitesse. L'analyse présentée dans la thèse suppose au contraire la présence d'un vent bipolaire semblable à celui observé dans le cas de RS Cnc mais dirigé selon un axe presque parallèle à la ligne de vue afin de donner l'impression d'un vent sphérique une fois projeté sur la carte du ciel. La particularité de la géométrie permet de reconstruire la densité et la température du gaz dans l'espace quand on fait l'hypothèse de vents stationnaires radiaux en équilibre thermique. Le succès de l'exercice fait son intérêt, le modèle fournissant une bonne description des observations, mais il ne faudrait pas en déduire que ce modèle est le seul qui rende correctement compte des observations; on doit au contraire en retenir que diverses interprétations sont possibles.

La présence d'inhomogénéités très importantes, nettement plus que dans le cas de RS Cnc, demande à l'évidence des observations de meilleure résolution spatiale si l'on veut obtenir des conclusions plus fiables. Dans ce cas, des observations utilisant l'interféromètre ALMA représenteraient un progrès substantiel sur la situation actuelle. La figure 2 montre la distribution dans le plan méridien de l'étoile de la densité effective reconstruite dans l'espace. La thèse fait un fréquent et très utile usage du concept de densité effective, défini de telle sorte que son intégrale le long de ligne de vue soit égale à celle de la densité de flux sur le spectre des vitesses Doppler.

Le chapitre 5 étudie une étoile dans une phase d'évolution beaucoup plus avancée que les deux étoiles précédentes, le Rectangle Rouge, une étoile post-AGB bien connue et étudiée par de nombreux auteurs. Il s'agit d'un archétype d'une proto-nébuleuse planétaire. Malgré cela, elle est le siège de vents dont la faiblesse de la vitesse surprend, avec un spectre Doppler à deux composantes, rappelant ceux de RS Cnc et EP Aqr. L'explication généralement retenue est que le Rectangle Rouge a déjà été le siège d'un ou de plusieurs super-vents successifs qui ont donné à son enveloppe circumstellaire la forme axisymétrique, très éloignée d'une sphère, qu'on lui connaît aujourd'hui. Une particularité du Rectangle Rouge est d'avoir son axe pratiquement perpendiculaire à la ligne de vue. Cette particularité interdit de mettre en évidence l'invariance de rotation par rapport à l'axe mais, si on l'accepte, rend possible la reconstruction dans l'espace de la densité effective. On dispose d'observations sur deux raies, CO(3-2) et CO(6-5), ce qui donne des renseignements sur la distribution des températures de l'enveloppe gazeuse. Sans avoir recours à un quelconque modèle, il est possible de mettre en évidence l'existence d'un volume équatorial en rotation autour de l'axe de l'étoile (Figure 3) séparé très nettement du reste de l'enveloppe gazeuse qui est le siège d'un vent bipolaire semblable à celui observé pour RS Cnc et EP Aqr. Il convient ici de remarquer que si la présence de rotation a été exclue dans le cas de RS Cnc aux échelles considérées (>100 UA), elle n'a pu l'être dans celui de EP Aqr, la géométrie particulière interdisant sa détection. On observe également une faible expansion du volume équatorial du Rectangle Rouge, cause de trajectoires en spirales illustrées en figure 3. Enfin, la figure 4 révèle une élévation de

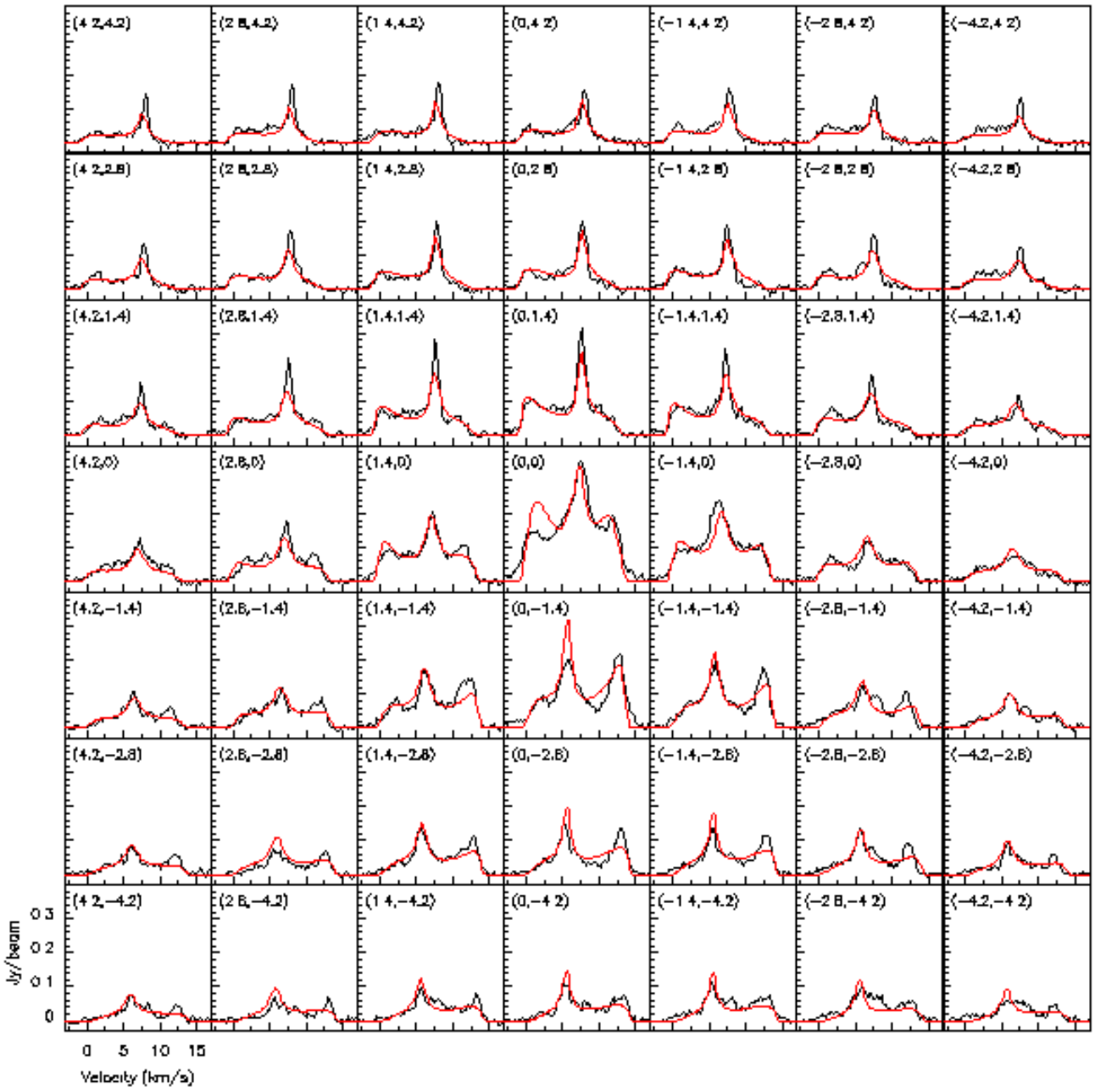

Figure 1a: RS Cnc: Carte spectrale des données CO(1-0) (en noir) et des résultats du modèle (en rouge).

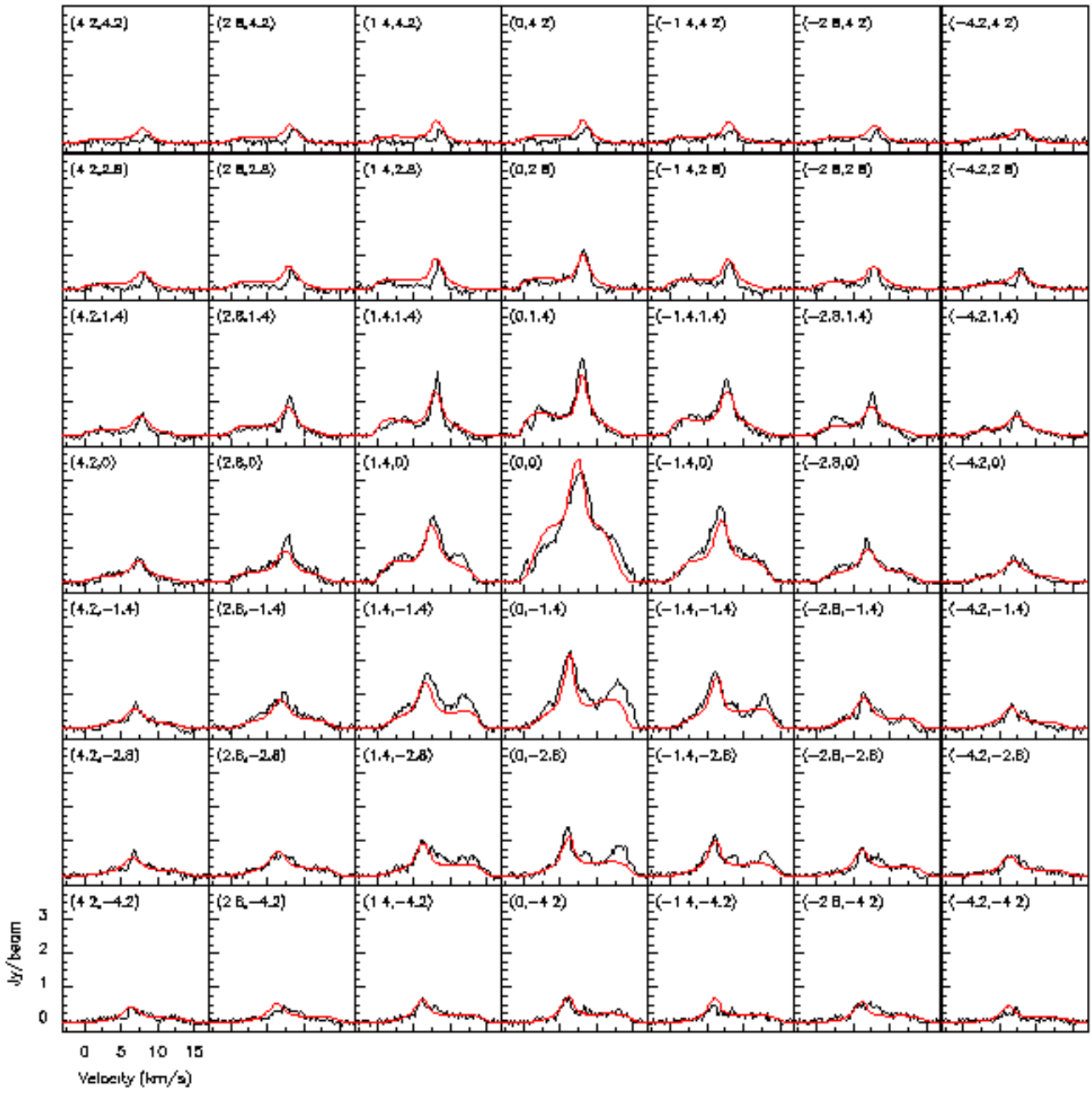

Figure 1b: RS Cnc: Carte spectrale des données CO(2-1) (en noir) et des résultats du modèle (en rouge).

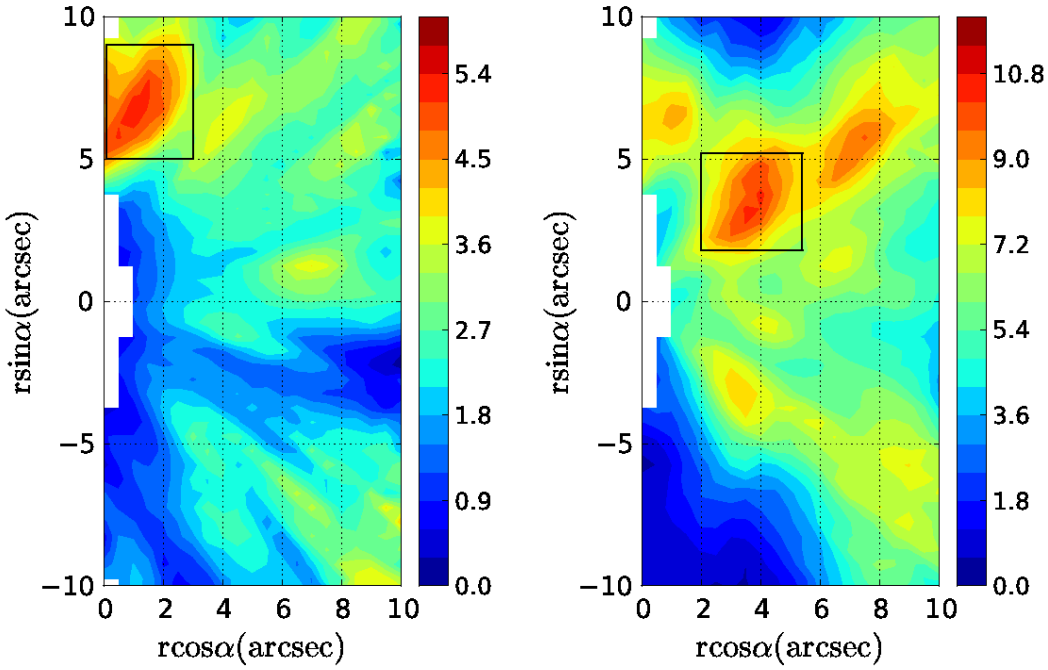

Figure 2: EP Aqr: Cartes de la densité effective reconstruite dans l'espace, multipliée par r^2, dans le plan méridien de l'étoile. Le code de couleurs est en unités de Jy beam^{-1}km s^{-1} arcsec. Les rectangles signalent des zones d'inhomogénéité importantes.

la température à l'interface entre le volume équatorial en rotation et les vents coniques en expansion, le premier étant à plus basse température que les seconds.

Le chapitre 6 applique les analyses précédentes aux cas de deux étoiles AGB supplémentaires, observées en CO avec les télescopes de l'IRAM, X Her et RX Boo, mettant encore une fois en évidence un vent bipolaire responsable de la structure à deux composantes des spectres Doppler. Puis il conclut en prenant acte des considérations développées dans les chapitres précédents. On fait entre autres la remarque que si la qualité des données en termes de résolution spectrale est en général suffisante, le besoin d'une meilleure résolution spatiale et d'une plus grande sensibilité est évident. En ce sens, ALMA ouvre une ère nouvelle en termes de fiabilité et de précision maintenant à portée de mains. Il marque la transition entre une situation où de nombreuses analyses reposaient sur une inspection visuelle des cartes spectrales et des diagrammes position-vitesse et une situation où des évaluations plus quantitatives deviennent possibles. L'origine des flux bipolaires observés reste mal comprise et les observations qui seront faites dans un futur proche permettront de progresser vers une meilleure compréhension de leur nature physique.

Le chapitre 7 étudie les observations en H I de l'interaction entre les vents stellaires et le milieu interstellaire. A grande distance de l'étoile, les molécules sont photo-dissociées: l'observation des régions où les vents interagissent avec le milieu interstellaire requiert d'autres traceurs, tels que grains de poussière ou atomes. Les premiers émettent dans l'infra rouge à basse température et constituent de fait d'excellents traceurs; mais, donnant lieu à une distribution continue de fréquences, ils n'offrent aucun

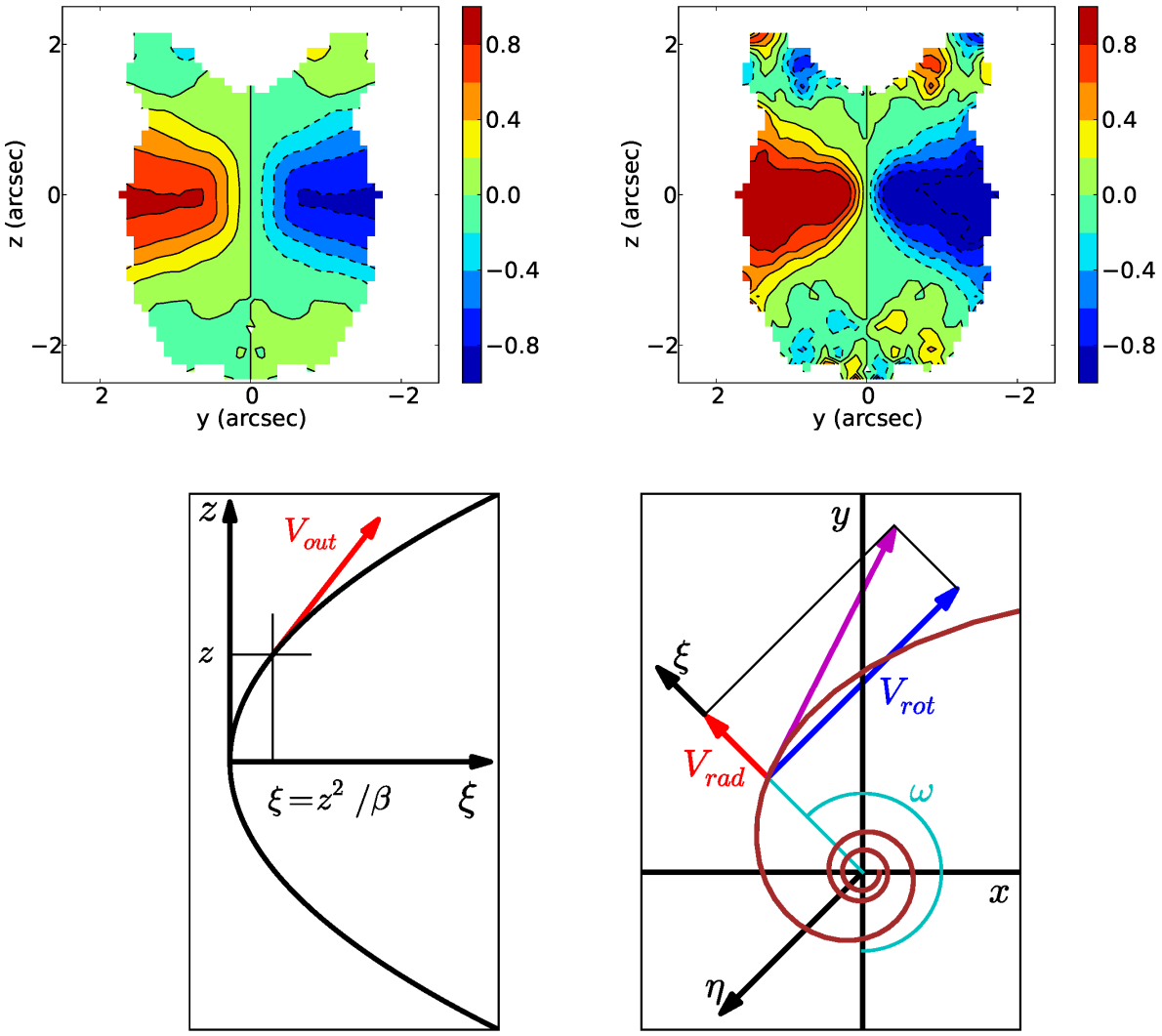

Figure 3: Rectangle Rouge. En haut: Cartes du ciel de l'asymétrie est-ouest de la vitesse Doppler pour CO(3-2) (à gauche) et CO(6-5) (à droite). En bas: Vitesse du gaz. A gauche dans les régions polaires dans le plan méridien de l'étoile et à droite dans la région équatoriale dans le plan équatorial de l'étoile.

renseignement sur la cinématique. Pour cela nous avons besoin de mesurer les vitesses, ce que permet l'observation de la raie H I de l'atome d'hydrogène. Cependant, en pratique, ces observations sont difficiles à cause de la faiblesse du signal et de la présence d'une importante contamination, provenant de l'hydrogène galactique présent aussi bien à l'arrière-plan qu'à l'avant-plan. De fait, les efforts initialement déployés pour détecter la raie H I émise par des étoiles évoluées ont échoué. Ce n'est qu'il y a une dizaine d'années que la raie H I a pu être observée en utilisant le télescope de Nançay rénové, observations rapidement suivies par une exploration systématique d'étoiles AGB et de nébuleuses planétaires révélant l'existence sous forme atomique d'une fraction importante de la masse gazeuse des enveloppes circumstellaires. Les observations faites à des distances de l'étoile allant jusqu'à deux parsecs montrent des raies dont les profils sont plus étroits que ceux observés plus près de l'étoile. On interprète ce fait

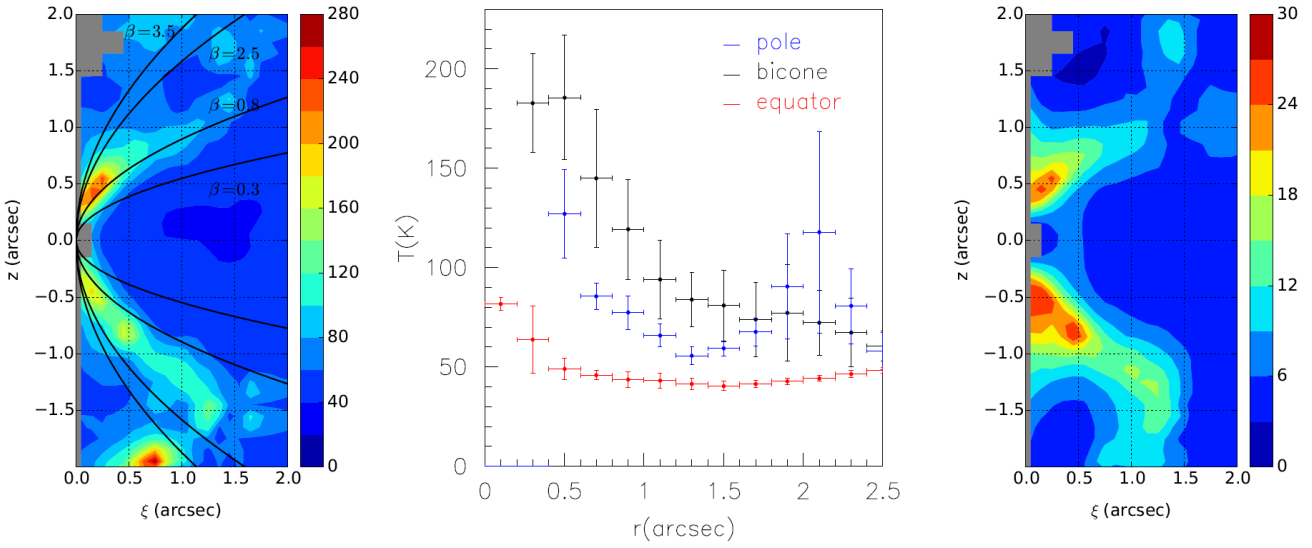

Figure 4: Rectangle Rouge. A gauche: carte des températures dans le demi-plan méridien de l'étoile, obtenu à partir de la densité effective. Au centre: distribution de la température du gaz, moyennée sur trois différents secteurs angulaires de latitude stellaire, en fonction de la distance r à l'étoile: les points rouges sont pour la région équatoriale, les points noirs sur le bicône à l'interface et les points bleus pour les régions polaires. Les barres d'erreur indiquent la dispersion dans chaque bin. A droite: densité du monoxyde de carbone (en molécules par cm^3) multipliée par r^2 (en $arcsec^2$).

comme résultant du ralentissement du vent en interaction avec le milieu interstellaire, ce qui est confirmé par la présence d'un gradient de vitesse dirigé systématiquement vers la vitesse du milieu ambiant.

Les émissions H I des étoiles étudiées dans les chapitres précédents sont passées en revue, confirmant l'image générale obtenue précédemment. Cependant, l'émission H I des étoiles post-AGB et des étoiles dont le taux de perte de masse est élevé n'a toujours pas été détectée. Ce qui semble surprenant dans la mesure où, dans tous les cas de figure, l'hydrogène moléculaire doit être dissocié à grande distance et produire une population importante d'hydrogène atomique. Une des raisons invoquées est un affaiblissement possible de l'émission H I dû à des effets de transfert radiatif. La thèse présente une contribution à la compréhension de ce problème en construisant un modèle simple visant à clarifier les effets d'absorption sur le fond galactique et ceux d'épaisseur optique. Trois scénarios différents sont étudiés, en accord avec des suggestions faites par divers auteurs dans la documentation disponible, tels que tenant compte de la présence de couches détachées. Des vents en expansion libre ont été détectés en H I dans seulement deux géantes rouges, Y CVn et Bételgeuse, impliquant qu'un tel scénario est sans doute favorisé par des sources en début de perte de masse. Dans le cas d'Y CVn, la présence d'une couche détachée entourant un vent en expansion libre, abruptement freiné au niveau du choc terminal, fournit un bon modèle du profil de la raie H I, comme on peut le voir en figure 5. Cependant, plusieurs sources à taux de perte de masse élevé, telles que WX Psc, NML Tau et IZ Peg, qu'on observe à des latitudes galactiques élevées, et qui sont donc relativement peu contaminées par le H I interstellaire, n'ont toujours pas été détectées en H I. Les simulations présentées dans la thèse ne permettent pas de rendre compte d'un tel résultat, suggérant que dans ces sources l'hydrogène moléculaire continuerait à dominer la composition des enveloppes circumstellaires jusqu'à de grandes distances de l'étoile centrale.

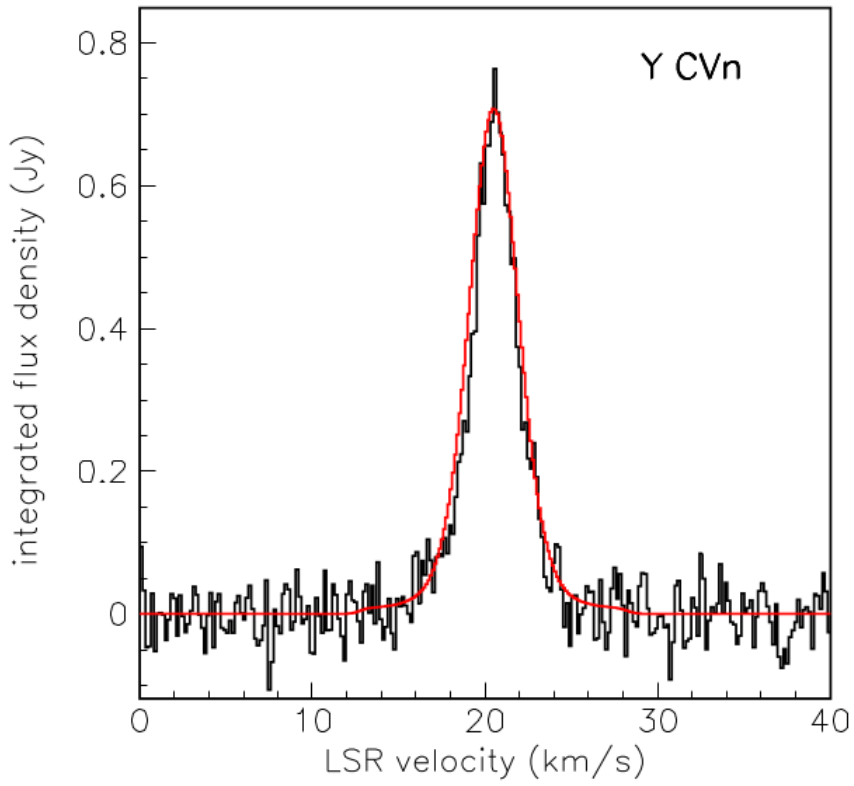

Figure 5: Distribution des vitesses Doppler de l'étoile Y CVn (en noir) et résultat du modèle utilisant un taux de perte de masse de 1.3 10^{-7} masses solaires par an et un vent central en expansion libre entouré d'une couche détachée couvrant des distances au centre de l'étoile allant de 2.8″ à 4.0″ (en rouge).

Enfin, le chapitre 8 propose quelques conclusions et offre quelques commentaires sur les perspectives dans les années à venir. Après avoir rappelé les limites du modèle proposé, qui ont été amplement discutées dans le corps du texte, on remarque les similitudes observées entre les vitesses des vents à différents stades de l'évolution des étoiles étudiées, suggérant que dans le cas du Rectangle Rouge il s'agit probablement d'une pure coïncidence. La persistance de vents polaires de vitesse relativement modeste sur une grande partie du séjour des étoiles étudiées sur la branche asymptotique et la présence précoce d'importantes inhomogénéités sont des caractéristiques importantes qui n'ont pas encore reçu d'explications satisfaisantes. L'intérêt d'observer simultanément au moins deux raies d'une même molécule mérite d'être souligné: de telles informations contiennent une riche source de renseignements sur la distribution dans l'espace des températures de la masse gazeuse.

Bien que les observations faites au Plateau de Bure ou au VLA, telles que celles qui ont été utilisées dans la thèse, aient permis à l'étude des étoiles évoluées de faire des progrès spectaculaires, la fiabilité et la précision des conclusions qu'on a su en tirer restent essentiellement limitées par la qualité de la sensibilité et de la résolution spatiale des instruments d'observation. Dans un futur proche, NOEMA et ALMA vont produire des observations dans le domaine des longueurs d'onde moléculaire et JVLA et FAST dans celui de la raie H I qui vont permettre à ces recherches de faire un nouveau bond en avant.

Tóm tắt

Từ giai đoan cuối của cuộc đời trên dải chính cho tới khi chết đi thành các sao lùn trắng, hầu hết các sao đều phát triển từ dạng đối xứng cầu sang các hình dạng mà thông thường là không đều của các tinh vân hành tinh rồi mất vào môi trường giữa các sao (ISM). Sự chuyển đổi này, với việc xem sao khổng lồ đỏ và sao tiệm cận khổng lồ đỏ (AGB) như các trạng thái trung gian quan trọng, là một đề tài nghiên cứu khó. Dạng chuyển đổi đầu tiên thường được quan sát là gió lưỡng cực với kiểu đối xứng trục đang thay thế đối xứng cầu. Rất nhiều các quan sát, cả bụi thông qua phát xạ hồng ngoại và khí thông qua các phát xạ phân tử, đặc biệt là carbon monoxide, đã cho thấy sự xuất hiện của kiểu đối xứng này. Điều đó có nghĩa là cần đưa ra một mô hình cho vỏ sao với bất biến quay quanh một trục sao xác định. Các cơ chế vật lý đóng vai trò làm cho sự đối xứng bị biến đổi như vậy vẫn chưa được hiểu rõ và rất nhiều quan sát được thực hiện nhằm làm sáng tỏ điều này. Sự có mặt của một sao đồng hành đang tích thêm khí từ sao già rất hay được đề cập đến, tuy nhiên vai trò của chuyển động quay và của từ trường - xung lượng góc và từ thông của sao được phân phối lại giữa lõi suy biến và lớp vỏ sao như thế nào - vẫn chưa được làm sáng tỏ. Việc có thể sử dụng số liệu đo đạc từ các hệ giao thoa vô tuyến, thường có độ phân giải cao về cả không gian và tần số, đặc biệt là ALMA (Atacama Large Millemettre/milimet Array), đang thúc đẩy lĩnh vực nghiên cứu này. Đây cũng là vấn đề mà luận án tập trung giải quyết.

Hai chương đầu của luận án là phần giới thiệu chung về đề tài nghiên cứu.

Chương 1 trình bày tổng quan về những hiểu biết của chúng ta về sao AGB và đưa ra bức tranh chung về hình dạng cũng như cấu trúc các lớp vỏ khổng lồ của chúng, các chất hóa học mà chúng sở hữu, cơ chế dãn nở khí thông qua vai trò trung gian của bụi, sự luân phiên giữa các quá trình đốt cháy hydrogen và heli gây ra các xung nhiệt, sự đối lưu làm các thành phần vật chất khác nhau giữa các lớp được trộn cùng nhau, vai trò đặc biệt của carbon monoxide trong việc xác định tính chất của các sao là sao carbon hay sao oxy, các hiện tượng biến đổi, v.v. Sự mất mát khối lượng được tạo ra khi các phân tử khí ở khoảng cách mà vận tốc trung bình của chúng vượt quá vận tốc thoát. Tốc độ mất khối lượng vào khoảng 10^{-8} đến 10^{-4} khối lượng mặt trời mỗi năm, chủ yếu là 10^{-7} ở giai đoạn đầu của sao AGB và vào cỡ 10^{-5} dưới dạng các siêu gió vào cuối giai đoạn AGB. Luận án này nghiên cứu các sao có tốc độ mất khối lượng khá chậm, vào khoảng 10^{-7} khối lượng mặt trời mỗi năm, ở các giai đoạn khác nhau của quá trình tiến hóa: EP Aqr là một sao AGB trẻ, RS Cnc đã trải qua nhiều lần "dredge-up" (quá trình đưa các nguyên tố nặng ở gần tâm ra ngoài vỏ sao) và Red Rectangle vừa rời nhánh AGB và đang trong quá trình trở thành một tinh vân hành tinh sau khi đã tạo ra một hoặc vài siêu gió. Chú ý rằng các sao được lựa chọn ở đây mặc dù đại diện cho một lượng đáng kể của các sao già nhưng không đại diện cho tất cả các sao. Thời gian một ngôi sao tồn tại ở các giai đoạn khác nhau của cuộc đời là khác nhau, một ngôi sao giống như Mặt trời của chúng ta dành khoảng mười tỷ năm trên dải chính, gần một tỷ năm ở giai đoạn khổng lồ đỏ, một vài triệu năm ở nhánh AGB, vài trăm nghìn năm để chuyển sang tinh vân hành tinh và thành một sao lùn trắng và nguội dần trong khoảng thời gian gần như vô hạn.

Chương 1 dành hẳn một phần để xem xét các cơ chế liên quan đặc biệt đến luận án: sự chuyển đổi từ dạng cầu sang dạng đối xứng trục và tương tác với ISM. Các quá trình khác nhau đã được đưa ra để mô tả sự chuyển đổi về hình dạng trong đó phổ biến nhất là hệ sao đôi. Tuy nhiên cơ chế này vẫn chưa thể giải thích tất cả các trường hợp: vai trò của bảo toàn momen xung lượng góc và từ thông trong một lớp vỏ khí đang dãn nở chậm rất khó mô hình hóa một cách chính xác nhưng lại không thể bỏ qua. Liên

quan đến tương tác với ISM, luận án cũng trình bày sự tương hỗ giữa CO và H I trong việc đưa ra những thông tin về mật độ, nhiệt độ và chuyển động của khí. Phát xạ H I lấn át CO ở khu vực xa tâm khi sự phân ly bởi phát xạ UV đến từ ISM trở nên mạnh mẽ.

Chương 2 tóm tắt các đặc trưng của các thiết bị, cách đo đạc và phương pháp xử lý số liệu liên quan đến nghiên cứu. Chương này trình bày những kiến thức cơ bản về thiên văn vô tuyến, cả cho kính đơn và hệ giao thoa, đồng thời cũng mô tả các kính thiên văn đã dùng để đo đạc số liệu cho luận án này bao gồm các kính thiên văn của IRAM, Pico Veleta và Plateau de Bure và kính thiên văn vô tuyến Nançay. Nó cũng nhắc lại các kiến thức cơ bản về vật lý lượng tử nguyên tử và phân tử bao gồm sự phát xạ và hấp thụ photon, phân bố ở các mức lượng tử và việc truyền sóng vô tuyến qua lớp vật chất bao quanh sao.

Chương 3 là chương đầu tiên trong số bốn chương trình bày nghiên cứu về các già cụ thể và cố gắng mô hình hóa cấu trúc và chuyển động của vật chất bao quanh sao. Nó nghiên cứu một sao loại S, RS Cnc, đã trải qua vài lần "dredge-up" và có tốc độ mất khối lượng vào khoảng vài lần 10^{-7} khối lượng mặt trời mỗi năm. Nghiên cứu sử dụng kết quả quan sát thông qua hai vạch CO(1-0) và CO(2-1) đo bởi các kính thiên văn của IRAM. Sau phần sơ lược về các quan sát đã thực hiện là phần trình bày một mô hình vỏ khí đơn giản với cấu trúc đối xứng trục. Phương trình truyền phát xạ được giải bằng cách cộng dồn theo từng bước nhỏ dọc theo đường ngắm. Mô hình này áp dụng được tất cả các kiểu cấu trúc khác nhau. Trong trường hợp RS Cnc, mật độ và vận tốc biến đổi liên tục từ xích đạo cho tới các cực. Sự hiện diện của gió sao dạng lưỡng cực đã có bằng chứng thuyết phục, chính cấu trúc này đã tạo ra hai thành phần trên phổ vận tốc. Việc đo đồng thời hai vạch phân tử có thể đưa ra những thông tin về phân bố nhiệt độ theo khoảng cách. Mật độ khí phân bố khá cầu mặc dù tính chất động học có dạng đối xứng trục. Sự tồn tại của sự không đồng nhất làm hạn chế về cả số lượng và độ chính xác của các kết luận có thể được rút ra từ các quan sát. Để hiểu chi tiết các cơ chế vật lý, đặc biệt là tính hợp lệ của giả thuyết dừng ("stationarity") và độ tin cậy của sự biến đổi vận tốc được chỉ ra từ mô hình, đòi hỏi các quan sát phải có độ phân giải không gian tốt hơn (với mục đích này, tôi cùng các đồng nghiệp đã đề xuất thực hiện thêm quan sát với IRAM, RS Cnc nằm ngoài trường nhìn của ALMA). Hình 1 hiển thị các phổ vân tốc của CO(1-0) và CO(2-1) đo được cùng với kết quả của các mô hình phù hợp nhất.

Chương 4 nghiên cứu sao EP Aqr, một sao loại M được cho là mới bắt đầu thời kì AGB bởi sự vắng mặt của technetium trong phổ tần. Nó có tốc độ mất khối lượng tương tự như RS Cnc và cũng có hai thành phần trên phổ vận tốc Doppler. Tuy nhiên, khác với RS Cnc, vận tốc Doppler phân bố đều trên bầu trời. Do vậy, trong một nghiên cứu trước đây, người ta đã đưa ra cấu trúc gió sao gồm nhiều lớp tương đối cầu có vận tốc xuyên tâm khác nhau để giải thích cho sự hiện diện của hai thành phần trên phổ vận tốc Doppler. Không giống như vậy, ở đây tôi giả sử gió sao có dạng lưỡng cực tương tự như đã thấy ở RS Cnc nhưng các cực này nằm trên một trục gần với đường ngắm, để có cùng dạng như các gió cầu khi chiếu trên bầu trời. Cấu hình đặc biệt này cho phép ta có thể tính được mật độ và nhiệt độ trong không gian, nhất là khi kết hợp với các giả thuyết hợp lý nhưng hơi chủ quan về gió dừng ở trạng thái cân bằng nhiệt. Đây là một bài tập thú vị và đã thành công trong việc tạo ra các kết quả rất khớp với số liệu đo đạc, tuy nhiên cũng không nên coi đây là mô hình duy nhất mà nên hiểu rằng có nhiều cách khác nhau để lý giải cho các kết quả quan sát. Sự hiện diện của những phân bố không đồng nhất, rõ ràng là cao hơn so với trường hợp của RS Cnc, cho thấy sự cần thiết phải có các quan sát với độ phân giải không gian cao để có thể rút ra các kết luận đáng tin cậy hơn. Các quan sát của ALMA với độ phân giải không gian cao trên một trường nhìn rộng là vô cùng cần thiết trong trường hợp này.

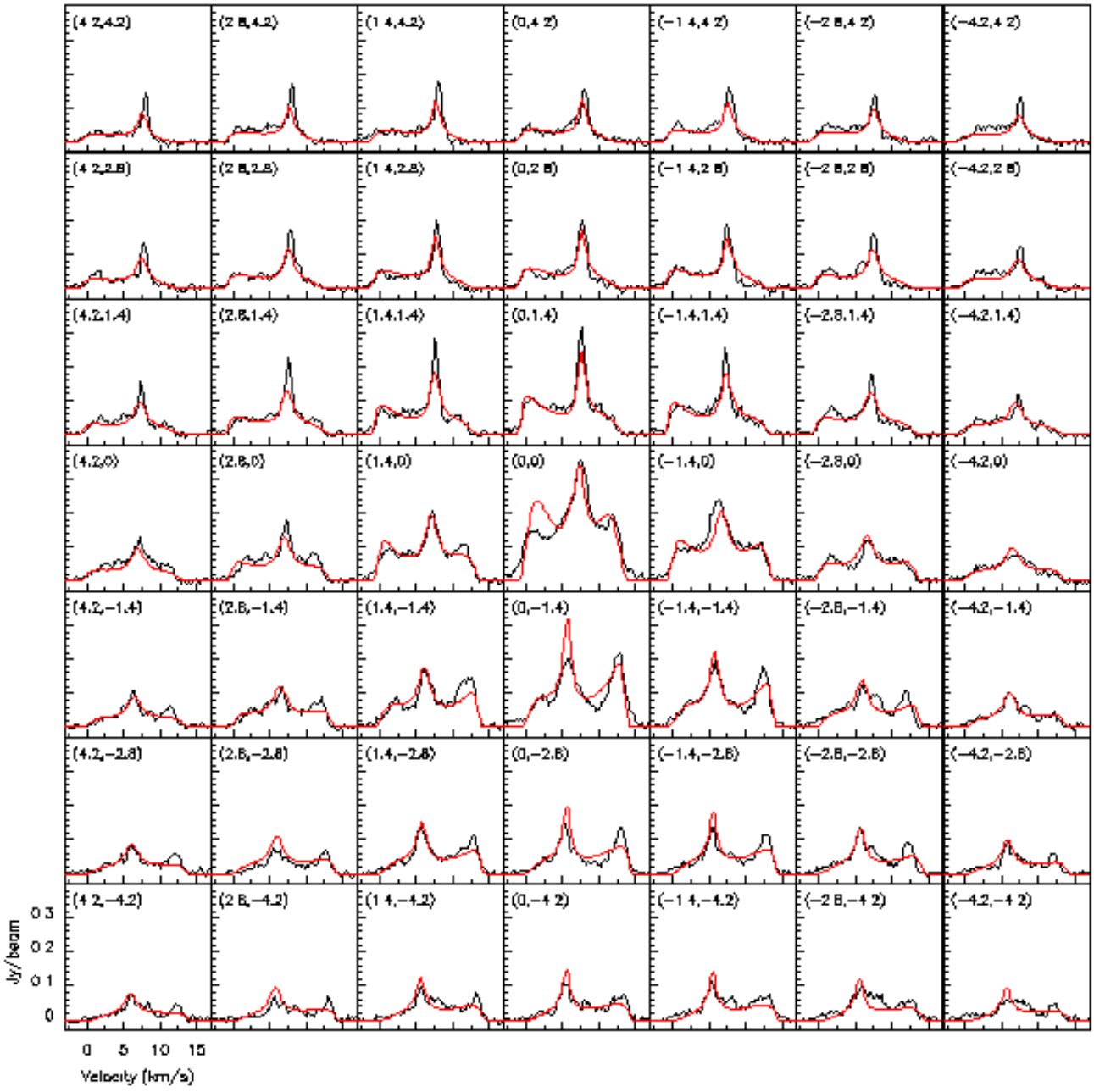

Hình 1a: RS Cnc: Các phổ vận tốc của CO(1-0) từ đo đạc (đen) and từ mô hình (đỏ).

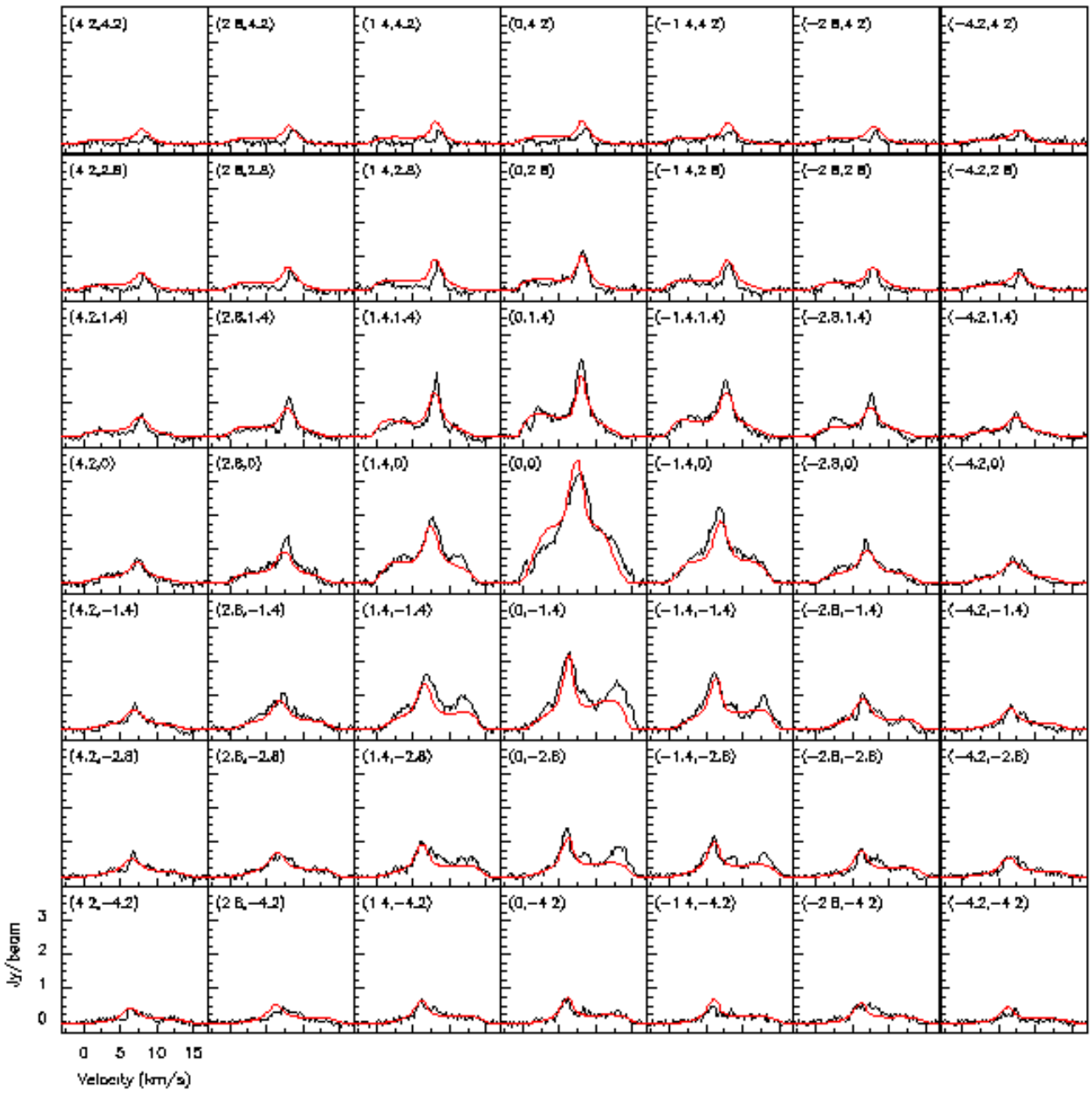

Hình 1b: RS Cnc: Các phổ vận tốc của CO(2-1) từ đo đạc (đen) and từ mô hình (đỏ).

Phân bố mật độ hiệu dụng trên mặt phẳng kinh tuyến của sao được chỉ ra trên hình 2. Mật độ hiệu dung được định nghĩa sao cho tích phân của nó dọc theo đường ngắm bằng tích phân của mật độ thông lượng trên dải toàn vận tốc Doppler. Đây là khái niệm được sử dụng nhiều trong luận án và tỏ ra vô cùng hữu ích.

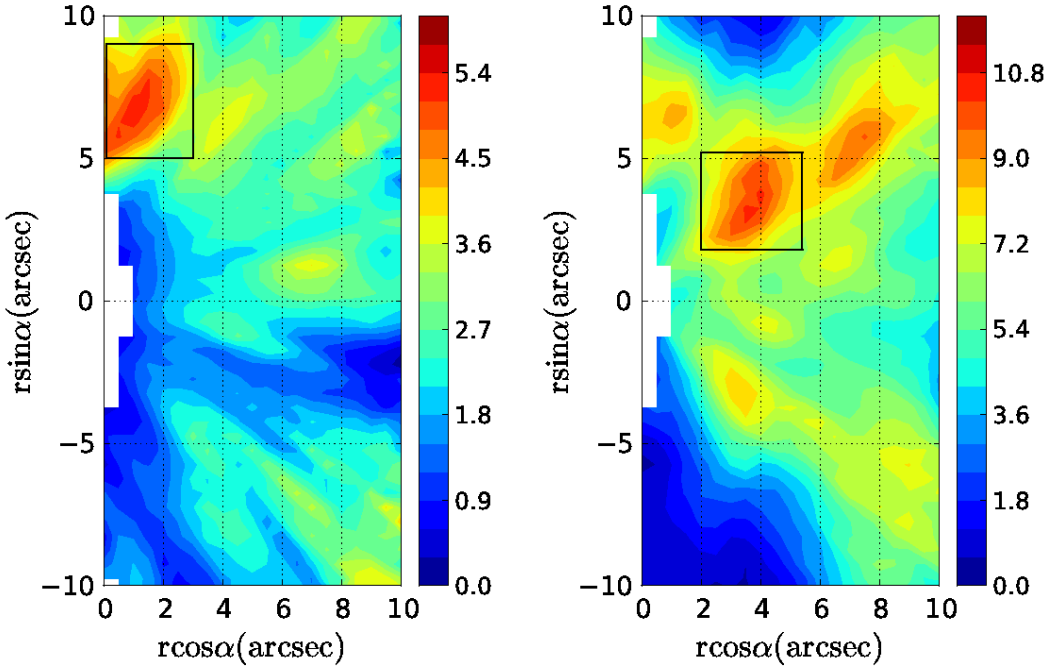

Hình 2: EP Aqr: Phân bố của mật độ hiệu dụng với nhân với r^2 trong mặt phẳng kính tuyến của sao. Đơn vị của thanh màu là Jy beam^{-1}km s^{-1}arcsec. Hình chữ nhật chỉ ra khu vực không đồng nhất.

Chương 5 nghiên cứu một sao già hơn so với hai sao trước, Red Rectangle. Đây là một sao hậu AGB nổi tiếng đã được nghiên cứu nhiều và cũng là hình mẫu của một tiền tinh vân hành tinh. Tuy vậy, gió sao của nó thổi chậm một cách đáng kinh ngạc và cũng có hai thành phần trên phổ vận tốc giống như ở RS Cnc và EP Aqr. Lời giải thích được chấp nhận nhiều nhất là Red Rectangle đã có một hoặc nhiều lần xuất hiện siêu gió liên tiếp để hình thành lớp vật chất bao quanh ở dạng hoàn toàn không phải cầu mà đối xứng trục như hiện nay. Một điều đặc biệt của Red Rectangle là trục của nó gần như vuông góc với đường ngắm. Mặc dù điều này ngăn cản chúng ta có thể kiểm tra tính đúng đắn của giả thuyết bất biến quay quanh trục nhưng với giả thuyết ta có thể tính toán được mật độ hiệu dụng trong không gian. Ngôi sao này đã được quan sát ở hai vạch phát xạ CO(3-2) và CO(6-5) nên cũng cho phép ta có được các thông tin về phân bố nhiệt độ của lớp vỏ khí. Một đặc điểm nổi bật của nó là bằng chứng rõ ràng, mà không cần đến bất kì mô hình nào, cho việc quay quanh trục sao ở vùng xích đạo (hình 3). Khu vực này có ranh giới rõ ràng với phần còn lại ở dạng lưỡng cực như đã thấy ở RS Cnc và EP Aqr. Chú ý rằng sự tồn tại của thành phần quay đã đươc đưa ra và bị phủ nhận trong trường hợp RS Cnc, nhưng trong trường hợp EP Aqr, ta không thể biết được do cấu hình đặc biệt của nó. Dấu hiệu dãn nở của Red Rectangle ở vùng xích đạo làm cho khí bị thổi ra theo hình xoắn ốc như trên hình 3. Hình 4 cho thấy sự phân bố nhiệt độ cao hơn ở khu vực giáp ranh giữa vùng vật chất đang quay ở gần xích đạo và vùng nón nơi vật chất đang dãn nở. Nhiệt độ ở vùng gần xích đạo nhỏ hơn nhiệt độ ở vùng khu vực hình nón.

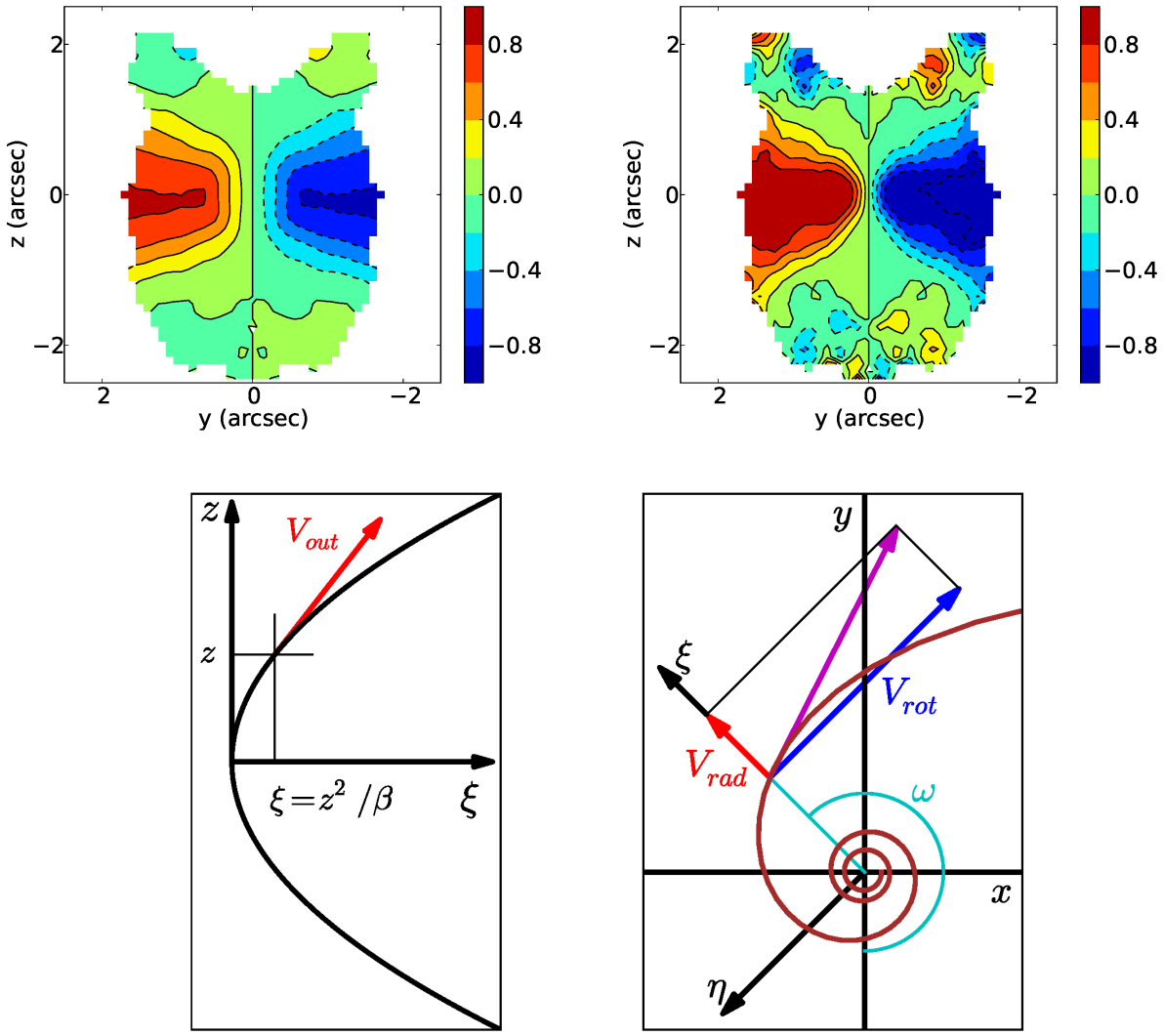

Hình 3: Red Rectangle. Bên trên: Bản đồ thể hiện bất đối xứng đông tây của vận tốc Doppler cho CO(3-2) (bên trái) và CO(6-5) (bên phải). Bên dưới: Vận tốc khí ở vùng cực (trên mặt phẳng kinh tuyến của sao, bên trái) và ở vùng xích đạo (trên mặt phẳng xích đạo của sao, bên phải).

Chương 6 mở rộng các phân tích trước đó cho hai sao AGB khác, X Her và RX Boo, đã được quan sát bởi các kính thiên văn của IRAM thông qua vạch phát xạ CO. Phân tích này cũng đưa ra bằng chứng cho cấu trúc lưỡng cực của gió sao, nguyên nhân hình thành cấu trúc hai thành phần trên phổ vận tốc Doppler. Cuối chương là phần điểm lại những nghiên cứu từ các chương trước. Đặc biệt, lưu ý rằng các số liệu thường đã có độ phân giải tần số đủ tốt, nhưng nhu cầu về độ phân giải không gian và độ nhạy cao vẫn vô cùng cần thiết. Dưới góc nhìn này, hệ giao thoa ALMA đang mở ra một kỷ nguyên mới về độ tin cậy và độ chính xác. Nghiên cứu cũng đánh dấu sự chuyển đổi từ các phân tích dựa trên việc kiểm tra bằng mắt thường các ảnh ở từng khoảng vận tốc, các phổ tần số tương ứng với từng vị trí trên bầu trời và các bản đồ vị trí-vận tốc sang việc phân tích một cách định lượng. Nguồn gốc của các gió dạng lưỡng cực vẫn chưa rõ ràng và việc tìm ra bản chất vật lý của nó sẽ vẫn là một hướng nghiên cứu chính trong

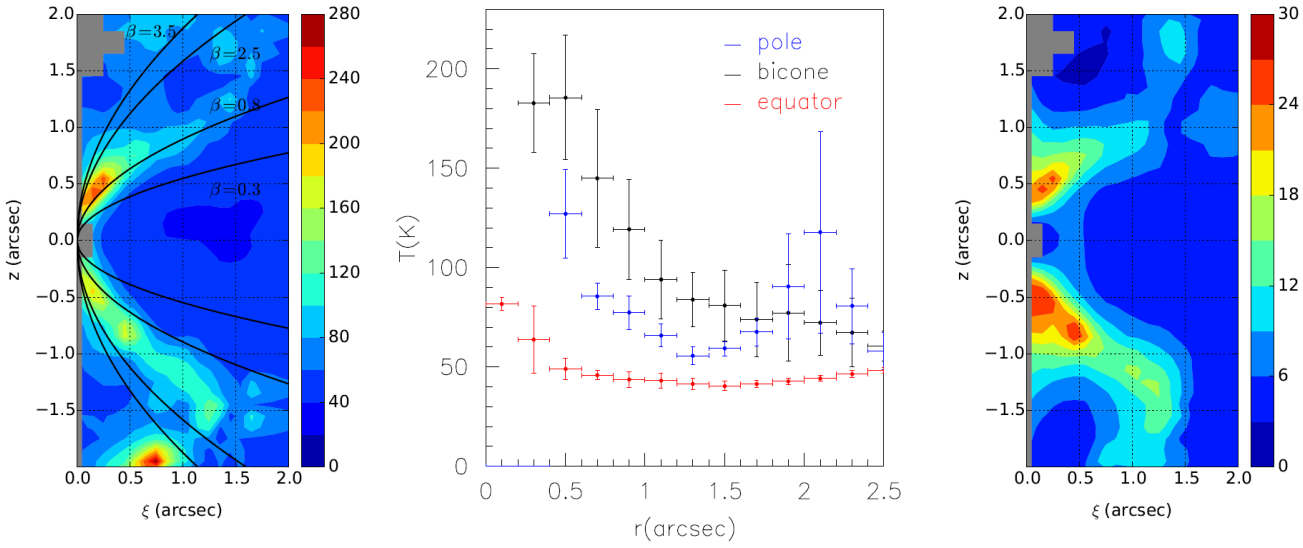

Hình 4: Red Rectangle. Bên trái: Phân bố nhiệt độ trên nửa mặt phẳng kinh tuyến của sao. Giữa: phân bố theo khoảng cách *r* của nhiệt độ khí trung bình trong ba khu vực: các điểm màu đỏ là khu vực xích đạo, màu đen là ở vùng bicone và màu xanh là vùng cực. Độ lớn của sai số thể hiện sự phân tán ở mỗi bin khoảng cách. Bên phải: mật độ CO (số phân tử trên mỗi cm^3) nhân với r^2 ($arcsec^2$).

tương lai gần.

Chương 7 nghiên cứu phát xạ H I từ khu vực tương tác giữa gió sao và ISM. Ở khoảng cách xa, các phân tử bị phân ly do trường phát xạ đến từ môi trường giữa các sao. Do đó, để quan sát các khu vực xa tâm sao, đặc biệt là khu vực xảy ra tương tác giữa gió sao và ISM, chúng ta cần các phát xạ khác, không phải từ các phân tử, như bụi và các nguyên tử. Bụi phát bức xạ trong vùng hồng ngoại ở nhiệt độ thấp và thật ra là một chất chỉ thị tuyệt vời, tuy nhiên nó lại có phân bố liên tục theo tần số nên không cung cấp các thông tin về động học. Để có được những thông tin này chúng ta cần những phép đo vận tốc mà những vạch phát xạ như H I có thể cung cấp. Tuy nhiên, trên thực tế đo phát xạ H I từ các sao già là rất khó vì tín hiệu H I thường yếu và thường trùng cả về vị trí và tần số với phát xạ đến từ tâm thiên hà hoặc từ các khu vực giữa nguồn và người quan sát. Thực tế, những nỗ lực ban đầu nhằm đo phát xạ H I từ các sao già đã không đem lại kết quả. Chỉ đến khoảng mười năm trước việc đo phát xạ H I sử dụng kính thiên văn vô tuyến Nançay mới được thực hiện thành công, ngay sau đó một cuộc khảo sát trên diện rộng đã được thực hiên với các sao AGB và các tinh vân hành tinh. Kết quả đo đạc đã chỉ ra rằng một phần lớn lượng khí ở môi trường bao quanh sao tồn tại ở dạng nguyên tử. Phổ tần đo được khi quan sát khu vực có khoảng cách cỡ 2 pc tính từ tâm sao hẹp hơn khi quan sát ở các khu vực gần tâm. Đây là kết quả của việc chuyển động chậm dần của gió sao khi tương tác với ISM. Điều này cũng đã được chỉ ra nhờ vào sự thay đổi vận tốc rõ rệt trong các quan sát bởi VLA.

Phát xạ H I từ các sao đã được xem xét để khẳng định sự đúng đắn của bức tranh chung. Tuy nhiên, phát xạ H I từ các sao hậu AGB và các sao AGB có tốc độ mất khối lượng cao vẫn chưa đo được. Điều này thật ngạc nhiên vì phân tử hydrogen phải bị phân ly ở khoảng cách lớn và tạo ra một lượng lớn các nguyên tử hydrogen. Một trong các lý do được đưa ra đó là những ảnh hưởng trong quá trình truyền bức xạ có lẽ đã làm giảm cường độ phát xạ H I. Để hiểu thêm về vấn đề này, một mô hình đơn giản đã được xây dựng nhằm hiểu rõ tác động của việc hấp thụ bức xạ nền và độ dày quang học. Nó xem xét ba trường

hợp khác nhau, phù hợp với những gợi ý của các tác giả trong các bài báo đã công bố, chẳng hạn như sự hiện diện của các lớp vỏ tách biệt (detached-shell). Các gió sao đang dãn nở tự do đã từng được phát hiện thông qua phát xạ H I từ hai sao khổng lồ đỏ, Y CVn và Betelgeuse. Do vậy mô hình này rất phù hợp để mô tả các nguồn ở thời kì đầu của quá trình mất khối lượng. Ở trường hợp Y CVn, sự hiện diện của "detached-shell" quanh khu vực gió sao dãn nở tự do, tạo ra do sự giảm tốc bất ngờ ở vị trí sốc, đã mô tả tốt phổ vạch như được chỉ ra trên hình 5. Tuy nhiên, một vài nguồn có tốc độ mất khối lượng cao như WX Psc, NML Tau và IZ Peg vẫn chưa đo được. Chúng nằm ở các vĩ độ cao của thiên hà, nơi các phát xạ H I được cho là yếu. Những mô phỏng trong luận án này chưa thể giải thích được những trường hợp như vậy, phải chăng ở các nguồn này phân tử hydrogen chiếm phần lớn trong vỏ sao, thậm chí ở cả các khu vực xa tâm.

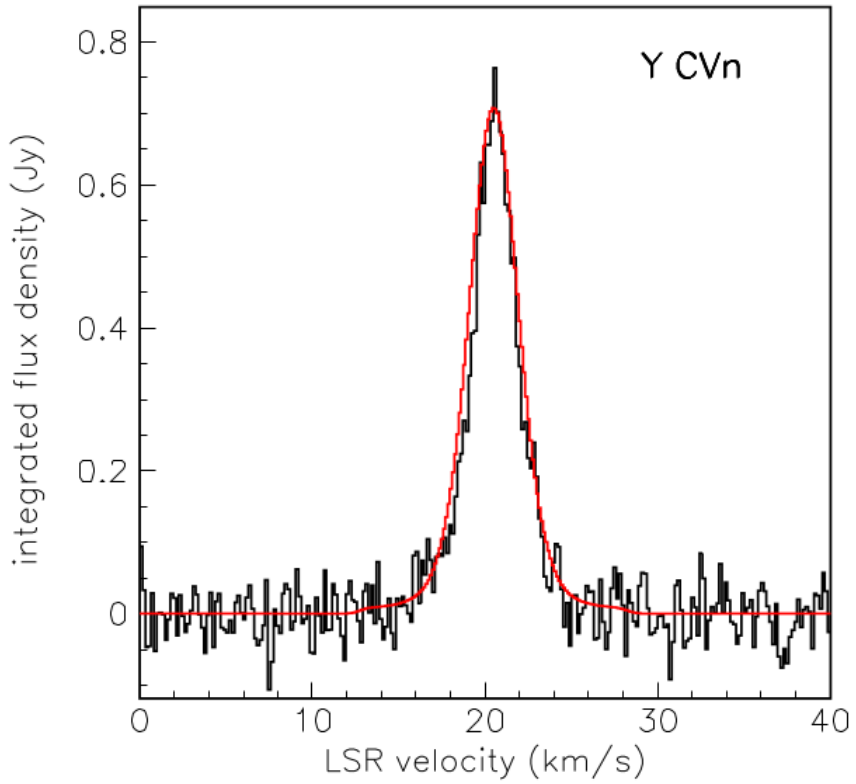

Hình 5: Phổ vận tốc của Y CVn từ số liệu đo đạc (đen) và từ mô hình với tốc độ mất khối lượng của sao là 1.3×10^{-7} khối lượng mặt trời một năm và bao quanh khu vực gió sao dãn nở tự do là một “detached-shell” nằm giữa bán kính 2.8″và 4.0″(đỏ).

Cuối cùng, chương 8 đưa ra một số kết luận và bình luận về những triển vọng tương lai. Sau khi điểm lại những giới hạn của mô hình đã được thảo luận trong luận án, tôi cũng bình luận thêm về sự tương đồng của các vận tốc gió sao đã được quan sát ở các giai đoạn tiến hóa khác nhau, và chỉ ra rằng trong trường hợp Red Rectangle, sự tương đồng này là ngẫu nhiên. Sự tồn tại của các gió cực chuyển động chậm trong khoảng thời gian dài ở giai đoạn AGB của sao và sự hiện diện quan trọng của sự bất đồng nhất ở ngay thời kì đầu của giai đoạn AGB là các tính chất quan trọng mà chúng ta vẫn chưa có lời giải thích thỏa đáng. Tầm quan trọng của việc quan sát ít nhất hai vạch phát xạ của cùng một phân tử

được nhấn mạnh là sẽ cung cấp một nguồn thông tin đáng kể về sự phân bố nhiệt độ của lớp vỏ khí. Các dữ liệu thu được bởi PdBI hoặc VLA, như luận án này đã sử dụng, đã tạo ra một bước tiến ngoạn mục trong sự hiểu biết của chúng ta về các sao già, độ tin cậy và độ chính xác của các kết luận được rút ra vẫn cơ bản bị giới hạn bởi độ nhạy và độ phân giải. Trong tương lai gần, các quan sát thông qua các phát xạ phân tử bởi NOEMA và ALMA và phát xạ hydrogen bởi JVLA và FAST sẽ cho phép chúng ta có thêm một bước tiến lớn hơn nữa.

Contents

[1] The content of this section has been published (Nhung et al. 2015a)
[2] The content of this chapter has been published (Nhung et al. 2015b)

[3] The content of this chapter has been published in Research in Astronomy and Astrophysics (Tuan Anh et al. 2015)

List of Figures

List of Tables

Chapter 1

INTRODUCTION

1.1 An introduction to AGB stars

1.1.1 An overview

Stars having a mass between 1 and 8 solar masses end their life on the Asymptotic Giant Branch where they spend the last 1‰ of their lifetime. They then evolve to Planetary nebulae (PNe) before ending as White Dwarfs (WD). AGB stars contribute to the enrichment of the ISM in both dust and nucleosynthesis products. There exist numerous reviews of the physics of AGB stars (see for example Wood 1994; Habing & Olofsson 2004; Herwig 2005; Marengo 2009; Bujarrabal 2009).

AGB stars are very luminous, in particular in the infrared, with bolometric luminosities between those of intermediate red giant and supergiant stars. They are easily identified not only in the Milky Way but also in other galaxies. Yet, most of the AGB sample that has been studied in detail is in the solar neighbourhood at distances of the order of a very few 100 pc. Due to their low effective temperature, they are very prominent in the infrared. Typical quantities are listed in Table 1.1 below.

Table 1.1: Typical AGB star parameters

Mass ($M_\odot$)	0.8 to 8
Radius (au)[a]	1 to 3
Effective temperature (K)	2000 to 3500
Luminosity ($L_\odot$)[b]	10^3 to 10^4
mass-loss rate ($M_\odot\ yr^{-1}$)	10^{-8} to 10^{-4}
Variability period (days)	30 to 3000
Time spent on AGB (years)	10^5 to 10^7

a) 1 au$\sim$200 $R_\odot$; 1 pc $\sim$2 10^5 au.
b) Namely -2.75 to -5.25 mag in bolometric magnitudes.

After exhaustion of the hydrogen in their core, Main Sequence (MS) stars enter a new phase where they burn helium in the core and hydrogen in a shell around it and where the core contracts up to a

point where electrons condense into a degenerate Fermi gas. The core is essentially made of oxygen and carbon, also neon and magnesium for the higher mass stars (i.e. light even-even nuclei with an α particle cluster structure). After having exhausted helium in their core they enter the early AGB phase where they burn helium in a shell around the core. This phase lasts typically 10^7 yr for a solar mass star, a duration that depends on the mass and composition of the star.

At some point, hydrogen burning resumes in the shell and the star enters the Thermally Pulsing (TP)-AGB phase with alternating periods of hydrogen burning and helium burning in the shell, the former lasting significantly longer than the latter. Hydrogen burned in the hydrogen shell produces helium that drifts to the helium shell just below. When the temperature and density of the helium shell reach values allowing for the triple α process to take place, $3\ ^4\mathrm{He} \rightarrow\ ^{12}\mathrm{C}+\gamma$, it triggers the so-called Thermal Pulse (TP) or helium shell flash.

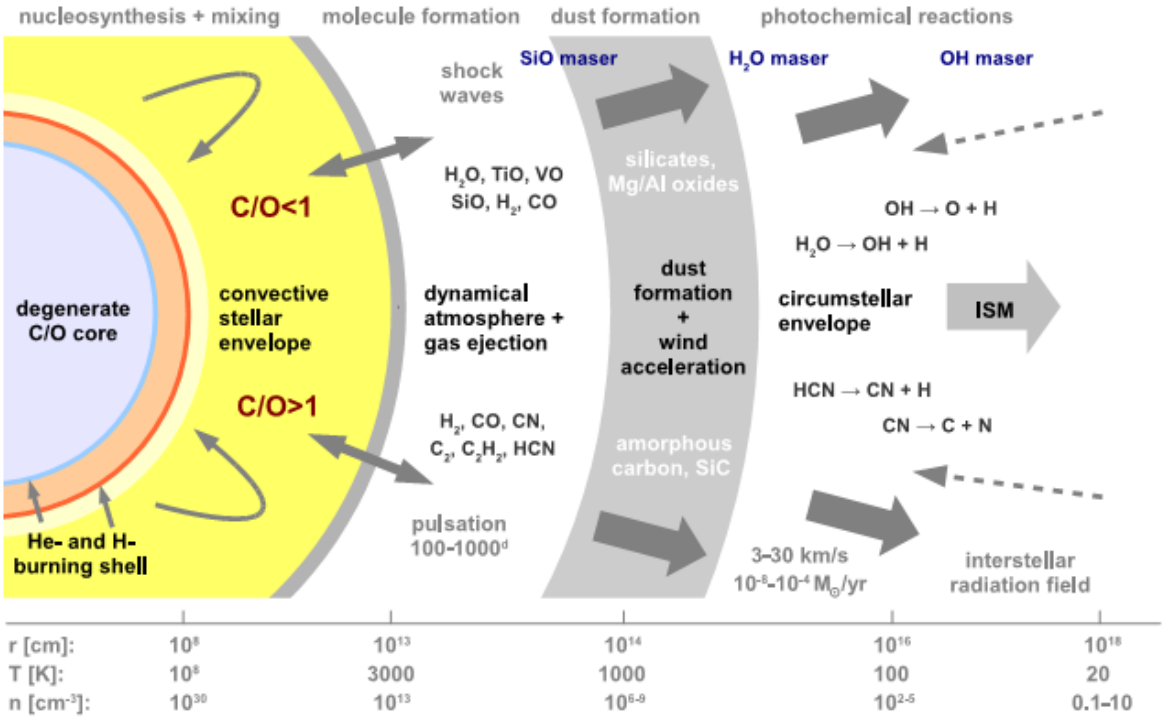

Figure 1.1: Sketch of the structure and environment of an AGB star (with the original idea from Le Bertre 1997).

Most of the energy released by a TP results in the expansion of the star envelope causing the hydrogen shell to reach higher radii where the temperature is not high enough to maintain hydrogen burning. The star enters a phase where helium burning dominates, however at a much lower rate than during the TP. The hydrogen burning shell contracts again up to the point where it re-ignites and takes over from helium burning. Several such cycles succeed each other, the time between two consecutive TPs is called the interpulse period. The luminosity increases after each TP. However, during each interpulse period, it varies with the process which the star goes through. After burning hydrogen, the luminosity decreases by $\sim 30\%$ due to the contraction of the envelope, then increases to as much as twice the pre-flash luminosity during He burning (Boothroyd & Sackmann 1988a). This variation occurs also when the star enters the phase of H burning, which takes most of the time in the interpulse period. The main parameters, such as the interpulse period and the luminosity during hydrogen shell burning, depend on

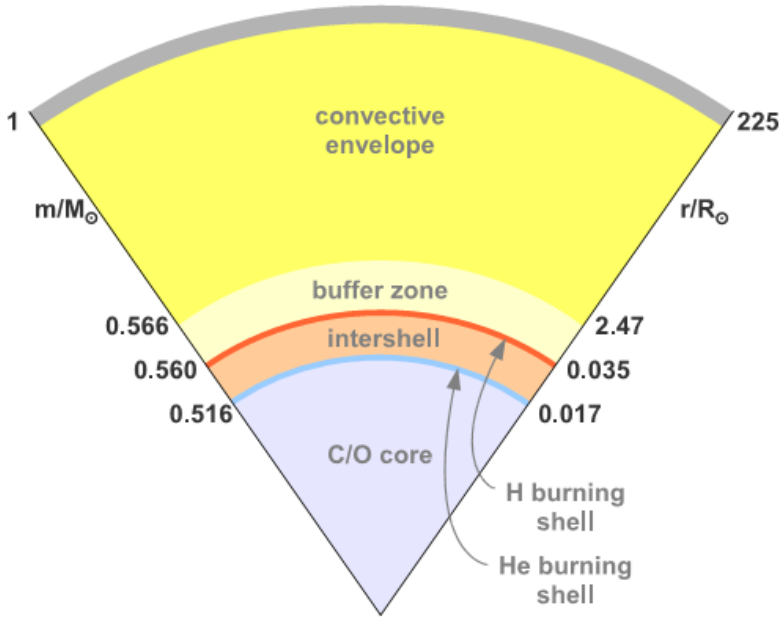

Figure 1.2: Mass and radius scales for an AGB star of one solar mass (Habing & Olofsson 2004).

the mass of the carbon/oxygen core, usually defined as the volume inside the radius where the hydrogen abundance is half that at the star surface (Paczyński 1970, 1975; Boothroyd & Sackmann 1988b,c). Figure 1.1 sketches an AGB star and its circumstellar envelope (CSE) and Figure 1.2 illustrates the mass and radius dimensions.

The core, which is already in the state of the future white dwarf, is very hot, 10^8 K, and dense. The H burning and He burning shells are separated by an intershell. Depending on star mass, a radiative buffer zone decouples the tiny interior part from the large, hot and less dense stellar envelope with huge convection cells. In the tenuous, warm and pulsating atmosphere, with temperatures around 3000 K, molecules are formed, depending on the C/O ratio. At radii of 5 to 10 star photospheric radii, the temperature is cool enough for molecules to condense into dust grains. The radiation pressure of the star on the grains initiates a slow wind that generates the mass-loss mechanism. In the outer, very diluted and cool CSE, most of the molecules are dissociated by the interstellar radiation field. Dust particles survive at temperatures around 10 K and will contribute to the formation of new stars and planets.

Figure 1.3 sketches the star evolution in the Hertzsprung-Russell diagram for a star having the same metallicitity as the Sun and twice its mass. A detailed sketch of the red giant branch (RGB) and AGB phases is shown in Figure 1.4.

AGB stars experience several thermal pulses until the convective envelope is dissipated. They undergo some tens of TPs over some 10^6 – 10^7 years. The lifetimes of the TP-AGBs are expected to become shorter at higher mass-loss rates and at lower metallicities (Rosenfield et al. 2014). As illustrated in Figure 1.5, H-burning is the main energy source between TPs. During a TP, He burning provides most of the star luminosity, up to 10^8 solar luminosities, and the H burning shell eventually extinguishes. Throughout the whole AGB evolution, the total luminosity goes up while the effective temperature slightly decreases.

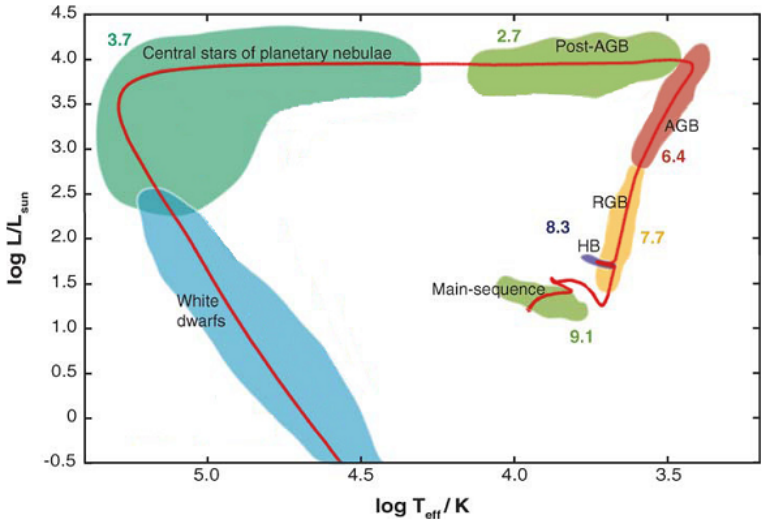

Figure 1.3: Evolution in the H-R diagram of a star having the metallicity of the Sun and twice its mass (Herwig 2005).The number labels for each evolutionary phase indicates the log of the approximate duration (in years).

1.1.2 Nucleosynthesis

Nucleosynthesis taking place in the various phases of the star life plays an essential role in the evolution of the star in particular and, globally, of interstellar matter in general. The mechanism mixing the nucleosynthesis products is referred to as dredge-up. One often talks of the third dredge-up for that occurring after a TP, reserving the name of first dredge-up for the stars on the Red Giant Branch (RGB) developing a deep convective envelope that mixes the mass layers formed during the MS phase and of second dredge-up for the particular case of stars having masses in excess of some 5 solar masses at the end of helium burning in the core. In the third dredge-up, the main products that are mixed into the convective envelope are the result of incomplete He burning (^{4}He, ^{12}C) and of the s-process, namely the slow neutron capture onto heavy elements (Gallino 1988; Gallino et al. 1990; Busso et al. 1992).

Figure 1.6 displays a TP with subsequent third dredge-up for a 2 solar mass AGB star. During a TP (at time zero) a pulse-driven convective zone (PDCZ) develops, mostly composed of ~75% ^{4}He and ~22% ^{12}C. After decline of He burning and disappearance of the PDCZ, the intershell region expands and H burning stops. The released energy from the shell flash causes the convective envelope to penetrate for a few hundred years into the mass zone previously occupied by the PDCZ, thus mixing recently produced ^{12}C into the stellar envelope.

The addition of carbon to the envelope enhances the C/O ratio which can reach a value larger than 1. Depending on the value of C/O ratio, one talks of oxygen-rich stars (C/O<1) and carbon-rich stars (C/O>1). Spectroscopically, one distinguishes between S-stars, characterized by ZrO and LaO bands, and C-stars having strong C_2 bands. In practice, there is a strong correlation between the spectroscopic classification and the C/O ratio, S-stars having C/O between ~0.8 and 1 and C-stars having C/O>1. The spectroscopic sequence M-MS-S-C, where M-giants show mostly TiO bands in their optical spectrum, is now understood to correspond to increasing values of both the C/O ratio and the abundance of s-process elements (Smith & Lambert 1990). Since CO is a strongly bound molecule in the atmosphere of cool stars, all C is locked in CO for M stars and all O is locked in CO for C stars. Only the remaining C or

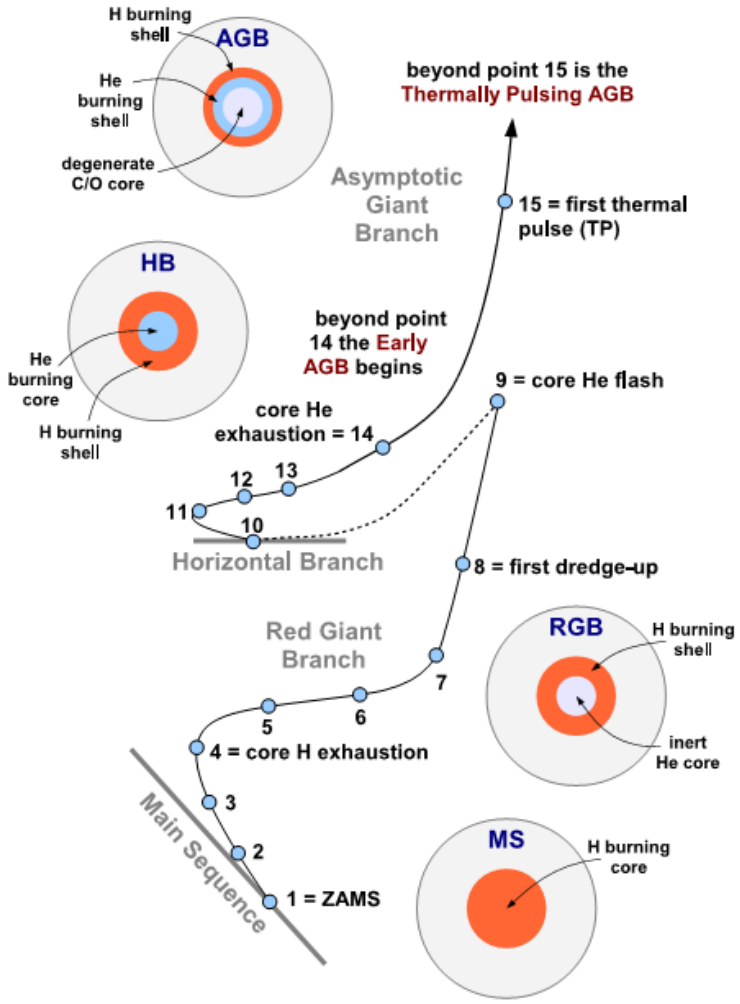

Figure 1.4: Details of the RGB and AGB evolution for a 1 solar mass star (Habing & Olofsson 2004).

O is available to form molecules like TiO in M stars or CN in C stars. This justifies the appellations of oxygen rich for M stars and carbon rich for C stars. Not all AGB stars go through the S and C phases.

There exist two neutron sources in AGB stars, both (α,n) reactions, one induced by ^{13}C, the other by ^{22}Ne, producing respectively ^{16}O and ^{25}Mg. The latter occurs only in high mass AGB stars, or at high temperatures during a He flash in low mass AGB stars. ^{13}C is produced via proton capture after the third dredge-up through the chain ^{12}C(p,α)^{13}N(β+ν)^{13}C. The s-process produces approximately half of the isotopes of the elements heavier than ^{56}Fe and multiple neutron captures produce the main components of the solar system distribution of s-elements.

1.1.3 Dust

AGB stars have large mass-loss rates, typically a billion times that of the Sun, $\sim 10^{-7}$ to $\sim 10^{-4}$ solar masses per year instead of $\sim 10^{-14}$. Dust grains form in their atmosphere which offers ideal conditions for dust formation: high density (10^9 cm^{-3}) and low temperature ($\sim$1500 K). They absorb optical photons

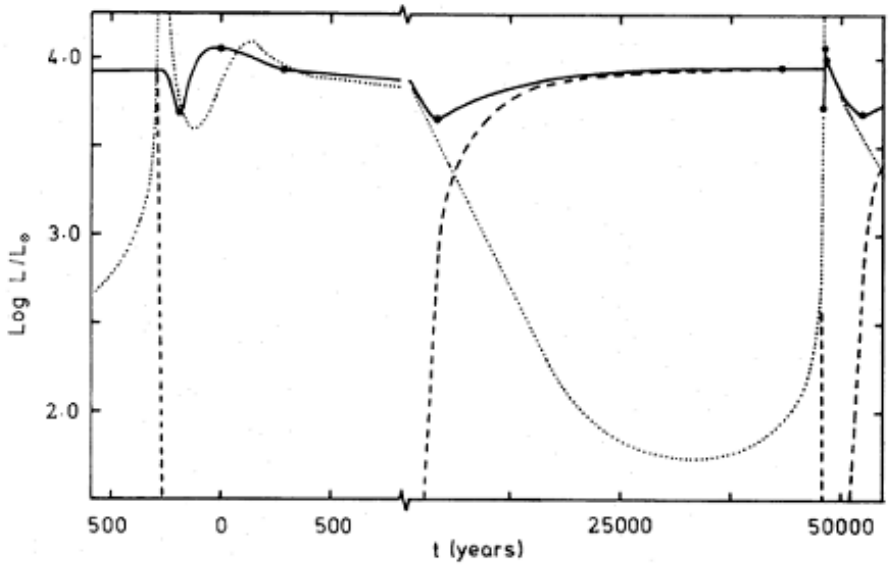

Figure 1.5: Surface luminosity (solid line) decomposed as H burning luminosity (dashed line) and He burning luminosity (dotted line) over a period covering two consecutive TPs for a 2 solar mass star (from Wood & Zarro 1981). Note the broken abscissa scale.

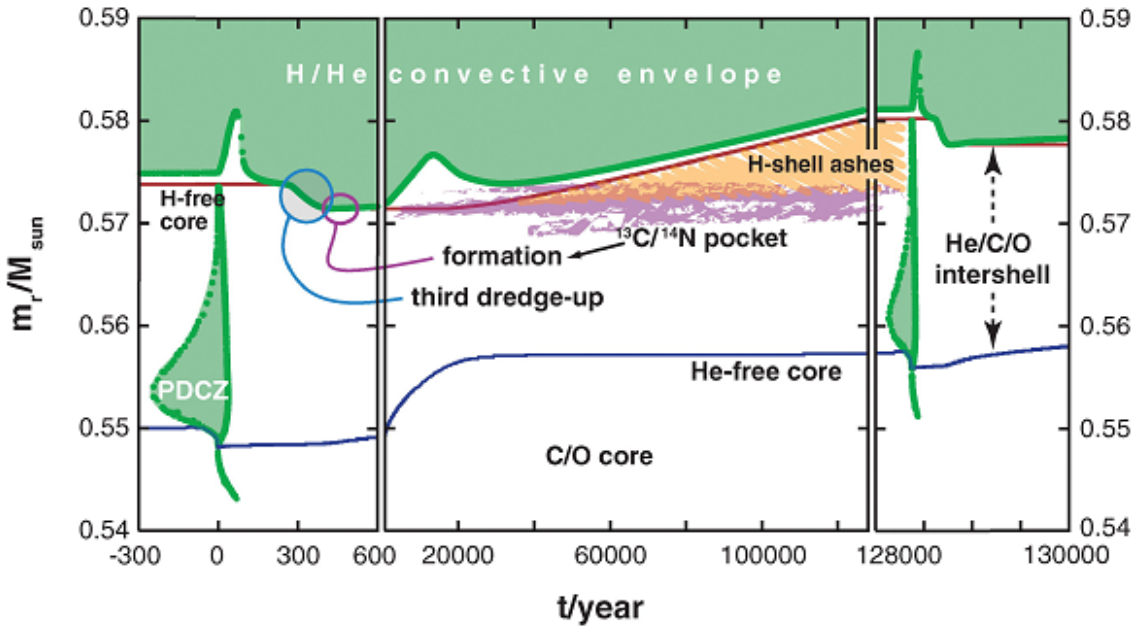

Figure 1.6: Third dredge-up in a 2 solar mass AGB star following a TP. The red and blue lines mark the boundaries of the H and He free core respectively. Convection zones are shown in green (Herwig 2005).

and re-emit in the near- to far-infrared. Infrared astronomy has collected a lot of data on AGB stars, in particular IRAS satellite with four photometric bands, 12, 25, 60 and 100 μm.

Presently, AGB stars produce most of the ISM replenishment in the solar neighbourhood, about 90% of the total, the remaining 10% being from Red Supergiants, Wolf-Rayet stars and Super Novae (Gehrz 1989; Sedlmayr 1994). To form dust, the temperature must be low enough to allow for conden-

sation and the density high enough to allow for sufficient interaction rate. Typically the grain temperature varies as a function of distance r as $T_*(\frac{1}{2}R_*/r)^{2/(4+s)}$ where T_* and R_* are the black body temperature and photospheric radius of the star and s is around unity. Dust emissions at different wavelengths probe different parts of the CSE. Typical condensation radii are between 5 and 10 stellar radii, in which range the temperature drops from 1000 K to 600 K and the total number density from 10^{10} to 10^8 cm^{-3}. Materials with particularly high condensation temperatures can condense as close as ~2 photospheric radii and act as seed particles for further grain growth (Lorentz-Martins & Pompeia 2000). After nucleation of seed particles, grains grow by coagulation (collisions), accretion and surface reactions. The growth efficiency is enhanced by the pulsation of the star and associated shock waves. The gas to dust mass ratio in the outflowing wind is typically between 100 and 300. Figure 1.7 shows a simulation of dust formation in the CSE of a carbon rich star (Woitke & Niccolini 2005). Typical grain densities are between 2.2 and 3.5 g cm^{-3} and sizes between a few nm to several μm.

Dust grains display special features in their spectra. In an oxygen rich environment, silicates and oxides are formed, while in a carbon rich CSE mainly carbonaceous dust is produced. Silicates, typical of oxygen-rich stars, show features near 10 and 20 μm associated with the stretching and bending mode of Si-O and O-Si-O respectively, in emission for lower mass-loss rates and in absorption for higher mass-loss rates. Silicon carbides display a feature at 11.3 μm. In comparison, the infrared excess of carbon rich stars, originating from the amorphous carbon dust, is mainly featureless. Most of the dust in O rich and C rich CSEs is amorphous and only a small amount, less than 10%, is in a crystalline state. Of the 90% of dust produced by AGB stars, about 65% are silicates and 25% carbonaceous (Gehrz 1989; Draine 2003).

The properties of dust species influence the shape of the SED. Dust absorbs the short wavelength radiation from the star and emits at longer wavelengths depending on its temperature. In order to distinguish between O rich and C rich AGB stars colour-colour diagrams can be used, such as combining the IRAS colour [12-25] and the near infrared colour [K-L]. O rich CSEs show a larger excess in the 10 to 20 μm range compared with C rich CSEs (Epchtein et al. 1987).

Finally, it must be noted that the temperature gradient in the non-equilibrium CSE is different for molecules and dust. Dust can cool and absorb more efficiently than gas. The change of the dust temperature follows the radiative equilibrium. Dust grains are generally heated by absorption of UV and visible radiation and cooled by the thermal emission of infrared photons. However, the radiative excitation of atoms, molecules or ions usually does not heat the gas (it's heated only if the medium is dense) because it does not produce kinetic energy. The gas is mainly heated by collisions and cooled by the expansion of the circumstellar envelope. In the inner part of the circumstellar envelope, the dust is usually warmer than the gas but in the interstellar medium, the dust can reach lower temperatures than the gas.

The process of dust formation is slowed down by what is called the "back warming effect": radiation cannot escape due to the high opacity, and heats up the environment. The temperature can reach high enough values to evaporate a considerable amount of dust particles and slow down the dust formation rate (Fleischer et al. 1992).

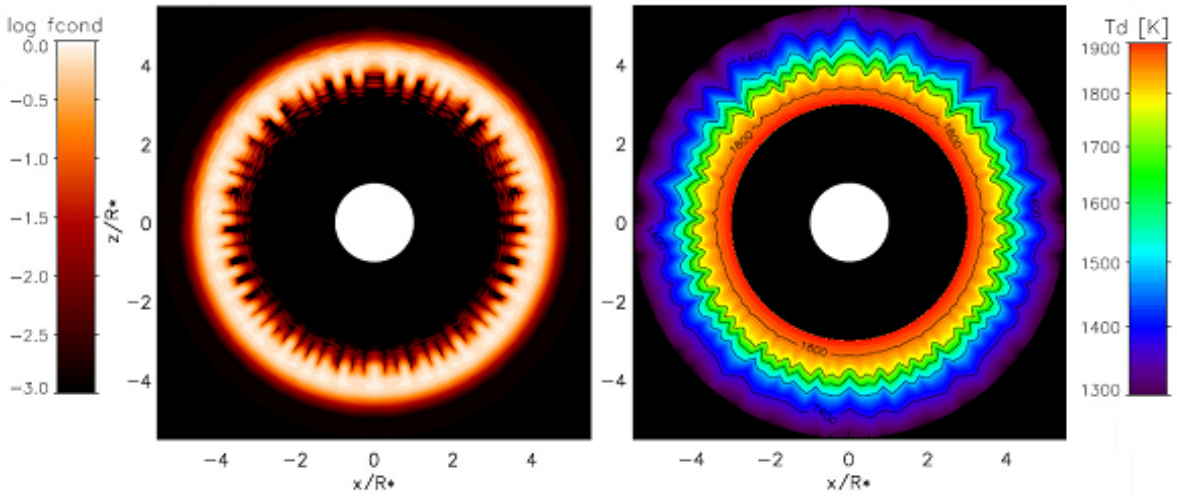

Figure 1.7: Formation of a dust shell around a carbon rich AGB star (Woitke & Niccolini 2005). The white disks mark the star photosphere and black regions are not included in the model. The star has C/O=2, T_{eff}=3600 K and $L/L_{\odot}$=3000. The degree of condensation is displayed in the left panel and the dust temperature in the right panel.

1.1.4 Gas molecules

Molecules form in the star atmosphere at ~3000 K. Among the main molecules are CO and HCN in carbon rich stars, CO in oxygen rich stars. The latter have also H_2O, OH and SiO with both masers and thermal emission. Table 1.2 lists the most abundant atoms and molecules under local thermal equilibrium (LTE) conditions, when the level populations of the molecule obey the Boltzmann distribution at the local kinetic temperature (Markwick 2000). With a model to calculate the excitation of the molecules in the circumstellar envelope, it is possible to derive mass-loss rates and abundances from observed rotational line emission profiles (Ramstedt et al. 2008).

Chemical equilibrium applies only close to the star where the time scale of chemical reactions is much shorter than the expansion of the gas. In general, abundances depend strongly on radius. Shock waves from the pulsation can heat, compress and trap the gas, enhancing OH, H_2O and SiO in O rich stars and producing polycyclic aromatic hydrocarbons (PAH) in C rich stars.

Gas molecules do not survive beyond ~1000 au due to photo-dissociation by the UV radiation of the interstellar radiation field. The photo-dissociation radius is different for each molecule. CO molecules survive until $10^{16} - 10^{17}$ cm depending on mass-loss rate and expansion velocity (Mamon et al. 1988).

The continuous absorption in AGB stars is dominated by H-bound-free and free-free absorption (except in ultraviolet and violet spectral ranges where photoionization of heavier elements like C, Si and Fe may be significant). In addition, Rayleigh scattering by H atoms and H_2 molecules is significant. However, this scattering varies with λ^{-4} and becomes less significant at infrared wavelengths. Molecular lines, vibrational and rotational, are very prominent in the infrared and radio. Figure 1.8 displays synthetic spectra of AGB stars with different C/O ratios (Gustafsson et al. 2003).

The extended atmospheric structure leads to the formation of distinct shells, called molspheres, with distinct molecular abundances. Hence different molecules are being probed at different wavelengths

Table 1.2: Most abundant atoms and molecules under LTE

O rich		C rich	
Species	Abundance	Species	Abundance
H_2	1	H_2	1
H	2.1E−1	H	3.5E−1
CO	1.1E−3	CO	1.6E−3
H_2O	2.9E−4	C_2H_2	2.2E−4
N_2	1.2E−4	C_2H	1.1E−4
SiO	6.9E−5	N_2	9.5E−5
S	2.6E−5	HCN	8.5E−5
OH	9.0E−6	Si	6.3E−5
SH	7.7E−6	CS	2.3E−5
O	1.3E−6	SiS	9.8E−6
H_2S	7.2E−7	C_3H	9.5E−6

and different distances from the star (Baschek et al. 1991; Scholz 2001; Mennesson et al. 2002; Tej et al. 2003; Ohnaka 2004).

Maser emission is common in AGB envelopes. By stimulated emission, the masing species amplifies the radiation. The typical brightness temperature of such strong maser emission is much higher than the local temperature. SiO masing regions are dominated by the mass-loss process and pervaded by shock waves associated with pulsation. Maser emission is also found at large distance (e.g. OH maser 1612 MHz at distances from ~ few 100 au to ~2000 au).

1.1.5 Variability

Most AGB stars are variable with periods in the 100 to 1000 days range. Over 90% of TP-AGB stars are variable at the level of at least a few % in amplitude (Wood et al. 1999). While most variations are caused by pulsation, a few are caused by episodic ejection of dust shells or orbiting dust clouds. Based on the values taken by the amplitude and period of the optical light curve, they are classified as Miras, semi-regulars (SR), and irregular (L). The oxygen rich Miras, with periods smaller than 300 days appear at high galactic height ~500 pc, compared with typical ~200-300 pc for M-, S- and C-variables. They are low mass stars that do not experience the third dredge-up and have no technetium in their spectrum.

AGB stars exhibit an important fourth class, known as OH/IR stars. They have high mass-loss rates (10^{-6} – 10^{-4} $M_\odot\,yr^{-1}$) and long pulsation periods. A dense dust-gas CSE makes them usually too faint to be observed in the visible. The re-emission of the dust particles at IR wavelengths excites the OH maser emission which was first detected from circumstellar envelopes by Wilson & Barrett (1968). The infrared amplitudes are much smaller than the visible amplitudes, because the shorter visible wavelengths are in the Wien part of the spectrum where the sensitivity to effective temperature is larger.

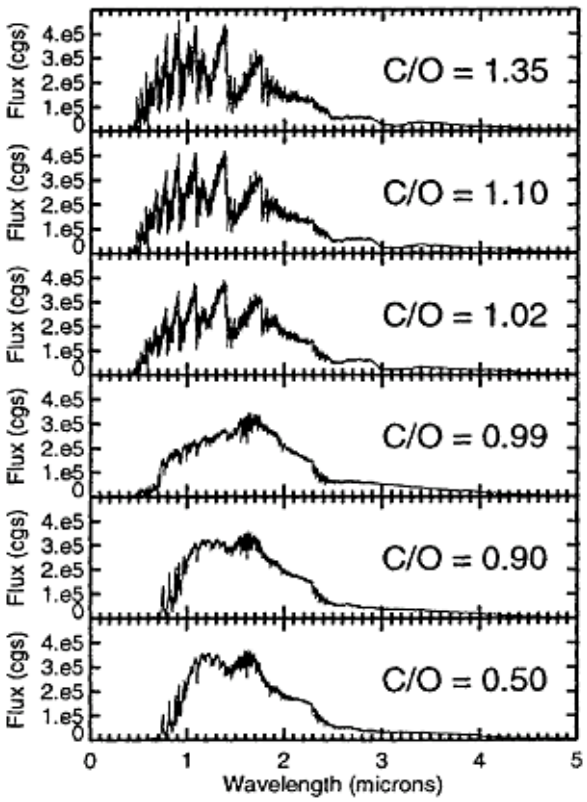

Figure 1.8: Synthetic spectra of AGB stars with different C/O ratios (Gustafsson et al. 2003).

Luminosities and periods are correlated as illustrated in Figure 1.9. The K magnitudes and variable periods were obtained from the 2.3 m telescope of the Australian National University and MACHO data, respectively. Sequence C includes mostly Miras which obey the relation $K_0 = 11.13 - 3.78(\log P - 2.4)$ (Hughes & Wood 1990). They are the largest amplitude variables. Sequence B stars have lower amplitudes (<0.5 mag) and are known as SR variables. The very low amplitude (<0.2 mag) Sequence A stars are called Small Amplitude Red Variables (SARVs). Sequence D stars present two kinds of periods: the primary period usually falls on sequence B and the long secondary period, which is 3-4 times longer than those of sequence C, falls on sequence D. Sequence E is populated by so-called First Giant Branch (FGB) stars. Their light curves are similar to those of eclipsing stars. Pulsations appear in the Early AGB period obeying the period-mass-radius (PMR) relation of Fox & Wood (1982), $P = P_0 R^{\alpha} M^{-\beta}$ with α between 1.5 and 2.5 and β between 0.5 and 1.0. As the radius, and hence the luminosity increases, new pulsation modes appear.

Radial oscillations result from sound waves resonating in the interior of the star. The physical process, called opacity or κ mechanism, results from ionization of hydrogen from energy produced in the contraction phase: the ionization increases the opacity and causes the layer to absorb the heat.

The mass-loss rate is observed to be correlated with their pulsation period (Schild 1989; Whitelock 1990; Wood 1990) suggesting that pulsation plays a role in the mass-loss mechanism (Bowen & Willson 1991; Fleischer et al. 1992; Höfner & Dorfi 1992).

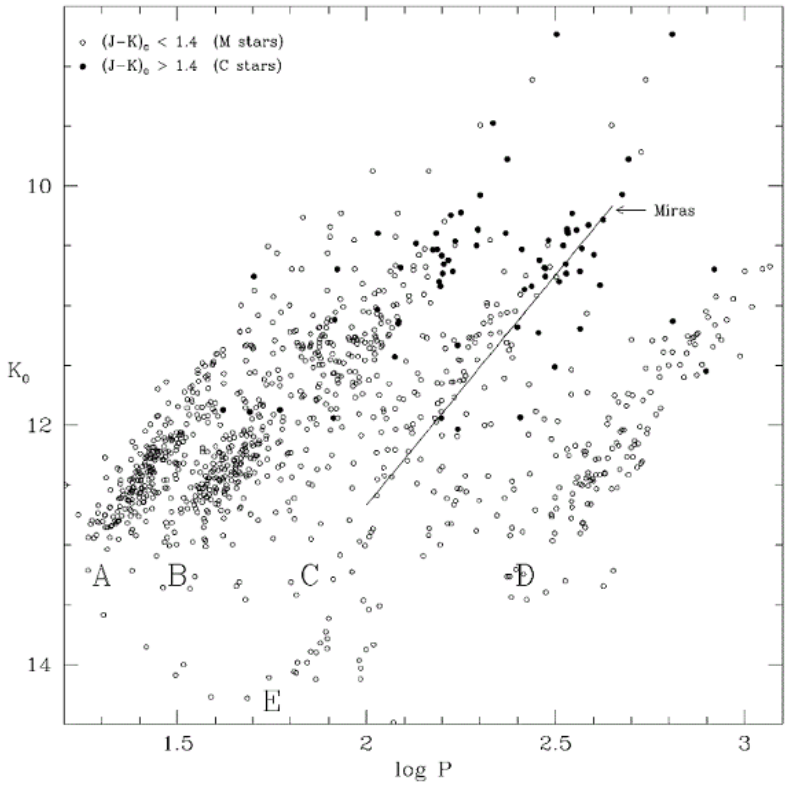

Figure 1.9: Period-luminosity relation for optically visible red variables in a 0.5°×0.5° region of the LMC. The solid line shows the Hughes & Wood (1990) relation for Miras.

1.1.6 Mass-loss rate

The mass-loss rate of AGB stars varies with time on different scales: on a few hundred days scale due to pulsation (Fleischer et al. 1999), on a few 10^4 years scale in relation with the thermal pulse cycle (Olofsson et al. 2000) and on some 10^5 years scale due to evolution on the AGB branch (Bedijn 1987), culminating with the formation of a superwind at the end of the AGB phase.

The wind driving mechanism, i.e. the source of outward momentum that overcomes gravity, could be provided by the gradient of gas pressure (thermal wind), by absorbing stellar radiation and re-emitting photons in all directions (radiation-driven wind) or by acceleration through waves (sound waves and shocks). The current understanding is that it is dominated by radiation absorbed by dust grains that transfer momentum to the gas by collisions. The winds of AGB stars are slow compared with other types of stars, typically 10 to 20 km s^{-1}, while mass-loss rates are high, typically 10^{-6} solar masses per year. This implies high gas densities: the wind must have its source in a dense environment. In order to lift the gas up in the regions where dust can condense, large amplitude pulsations are essential.

Figure 1.10 shows how the pulsation leads to large scale motion of the outer layers, part of which escapes gravity. The higher opacity of dust compared with the gas from which it was formed leads to an effective acceleration. Further grain growth and acceleration is regulated by the competition between falling temperatures that favour condensation and decreasing gas density that slows down grain growth. The final degree of condensation and the abundance determine the terminal velocity of the pulsation-

enhanced dust-driven wind and the mass-loss rate (Winters et al. 2000).

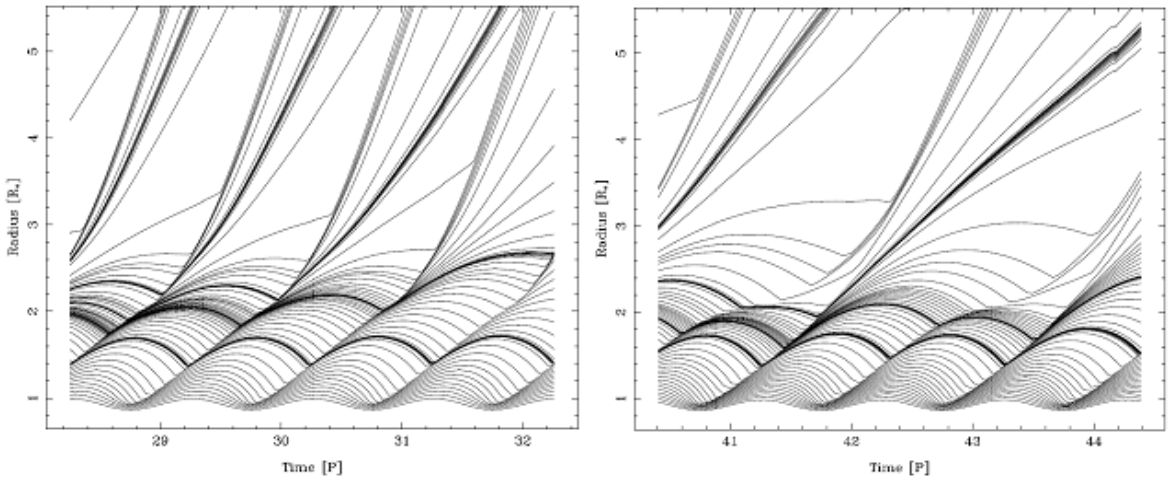

Figure 1.10: Positions of selected mass shells in AGB atmospheres for two C/O values, 1.77 (left) and 1.49 (right) (Höfner & Dorfi 1997). Time is measured in piston periods P and radius in units of stellar radius. Model parameters are (L_*, M_*, T_* and P): 10^4 $L_\odot$, 1.0 $M_\odot$, 2700 K and 650 days.

In the present hydrodynamical models, the wind at dust nucleation radius starts subsonic and reaches supersonic velocities at sonic point. With increasing MS star mass, i.e. with increasing luminosity and higher metallicity, the terminal velocity increases, reaching typically 15 to 20 km s^{-1}. At some 5 stellar radii, the wind velocity has already reached 90% of the terminal velocity. The terminal velocity depends also on the underlying chemistry, carbon rich CSEs expanding faster than oxygen rich CSEs for similar mass-loss rates and pulsation behaviours.

While it is commonly agreed that dust is the main accelerating agent, the difficulty is to obtain grains that are opaque enough to absorb a sufficient quantity of radiation from the star, but that are transparent enough not to sublimate at radii where the radiation pressure is high enough. It was already noted in 2006 (Woitke 2006) that too little radiation pressure is exerted on dust to accelerate the winds of oxygen-rich AGB stars. The recent observation of dust grains at very small radii (Norris et al. 2012) offers a solution to this puzzle. They present spatially-resolved, multi-wavelength observations of circumstellar dust shells of three AGB stars. When imaged in scattered light, dust shells are found at remarkably small radii (<~2 stellar radii) and with unexpectedly large grains (~300 nm radius). This proximity to the photosphere argues for dust species that are transparent to starlight and therefore resistant to sublimation by the intense radiation field. While transparency usually implies insufficient radiation pressure to drive a wind, the radiation field can accelerate these large grains via photon scattering rather than absorption − a plausible mass-loss mechanism for lower-amplitude pulsating stars.

From the observations in calcium ionization lines from red giant CSs, Reimers (1975) described the mass-loss rate of red giants, $\dot{M} = \eta L_* R_* / M_*$, with L_*, R_*, M_* standing for luminosity, radius and mass of the star in solar units. However, this relation does not work well for AGB stars: their mass-loss rate must be estimated from the circumstellar CO radio line (Knapp & Morris 1985) and from dust continuum emission. The CO lines are strong, the energy level diagram is simple and radiative transition rates and collisional cross sections are known. Various authors have proposed formulas meant to evaluate

the mass-loss rate for various types of AGB stars, such as Schöier & Olofsson (2001) for bright C stars. However, as pointed out by Willson (2007) and Ramstedt et al. (2008) such ad hoc formulas should be used only to provide an order of magnitude estimate of the mass-loss rate, the complexity of the problem making reliable predictions difficult. A summary of the current situation is given by Ramstedt (2009a).

As the final white dwarf mass does not exceed 1.4 solar mass, it is clear that stars with MS progenitor masses of up to 8 solar masses have to lose much more material than lower mass stars in the AGB phase. Figure 1.11 displays the evolution of a 1.5 solar mass star during the AGB phase. Luminosity, L, period, P and expansion velocity, v gradually increase while the effective temperature decreases. The extremely enhanced mass-loss rate at the end of the AGB phase causes a steep decline of the mass. After this "superwind" epoch, a hot white dwarf remains with a stellar envelope mass not exceeding 1‰ of a solar mass. The figure also shows the correlation of mass-loss with TPs, on a time scale of 10^2 to 10^3 yr. The total mass return of all AGB stars in the Galaxy is presently estimated to exceed 0.3 solar masses per year (Habing & Olofsson 2004).

The idea that the wind accelerates at the end of the AGB phase from velocities in the 30 km s^{-1} ballpark to velocities in the 100 km s^{-1} ballpark, and that the new "superwind" interacts with the old wind to eject huge masses of gas is old and well accepted (Kwok et al. 1978; Kwok 2002). However, the mechanism that triggers such "superwinds" is unclear. It has been suggested (Lagadec & Zijlstra 2008) that superwinds have a dual trigger: either when sufficient excess carbon builds up for efficient formation of carbonaceous dust or when luminosity reaches a value sufficient for producing a silicate-dust-driven wind.

1.2 Asymmetries in AGB and Post AGB stars

1.2.1 Generalities on asymmetries

Stars are spherical during most of their life but toward the end of the AGB phase, non-spherical shapes of the circumstellar envelope become common. In particular bipolar outflows suggest an axi-symmetric envelope with an equatorial concentration in a disk or torus. With the transition from a post AGB star to a Planetary Nebula (PN), departure from symmetry becomes more and more prominent resulting in a zoo of very different morphologies (Figure 1.12).

The transition from sphericity to small asymmetries in the AGB phases and extreme asymmetries in PNe is not understood in details. Possible causes include stellar rotation, binarity, magnetic fields, large convection zones or clumpiness of the wind.

AGB stars, Post-AGB stars (for a review see van Winckel 2003) and young Planetary Nebulae have been observed at infrared, mid-infrared, far-infrared, millimetre and submillimetre wavelengths. Morphologies including a bipolar outflow and/or an equatorial disk or torus have been observed in both the dust and molecular gas content of the CSE.

Bipolar outflow is common in PN and sometimes in post-AGB stars (Lagadec et al. 2011) but rarely in AGB stars. The velocity spectra appear as a superposition of a narrow component associated

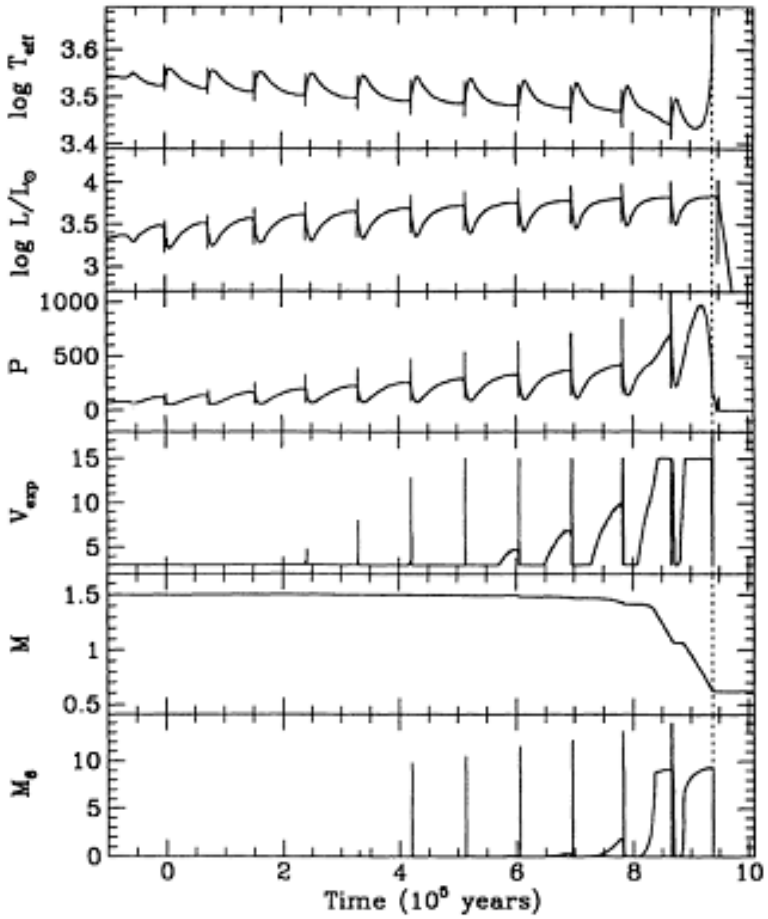

Figure 1.11: Time dependence (starting from the first TP) of various quantities during the TP-AGB phase of a star having a mass of 1.5 solar masses. The dotted line marks the end of the AGB phase. M_6 is the mass-loss rate in units of 10^{-6} solar masses per year (Vassiliadis & Wood 1993).

with the slowly expanding structure (sphere or shell or torus) and a broader component associated with the bipolar outflow (Libert et al. 2010b). Superwind velocities, of several tens of $\mathrm{km\,s^{-1}}$, are only observed at the late post-AGB or PN phases. The bipolar outflow is often associated with a torus of dust and gas, to which it is perpendicular, a compact Keplerian disk or torus in the early phases, an expanding torus in the late phases (Castro-Carrizo et al. 2012). The formation of the bipolar outflow is still not clear. Rotation may be invoked to explain some of the observed axisymmetry (Dorfi & Höfner 1996) but the most popular models rely on binarity and/or magnetic fields. Binarity is claimed as being a cause of the formation of the torus (Maercker et al. 2012).

The interaction between the two material flows of different velocities and/or densities can produce arcs, bow shocks or head-tail structures (Matthews et al. 2013; Cox et al. 2012) in the outer part of the circumstellar envelope. The bow shocks usually appear in strong wind stars and fast moving stars. They are the results of the wind-ISM interactions (see models of Keppens et al. 2012; Villaver et al. 2003).

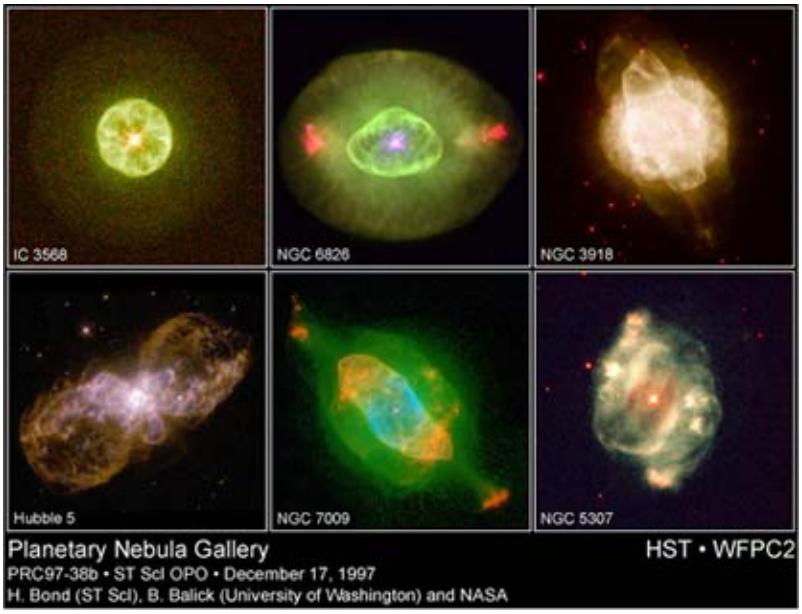

Figure 1.12: A HST gallery of Planetary Nebulae.

1.2.2 Binaries

Many cases of binary AGB, post-AGB and PN have been reported. The role of close companions in triggering important asymmetries has been studied extensively (for reviews see Jorissen 2004; Pols 2004).

Figure 1.13 (Jorissen 2004) summarizes binary evolution involving mass transfer from an AGB star. Spectral families for single stars are listed in the left column while the right column identifies classes of peculiar red star (PRS) requiring binarity. Stars with excess C and Ba at their surface are represented by hatched disks. It is essential to distinguish between binaries where the AGB star is the less evolved of the pair from binaries where the AGB star is the more evolved of the pair. In the first of these cases, the companion is a white dwarf and the AGB star has been polluted earlier on, when the companion was on the AGB branch, in particular by s-process elements. A diagnostic is the over-abundance of barium (one speaks of barium stars). Of particular interest is technetium (Tc), which has no stable isotope, and which therefore disappears before the secondary star enters the AGB branch. Hence the essential distinction between intrinsic S stars, which display Tc lines and therefore are themselves producing Tc and extrinsic S stars, which although having entered the AGB branch have not yet produced Tc of their own but are polluted by other s-process elements accreted when the primary star was evolving on the AGB branch (Jorissen et al. 1993; Groenewegen 1993; Jorissen et al. 1998).

Mass transfer may occur by Roche lobe overflow, with matter leaking through the Lagrange point L1, tidal interactions or eccentricity pumping (Dermine et al. 2013) and results in a common circumbinary envelope or a torus/disk surrounding the companion. Most studies are on close binaries and give evidence for the role of the companion in shaping the asymmetric morphology with an equatorial torus (see for example van Winckel et al. 2009; Jorissen et al. 2009).

In the case of wide binaries, the companion plays a lesser role but is still likely to accrete some gas

and induce a weak asymmetry or produce structures such as spirals or detached shells (He 2007; Perets & Kenyon 2012; Mastrodemos & Morris 1999; Soker 1999; Maercker et al. 2012). The case of Miras, which are mostly second generation AGB "symbiotic" binaries, with a white dwarf companion, has been much studied.

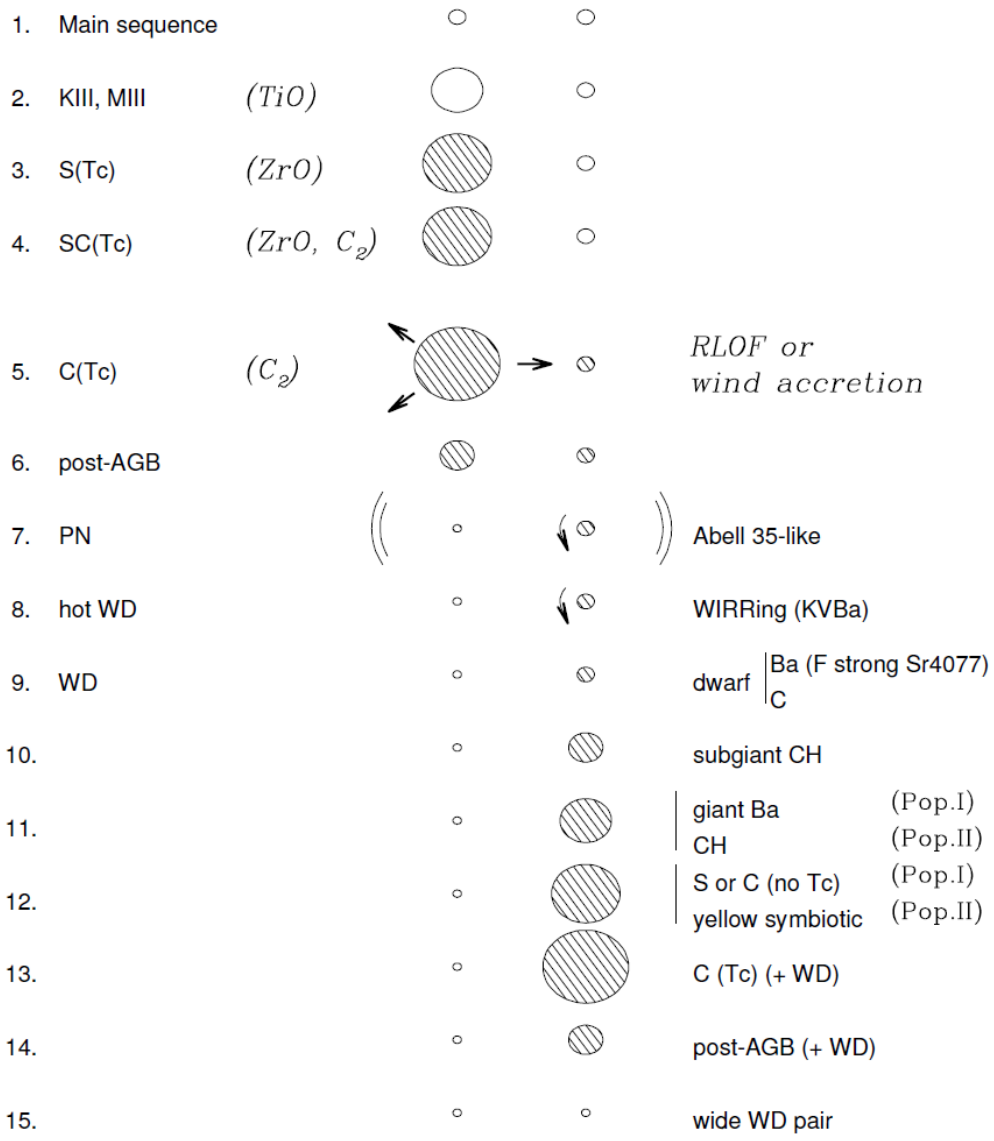

Figure 1.13: Schematic evolution of close binaries (Jorissen 2004).

A qualitative description of the main features of the mass transfer mechanism in the so-called "transient torus" scenario (Frankowski & Jorissen 2007) is sketched in Figure 1.14. It starts with wind accretion around the companion, then tidal forces and expansion of the AGB star bring it closer to its Roche lobe and matter is funnelled through Lagrange point L1; matter escaping through the vicinity of L2 starts forming a spiral that evolves to a thick circumbinary torus which expands and leaves behind a Keplerian circumbinary disk. The orbital parameters are not much affected by this mass transfer mechanism because only a small part of the ejecta is set in Keplerian motion, removing only little angular momentum from the binary

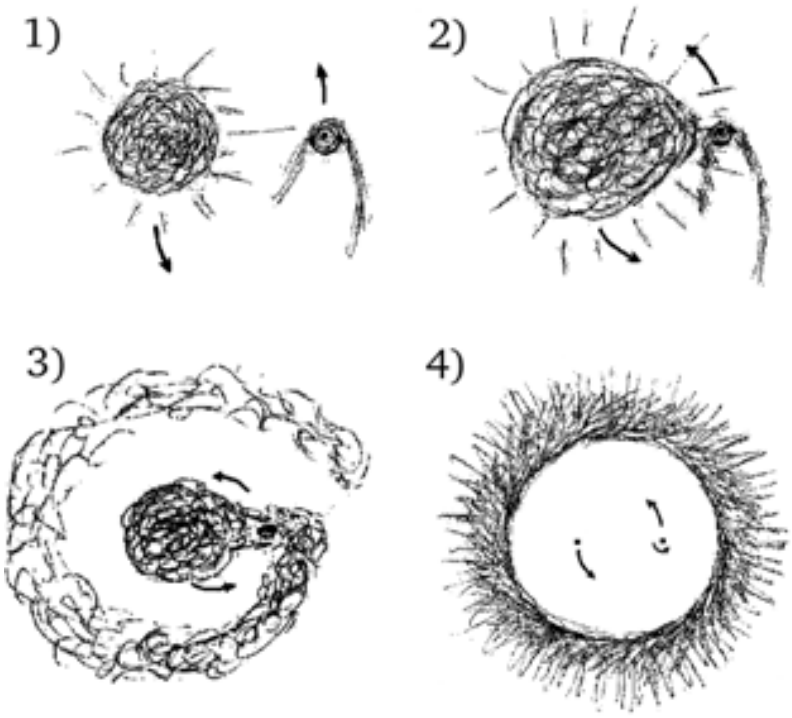

Figure 1.14: The transient torus scenario (Frankowski & Jorissen 2007).

1.2.3 Magnetic fields

Ground state OH maser emission from evolved stars is usually polarized providing a powerful probe of the magnetic field structure in the outer regions of circumstellar envelopes. Measurements performed using OH, H_2O and SiO masers give evidence for magnetic fields at mG scale or more associated with bipolar morphologies, the masers occurring on the bipolar outflow at large distances from the central star (Wolak et al. 2011; Amiri 2011; Inomata 2007; Vlemmings et al. 2006). Recently (Pérez-Sánchez et al. 2013) radio emission with a SED consistent with a synchrotron jet embedded in a sheath of thermal electrons has been observed on a post-AGB star and found to have the same morphology as observed in the mid-infrared (Figure 1.15). The jet is collimated by a ~1 mG magnetic field at ~7000 au from the central star. There have also been sub-millimetre polarimetric observations revealing the magnetic field lines by measuring the dust alignment (Sabin et al. 2007) that give evidence for the magnetic field to align with both the equatorial torus and the bipolar outflow in post-AGB stars and young PNe.

Modelling the magnetic field structure from first principles has been attempted by several authors, each stressing different aspects or features of the mechanism at play (Matt et al. 2000; Soker 2002; Huarte-Spinosa et al. 2012; Dennis et al. 2009). Particularly interesting is the argument that an AGB star can generate a strong magnetic field having as its origin a dynamo at the interface between the rapidly rotating core and the more slowly rotating envelope of the star (Blackman et al. 2001). The fields are strong enough to shape the bipolar outflow that produces the observed morphology of the post-AGB star and planetary nebula. Magnetic breaking of the stellar core during this process may also explain the puzzlingly slow rotation of most white dwarf stars. Such dynamo action has recently been successfully incorporated in MHD models (Pascoli & Lahoche 2010).

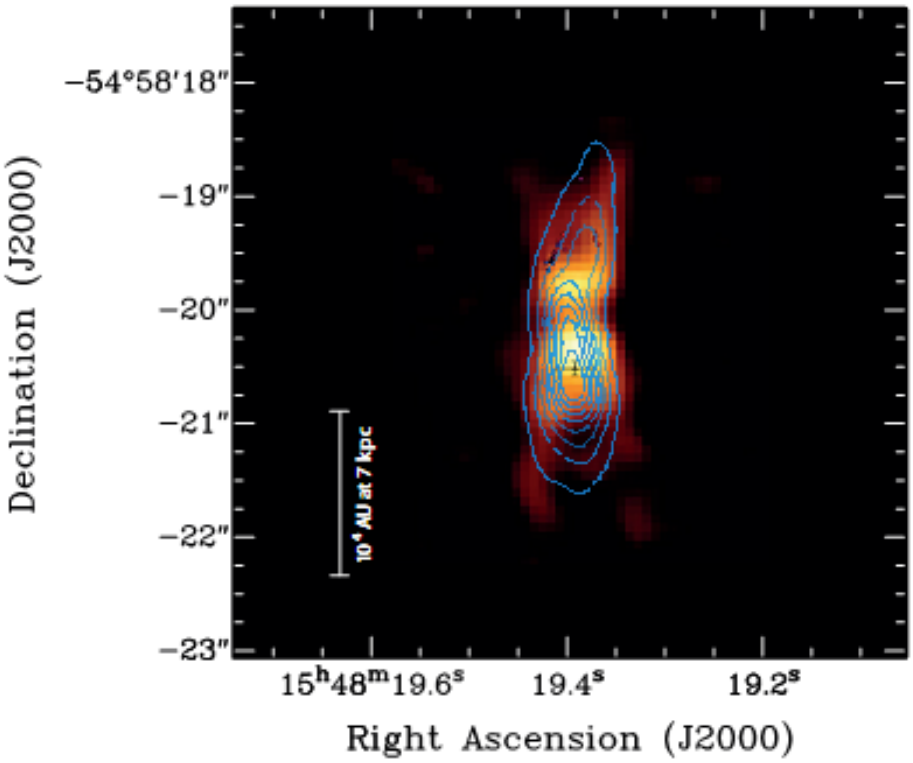

Figure 1.15: Radio continuum map of post-AGB star IRAS 15445-5449 at 22.0 GHz (contours) overlaid on the mid-infrared VLTI image.

1.2.4 Interaction with the ISM

The interaction of the wind of evolved stars with their ISM environment (for a recent review see Villaver et al. 2012) shows the expelled wind sweeping up the surrounding interstellar medium. Evidence for the interaction of the stellar wind of AGB stars with the ISM has been obtained by Herschel in far-infrared with different morphologies (Cox et al. 2012). Strong correlations between the star velocity with respect to the ISM and the morphology of the source are predicted and observed.

Atomic hydrogen is a good tracer of the interaction of the circumstellar envelopes of evolved stars with their ISM environment. Hydrogen dominates the stellar wind and is mostly in atomic form in the stellar atmosphere as long as the effective temperature exceeds 2500 K (Glassgold & Huggins 1983). It is expected to remain in atomic form in the expanding wind and to be protected from photoionization by the ISM H I that absorbs UV photons of energy sufficient to ionize the atom. However its detection is difficult due to the contamination by the very same ISM H I emission, making it difficult in practice. Recent observations have been recently reported (Matthews et al. 2011; Matthews & Reid 2007; Libert et al. 2008, 2009, 2010a; Gardan et al. 2006; Le Bertre et al. 2012; Gérard & Le Bertre 2006). Most observations reveal the presence of a narrow component, $\leq$3 km s^{-1}, centred on the stellar velocity and, in some cases, of a wake of gas in the direction opposite to the movement of the star in the ISM.

Observations in the far infrared (Mayer et al. 2011; Ueta et al. 2010; Jorissen et al. 2011) give evidence for shock and turbulence as well as for bipolar asymmetry correlated with the star movement in the surrounding ISM (Raga & Cantó 2008).

1.3 Outline

In this thesis I present my contribution to the study of mass losing AGB stars and of their circumstellar environments. I have been mainly interested in the development of stellar outflows, and in the interaction with their surrounding medium, in which stellar matter is eventually injected.

To probe these environments I have used the emission from two tracers. The carbon monoxide (CO), through its rotational lines in the millimeter range, can probe the inner regions of the circumstellar shells, out to its photodissociation by UV radiation from the interstellar radiation field. On the other hand, the atomic hydrogen (H I) line at 21 cm can probe, in principle, the entire circumstellar shell (CS), although with a lower sensitivity and spatial resolution than CO. It is therefore better fitted to the study of the external parts of CSs.

The heterodyne technique used in the radio range offers the possibility to observe these sources with a very high spectral resolution, which is perfectly suited to resolve the CO and H I line profiles, allowing us to explore the kinematics of the relatively slow outflows of red giants. In chapter 2, I will present a few facts on radioastronomy with emphasis on the telescopes that have produced the data discussed in this thesis, and on the formation of the CO and H I radio lines.

In chapter 3, I discuss in detail the case of an S-type star (RS Cnc) that has been observed in CO lines with the IRAM telescopes, as well as in H I with the VLA. In this chapter I concentrate on the modelling of the spatially resolved CO line profiles, an approach that has been at the heart of my research. Furthermore, the complementarity between H I and CO is illustrated in a paper on RS Cnc, now published in A&A (Hoai et al. 2014, reproduced in an appendix).

In the following chapters, I present results of the CO modelling of other sources observed at IRAM, EP Aqr (Chap. 4), and X Her and RX Boo (Chap. 6), three M-type stars, and with ALMA, HD 44179 (the Red Rectangle, Chap. 5), a post-AGB star.

Finally, in chapter 7, I discuss the formation of the H I line profile in various cases of mass losing AGB stars, and explore several effects that might explain the lack of detected emission from stars with high mass-loss rates. I present also a modelling of the spatially resolved H I line profiles of Y CVn, a carbon star observed with the VLA.

In chapter 8, I summarize the main results obtained through this work, and present my objectives for the future.

In my work, I concentrated on AGB stars with low mass-loss rate (10^{-7} solar masses per year) in order to limit the hiding effect of large optical depth close to the central star. They are also the sources for which the H I line is more easily detected. This introduces a selection bias in my sample of sources, that should be kept in mind when interpreting the results of this thesis.

Chapter 2

RADIO ASTRONOMY

2.1 Overview

Radio waves have wavelengths in the millimetre to kilometre range. Above 100 m they are reflected by the ionosphere and cannot reach ground but in space, beyond the ionosphere, one can in principle detect radio waves from celestial sources up to 10 km wavelength. The first radio astronomical observations were made in 1932 by Karl Jansky, a Bell Lab physicist who detected cosmic radio noise from the Milky Way while investigating radio disturbances interfering with transoceanic communications. Since then, astronomers have built many radio telescopes with sophisticated systems that allow for a high angular resolution resulting in the production of detailed radio pictures of celestial objects.

Radio astronomy developed fast after World War II, focusing first on the most intense radio sources: Sun, Super Nova Remnants (SNR), the centre of the Milky Way (SgrA*), quasars, Active Galactic Nuclei (AGN). The 21 cm hydrogen line allowed for the exploration of the galactic and extra galactic Universe. Millimetre radio astronomy developed in the last quarter of the XXth century.

Radio telescopes have two basic components: a large radio antenna (or set of antennas) and sensitive radio receivers (Figure 2.1).

In most cases, incoming signals are collected by the dish of the antenna and reflected by its parabolic surface to the focus where there is either a receiver (possibly multiple) or another reflector (sub-reflector) before focusing on the receiver. Usually, the sub-reflector and the receiver are fixed with respect to the primary dish, which is movable. However, in some cases (such as Arecibo, FAST), the primary dish is fixed and the receiver is movable. The receivers are cooled down to 3 K in order to minimize thermal noise. A single receiver responds to one polarization component, double receivers being required to observe both polarization components simultaneously.

Monochromatic fluxes (also called flux densities, i.e. fluxes per unit of frequency) are expressed in Jansky (10^{-26} Wm^{-2}Hz^{-1}). When the flux has its source in thermal emission, the frequency spectrum is that of a black body with a Planck distribution multiplied by the emissivity. In the case of radio waves, where one is dealing with large wavelengths, the Planck relation reduces to the so-called Rayleigh-Jeans relation: the flux density I is related to the black body temperature T through the relation $I =$

$2kT/\lambda^2$ where k is Boltzmann's constant and λ the wavelength. The minimum detectable temperature (or detectable change in temperature) is equal to $T_{min} = T_r/\sqrt{B\tau}$ where B is the bandwidth of the detector, τ the integration time and T_r the noise temperature of the receiver. The minimum detectable flux is therefore $2kT_{min}/\lambda^2$. With a fixed noise temperature receiver, we can detect a smaller level of temperature by increasing the bandwidth and/or the integration time.

Figure 2.1: The 30 m dish of the IRAM Pico Veleta radio telescope.

The sensitivity of a radio telescope, the ability to measure weak sources of radio emission, is proportional to the area and efficiency of the antenna and the sensitivity of the radio receiver used to amplify and detect the signal. For broadband continuum emission the sensitivity also trivially depends on the bandwidth observed.

The angular resolution, or ability of a radio telescope to distinguish two neighbour sources, namely fine details in the sky, is limited by diffraction: it is proportional to the ratio between the wavelength of observation and the diameter of the antenna of the instrument. The angular resolution is also affected by atmospheric turbulences causing changes of the signal phase. At radio wavelengths, relevant turbulences mostly come from the water vapour confined within the troposphere (<10 km). The atmospheric transmission of the signal is lower at larger amount of water vapour (Figure 2.2). The amount of water vapour is highly variable in time. Thus, we need a real-time calibration of signal attenuation and phase fluctuation. Determining and removing the phase noise are essential tasks in interferometer observation.

Radio waves penetrate much of the gas and dust in space as well as the clouds on certain frequency windows of planetary atmospheres and pass through the terrestrial atmosphere with little distortion. In principle, radio astronomers can therefore obtain a much clearer picture of stars and galaxies than is possible by means of optical observation from ground. However this would require the use of very large antennas.

The first large parabolic antenna was built in Jodrell Bank (United Kingdom) in 1957 with a diam-

eter of 75 m for wavelengths larger than 15 cm. The largest movable parabolic antennas are 100 m in diameter (Effelsberg, Germany and Green Bank Telescope (GBT)). Building significantly larger movable antennas is not possible: thermal and mechanical deformations distort the shape of the dish beyond the permissible limit, i.e. a fraction of a wavelength – typically one tenth. Better angular resolutions are achieved with interferometers with baselines that may be as large as the Earth diameter or even larger when a satellite is used in combination with ground-based telescopes. Fixed antennas built on ground, as the Nançay radio telescope, the Arecibo (Porto Rico, 300 m diameter) and FAST (China, 500m diameter) antennas offer excellent sensitivities, however with limited angular resolution compared with interferometers.

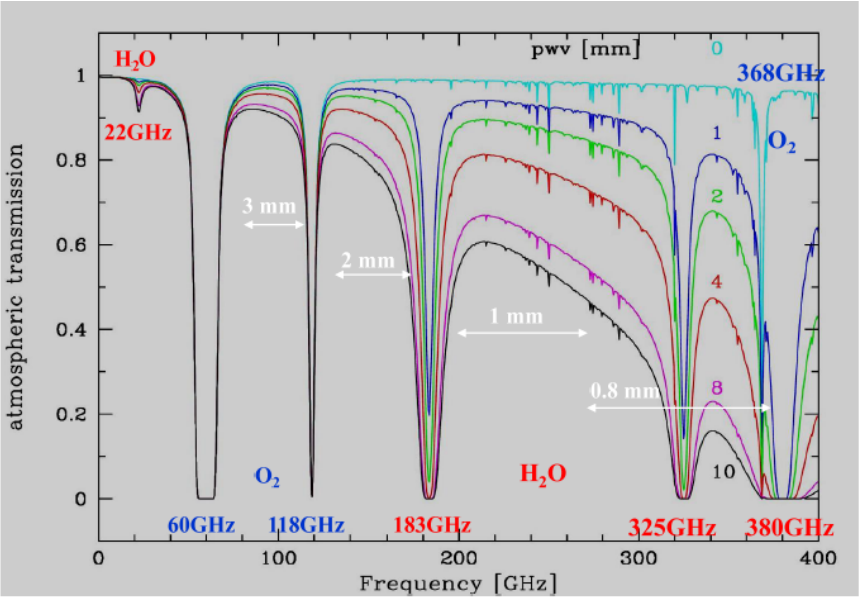

Figure 2.2: Dependence on frequency of the atmospheric transmission at PdBI (2550 m). The different transmission curves are calculated for the amounts of water vapour (in mm) given on the right.

Radio sources can produce radio waves by thermal emission (usually resulting from the thermal movement of electrons and ions in a plasma) or by non-thermal emission (such as synchrotron radiation or maser). Thermal emission obeys the Rayleigh Jeans relation. In addition to such continuous spectra there are also line spectra in radio astronomy as there are in the visible and IR. Among these the 21cm hydrogen line, corresponding to the spin-flip of the electron of a neutral hydrogen atom, and the millimetre rotation lines of the CO molecule, both used in the present work, are ubiquitous. Line spectra allow for a measurement of the Doppler velocity of the source. Measuring the polarization of radio waves, which requires two independent receivers, provides useful additional information.

2.2 Radio instruments

2.2.1 Antennas

The elements of a standard radio telescope are the reflector, feed, transmission line and receiver. The reflector collects power from an astronomical source and provides directionality. The power collected by an antenna is approximately given by $P = I_\nu A \delta\nu$ where I_ν is the flux density on Earth from some astronomical source, A is the effective area of the antenna and $\delta\nu$ is the frequency interval or bandwidth of the measured radiation. An antenna operates the same way whether it is receiving or transmitting radiation (so-called reciprocity theorem). So the response pattern of an antenna, or Point Spread Function (PSF), is the same whether the antenna is receiving or emitting. It has a typical cardinal-sine (rectangular aperture), or Airy (circular aperture) shape, with a central lobe of size $\theta = \lambda/D$ (where λ is the wavelength and D the dish diameter) surrounded by side lobes (Figure 2.3). The beam width (the width of the central lobe) θ is also a measure of the directivity of the antenna. More precisely, the angular pattern of the electric field in the far-field is the Fourier transform of the electric field distribution across the aperture.

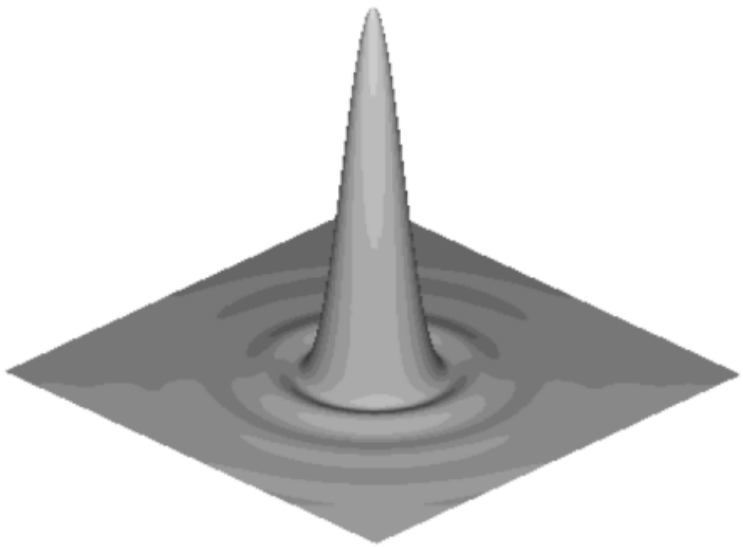

Figure 2.3: PSF pattern of a typical parabolic antenna response.

Radio and radar engineers normally speak about antennas in terms of their gain in dB calculated as the ratio of powers P or voltage V: $G = 10\lg(P_{out}/P_{in}) = 20\lg(V_{out}/V_{in})$. A factor 2 in power or voltage is 3 dB in gain (+ for amplification and − for attenuation), a factor 10 is 10 dB. The gain, G, of an antenna relative to the full solid angle 4π is related to its effective collecting area, A, by $G = 4\pi A/\lambda^2$ where λ is the wavelength. This means that the power collected in the pointing direction by an effective area A is G times higher than what an ideal isotropic antenna would collect, namely $\lambda^2/4\pi$. The beam solid angle is $\Omega_A = 4\pi/G$ corresponding to a cone of arctan$(2/\sqrt{G})$ half aperture (measured in radians). The gain is therefore related to the directivity of the antenna: an antenna with a smaller beam will have a higher gain. The effective aperture of an antenna is always smaller than its physical aperture due to the power

dissipation caused by heating in the resistance of its elements, non-uniform illumination on its feed, and scattering radio waves by structural supports and diffraction at the aperture edge. Their ratio (aperture efficiency) is between 0.35 to 0.7 and can range up to 0.9 in some cases. Parabolic dishes, in particular when unobscured and equipped with compensating deformation structures collect well the radio waves and have a high aperture efficiency.

The noise is a very important performance parameter along with the gain or equivalent effective aperture. In radio astronomy, it is characterized by system noise temperature which includes receiver temperature and antenna noise temperature. With the availability of excellent Low Noise Amplifiers (LNAs), optimizing the antenna efficiency is less important than optimizing the ratio of efficiency to system noise temperature or gain over system temperature, G/T_s. This means that using a feed with low side lobes and slightly under-illuminating the dish may reduce T_s by more than it reduces G and so improve sensitivity.

Receiver noise originates from Ohmic losses in electronic circuitry. The antenna noise can be divided into two types: one due to the loss resistance of the antenna and the other to electromagnetic radiation of non-zero temperature objects in the surrounding environment: ground, spillover, atmospheric noise and even sky noise (air showers, CMB...). While the atmospheric and sky noise cannot be acted upon, the other noises can be made small by a good design. Sky noise is frequency dependent but never gets any lower than the 2.7 K cosmic microwave background. Atmospheric and sky noise are time dependent. The lowest system noise achievable is about 18 K with ground-based telescopes.

2.2.2 Receivers

After the antenna, the first stage of the receiver, the low-noise amplifier (LNA), is probably the most important component of a radio telescope. Since the signals are so weak, the noise performance of the receiver is crucial, and this leads to extraordinary efforts, such as cryogenic cooling, to reduce noise in the LNA. The noise performance of radio-astronomy receivers is usually characterized by an equivalent system temperature, Tsys, referred to the feed or even to outside Earth's atmosphere. Using temperature units for the system allows direct comparison with source temperatures. Typical system temperatures of ground-based antennas are ten to a hundred K for centimetre wavelengths or up to several hundred K for millimetre and sub-millimetre wavelengths.

Most receivers use so-called super heterodyne schemes. The goal is to transform the frequency of the signal (SF) down to a lower frequency, called the intermediate frequency (IF) that is easier to process, but without losing any of the information to be measured. This is accomplished by mixing the SF from the LNA with that from a local oscillator (LO) and filtering out any unwanted sidebands in the IF. A bonus is that the SF can be shifted around in the IF, or alternatively, the IF for a given SF can be shifted around by shifting the LO.

Inside radio-astronomy receivers, a signal is usually represented by a voltage proportional to the electric field (as collected by the antenna). As it averages to zero, one needs a device that produces an output proportional to the square of the voltage, a so-called square-law detector, and that averages over at least a few cycles of the waveform.

It is not unusual to detect and measure signals that are less than 0.1% of the system noise. The increase in power, measured in K, due to the presence of a radio source in the beam is given by $2kT_a = AI$ where A is the effective aperture (or aperture efficiency times physical aperture), I is the radio flux density in $\mathrm{Wm^{-2}Hz^{-1}}$, and k is Boltzmann's constant, 1.38 10^{-23} $\mathrm{WHz^{-1}K^{-1}}$. While voltages in the antenna add up linearly at a given time, the lack of coherence between signal and background (unrelated phases) implies that they must be added in quadrature (i.e. the square root of the sum of their squares) to obtain the summed voltage averaged over several SF periods: it is indeed power that is relevant. Note that the factor of 2 in the left hand side of the above relation is because radio astronomers usually define the flux density as that present in both wave polarizations, but a receiver is sensitive to only one polarization. If the receiver gain is perfectly stable, our ability to measure small changes in signal is proportional to the square root of the time of integration.

All the final processing of a radio telescope output is done with a computer, after conversion in an Analogue to Digital Converter (ADC) of the analogue voltage from the detector to numbers that can be processed in software.

Radio astronomy is often limited by radio frequency interference (RFI) especially at low frequencies. The spectrum is overcrowded with transmitters: Earth-based TV, satellite TV, FM, cellular phones, radars, and many others. Radio astronomy has some protected frequency bands, in particular at 21 cm, but these bands are often contaminated by harmonics accidentally radiated by TV transmitters, intermodulation from poorly designed transmitters, and noise from leaky high-voltage insulators and automobile ignition noise. Some of the worst offenders are poorly designed satellite transmitters, whose signals come from the sky so that they affect even radio telescopes that are well shielded by the local terrain. Radio telescopes and their receivers can be made more immune to interference by including a band pass filter following the LNA.

2.3 Interferometry

A radio interferometer uses several antennas to take advantage of the fact that the angular resolution is measured by the ratio of the wavelength to the largest baseline (largest distance between two antennas) while the sensitivity is determined by the total area of antennas. The difficulty is to keep track of the coherence of the waves simultaneously detected in each antenna when summing the detected signals.

A non-zero aperture (diameter D) looking at a point source at infinity in direction θ with respect to the normal to the aperture requires an integration over all rays crossing the aperture. The image corresponds to the locus of "in-phase" points at $x = x_0$. A point source produces an extended image centred on x_0; its distribution is called the Point Spread Function (PSF) and the angular resolution at wavelength λ is $\delta\theta \sim \lambda/D$.

The PSF, here defined in image coordinates ($\boldsymbol{x}$), as in the focal plane of an optical telescope (direct imaging), may also be expressed in sky coordinates ($\boldsymbol{\xi}$) since there is a one-to-one relation between $\boldsymbol{x}$ and $\boldsymbol{\xi}$. Then it corresponds to the image in the sky of a point source located at the focus of the telescope. This is precisely the situation in radio astronomy where the focal plane is only explored at the focus by an effectively point-like receiver. The PSF expressed in sky coordinates corresponds then to the lobes of the

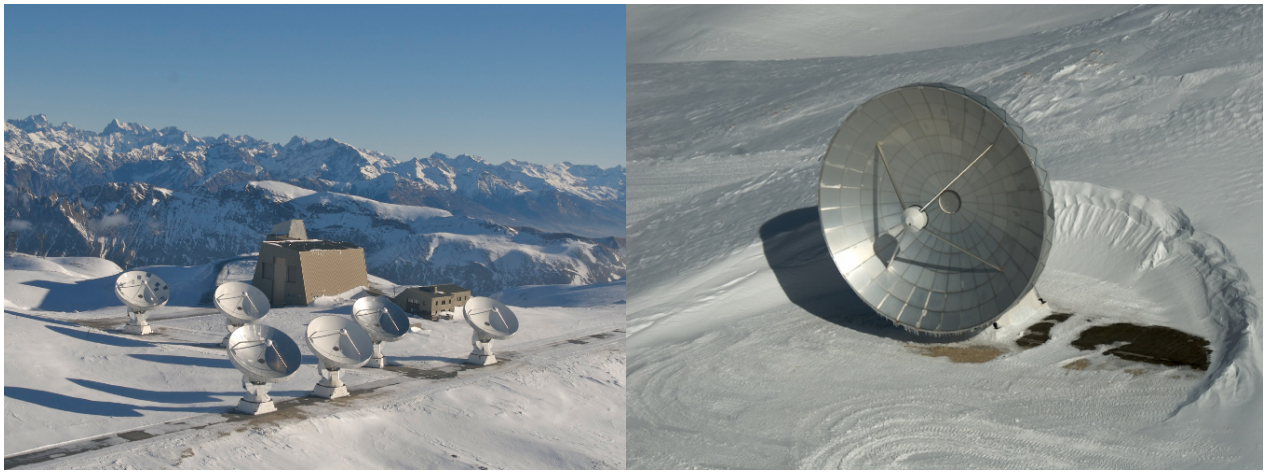

Figure 2.4: Plateau de Bure Interferometer: overall view (left) and a single dish (right).

antenna and the main lobe is called the beam. In practice, in radio astronomy, one never refers to image coordinates in the focal plane, but one expresses in sky coordinates both the source brightness $B(\boldsymbol{\xi})$ and its image $I(\boldsymbol{\xi})$ which is therefore the convolution of the brightness by the PSF, written $I = B * PSF$.

An interferometer detects the interference pattern of many coherent waves. We assume that two antennas A1 and A2, separated by a distance $\lambda\boldsymbol{b}$ (baseline $\boldsymbol{b}$ measured in units of wavelength λ), observe a same source at direction $\boldsymbol{\xi}$ in the sky plane. The waves seen at A1 and A2 are $E\exp(i\omega[t + \tau_G/2])$ and $E\exp(i\omega[t - \tau_G/2])$ where τ_G is the time delay corresponding to the geometric delay $\tau_G = \lambda\boldsymbol{b}\boldsymbol{\xi}/c{=}2\pi\boldsymbol{b}\boldsymbol{\xi}/\omega$. Neglecting the PSF of each individual antenna, the sum of the two signals is $E\exp(i\omega t)2\cos(\omega\tau_G/2)$.

The first factor oscillates much faster than the second and gives an effective power $\frac{1}{2}E^2 = \frac{1}{2}B$. Hence the detected power:

$$\frac{1}{2}B4\cos^2(\omega\tau_G/2) = B[1 + \cos(\omega\tau_G)] = B + B\cos(2\pi\boldsymbol{b}\boldsymbol{\xi}) \tag{2.1}$$

The first part (the continuum part) is kept in additive correlators of optical/IR interferometry but not in multiplicative correlators of radio interferometry.

In the radio astronomy case, the output of the correlator is:

$$r = \iint \boldsymbol{A}(\boldsymbol{\xi})\boldsymbol{B}(\boldsymbol{\xi})\cos(2\pi\boldsymbol{b}\boldsymbol{\xi})d\Omega \tag{2.2}$$

where $A(\boldsymbol{\xi})$ is the antenna pattern and $B(\boldsymbol{\xi})$ the sky brightness distribution.

When an interferometer is tracking a source in direction $\boldsymbol{\xi}_0$; $\boldsymbol{\xi} = \boldsymbol{\xi}_0 + \boldsymbol{\sigma}$,

$$r = \cos(2\pi\boldsymbol{b}\boldsymbol{\xi}_0)\iint \boldsymbol{A}(\boldsymbol{\sigma})\boldsymbol{B}(\boldsymbol{\sigma})\cos(2\pi\boldsymbol{b}\boldsymbol{\sigma})d\Omega - \sin(2\pi\boldsymbol{b}\boldsymbol{\xi}_0)\iint \boldsymbol{A}(\boldsymbol{\sigma})\boldsymbol{B}(\boldsymbol{\sigma})\sin(2\pi\boldsymbol{b}\boldsymbol{\sigma})d\Omega \tag{2.3}$$

Setting, $\iint \boldsymbol{A}(\boldsymbol{\sigma})\boldsymbol{B}(\boldsymbol{\sigma})\cos(2\pi\boldsymbol{b}\boldsymbol{\sigma})d\Omega = |\boldsymbol{V}|\cos(\Phi_V)$

and $\iint \boldsymbol{A}(\boldsymbol{\sigma})\boldsymbol{B}(\boldsymbol{\sigma})\sin(2\pi\boldsymbol{b}\boldsymbol{\sigma})d\Omega = |\boldsymbol{V}|\sin(\Phi_V)$

$$r = \cos(2\pi\boldsymbol{b}\boldsymbol{\xi}_0)|\boldsymbol{V}|\cos(\Phi_V) - \sin(2\pi\boldsymbol{b}\boldsymbol{\xi}_0)|\boldsymbol{V}|\sin(\Phi_V) = |\boldsymbol{V}|\cos(2\pi\boldsymbol{b}\boldsymbol{\xi}_0 - \Phi_V) \tag{2.4}$$

$\boldsymbol{V} = |\boldsymbol{V}|\exp(i\Phi_V) = \iint \boldsymbol{A}(\boldsymbol{\sigma})\boldsymbol{B}(\boldsymbol{\sigma})\exp(2\pi i\boldsymbol{b}\boldsymbol{\sigma})d\Omega$ is the Fourier transform of the brightness, called complex visibility. The real and imaginary part of the visibility can be measured by delaying one of the two signals by 0 or $\pi/2$ in phase (Figure 2.5).

Each pair of antennas gives two distance vectors corresponding to two points in (u, v) plane (or Fourier plane) $\boldsymbol{b}$ and $-\boldsymbol{b}$. At each point in the Fourier plane, we have one corresponding complex visibility and $\boldsymbol{V}(-\boldsymbol{b}) = \boldsymbol{V}^*(\boldsymbol{b})$.

What is measured by the interferometer is therefore the visibility, which is the Fourier transform in the Fourier (u, v) plane (baseline $\boldsymbol{b}$) of the brightness in the sky $\boldsymbol{B}(\boldsymbol{\xi})$. If one has measured the visibilities everywhere in the Fourier plane, one simply Fourier transforms back to sky coordinates to obtain the brightness in the sky. In practice, one has explored the Fourier plane in only a limited number of points, $\boldsymbol{b}_k$ where, for each pair of antennas, one has measured two numbers, say $|V_k|e^{\pm i\Phi_k}$, from which one can construct a map $\boldsymbol{B}(\boldsymbol{\xi}) = \sum_k 2|V_k|\cos(2\pi\boldsymbol{b}_k\boldsymbol{\xi} - \Phi_k)$ called the dirty map because of the "dirty" PSF it corresponds to. Indeed, the visibilities given by a point source in direction $\boldsymbol{\xi}_0$ read $V(\boldsymbol{b}_i) \sim \exp(2i\pi\boldsymbol{b}_i\boldsymbol{\xi}_0)$ for baseline $\boldsymbol{b}_i$; the dirty map, which in this case is called the dirty beam, is therefore $\boldsymbol{B}(\boldsymbol{\xi}) \sim 2\sum_i \cos[2\pi\boldsymbol{b}_i(\boldsymbol{\xi} - \boldsymbol{\xi}_0)]$. It is maximal at $\boldsymbol{\xi} = \boldsymbol{\xi_0}$, but will only look as a decent PSF if the (u, v) coverage is good enough. The dirty map is the convolution of the brightness distribution and the dirty beam. Note that we introduce here the concepts of beam and PSF for the interferometer as a whole, defined as the image of a point source, they have nothing to do with the beam (usually called primary beam) or PSF of each single dish that defines the field of view. In order to get as nice as possible a dirty beam, one needs to optimize the (u, v) coverage.

In each antenna configuration of an interferometer, the number of baselines (or spatial frequencies) is limited. The spatial resolution is minimal at smallest baseline and maximal at largest baseline. In order to increase uv coverage, one may move telescopes on ground (multi-configuration) and/or let the Earth rotation move them for us (supersynthesis). An incomplete uv coverage produces artefacts on the image such as a negative value around the emission region. We can overcome this problem by interpolating/extrapolating the missing information in the uv plane.

An important consequence out of filtering the small spatial frequencies of the interferometer instruments is to reduce the measured flux. This can be corrected by interpolation when the size of the source is $\sim 1/3$ smaller than the primary beam but not for larger size sources. To fill in the missing information at low spatial frequencies, one uses single dish telescopes having a size larger or equal to the diameter of the interferometer antenna. This technique is called "short-spacing".

In the radio interferometry jargon, one says that to "clean" the dirty map, one needs to "deconvolve" the effect of the PSF. This is called "deconvolution". Here, to "clean" the dirty map means to produce a map that would be obtained with a well behaved PSF, which one calls the "clean beam".

Once data have been acquired by an interferometer, their reduction and analysis proceeds in three phases: calibration transforming from raw data to visibilities, imaging/deconvolution and analysis. Imag-

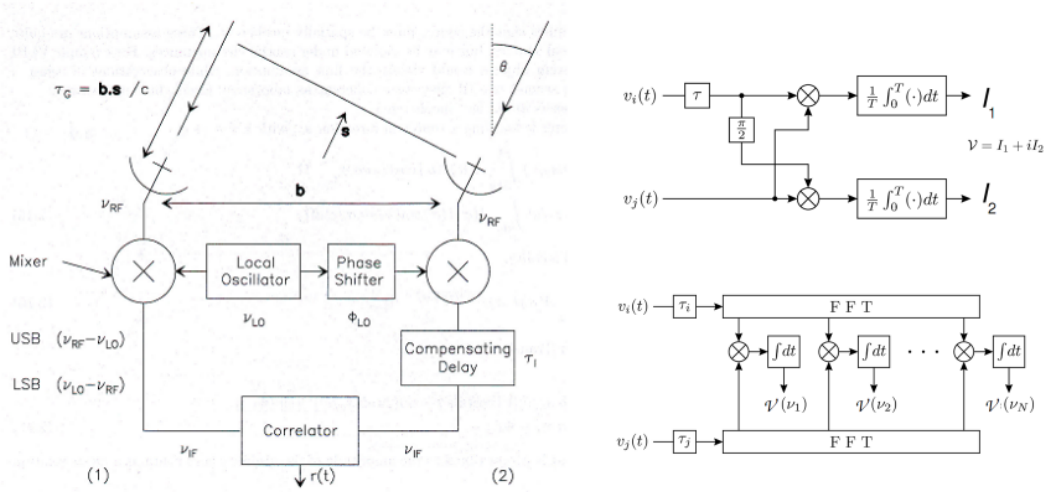

Figure 2.5: Left: Principle schematics of the on-line treatment of the signals from a pair of antennas. Right: Principle schematics of measurement of two visibility components.

ing and deconvolution produce a set of spectra cubes, or data cubes, consisting of 2 sky coordinates and one frequency of which the visibility has been measured. In the presence of a line, the frequency can be used to calculate the Doppler shift, namely the component of the velocity along the line of sight. The continuum below the line, after integration over some frequency interval, provides an image of the source independent of velocity.

The complex visibility W_{ijk} measured on the baseline from antenna i to antenna j in frequency channel k is related to the true object visibility V_{ij} by

$$W_{ijk} = g_i(t)g_j^*(t)b_{ijk}(t)V_{ij}(u_k(t), v_k(t)) + noiseterm \tag{2.5}$$

where $u_k(t)$ and $v_k(t)$ are the Fourier coordinates, called spatial frequencies, corresponding to baseline ij at time t and frequency k. Calibrating the data means calculating the complex "calibration curves" $g_i(t)$ and $b_{ijk}(t)$. For the relatively narrow bandpass of millimetre astronomy, $u_k(t)$ and $v_k(t)$ are almost independent of the frequency channel k. The function $b_{ijk}(t)$ is the bandpass of the detection system, and is usually almost independent of time. It can be formally decomposed in a product of an RF bandpass, caused by receivers and cables and usually with weak dependence on frequency, and an IF bandpass, caused by the back-end and correlator. For $g_i(t)$, one must separate the amplitude and phase calibrations since amplitude and phase errors have very different origins. Amplitude errors are related to several effects: atmospheric absorption, receiver gain, antenna gain (affected by pointing errors, defocusing, surface status and systematic elevation effects), and correlation losses due to phase noise. Phase errors may come from delay errors, baseline errors, or a slow drift in atmospheric or receiver phases.

Corrections associated with atmospheric absorption and receiver gain are determined from "chopper wheel" calibrations. This procedure measures the counts on hot load (273K), cold load (4K) and empty sky, then computes the system temperature, the gain receiver and atmospheric opacity. Because of the atmospheric fluctuations and receiver gain drift, this must be done very often (every 20 minutes at PdBI). At the same time, this provides the correction for the amplitude passband. The atmospheric

model calculations are done on-line to help monitoring data quality, and applied to the data. However, the calibration parameters are stored in the headers as well as the overall amplitude factor applied. It allows repeating at any stage in data reduction process.

Phase errors introduced in the back-end are measured by connecting all correlator inputs to a same source of white noise. Phase calibration, needed to correct raw visibilities for instrumental and atmospheric short-term phase fluctuations, is done by repeatedly observing a nearby point source (usually a strong quasar) for which the measured phases should be zero if delays are correctly tracked. Observing a strong calibrator gives information for flux calibration.

Imaging, which consists in computing the dirty image and the dirty beam from the measured visibilities and the sampling function, uses Fast Fourier Transform, implying a first stage of gridding of the visibilities on a regular grid in the (u, v) plane. Gridding requires a large enough sampling frequency to avoid artefacts (known as aliases). Sampling in the (u, v) plane is obtained with a cell size equal to the antenna radius (this is the smallest spatial frequency that the interferometer can be sensitive to, namely the natural resolution in the (u, v) plane).

Natural weighting assigns to each visibility a weight equal to the reciprocal of the noise variance, $1/\sigma^2$. It maximizes the point source sensitivity in the final image. Robust weighting is meant to enhance the contribution of the large spatial frequencies to increase the spatial resolution at the cost of a lesser sensitivity to point sources.

Once the dirty beam and the dirty image have been calculated, one wants to derive an astronomically meaningful result, ideally the sky brightness. The goal of deconvolution is to find a sensible intensity distribution compatible with the measured visibilities. It proceeds by successive iterations. In order to have a better evaluation of the map, we need to remove the effect of the side lobes in the dirty map, using a Gaussian fit to the main lobe of the dirty beam.

2.4 The Nançay and Pico Veleta radio telescopes

The Nançay radio telescope (Figure 2.6) uses the so-called Kraus design that had been first pioneered in Ohio with the Big Ear radio telescope. It includes a plane mirror, 40 m wide and 200 m long, which rotates around a horizontal axis in order to send the image of the source on a fixed spherical mirror, 560 m radius, while its elevation varies. At the focus of the spherical mirror (i.e. half-way to the center sphere), a mobile focal receiver follows the source while it crosses the meridian. The duration of the observation does not exceed one hour for a source. The telescope is capable of observing objects with a declination greater than $-39°$. It operates on decimetric wavelengths and both mirrors are made of a square mesh grid with 2 cm mesh size (1.25 cm holes) positioned with an accuracy of ~5 mm. Observations are typically undertaken at frequencies of 1400 MHz (21 cm wavelength), 1660 MHz (18 cm) and 3330 MHz (9 cm).

Observations at millimetric wavelengths require a dry site at high altitude in order to minimize the effect of atmospheric absorption, in particular of water vapour. The Pico Veleta radio telescope (Figure 2.1) is located in Sierra Nevada (Spain) at 2850 m altitude. It is operated by IRAM (Institut de Radioastronomie Millimétrique). IRAM was created in 1979 as a joint Institute between CNRS

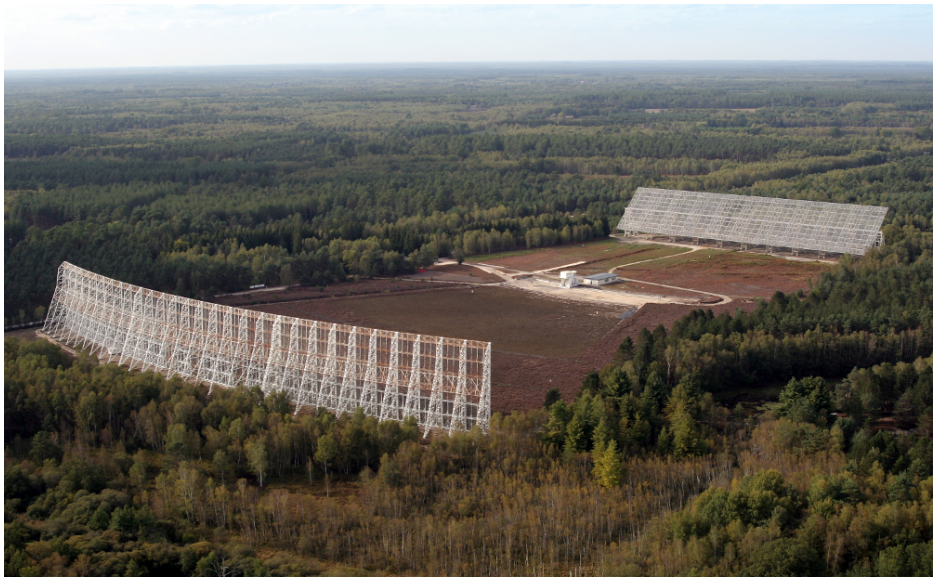

Figure 2.6: The Nançay (France) radio telescope. The tilting plane mirror in the background sends an image of the source to the fixed spherical mirror in the foreground. The mobile receiver system is visible between the two mirrors.

(France), the Max Planck Gesellschaft (Germany) and the Instituto Geográfico Nacional (Spain) with the aim to study cold media such as interstellar dust and molecular gas in the Solar system, the Milky Way and other galaxies up to cosmological distances. Built on a concrete pedestal, the 30 meter telescope rotates on an alt-azimuth mechanism with a tracking precision better than 1 arcsecond. Signals are captured by the large 30 meter parabolic surface of the antenna and bounced off the surface towards the sub-reflector. They are then aimed at the receivers inside the antenna cabin which convert them to a lower frequency by combining them inside the mixer-block with a locally produced signal at a frequency similar to that of the original signal. The super-conducting junction of the mixer sends out the signal having a different frequency between the two of incoming signals, the so-called intermediate frequency, which is low enough to be amplified. Located in the main building, an auto-correlator processes the signals removing any parasitic background noise.

The parabolic dish is comprised of 420 aluminium mechanically adjustable panels with a surface precision of 55 microns. Mechanical adjustments are also applied to the structure to compensate for the different gravitational forces it undergoes when the antenna moves from vertical to horizontal position. The focal antenna cabin houses a variety of receivers allowing for different observations. Signals are distributed to the various receptors by a series of high precision mirrors. Data transfer between the receiver cabin and the control room is achieved with an array of low-loss cables.

2.5 The Plateau de Bure and VLA interferometers

The present work uses data collected at the Plateau de Bure interferometer (PdBI), also operated by IRAM. It operates a six-antenna radio-interferometer in various configurations (A, B, C, D) on Plateau de Bure (2550 m, French Alps, Figure 2.4). Baselines may reach 760 m east-west and 368 m north-south

producing an angular resolution ∼0.3″(at 0.8 mm). Each antenna is 15 m in diameter. The primary beam of each antenna defines the field of view of the array. At 100 GHz, meaning a 3 mm wavelength, the primary beam has a FWHM of ∼45″ and the synthesized resolution can reach ∼1″. The typical sensitivity at 115 GHz for a one hour integration in a 3.6 GHz bandwidth is from 0.16 to 0.3 mJy and from 0.06 to 0.08 mJy for a full synthesis (2 configurations, or 11 hours on source). The interferometer is presently being upgraded and will become the NOrth Extended Millimeter Array (NOEMA). In 2018, NOEMA will be operated with 12 15-m antennas with tracks up to 2000 m and equipped with improved reception systems and state of the art electronic equipment.

The Very Large Array (Figure 2.7), located in New Mexico (USA), consists of 27 radio antennas in a Y-shaped configuration, each 25 m in diameter. Four different antenna configurations are available: A, B, C and D with maximum antenna separations of respectively 36.4 km, 11.1 km, 3.4 km and 1.0 km. Configurations are modified every four months or so. The highest resolution that can be obtained is 0.04 arcseconds at 43 GHz. At 21 cm in the D configuration, the angular resolution is ∼1′. The minimal elevation is 8° and the frequency coverage 74 to 50,000 MHz (400 to 0.7 cm). The VLA has been recently upgraded with state of the art receivers and correlators. On this occasion (2012), it has been renamed the Karl Jansky Very Large Array (JVLA).

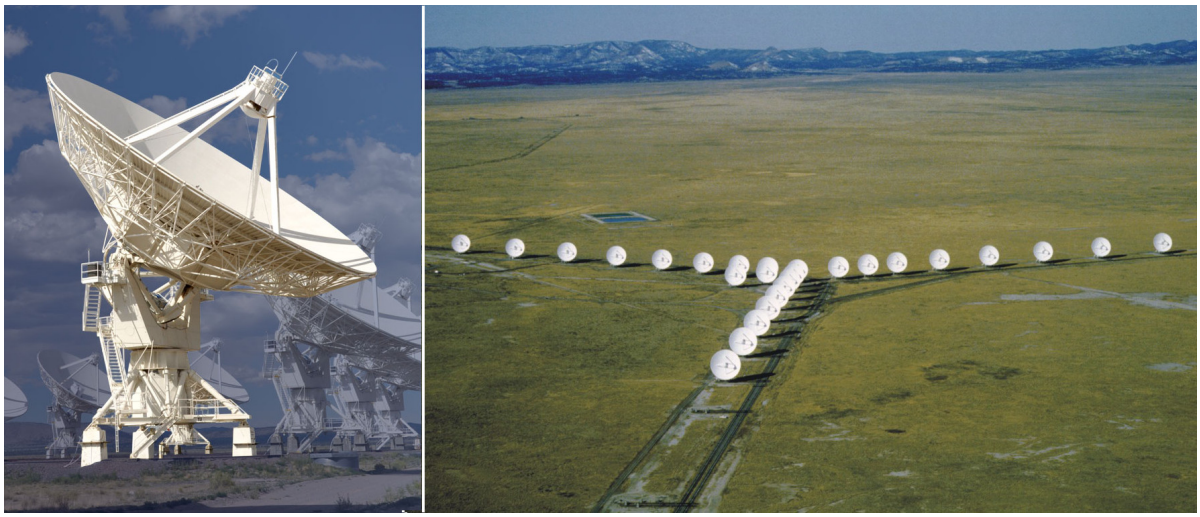

Figure 2.7: An antenna of the VLA (left) and an overview of the whole array (right).

2.6 The 21 cm line

The 21 centimetre line, also referred to as atomic hydrogen line or H I line, is associated with the hyperfine transition of the atomic hydrogen in the ground state. Its frequency is 1420.40575177 MHz, equivalent to the vacuum wavelength of 21.10611405413 cm in free space. This wavelength is in the microwave radio range where waves can penetrate the clouds of interstellar cosmic dust that are opaque to visible light.

Hyperfine splitting (Figure 2.8) is the result of the spin-spin interaction between the electron and proton spins in the hydrogen atom. This transition is highly forbidden (it has ΔF=0) with an extremely

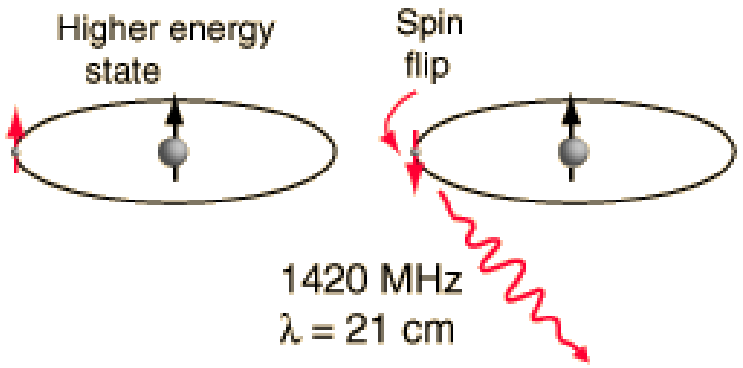

Figure 2.8: Hyperfine splitting of the hydrogen ground state

small probability of 2.9×10^{-15} s^{-1}. This means that the time for a single isolated atom of neutral hydrogen to undergo this transition is around 10^7 years and therefore difficult to observe. However, as the total number of atoms of neutral hydrogen in the interstellar medium is very large, this emission line is easily observed by radio telescopes. Moreover, the lifetime can be considerably shortened by collisions with other hydrogen atoms and interaction with the cosmic microwave background. The line has an extremely small natural width because of its long lifetime, so most broadening is due to Doppler shifts caused by the turbulence and thermal broadening which is proportional to $\sqrt{T/m}$.

The H I line at 21 cm was first predicted in 1944 by van de Hulst. It was first detected in 1951 by Ewen and Purcell and published after their data were corroborated by Muller and Oort. The first maps of the neutral hydrogen in the Galaxy were made in 1952 and revealed the spiral structure of the Milky Way. Hydrogen line observations have also been used indirectly to calculate the mass of galaxies, to put limits on any changes over time of the universal gravitational constant and to study dynamics of individual galaxies.

The 21 cm line is an excellent probe of the interstellar medium (ISM). Galaxies are filled with a very diffuse distribution of neutral hydrogen gas which has a typical density of about 1 atom cm^{-3}. The interstellar medium is far too cool to excite the UV or optical transitions of hydrogen, but the 21 cm hydrogen line reveals neutral hydrogen distributed in clumps with cool, denser regions called "clouds" that rather look like filaments. These regions have a typical temperature of about 100 K and a density between 10 and 100 atom cm^{-3}. Surrounding the clouds is a warmer lower density medium with about 0.1 atom cm^{-3} and T ~8000 K. The Milky Way has about 3 billion solar masses of H I gas with about 70% of it further out from the galactic centre than the Sun. Most of the H I gas is in the disk and is located within 220 pc from its mid-plane.

Denser (n_{H_2}>1000 molecules cm^{-3}), cold (T~10 K) clouds of molecular hydrogen and dust, known as molecular clouds or dark clouds are the birthplaces of stars. We do not detect molecular hydrogen directly, but infer its characteristics from other molecules, most often CO. Over hundred other molecules have been detected. A Giant Molecular Cloud may have a mass of 10^6 solar masses and a diameter of 45 pc; there are thousands of them in the Milky Way where the total mass of molecular gas is estimated to be about equal to, or perhaps somewhat less (~25%) than, the mass of H I gas.

2.7 Molecular lines: CO rotation lines

The discovery of interstellar molecules is less than fifty years old. We now estimate that half of the interstellar matter in the inner part of the Milky way is molecular and the list of known interstellar molecules is well above one hundred long. While many of these molecules are found in abundance on Earth, about 50% of the compounds found in the ISM are not stable in normal laboratory conditions, namely free radicals and molecular ions. Molecules are present in two types of objects: molecular clouds (Figure 2.9) and circumstellar envelopes of AGB stars. Molecular clouds have gas kinetic temperatures in the 10 K to 50 K range, possibly reaching up to 1000 K in confined regions toward young stars and circumstellar envelopes are cold in the outer part and get hotter nearer to the star, again reaching the 1000 K range.

Densities of molecular clouds are in the range of 10^3 to 10^6 molecules cm^{-3} and densities of circumstellar envelopes decrease from 10^5 cm^{-3} near the star to 10 cm^{-3} in the outer shells. Molecules have rotational, vibrational and electronic energy levels (Figure 2.10) giving transitions in different wavelength regions, respectively millimetre/sub-millimetre (~30 to 300 GHz), infrared and optical/UV.

A diatomic molecule has a moment of inertia $I = \mu r^2$, μ being the reduced mass $\frac{m_1 m_2}{m_1+m_2}$, which defines the spacing between energy levels, a level of angular momentum J having energy $BJ(J+1)$ with the rotational constant $B = \frac{1}{2}\hbar^2/I$. Hence the photon frequency for a $J \rightarrow J-1$ transition: $\nu = BJ(J+1) - BJ(J-1) = 2BJ$.

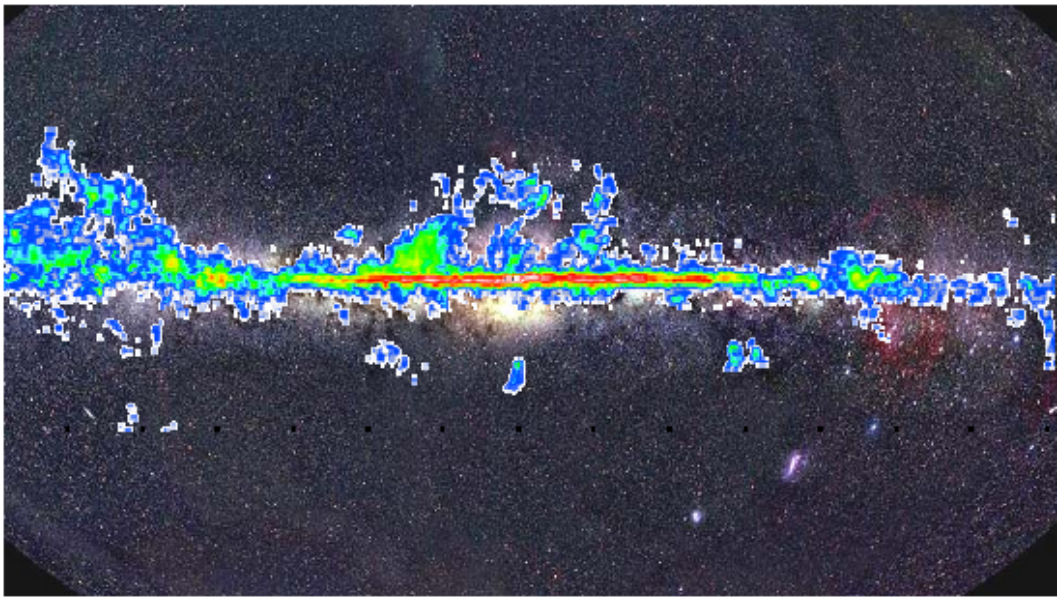

Figure 2.9: The distribution of molecular clouds in the Milky Way as traced at 115 GHz by the CO(1-0) transition (galactic coordinates with galactic centre in the centre of the figure) (Dame et al. 2001).

While the dominant molecular species in the ISM is H_2, its absence of dipole moment implies that its low energy levels produce quadrupole transitions with small transition probabilities that can only be excited by collisions at high temperatures or by UV radiation. The lowest energy transition occurs at a wavelength of 28 μm, for which the atmosphere is opaque. Thus, it only can be detected by space telescopes. As a consequence, most of what we know comes from CO tracer.

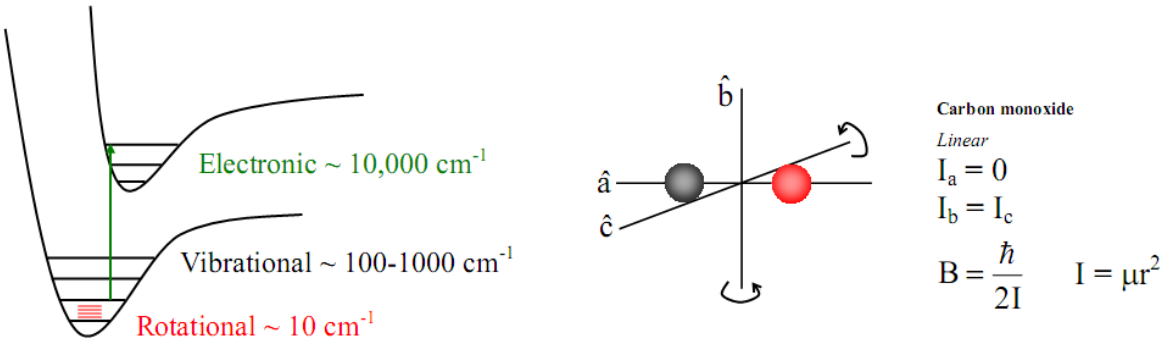

Figure 2.10: Left: Energy levels of a molecule. Right: Rotation of a diatomic molecule.

For a transition between a lower level l and an upper level u the absorption coefficient is given by the difference between a pure absorption term and a stimulated emission term:

$$\kappa_\nu = \frac{h\nu}{4\pi}(n_l B_{lu} - n_u B_{ul}) \tag{2.6}$$

where n_l and n_u are number densities of gas at level l and u, B_{lu} and B_{ul} Einstein's absorption and stimulated emission coefficient respectively. In the local thermal equillibrium at a temperature T,

$$\kappa_\nu = \frac{c^2}{8\pi\nu_{ul}^2} A_{ul} n_u (e^{\frac{h\nu}{kT}} - 1) \tag{2.7}$$

Integrating over the line of sight, one obtain the optical depth:

$$\tau_\nu = \int \kappa_\nu ds = \frac{c^2}{8\pi\nu_{ul}^2} A_{ul} N_u (e^{\frac{h\nu}{kT}} - 1) \tag{2.8}$$

where N_u is the column density of the molecules in the upper state and A_{ul} the transition probability for the line. Depending on the value of the temperature, the line appears in emission or in absorption. The excitation temperature depends on the relative importance of radiative vs collisional processes: it is the harmonic mean between the radiation and kinetic temperatures weighted by the relative collisional and radiative de-excitation terms.

The ratio of the radiative and collisional rates is the ratio of the density to the critical density for the transition. As different molecular lines have different critical densities, line visibility can serve as an approximate density diagnostic. In the case of CO(1-0) (115 GHz), the critical density (10 K) is ~1000 cm^{-3}.

2.8 Transfer of radiation

The transfer of radiation is well introduced in the book of Lequeux (2005). The propagation of radiation through a medium is affected by emission, absorption and scattering processes. At radio wavelengths, the effect of scattering is insignificant. The transfer of radiation depends only on emission and absorption intensity:

$$\frac{dI(\boldsymbol{s},\nu)}{d\boldsymbol{s}} = \eta_{emis}(\boldsymbol{s},\nu) - \kappa(\boldsymbol{s},\nu)I(\boldsymbol{s},\nu) \tag{2.9}$$

where $I(\boldsymbol{s})$ is the intensity of the radiation after propagation through a small depth of medium ds. η_{emis} is the emissivity and κ is the absorption coefficient. They are complicated functions of the local characteristics of the gas: density, temperature.

The emissivity of a given area is:

$$\eta_{emis}(\boldsymbol{s},\nu) = \frac{h\nu}{4\pi} f_J n_{gas}(\boldsymbol{s}) A(\nu) \tag{2.10}$$

with $n_{gas}(\boldsymbol{s})$ is the number density of the circumstellar envelope, f_J and $A(\nu)$ are the fractional population of quantum state J and emission probability of the gas to emit at frequency ν. In the local thermal equilibrium approximation, $f_J = g_J \frac{\exp -\frac{E_J}{kT}}{Q(T)}$ with the partition function $Q(T) = \sum_i g_i e^{-\frac{E_i}{kT}}$ where g_J and E_J are $2J+1$ and $BJ(J+1)$ respectively. At thermal equilibrium, the partition function of CO rotational emission is approximately $\frac{T}{2.76}$ K. The fractional population in different rotational levels is displayed in Figure 2.11 as a function of kinetic temperature. However, the excitation temperature can be higher than the kinetic one in dense gas volumes due to the trapping line photons effect. Thus, the population can be changed.

In the case of H I emission, most of the atomic hydrogen is in the fundamental state and distributed in 2 hyperfine levels with the ratio of the statistical weights between the lower and higher level being 1/3, thus $f_J = 3/4$.

Radio radiations have wavelengths too long to be absorbed by the dust. The absorption mentioned here is the self-absorption which is decided by the properties of the gas in the medium. The absorption coefficient $\kappa(s,\nu)$ is calculated as:

$$\kappa(s,\nu) = \frac{c^2 n_l(\nu) g_u}{8\pi\nu^2 g_l} A(\nu)[1 - \exp(-\frac{h\nu}{kT_K})] \tag{2.11}$$

where $n_l(\nu)$ is the number density of the gas at level l, g_l, g_u are the statistical weights of two levels u and l. T_K is the kinetic temperature of the gas.

The effect of absorption in CO spectra is very small when the mass loss rate is lower than 10^{-7} $M_\odot\,yr^{-1}$. With mass-loss rate higher than 10^{-6} $M_\odot\,yr^{-1}$, the absorption does not only decrease the radiation intensity but also round the shapes of profiles. Figure 2.12 displays the effect of self-absorption on the spatial integrated profile of a 4″ spherical wind expanding with a constant velocity of 8 $km\,s^{-1}$. The CO abundance in the star is 4×10^{-4} and hydrogen is assumed to be 90% of the total number of particles (meaning 70% in total mass). The temperature decreases with radius with a slope of 0.7 in log-log scale

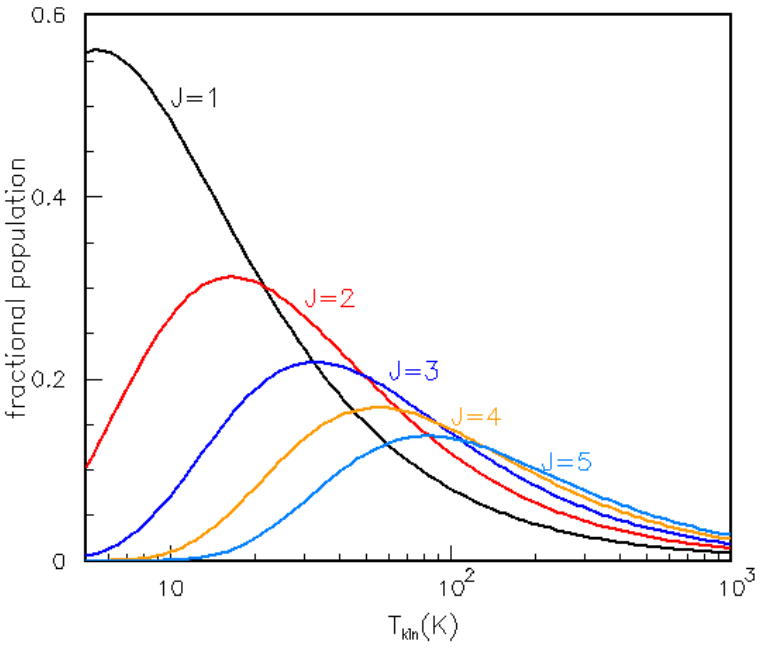

Figure 2.11: Dependence of the fractional population at different rotational levels of CO molecule on kinetic temperature.

($T = 580(r/0.1)^{-0.7}$, r expressed in arcsecond and T in K) and the source is unresolved. CO molecules emit the rotational lines in thermal equilibrium. The wind is stationary, the mass-loss rate is independent in time. The absorption is stronger at higher mass loss rate and stronger in CO(2-1) than in CO(1-0). In reality, because of the decreasing outward of the temperature, the absorption of the blue-shifted part is a bit more than that of the red-shifted part (Figure 2.13). This effect is stronger in CO(2-1) than in CO(1-0). It shows that radiative transfer effects should be taken into account for sources with high mass loss rate and also for CO lines of higher excitation.

At 21 cm, $\frac{h\nu}{kT} << 1$, we have, to a good approximation,

$$\kappa(\boldsymbol{s}, \nu) = \frac{3c^2 n_H(\nu)}{32\pi\nu^2} A(\nu) \frac{h\nu}{kT_K} \tag{2.12}$$

The optical depth is $\tau(\nu) = \sum \kappa(\boldsymbol{s}, \nu) d\boldsymbol{s} = 2.597 \times 10^{-15} N(\mathrm{H\,I})/T_K$. $N(\mathrm{H\,I})$ is the column density of H I. In the optically thin case, $T_B(\nu) = \tau(\nu) T_K \sim N(\mathrm{H\,I})$. The spectrum in H I does not depend on temperature, it only depends on the density of the gas. The column density, thus, can be determined from the spectrum integral, $N(\mathrm{H\,I})(\mathrm{atom\,cm^{-2}}) = 1.8224 \times 10^{18} \sum T_B(\nu) d\nu$. The total mass of H I in the unit of solar masses is: $M(\mathrm{H\,I}) = 2.36 \times 10^{-7} d^2 \sum S(V) dV$ where d is the distance of the star to Earth in pc, $S(V)$ is the integrated spectrum in Jy and V is the velocity in $\mathrm{km\,s^{-1}}$.

When the source is in front of a warmer background, we may see a line in absorption which is not only due to self-absorption, but also to the absorption of the background by cool material in the source. Assuming that the background is spatially uniform, the brightness temperature in the source direction (ON position) is $T = T_S\{1 - \exp[-\tau(\nu)]\} + T_b \exp[-\tau(\nu)]$ where T_S and T_b are the temperatures of the

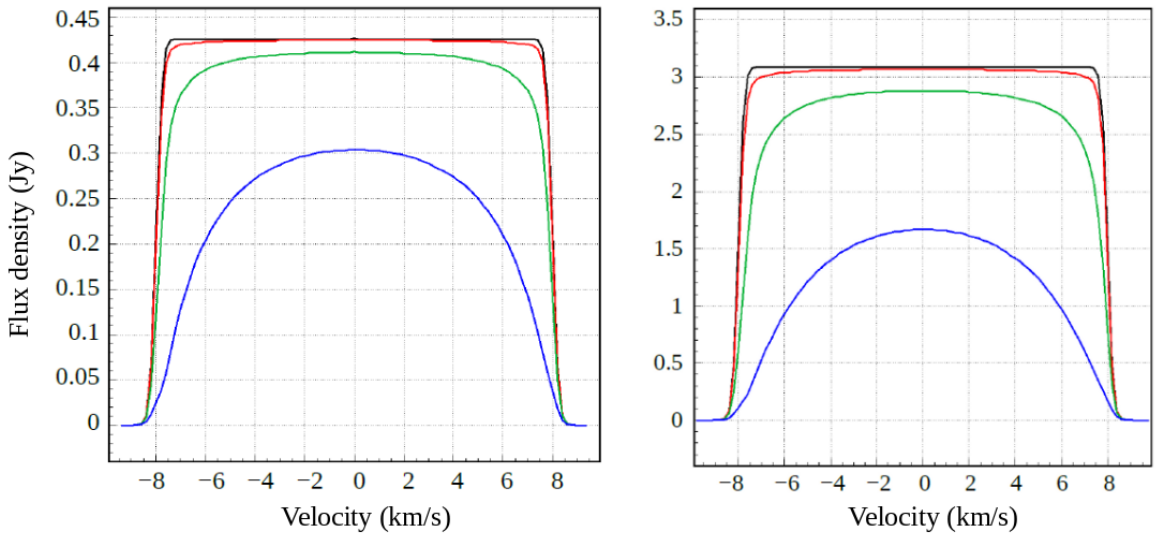

Figure 2.12: The CO(1-0) (left) and CO(2-1) (right) fluxes of 4″ spherical winds expanding with velocity 8 km s^{-1} without absorption effect (black) and with the effect at different values of mass loss rates: 10^{-7} M$_\odot$ yr^{-1} (red), 10^{-6} M$_\odot$ yr^{-1}(×0.1, green) and 10^{-5} M$_\odot$ yr^{-1}(×0.01, blue). Distance of the source is d=122 pc.

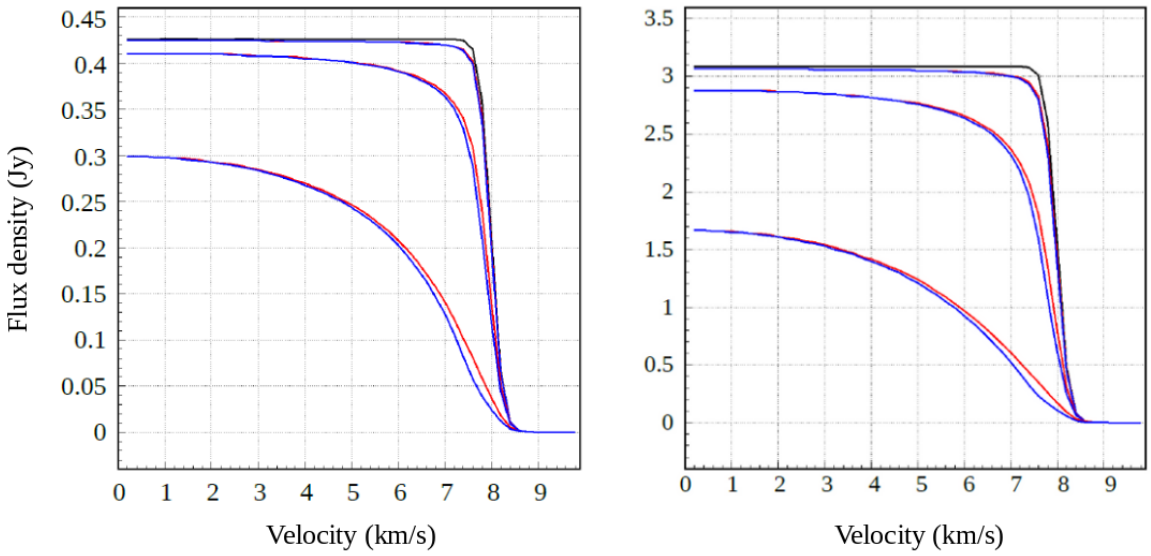

Figure 2.13: The comparison between the red-shifted parts (red) and the blue-shifted parts (blue) of the CO(1-0) (left) and CO(2-1) (right) fluxes shown in Figure 2.11. The black line shows the flux without the absorption effect.

source and background respectively. In practice, T_b is determined from the observation in OFF position. After subtracting ON-OFF, the spectrum is $T' = T - T_b = (T_s - T_b)\{1 - \exp[-\tau(\nu)]\}$. Figure 2.14 displays an absorption feature caused by a background and optical depth of the source having Gaussian profiles. Due to the absorption, the central velocity and the terminal velocity of the wind in observation can be different from the real value (Levinson & Brown 1980).

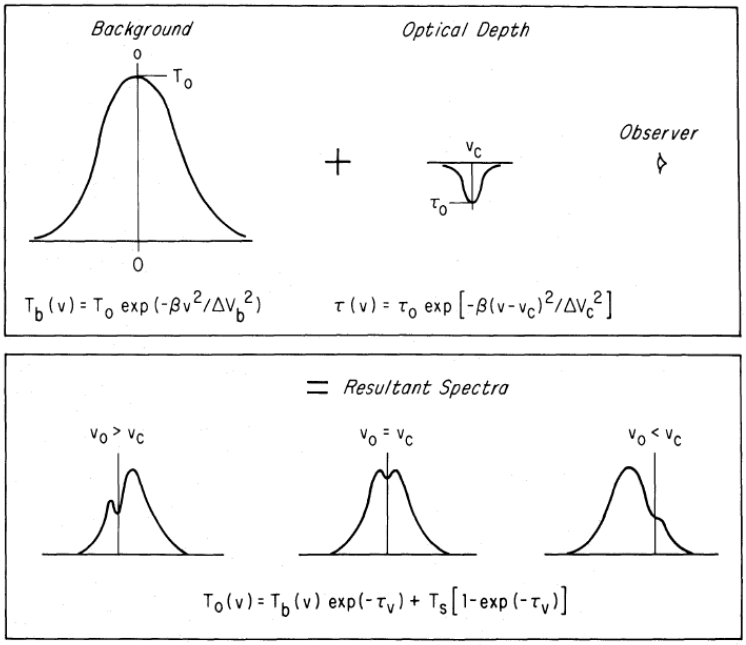

Figure 2.14: Observed absorption spectra caused by a background and optical depth of the source having Gaussian distributions (Levinson & Brown 1980).

Chapter 3

RS Cnc: CO OBSERVATIONS AND MODEL

3.1 Introduction

RS Cnc (also known as HD 78712, HR 3639) is located in the constellation of Cancer at a right ascension of 9h10min38.798s and a declination of 30°57′47.30″ (2000.0 position; van Leeuwen 2007). It is a variable TP-AGB S star (Stephenson 1984) displaying technetium lines in its spectrum (Peery 1971; Wallerstein & Dominy 1988; Lebzelter & Hron 1999; Little et al. 1987). Silicate emission features have been revealed at 10 μm (IRAS, Speck et al. 2000). Its spectral type is M6eIb-II(S), (also quoted M6IIIase and M6S) and its variability type SRc (General Catalogue of Variable Stars).

The distance of the star has been estimated from Hipparcos parallax data with increasing precision over time: 122 pc (Perryman et al. 1997) 129 pc (Famaey et al. 2005) and 143 pc (van Leeuwen 2007). The star radius has been estimated at various wavelengths: ∼14 mas (384 $R_\odot$) using Hipparcos data (Dumm & Schild 1998); varying between 13 and 17 mas (Chagnon et al. 2002) in L-band (from 3.4 to 4.1 μm); as a shell of 112 arcsec at 70 μm (Geise 2011).

RS Cnc was found to be extended in the IRAS data at 60 μm with evidence of a detached shell (R_{in} =1.0′ and R_{out}=5.8′; Young et al. 1993). Hipparcos data (Dumm & Schild 1998) imply an effective temperature of ∼3226 K (see also Dyck et al. 1996; Perrin et al. 1998), and a luminosity of ∼3600 $L_\odot$ (at d=122 pc). With a temperature much higher than 2500 K, and following Glassgold & Huggins (1983), we expect that most of the hydrogen be in atomic form from the stellar atmosphere outwards. The average V magnitude is 5.95 (B_T=7.86 and V_T=6.27 from Tycho). Mass-loss rates (in units of $10^{-7}\,M_\odot\,yr^{-1}$), corrected for distance of 143 pc, have been evaluated at 5.7 (Knapp & Morris 1985); between 0.17 and 0.73 (Knapp et al. 1998) and between 0.66 and 3.2 (Libert et al. 2010b) for two-component wind.

Radial LSR velocity of $\sim 7\ km\,s^{-1}$ have been measured (Knapp & Morris 1985; Libert et al. 2010b). Hipparcos data give a proper motion of ~ -11.12 mas/yr in right ascension and ~ -33.42 mas/yr in declination (van Leeuwen 2007). After correcting for the solar motion toward the apex, the star is therefore moving in south-east direction (PA=137°) in the sky plane at $17\ km\,s^{-1}$ and moving in space at $18.4\ km\,s^{-1}$.

RS Cnc has been observed at various wavelengths. The IRAS/LRS infrared SED (Figure 3.1 right)

displays features at ~10 and ~20 μm, as is typical of such mass-lossing oxygen rich stars. The 70 μm map (Geise 2011, Figure 3.1 left) shows a tail in the South East-North West direction, opposite to the star motion.

Observations in CO and H I (Hoai et al. 2014; Libert et al. 2010b; Matthews & Reid 2007) are displayed in Figure 3.2. While the H I data show a trailing tail opposite to the star movement, the CO data give evidence for a bipolar outflow (PA~10°, inclination ~50° to the plane of the sky, velocity ~8.0 km s^{-1}) superimposed on a spherical, or nearly spherical, low velocity (~2.4 km s^{-1}) expansion (Libert et al. 2010b).

The variability has been studied over twenty years (Percy & Desjardins 1996; Percy et al. 2001; Adelman & Dennis 2005; Howarth 2005) displaying a complex pattern of different periods (Figure 3.3). Two periods, around 130 days (122 and 135 days have been quoted) and 240 days (248±7 and 228) dominate the scene and a period of the order of 500 days seems also to contribute.

Finally, Figure 3.4 compares RS Cnc parameters with those of similar stars (Ramstedt et al. 2009).

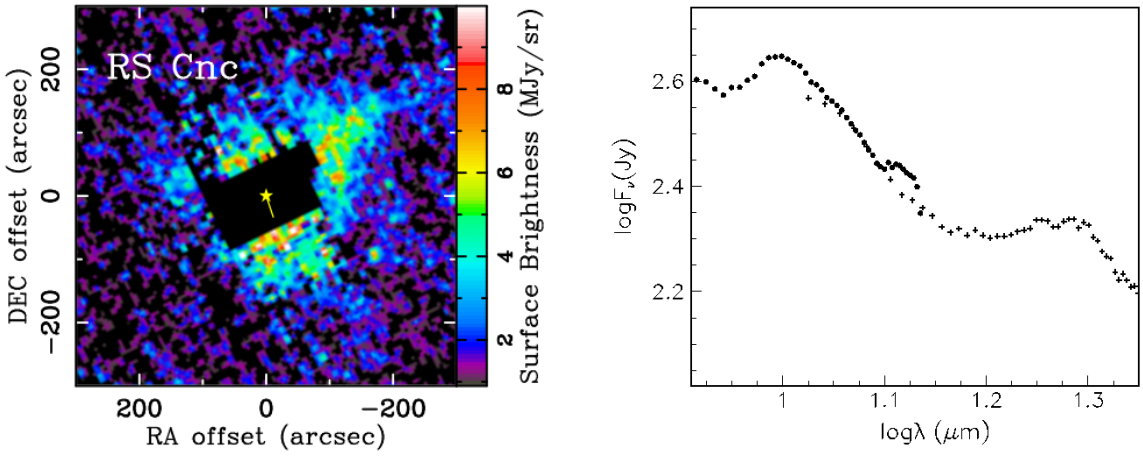

Figure 3.1: Spitzer 70 μm map (Geise 2011) (left) and IRAS/LRS infrared SED (right) of RS Cnc.

3.2 Review of the 2004-2005 and earlier CO observations

The CO(1-0) emission from RS Cnc was first detected by Knapp & Morris (1985) using the 7-m antenna of Bell Laboratories. The central velocity is 6.8 km s^{-1} and the terminal velocity of the envelope is 5.3 km s^{-1}. The mass-loss rate is evaluated at 2.9 10^{-7} M$_\odot$ yr^{-1}. Nyman et al. (1992) also detected this source in CO(1-0) line with a line centred on V$_{LSR}$=7.5 km s^{-1}.

The source was then observed by Knapp et al. (1998), using the 10.4 m telescope of the Caltech Sub-millimetre Observatory, thus providing high spectral resolution profiles for both the CO(2-1) and the CO(3-2) lines. In these spectra, the lines are centred on 7.5 km s^{-1}and exhibit a composite profile made of a narrow feature, of line half-width of ~2.6 km s^{-1}, superimposed on a broader of line half-width of ~8.0 km s^{-1}. Knapp et al. (1998) interpret these as produced by two successive winds with different expansion velocities (2.6 km s^{-1} and 8 km s^{-1}) and different mass-loss rates (2.3×10^{-8} M$_\odot$ yr^{-1} and

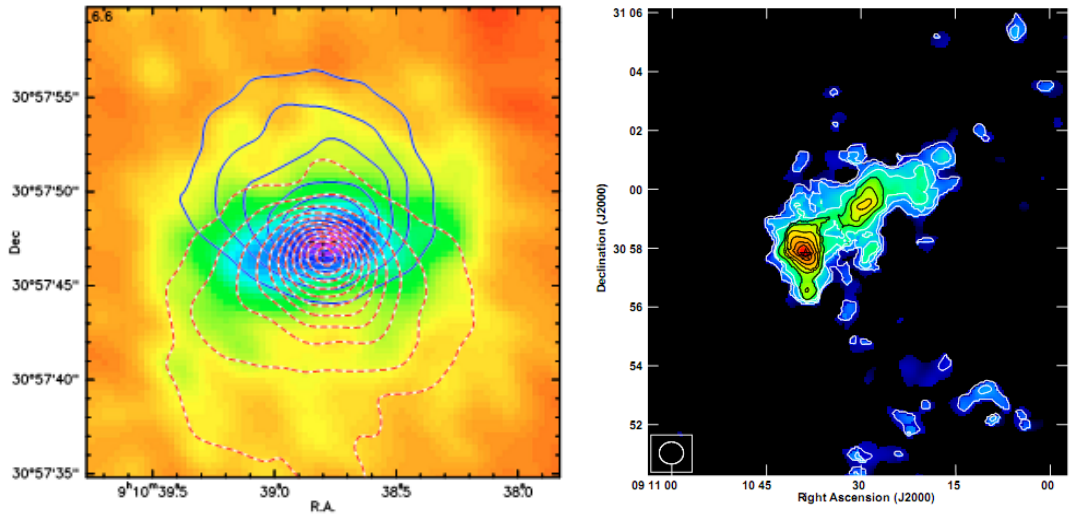

Figure 3.2: Radio maps (Hoai et al. 2014; Libert et al. 2010b). Left, bipolar structure in CO(1-0); blue lines are integrated between -2 and 3 km s^{-1} and red lines between 9.5 and 16 km s^{-1}, the background image being at 6.6 km s^{-1}; Right, H I total intensity map. Note the very different scales.

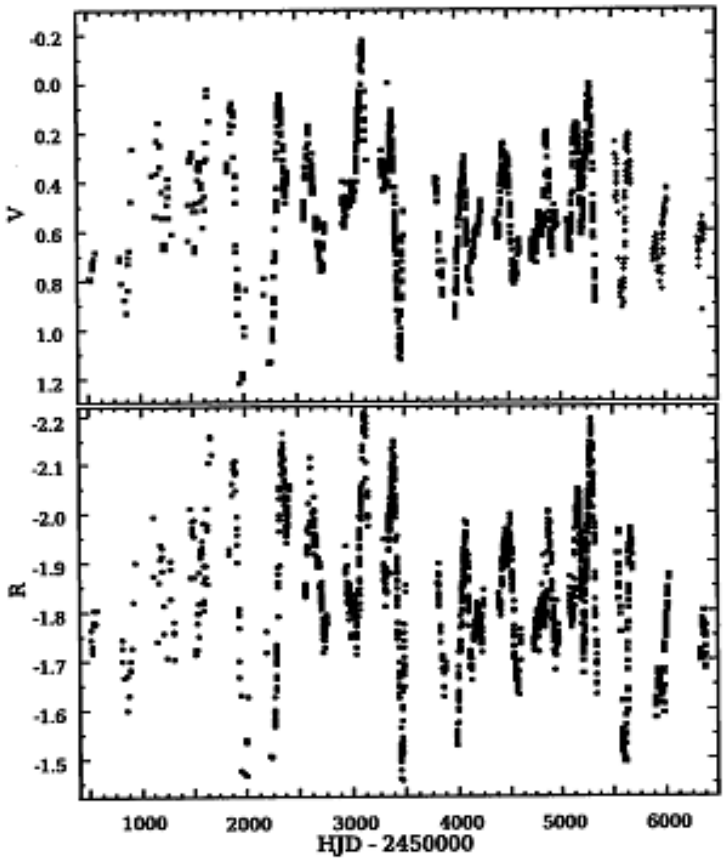

Figure 3.3: Variability data (Percy et al. 2001; Adelman & Dennis 2005).

$1.0\times10^{-7}\,M_\odot\,yr^{-1}$). Such profiles are not uncommon among AGB stars, more frequent among semi-regular variables than among Mira's. A possible interpretation, favoured by Knapp et al. (1998), is

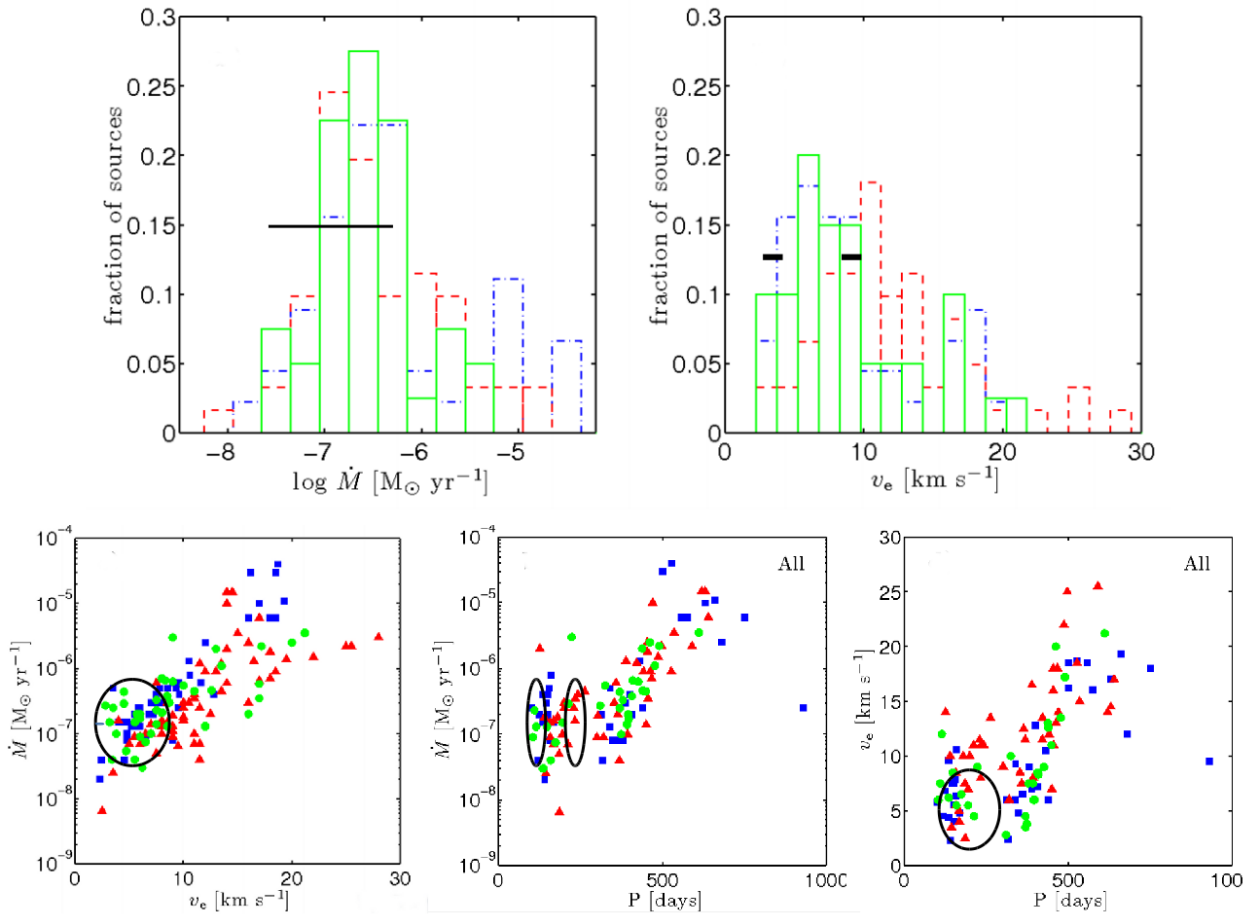

Figure 3.4: Top: mass-loss rate (left) and gas expansion velocity (right) distributions for S-type stars (solid green line, 40 stars), M-type stars (dashed-dotted blue line) and carbon AGB stars (dashed, red line). Bottom: mass-loss rate vs gas expansion velocity (left) and versus periods (middle); gas expansion velocities vs periods (right). Green dots are for S stars, blue squares for M stars and red triangles for carbon stars. In all panels, RS Cnc is shown in black.

that a change in the wind properties could occur when the central star undergoes a major change in its history (e.g. luminosity, pulsation mode, or chemistry), the new wind being the mark of the onset of a new mass-loss phase.

Neri et al. (1998) also observed RS Cnc in CO(1-0) using the IRAM Plateau de Bure Interferometer (PdBI) in combination with the IRAM 30-m telescope and CO(2-1) using the 30-m telescope. The observations were performed in October 1990 using the three PdBI antennas available at that time. The authors found an extended CO shell, with a size of about 10″. The position-velocity diagrams indicate that the envelope is not spherically symmetric and suggest a bipolar geometry. Nevertheless, their spatial resolution, ∼7″ in CO(1-0), as well as their spectral resolution, 1.3 km s^{-1} in CO(2-1) and 2.6 km s^{-1} in CO(1-0), were not sufficient to reveal more details.

Recently, Libert et al. (2010b) observed again RS Cnc in CO(1-0) and CO(2-1) simultaneously using the Plateau de Bure Interferometer and the Pico Veleta 30-m telescope. The interferometer data were obtained between November 2004 and April 2005 using 6 antennas in 3 configurations (B, C, D),

giving a beam of ∼2.6″ × 2.0″ in CO(1-0) and twice as small in CO(2-1).

On-the-fly (OTF) maps centred on the stellar position of RS Cnc were obtained in April 2005 using the 30-m dish. The interferometer and single dish data were then merged together to solve the short spacing problem.

Both CO and H I observations were reported, the latter over a much larger field of view. In the present section, we concentrate on the former, the H I observations are discussed in Chapter 7. The line profiles measured on the OTF single dish maps are displayed in Figure 3.5. They are composite and show two components of half-widths ∼2 km s^{-1} and ∼8 km s^{-1} respectively. As the broad component reveals a bipolar structure, it suggests defining an equatorial region perpendicular to it, from where the narrow velocity component seems to originate. The data are summarized in Table 3.1. The images obtained by merging single dish with interferometer data on the line are shown in Figure 3.6. Azimuthally averaged intensity profiles are displayed in Figure 3.7. The radial extension of the CO(1-0) shell is approximately 50% larger than that of the CO(2-1) shell. This result reveals different emission or absorption conditions, the latter being however not expected to cause such a large difference.

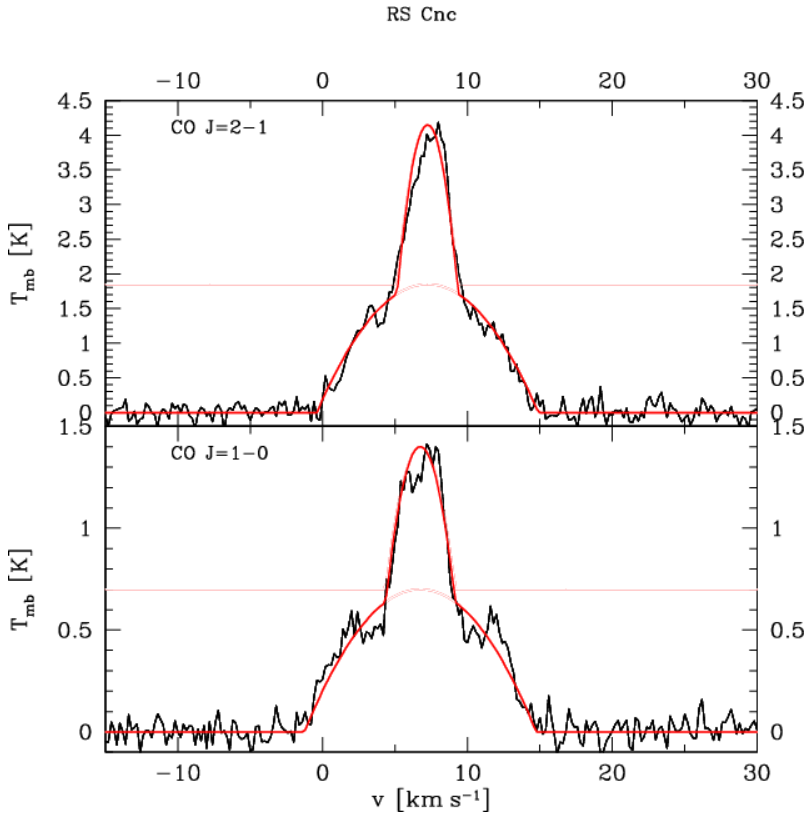

Figure 3.5: 30 m dish spectra centred on RS Cnc. The fit of a two-wind model is shown in red. The abscissas are in km s^{-1} and the spectral resolution is smoothed to 0.2 km s^{-1}.

The channel maps in CO(1-0) and CO(2-1) confirm the presence of a bipolar flow, supported by the position-velocity diagrams displayed in Figure 3.8. Maps integrated over each jet separately are shown in Figure 3.9. The slow wind component is better described by an expanding than by a rotating equatorial volume.

A simple toy model, illustrated in Figure 3.10, is found to give a satisfactory description of the

Table 3.1: Two-wind description of the CO(1-0) and CO(2-1) lines of RS Cnc (Libert et al. 2010b).

Line	Component	V_c (km s^{-1})	V_{exp} (km s^{-1})	T_{mb} (K)
CO(1-0)	broad	6.75(0.25)	8.0(0.5)	0.70(0.05)
	narrow	6.75(0.25)	2.4(0.1)	0.70(0.05)
CO(2-1)	broad	7.25(0.25)	7.65(0.50)	1.85(0.10)
	narrow	7.25(0.25)	2.1(0.1)	2.3(0.1)

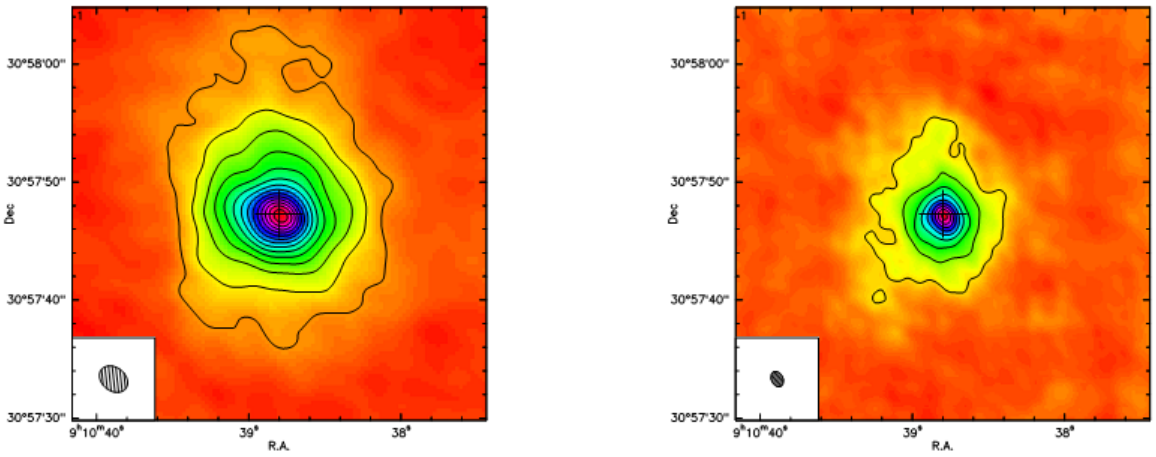

Figure 3.6: CO(1-0) (left) and CO(2-1) (right) emission of RS Cnc integrated over the width of the line (−2 to 17 km s^{-1}).

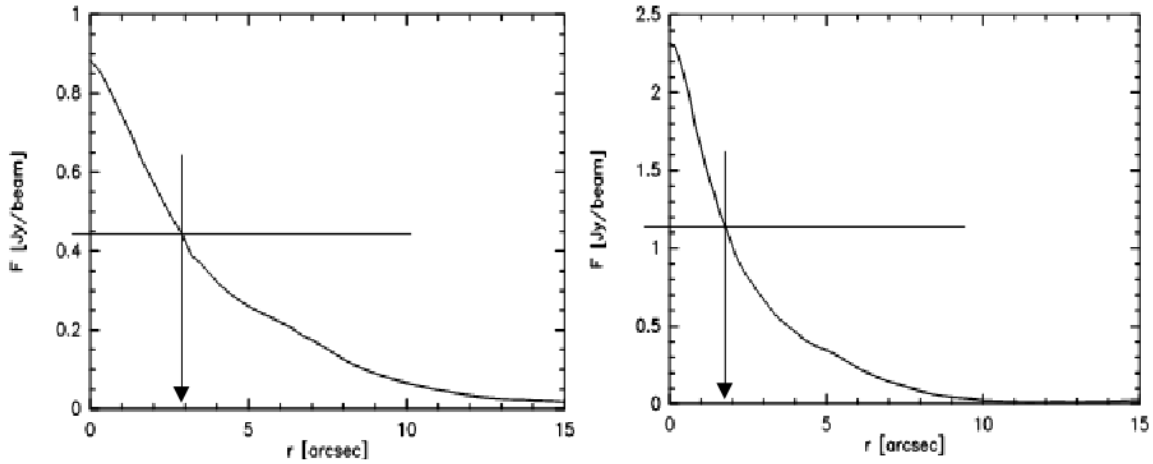

Figure 3.7: CO(1-0) (left) and CO(2-1) (right) brightness distributions in the central velocity channel at 7 km s^{-1} (of width 0.8 km s^{-1}). Arrows show widths at half maximum, ∼2.8″ and ∼1.7″ respectively.

essential features of the data. Note that the equatorial wind is called a disk in spite of its very broad angular aperture (90°). Indeed, the gap between it and the bicone can very well be made to cancel without altering the quality of the fit. The hypothesis of radial flow neglects micro-turbulent motions of ∼0.5 km s^{-1} that are expected to exist (Schöier & Olofsson 2001). Some thermal broadening, ∼1 km s^{-1}, is expected to occur, especially near the centre where the CO temperature can reach ∼1000K.

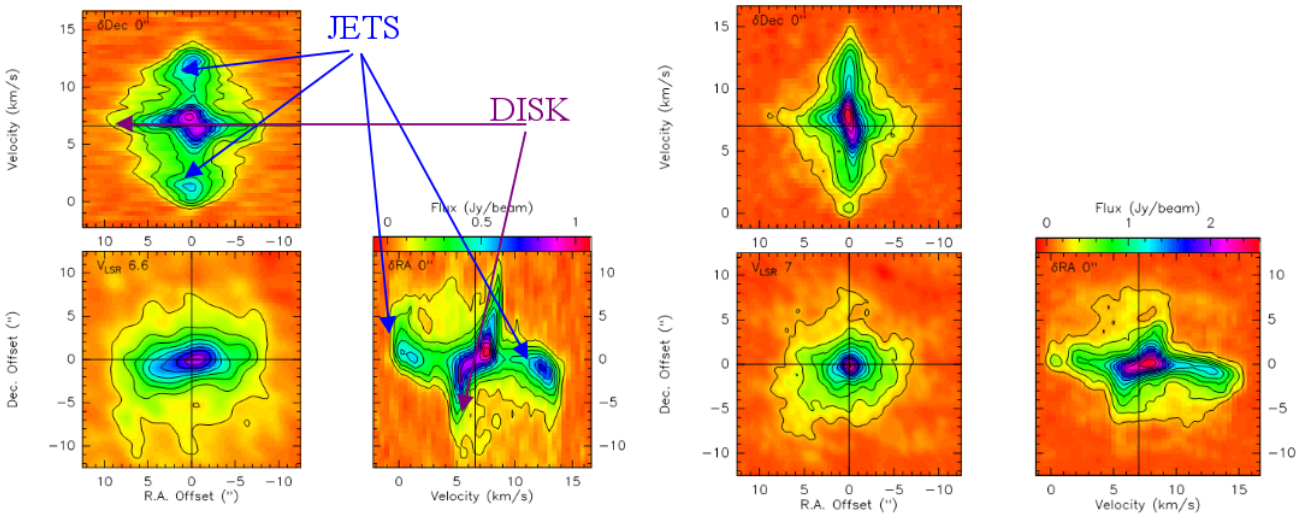

Figure 3.8: Position-velocity diagrams for CO(1-0), left, and CO(2-1), right.

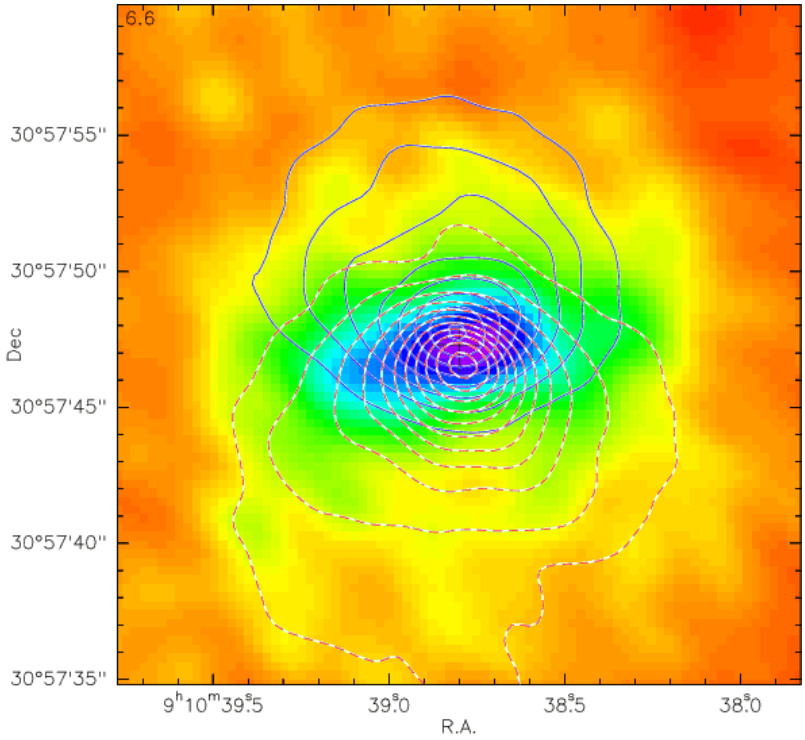

Figure 3.9: Bipolar structure in CO(1-0). Blue lines: emission integrated between -2 km s^{-1} and 3 km s^{-1}. Red dotted lines: emission integrated between 9.5 km s^{-1} and 16 km s^{-1}. The background image shows the 6.6 km s^{-1} channel.

3.3 The new 2011 observations

New CO(1-0) data were obtained in configurations A and B during winter 2011 (January 10 to February 8, 2011), baselines extending up to 700 m, giving a beam of 0.9″×0.8″ and allowing to achieve a slightly better spatial resolution in CO(1-0) than was obtained in the previous data set on CO(2-1). The new data were obtained in dual polarizations and cover a bandwidth of 3.6 GHz centred at 115.271 GHz, the

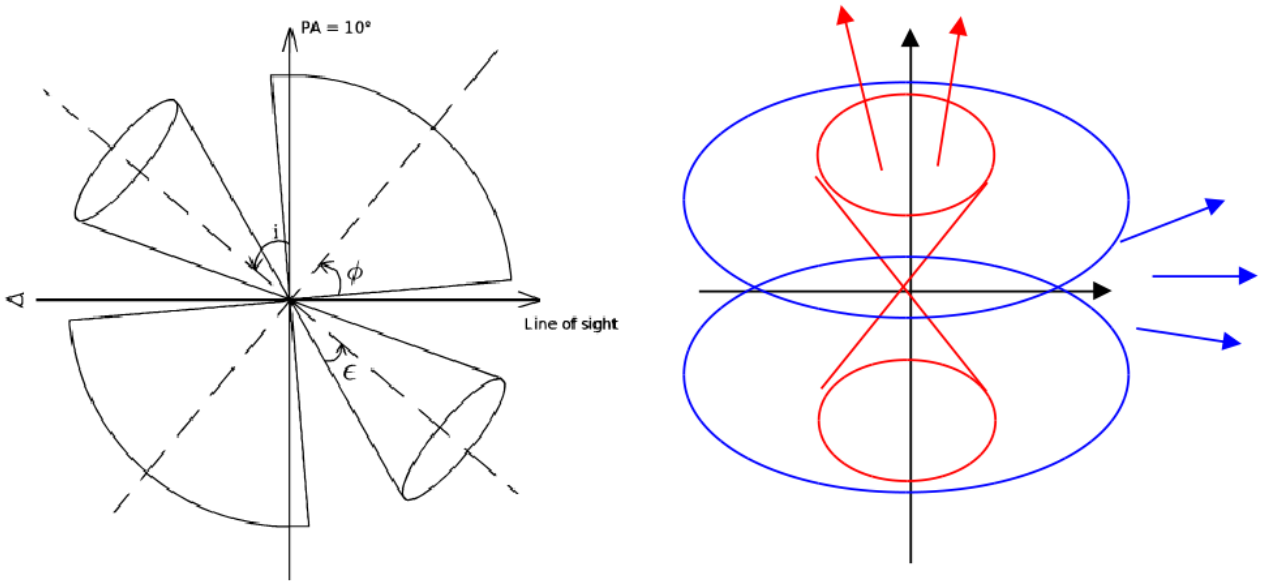

Figure 3.10: Wind model of Libert et al. (2010b). The jet axes are nearly (PA=10°) in the north-south plane, tilted by 45° with respect to the line of sight, the jet moving toward us aiming north. The half aperture of the jet cones is $\varepsilon = 20°$. The disk is normal to the jets with a half aperture $\varphi = 45°$.

nominal frequency of the CO(1-0) line. Two units of the narrow band correlator were set up to cover the CO line with a spectral resolution of 39 kHz over a bandwidth of 20 MHz, and the adjacent continuum was observed by the wideband correlator WideX (Wideband Express) with a channel spacing of 1.95 MHz. The observations result in 12h of on-source integration time with the 6 element array and reach a $1-\sigma$ thermal noise level of 12 mJy/beam in 0.2 km s^{-1} channels. The new data have been merged with the previous ones.

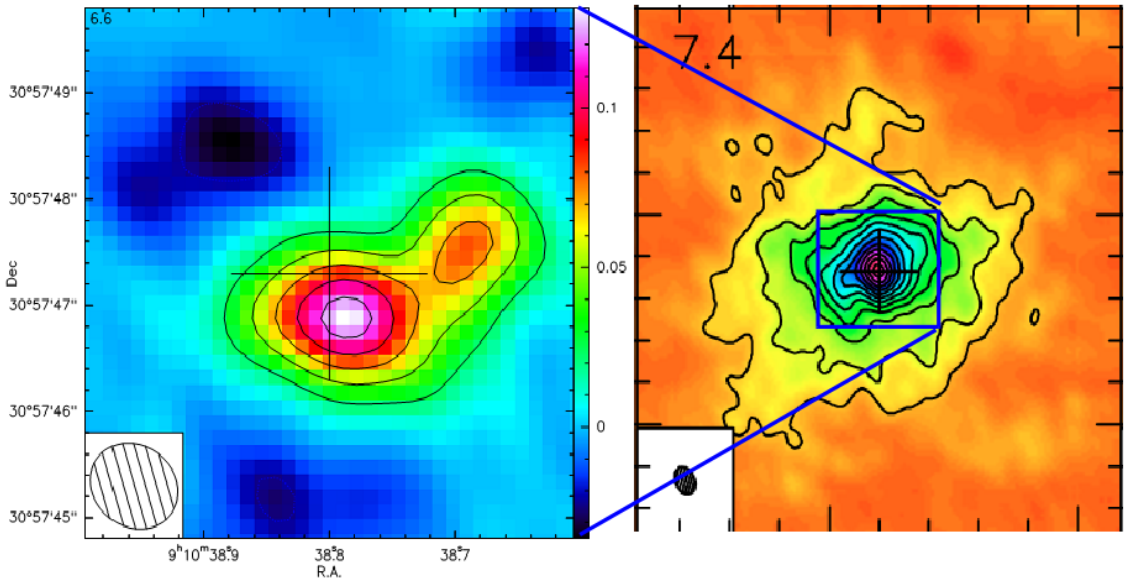

Figure 3.11: The 6.6 km s^{-1} CO(1-0) map (2011, left panel) compared with the 7.4 km s^{-1} CO(2-1) map (2004-2005, right panel).

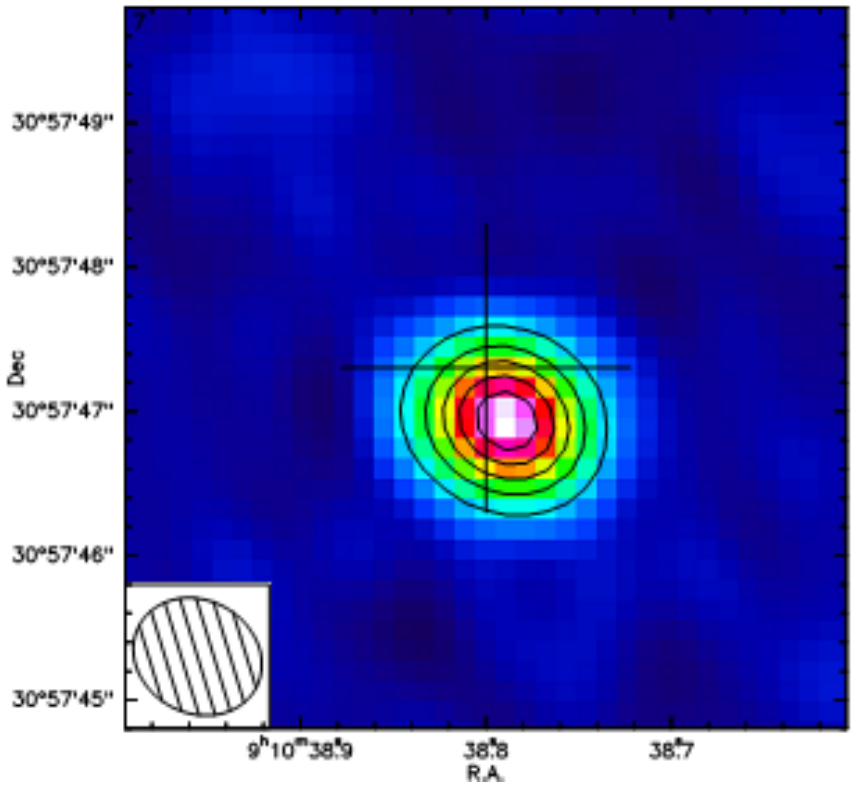

Figure 3.12: Continuum map at 115 GHz of RS Cnc (A+B configuration data obtained in 2011). The cross corresponds to the 2000.0 position of the star. The contour levels are separated by steps of 0.90 mJy/beam (20σ).

A remarkable feature of the new data is the presence of a companion – or something mimicking it – at about 1″ WNW of the star and at Doppler velocities between 5.8 km s^{-1} and 6.8 km s^{-1}. It is displayed in Figure 3.11 where it is compared with the map obtained in 2004-2005 on CO(2-1) at 7.4 km s^{-1} by Libert et al. (2010b). The latter, as well as its neighbour image at 7.8 km s^{-1}, displays an elongation in the same direction that may be due to the same cause; the difference in mean velocities, in excess of ∼1 km s^{-1}, is now known to be due to a small imprecision in the calculation of the CO(1-0) velocity.

Another asset of the new observations is the availability of new WideX data to produce a continuum image of RS Cnc at 115 GHz, displayed in Figure 3.12. The data were integrated over a 2 GHz band, excluding the high frequency portion of the band that is affected by atmospheric absorption (O_2 at 118.7 GHz). A single point source is clearly detected. The source is unresolved, and there is no evidence of a companion. It has a flux density of 5.4±0.3 mJy, which is consistent with the flux density reported by Libert et al. (2010b). It is slightly offset south-west with respect to the centre of phase because we used the coordinates at epoch 2000.0 from Hipparcos.

The data are presented in more detail in Hoai et al. (2014). In this paper, we also presented a first modelling of CO(1-0) and CO(2-1) spectral maps. More recently, we have reanalysed the CO data and developed an improved modelling which is presented in following section. The paper Hoai et al. (2014), which includes also a discussion of the H I data obtained at VLA in configurations C and D, is reproduced in the appendix A.

3.4 Modelling the wind

3.4.1 Overview

The merged data are available in the form of two sets of 13×13 continuum subtracted velocity spectra, one for CO(1-0) and one for CO(2-1), covering 18.2″×18.2″ (1″ corresponds to ∼140 au). Each spectrum in each cell is corresponding to the spectrum measured in a circular beam of 1.2″ (FWHM, Gaussian profile) and includes 101 velocity bins of 0.2 km s^{-1} each. The separation between cell centres is 1.4″. In the present section the analysis is mostly restricted to the 49 (7×7) central spectra covering 9.8″×9.8″.

Following Libert et al. (2010b) we aim at finding a model including a bipolar flow with an expansion velocity of ∼8 km s^{-1} and a slower equatorial wind (∼2 km s^{-1}) that describes the data as accurately as possible. Technically, this is done by varying the parameters of the model to minimize the χ^2 of the fit to the data, evaluated with uncertainties of 14 mJy/beam in each of the individual spectra. In a first phase, the fit is limited to the CO(1-0) data; the analysis of the CO(2-1) data follows, making use of the results obtained, and of the lessons learned, in the CO(1-0) analysis.

We take as default a simple model where the wind velocity, $V(\gamma, r)$, is a smooth function of the sine of the star latitude, γ, and of the distance r to the centre of the star (see section 3.4.2). Namely, the wind is supposed to be purely radial, free of turbulences and in local thermal equilibrium. Moreover, it is supposed to have been in such a regime for long enough a time, such that the radial extension of the gas volume is governed exclusively by the UV dissociation of the CO molecules by interstellar radiation and does not keep any trace of the star history. The flux of matter $f_{\dot{M}}(\gamma)$ is also supposed to be a smooth function of γ. Assuming the wind to be stationary, the density $n(\gamma, r)$ is then defined at any point from the relation $f_{\dot{M}}(\gamma) = r^2 V(\gamma, r) n(\gamma, r)$. The bipolarity of the flow is parameterized as a function of γ using Gaussian forms centred at the poles:

$$F(\gamma) = \exp(-\frac{(\gamma - 1)^2}{2\sigma^2}) + \exp(-\frac{(\gamma + 1)^2}{2\sigma^2}) \tag{3.1}$$

where σ is a parameter to be adjusted. This function is used to define the γ dependence of both the wind velocity and the flux of matter:

$$\begin{aligned} V(\gamma, r) &= V_1 F(\gamma) r^{\alpha_1} + V_2 r^{\alpha_2} \\ f_{\dot{M}}(\gamma) &= f_{\dot{M}_1} F(\gamma) + f_{\dot{M}_2} \end{aligned} \tag{3.2}$$

Hence the density,

$$n(\gamma, r) = r^{-2} \frac{f_{\dot{M}_1} F(\gamma) + f_{\dot{M}_2}}{V_1 F(\gamma) r^{\alpha_1} + V_2 r^{\alpha_2}} \tag{3.3}$$

In practice, while $F(\gamma)$ is close to unity at the poles, it does not cancel at the equator where it takes a value ε>0. The velocity and flux of matter are therefore $V_1 r^{\alpha_1} + V_2 r^{\alpha_2}$ and $f_{\dot{M}_1} + f_{\dot{M}_2}$ at the poles and

$\varepsilon V_1 r^{\alpha_1} + V_2 r^{\alpha_2}$ and $\varepsilon f_{\dot{M}_1} + f_{\dot{M}_2}$ at the equator. In particular, the velocity gradients, $\delta V / V \delta r$ read

$$\frac{\alpha_1 V_1 r^{\alpha_1 - 1} + \alpha_2 V_2 r^{\alpha_2 - 1}}{V_1 r^{\alpha_1} + V_2 r^{\alpha_2}} \text{ at the poles} \tag{3.4}$$

and

$$\frac{\varepsilon \alpha_1 V_1 r^{\alpha_1 - 1} + \alpha_2 V_2 r^{\alpha_2 - 1}}{\varepsilon V_1 r^{\alpha_1} + V_2 r^{\alpha_2}} \text{ at the equator.} \tag{3.5}$$

For r-independent wind velocities, $\alpha_1 = \alpha_2 = 0$, the velocity and flux of matter are $V_1 + V_2$ and $f_{\dot{M}_1} + f_{\dot{M}_2}$ at the poles and $\varepsilon V_1 + V_2$ and $\varepsilon f_{\dot{M}_1} + f_{\dot{M}_2}$ at the equator. For $\alpha_1 = 0$, the velocity gradients are

$$\frac{\alpha_2 V_2 r^{\alpha_2 - 1}}{V_1 + V_2 r^{\alpha_2}} \text{ at the poles} \tag{3.6}$$

and

$$\frac{\alpha_2 V_2 r^{\alpha_2 - 1}}{\varepsilon V_1 + V_2 r^{\alpha_2}} \text{ at the equator.} \tag{3.7}$$

These examples show that one must be careful not to simply interpret the quantities with index 1 as qualifying the jets and those with index 2 as qualifying the equatorial wind.

This simple model uses seven parameters: V_1, V_2, $f_{\dot{M}_1}$, $f_{\dot{M}_2}$, α_1, α_2 and σ. In addition, the direction in space of the axis of the bipolar outflow, meaning two angles, needs to be adjusted; this implies a minimum of 9 parameters to be adjusted with a χ^2 minimization process. For this we have used the MINUIT package from CERN.

Other quantities that need to be defined, even if not varied, include:

- the star Doppler velocity, V^*
- the star offsets in right ascension and declination, ΔRA and ΔDec.
- an effective smearing parameter acting on the Doppler velocities and accounting for thermal broadening and other possible effects.
- the extension of the beam.
- the r-dependence of the temperature.
- the emission and absorption mechanisms.

The latter two are discussed in paragraph 3.4.3. Smearing accounts for both thermal broadening and an ad hoc instrumental resolution of 0.2 km s^{-1}. Thermal broadening caused by the Doppler shift of

the radiating particles, is taken into as $0.02\sqrt{T}$ km s^{-1}, where T is the temperature measured in Kelvins. The thermal velocity distribution is a Gaussian with standard deviation $\sigma_v = \sqrt{kT/m}$. In the circumstellar envelope, at 1000K, the thermal broadening has a standard deviation of $\sigma_v = 0.5$ km s^{-1} meaning $\frac{1}{2}$FWHM=0.6 km s^{-1}. But actually, in the CO region, the temperature spans from 20K to 1000K and $\frac{1}{2}$FWHM spans between ~0.1 km s^{-1} and 0.6 km s^{-1}. The effect is quite small for CO. Attempts to increase it artificially did help somewhat in improving the quality of the fits, in particular in confining the velocity gradients near the star, but not enough to be retained as a serious option.

The convolution with the beam is considered. However in the case of very extended source (~10″) and small beam size (1.2″) like RS Cnc, the convolution result is almost the same as that obtained by using a pencil beam and multiplying by the beam area. In order to save computing time, in the model, the spectrum in each cell is obtained from the integral of the emission and absorption along its central line of sight, properly accounting for the beam area. A special treatment applies to the central cell, where 100 spectra integrated along an array of equally spaced lines of sight are integrated.

3.4.2 Adequacy of the model

In the present paragraph, we anticipate on the results of the best fit and discuss qualitatively the adequacy of the assumptions being made and of the form chosen for $F(\gamma)$. There is much arbitrariness in the choices that have been made; yet, they generally rest on the result of various attempts to use different assumptions, which have been tried and found to give less good fits to the data, or at least no significant improvement. We briefly mention the most important of these.

Allowing for the coexistence of two winds having different velocities, as argued by Knapp et al. (1998), implies defining the history of the expansion of the circumstellar envelope. Indeed, at a given point in space, the wind cannot have several velocities, but only one. One of the two winds must therefore have appeared after the other and be dominant in a region of space, the other being dominant outside this region. We found no evidence in the data for such a hypothesis and accepted that the vector field of velocities and the scalar fields of temperatures and densities could be taken as stationary. At a velocity of 2 km s^{-1}, the wind takes ~3000 years to reach a 10″ radius; we therefore assume implicitly that the dynamics of expansion has not changed during the past 3000 years or so.

Allowing for rotation around the axis of the bipolar outflow in the equatorial region (namely with a dependence of the form $1-F(\gamma)$ on star latitude) was found to improve the quality of the fit by ~8%. The tangential component of the wind velocity was taken to be of the form: $V_{rot}[1-F(\gamma)](r/r_0)^{N_{rot}}$ ($N_{rot} = -1/2$ for a Keplerian disk) with r_0=0.1″. The best fit values were V_{rot} ~4.4 km s^{-1} and $N_{rot} \sim -3/4$. Namely, at the equator and 1″ radius, the rotation velocity had already declined to 0.8 km s^{-1}. While significant, the improvement of the quality of the fit was not considered sufficient to pursue such study, the extreme centrality of its domain of influence being considered too small with respect to the beam size.

The form adopted for the velocity gradients is quite arbitrary and is only the result of numerous attempts at improving the quality of the fit by allowing for an r-dependence of the wind velocity. Power law dependence of the radial velocity is commonly assumed for single winds (see e.g. Nguyen-Q-Rieu et al. 1979). While the need for a velocity gradient is clear for both the polar and equatorial winds, that of

making a difference between them is less obvious. In the final fits (Nhung et al. 2015a), an exponentially decreasing gradient, which reaches a plateau, was preferred to a power law, which keeps indefinitely increasing, but both give similar results. It has the form $V(\gamma, r) = V_1 F(\gamma)(1-\lambda_1 e^{-r/2.5''}) + V_2(1-\lambda_2 e^{-r/2.5''})$.

Among many other attempts to achieve a significant improvement of the fits to the observed data, we studied a model allowing for the molecular flow to deviate from radial in a way illustrated in Figure 3.13. In no case were we able to produce significantly better fits.

The model of Libert et al. (2010b) implies the presence of a gap between the polar and equatorial winds. The formalism used in the present study excludes such possibility. While a continuous variation of the parameters as a function of star latitude sounds qualitatively more physical than sudden changes, a quantification of this statement is desirable. One approach has been to allow for an increase of the density at the equator; however, the widths in latitude demanded by the fits for both the bipolar outflow and the newly introduced equatorial enhancement are such that they effectively overlap, excluding the possibility of a narrow gap between the two. While evidence for a bipolar outflow is overwhelming, that for a disk is therefore much weaker, at least if one understands "disk" as a concentration near the equator. To quantify this statement, we take for $F(\gamma)$ the form used by Libert et al. (2010b), namely $F(\gamma) = F_1(\gamma) + F_2(\gamma)$ with $F_1(\gamma) = 1$ for $|\gamma| > 1 - a_{jet}$ and 0 elsewhere and $F_2(\gamma) = 1$ for $|\gamma| < a_{disk}$ and 0 elsewhere. a_{disk} and a_{jet} are the widths of disk and jet in sine of the star latitude, γ. Defining $a_{gap} = 1 - a_{jet} - a_{disk}$ evidence for a "disk" implies $a_{gap} >> 0$. The best fit result for a zero gap is $a_{jet} = 0.546$ and $a_{disk} = 0.454$ with densities (at r =0.1″) $\rho_{jet} = 11.6\ 10^6$ H cm^{-3} and $\rho_{disk} = 10.7 \times 10^6$ H cm^{-3} for CO(1-0). Keeping the wind velocities at their best fit values, we study what happens when we make the disk narrower up to the point where it disappears and, similarly, what happens when we make the jets narrower up to the point where they disappear. When we vary the disk, we keep the jets unchanged and conversely, when we vary the jets, we keep the disk unchanged. What we vary is simply the width a and the density ρ of the structure that is studied. The results are summarized in Figure 3.14 that shows the dependences on a of the value of χ^2 and of the product $a\rho$. We choose to show $a\rho$ rather than ρ because, when the disk is varied, $a\rho$ stays nearly constant. The results displayed in Figure 3.14 illustrate clearly that the width of the disk is essentially irrelevant: if you want a narrow disk, you simply scale its density up accordingly and the fit is just as good. On the contrary, when you make the jets narrower than their best fit value, the quality of the fit deteriorates and making the jet density higher is not sufficient to compensate. It seems therefore better to talk of an equatorial waist for the low velocity wind adding to the bipolar outflow rather than a disk-like flow.

3.4.3 Emission, absorption and dissociation

The r-dependence of temperature is taken from Schöier & Olofsson (2010, private communication) and modelled with a power law of index −0.7 as illustrated in Figure 3.15. The spontaneous emission probabilities are 7.4 10^{-8} s^{-1} for CO(1-0) and 7.1 10^{-7} s^{-1} for CO(2-1), and the populations of the $J = 1$ and $J = 2$ levels are calculated under the hypothesis of local thermal equilibrium, proportional to $\frac{2J+1}{T} \exp(-\frac{E_j}{kT})$ (see section 2.8). We have attempted to modulate the temperature as a function of r in order to improve the quality of the CO(1-0) fit, however without success. We shall see later, however, that this becomes essential when fitting the CO(1-0) and CO(2-1) data together. The parameters defining

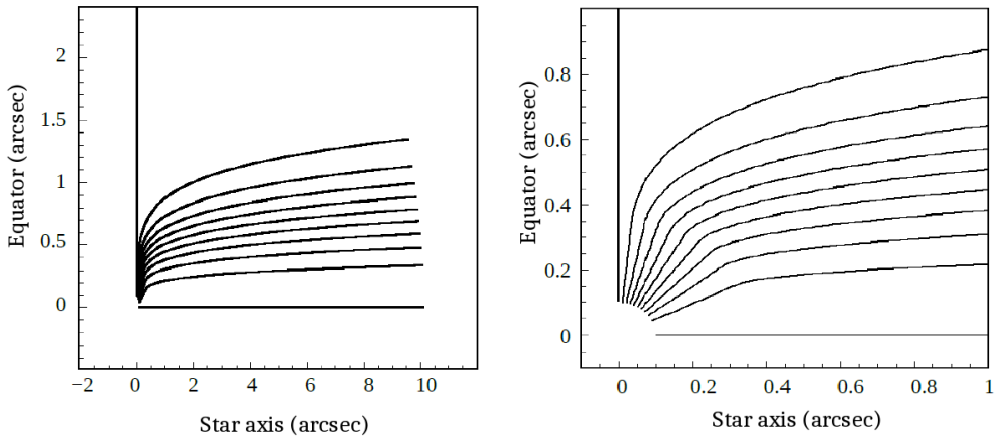

Figure 3.13: Meridian plane configuration of the molecular outflow for the model allowing for non-radial velocities. The curves are equally spaced in γ (steps of 0.1). The abscissa is the star axis, the ordinate on a radius along the equator, both in arcseconds. The right panel is a zoom of the left panel for r<1″.

emission and absorption were therefore kept fixed at their standard local thermal equilibrium values during the χ^2 minimization process. To translate the CO masses into hydrogen masses we use abundance ratio [CO]/[H] ~4.0 10^{-4} from Smith & Lambert (1986) and asumming all carbon in CO. With stars having masses of the Sun, the abundance ratio [He]/[H] is 1/9 so the mass of hydrogen is 9/13~70% of the total mass.

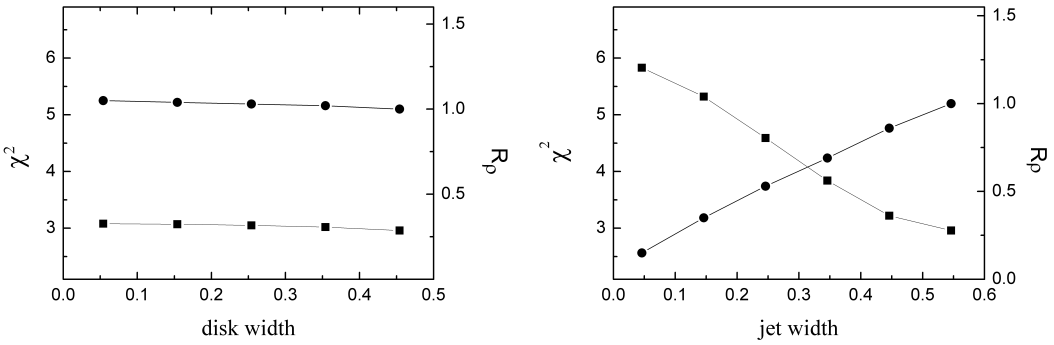

Figure 3.14: Dependences on a of the value of χ^2 (square symbols, left hand scales) and of the product $a\rho$ normalized to its zero-gap value (R_ρ, dotted symbols, right hand scales) for the disk (left panel) and the jet (right panel) respectively

The radial extensions of the CO(1-0) outflow are ~16″ (3.5 10^{16} cm) for the polar winds and ~10″ (2.2 10^{16} cm) for the equatorial wind (Libert et al. 2010b). They can be compared with the values given by the relation $\xi = \xi_0 \exp[-\ln 2(\frac{r}{r_{1/2}})^\zeta]$ proposed by Mamon et al. (1988) where ξ, ξ_0 are the CO abundance at distance r to the star centre and at $r = 0$, $r_{1/2}$ is the distance at which 50% CO molecules are dissociated and ζ defines the slope of abundance versus r in log-log scale. The values of ζ and $r_{1/2}$ are displayed in Figure 3.16. For a mass-loss of 10^{-7} $M_\odot$ yr^{-1}, we find $r_{1/2}$ ~2.2 10^{16} cm (~10″) and ζ ~2.1 at a velocity of 7.5 km s^{-1}. The value of χ^2 changes by less than 5% when $r_{1/2}$ and ζ vary in the range of 9 to 15″ and 2.1 to 3 respectively. The data show therefore that their radial extensions are indeed governed by CO photo-dissociation, as was assumed a priori in the model. The relation given by Mamon et al.

(1988) is used in the model with ζ=2.1.

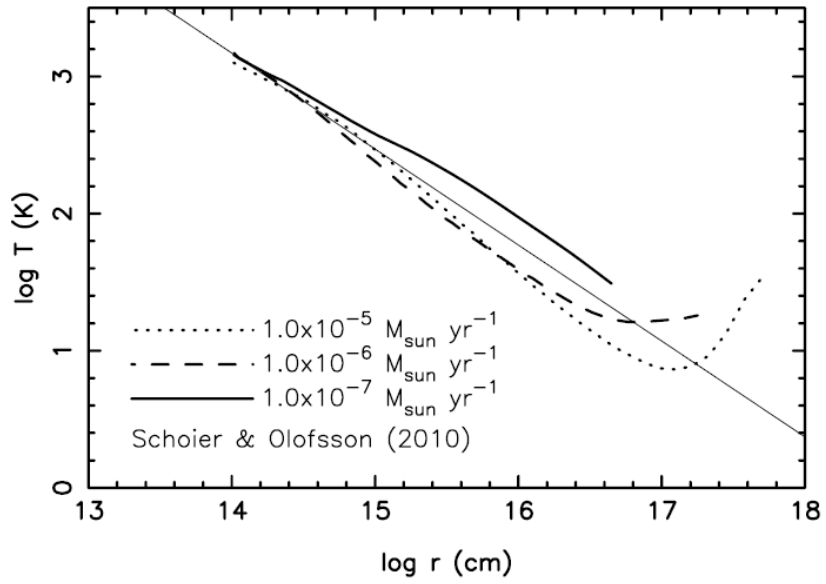

Figure 3.15: Dependence of log(T[K]) on log(r[cm]) (r is the distance to the central star) used in this work (full straight line, α=0.7) compared with the results obtained by Schöier & Olofsson (2001) for three different mass-loss rates. Remember that 10″=2.14 10^{16} cm.

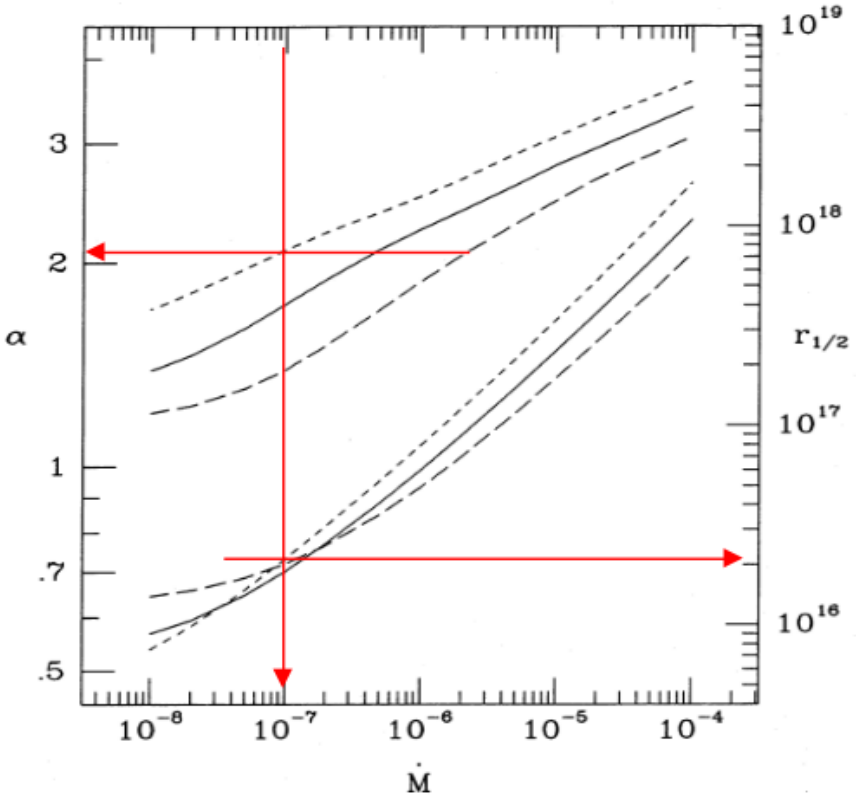

Figure 3.16: Values of ζ (upper curves, left scale) and $r_{1/2}$ (lower curves, right scale) as a function of $\dot{M}$. The short-dashed curves correspond to V=7.5 km s^{-1}, the others to 15 and 30 km s^{-1} (Mamon et al. 1988).

3.4.4 Fitting the CO(1-0) and CO(2-1) data

The synthesized spectra are produced by integrating the emitted flux, reduced by the absorbed flux, along the line of sight in steps of 0.05″ from −20″ to 20″ (here arcseconds are meant to be distances in x equal to ∼143 au corresponding to 1″ in y or z). A cut-off is applied at 0.1″ (∼17 R_{star}) in r in order to avoid divergences in powers of $1/r$. The best fit values of the model parameters for CO(1-0) and CO(2-1) are listed in Table 3.2 and the spectral maps are displayed in Figure 3.17 and Figure 3.18.

Table 3.2: Best fit parameters obtained for the CO(1-0) and CO(2-1) data.

Parameter	Best fit value (CO(1-0))	Best fit value (CO(2-1))
$AI(^\circ)$	52.4	52.4
$PA(^\circ)$	10.4	10.4
σ	0.342	0.297
V_1 (km s^{-1})	3.52	3.00
V_2 (km s^{-1})	1.73	1.61
$f_{\dot{M}_1}$ (10^{-8}M$_\odot$ yr^{-1} sr^{-1})	1.27	0.61
$f_{\dot{M}_2}$ (10^{-8}M$_\odot$ yr^{-1} sr^{-1})	0.64	0.41
α_1	0.16	0.22
α_2	0.13	0.22
V_*	6.6	7.1
ΔRA	0.15	0.075
ΔDec	0.37	1.875

Figure 3.19 (down-right) displays the dependence on r of the wind velocities at $\gamma = \pm 1$ (poles) and $\gamma = 0$ (equator). The velocity gradient is found to be significantly steeper at the formers than at the latter. The dependence of the flux of matter and velocities on the sine of the star latitude are shown in Figure 3.19 (upper panels). They are both nearly three times as large at the poles as at the equator so that the density distributions on sine of latitude are almost flat (Figure 3.19, down-left). The value of σ, 0.342, means 20°, or 47° for the FWHM aperture of the bipolar outflow.

3.5 Central symmetry

In the course of comparing the CO data with the prediction of a simple model, we noted that the former did not fully obey the central symmetry that is built in the latter. The present section studies the central symmetry of the gas distribution and kinematics of RS Cnc, namely to which extent diametrically opposite gas volumes (with respect to the centre of the star) have equal densities and temperatures and opposite velocities.

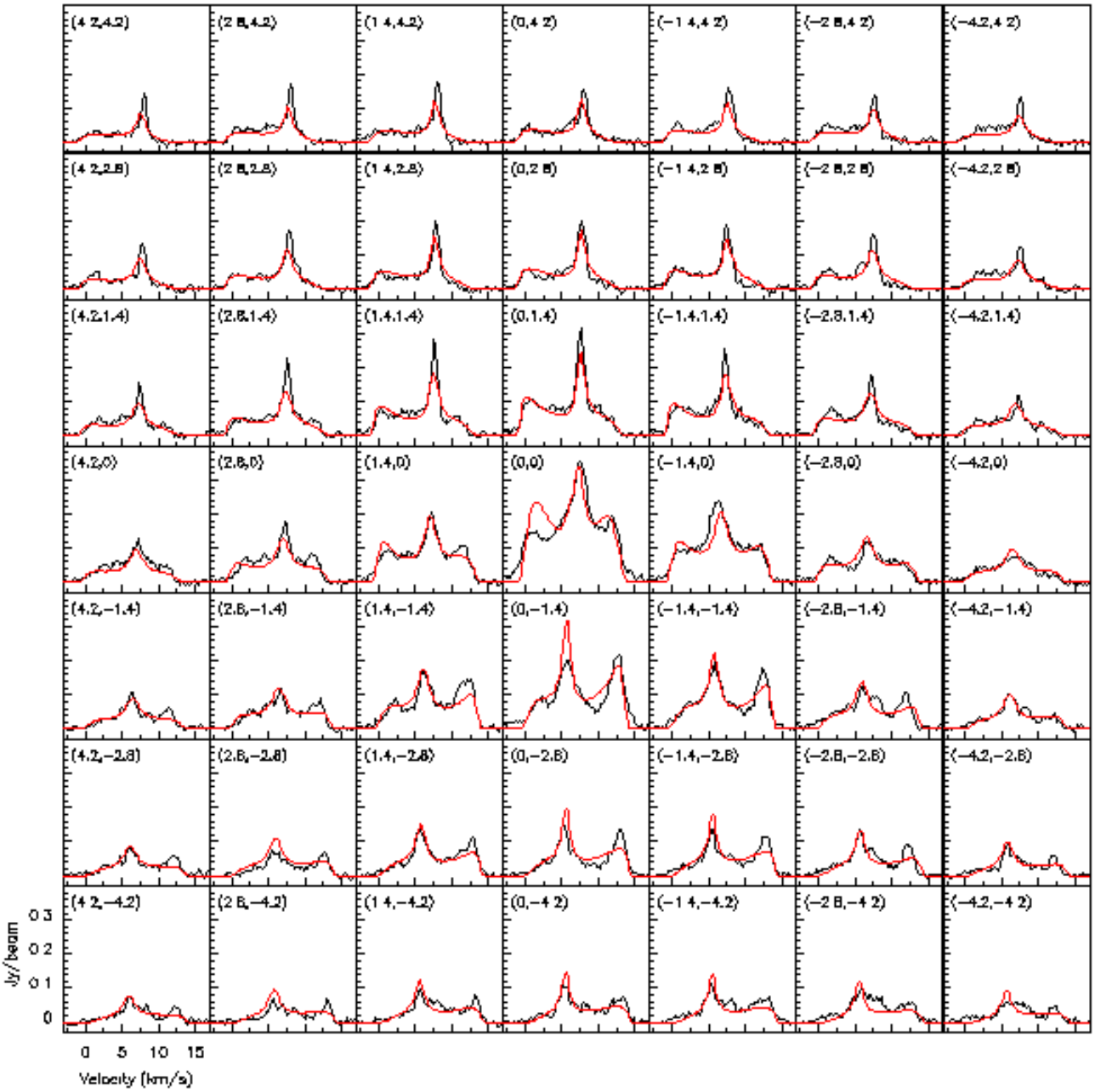

Figure 3.17: Spectral map of the CO(1-0) data (black) and best fit (red).

3.5.1 Signatures of central symmetry

In the optically thin limit, if the star velocity, the temperature and the density distributions obey central symmetry, the flux density measured at Doppler velocity V_x in a pixel having sky coordinates y and z obeys the relation $f(V_x, y, z) = f(-V_x, -y, -z)$. This relation remains valid in the presence of a small smearing of the Doppler distributions, whether of instrumental or physical origin. The difference between a spectrum at (y, z) and the mirror spectrum at $(-y, -z)$ must therefore cancel: $\Delta_{mir}(V_x, y, z) = f(V_x, y, z) - f(-V_x, -y, -z) = 0$. Their sum reads (the index *mir* standing for mirror) $\sum_{mir}(V_x, y, z) = f(V_x, y, z) +$

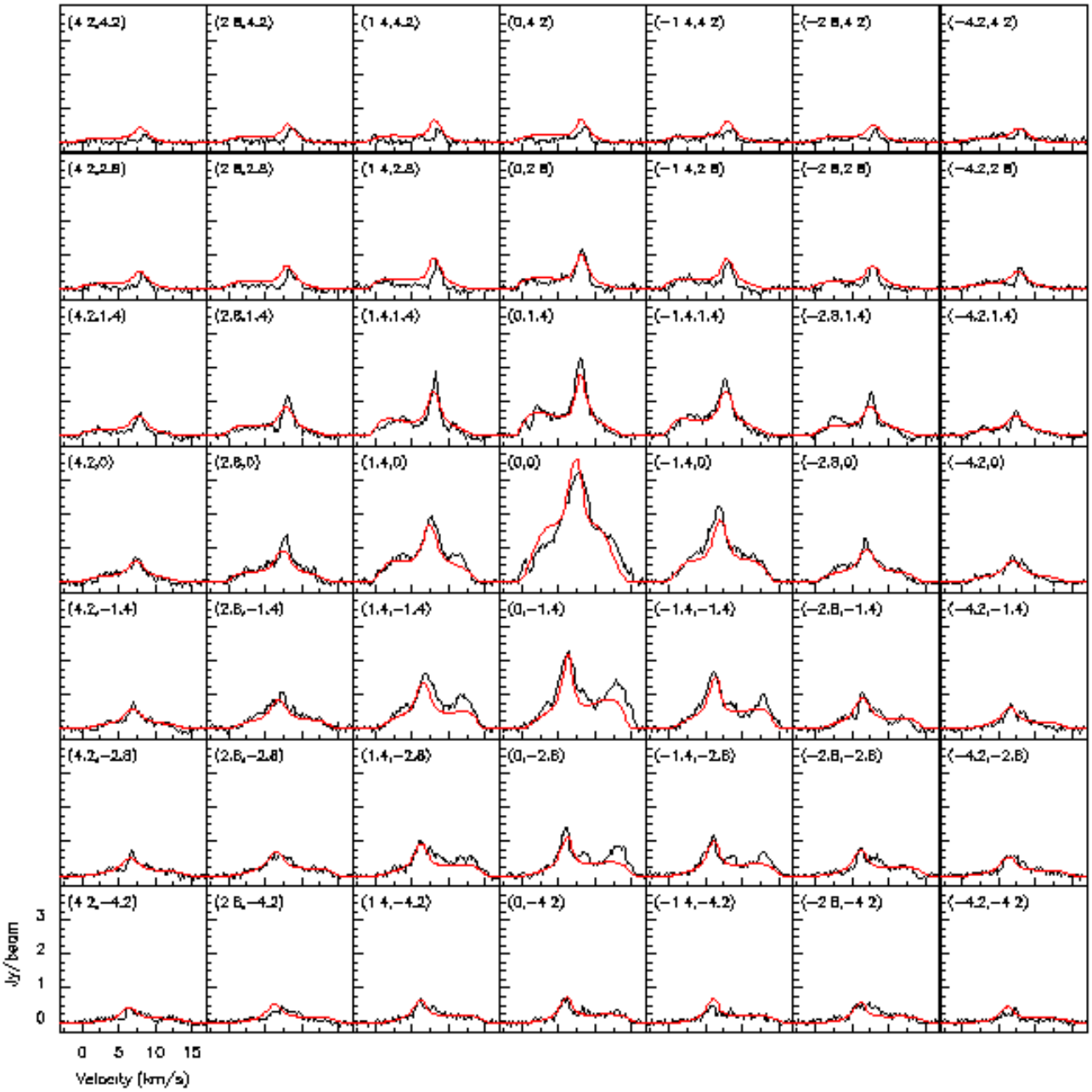

Figure 3.18: Spectral map of the CO(2-1) data (black) and best fit (red).

$f(-V_x,-y,-z) = \sum_{mir}(-V_x,-y,-z)$ and, when summing over y and z, $\sum_{mir}(V_x) = \sum_{mir}(-V_x)$.

The sum of a spectrum measured at (y,z) and that measured at $(-y,-z)$ reads (the index *dir* standing for direct) $\sum_{dir}(V_x,y,z) = f(V_x,y,z) + f(V_x,-y,-z) = f(V_x,y,z) + f(-V_x,y,z) = \sum_{dir}(-V_x,y,z)$ and their difference: $\Delta_{dir}(V_x,y,z) = f(V_x,y,z) - f(V_x,-y,-z) = f(V_x,y,z) - f(-V_x,y,z) = -\Delta_{dir}(-V_x,y,z)$. Note that the relation $\sum_{mir}(V_x) = \sum_{mir}(-V_x)$ is obeyed by construction.

The three relations $\Delta_{mir} = 0$, $\sum_{dir}(V_x) = \sum_{dir}(-V_x)$ and $\Delta_{dir}(V_x) = -\Delta_{dir}(-V_x)$ are therefore signatures of central symmetry. As $\Delta_{dir}(V_x) = -\Delta_{dir}(-V_x)$ applies to any value of (y,z) its average must be calculated over half the (y,z) plane (when summing over the full plane, it cancels by construction).

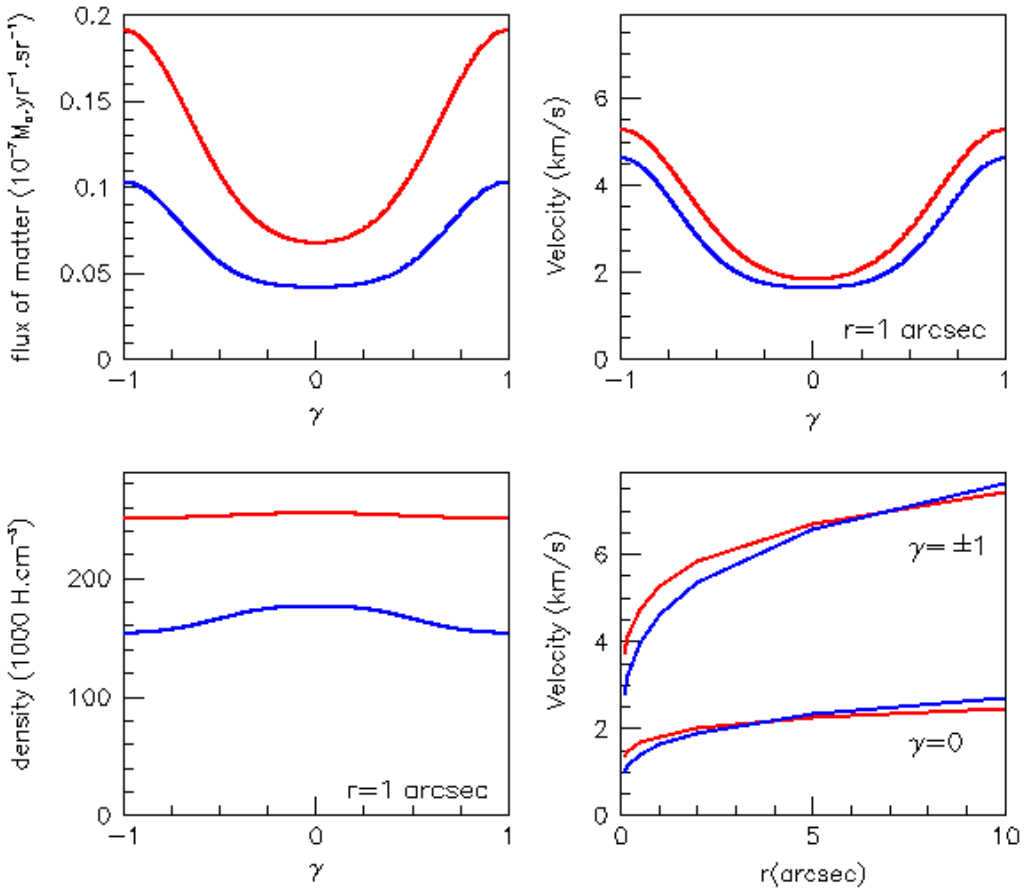

Figure 3.19: Best fit results of CO(1-0) (red) and CO(2-1) (blue): Dependences on sine of the latitude, γ, of the flux of matter (up-left), of the velocity at $1''$ (up-right) and of the density at $1''$ (down-left); and r-dependence of the velocity (down-right) at equator (lower curves) and poles (upper curves).

3.5.2 Central asymmetry in the CO(1-0) data

The evaluation of the four quantities $\sum_{mir}$, Δ_{mir}, $\sum_{dir}$ and Δ_{dir} implies the knowledge of the star velocity and position. The analysis presented here uses star declination (30°57′47.3″) and right ascension (9h10min38.80s) at epoch 2000.0, as measured from Hipparcos data (van Leeuwen 2007) on which the set of velocity spectra is centred. The star Doppler velocity, on which the velocity spectra themselves are centred, is taken from the analysis presented in the preceding section. Its value, V_x = 6.6 km s^{-1}, is the result of a fit to the observed data of a model including a bipolar outflow with a typical wind velocity of ∼8 km s^{-1} decreasing to ∼2 km s^{-1} near the equator (referred to as "standard model" in what follows). The zero of the velocity scale used in the present analysis corresponds therefore to V_x=6.6 km s^{-1} (cf. Table 3.2), positive values being red shifted and negative values blue shifted. The standard model is centrally symmetric with respect to the star except for a small absorption, which, however, induces negligible asymmetries. The pivot velocity used to produce mirror spectra is taken equal to the star velocity unless specified otherwise.

The velocity distributions of $\sum_{dir}$, Δ_{dir}, $\sum_{mir}$ and Δ_{mir}, evaluated over the 7×7=49 central velocity

spectra of the CO(1-0) data are displayed in Figure 3.20. Significant asymmetries are evidenced. The $\sum_{dir}$ distribution suggests its being made of two symmetric distributions, a broad distribution centred at v∼0 and a narrow distribution centred at v∼1 km s^{-1}.

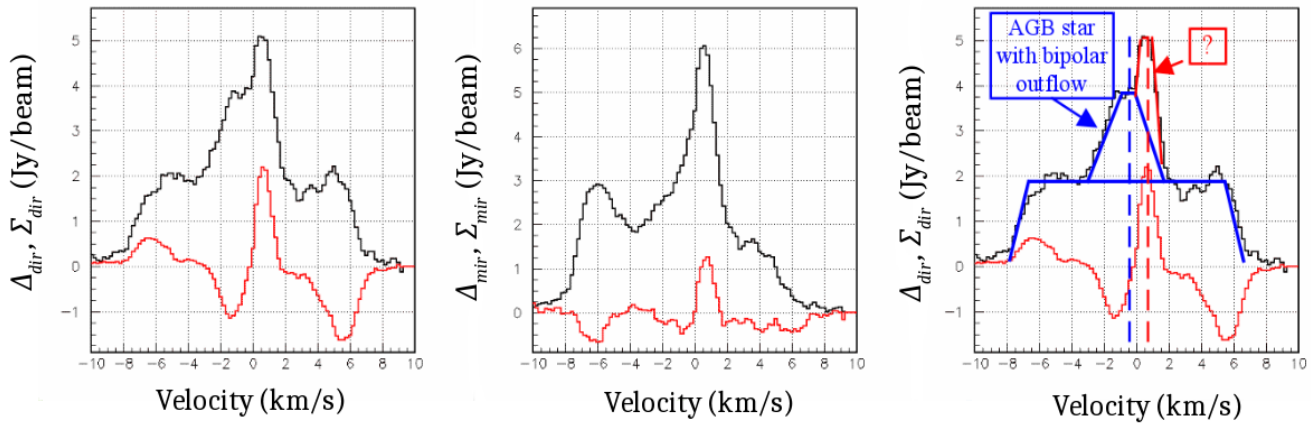

Figure 3.20: Velocity distributions summed over the northern half of the velocity spectra (24 cells) of the CO(1-0) data. Left: Δ_{dir} (red) and $\sum_{dir}$ (black), central symmetry would require $\sum_{dir}(-V_x) = \sum_{dir}(V_x)$ and $\Delta_{dir}(-V_x) = -\Delta_{dir}(V_x)$. Centre: Δ_{mir} (red) and $\sum_{mir}$ (black), central symmetry would require Δ_{mir}=0. Right: Schematic two-component interpretation of the CO(1-0) lack of central symmetry.

In order to map the distribution of the central asymmetry, we decompose the contents of each pair of (V_x, y, z) and $(-V_x, -y, -z)$ bins into a common value f_{sym} (the smaller of the two values) and an excess f_{exc} (the difference between the larger and the smaller). The resulting distributions of $R_{asym} = f_{exc}/\sum f_{sym}$, where the sum extends over the whole velocity spectrum at the relevant position of the line of sight, measures the relative central asymmetry. They display important regularities that can be schematically summarized as a dominance of a narrow velocity spike between ∼0 and ∼2 km s^{-1} in the northern part of the sky (with respect to the star) and a dominance of a broad span of velocities in the southern part. This is illustrated in Figure 3.21 where the R_{asym} distributions, summed over the 21 (3×7) northern and 21 southern spectra separately, are displayed.

3.5.3 CO(1-0): mapping the asymmetric excess

A potential source of central asymmetry is an offset of the star location with respect to the centre of the set of velocity spectra. Indeed, between year 2000 and the time at which observations were made, the star is known from Hipparcos data (van Leeuwen 2007) to have drifted by −11.12 mas/yr in right ascension and −33.42 mas/yr in declination. While the set of velocity spectra is centred on the star location at epoch 2000.0, observations have been made at different times and merged without taking account of the star proper motion between separate sets of observations. A first set of CO(1-0) and CO(2-1) data was taken at Plateau de Bure in November 2004 (Libert et al. 2010b) followed by on-the-fly observations at Pico Veleta in April 2005. New, better quality data were then obtained from Plateau de Bure in January and February 2011 on the CO(1-0) line. The data used in Hoai et al. (2014) and in the present work are the result of merging these different observations and therefore imply a small smearing of the measured

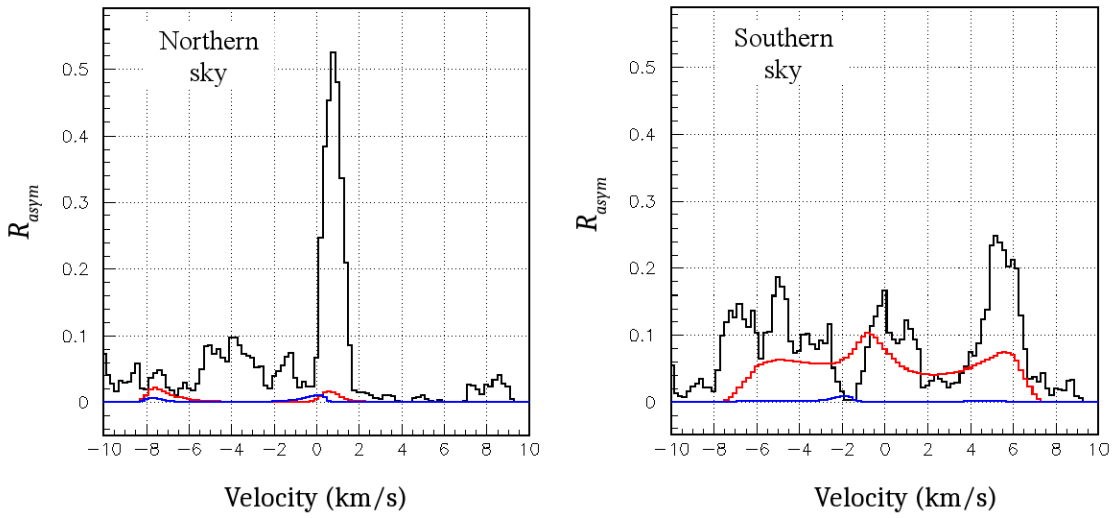

Figure 3.21: Distributions of R_{asym} summed over the 21 (3×7) northern (left) and 21 southern (right) spectra of the CO(1-0) data (black line). The standard model predictions are shown for zero offset (blue) and for an offset of 0.15″ West and 0.37″ South (red).

quantities. The continuum map reported in Hoai et al. (2014), which uses 2011 Plateau de Bure observations exclusively (Figure 3.12), shows a displacement of 0.14±0.04″ West and 0.35±0.04″ South in very good agreement with the predicted drift of 0.122″ West and 0.370″ South. In order to evaluate the effect of such an offset on the central symmetry, we use the standard model to calculate the asymmetry that it induces. The result, displayed in Figure 3.21, is in good qualitative agreement with the southern excess observed in the data. Indeed, when the star moves south, each southern spectrum probes higher densities and each northern spectrum lower densities, in an approximately constant ratio. This result, having revealed an effect that was previously thought to be negligible, gives confidence in the reliability and sensitivity of the method.

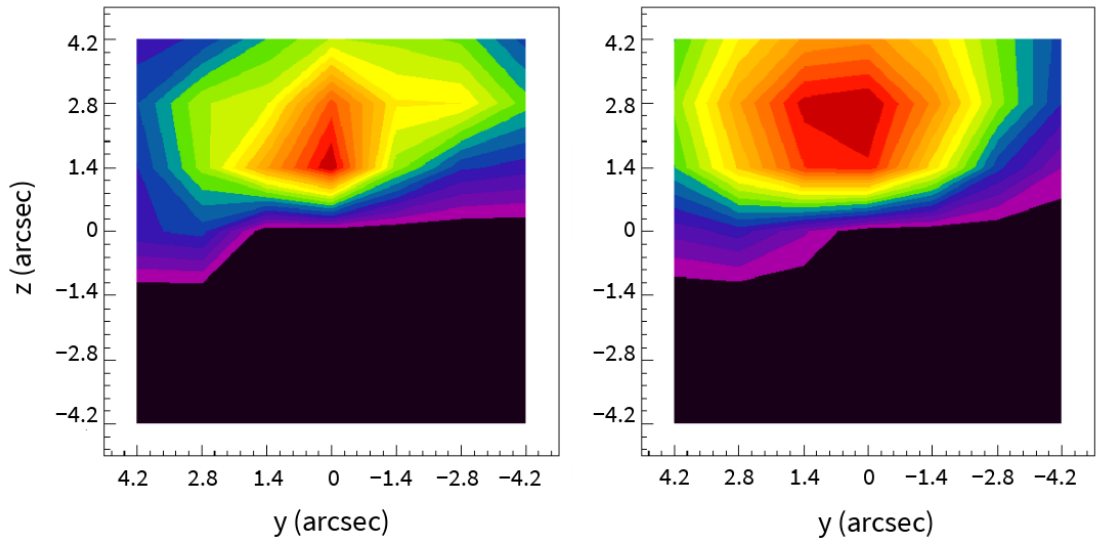

Figure 3.22: Mapping the northern excess of the CO(1-0) data (left panel) and of the prediction of the standard wind model modified to include a static cool sphere of gas in the northern sky (right panel, see text).

The position offsets associated with the proper motion of the star do not account for the northern excess displayed in Figure 3.21 (left). This northern excess is dominated by a spike confined to the velocity interval [0.2 km s^{-1}, 2.2 km s^{-1}]. Mapping R_{asym} for velocities confined to the spike velocity interval shows a broad coverage over the northern part of the sky. Whatever is causing the excess, it looks as if it were associated with a large volume of cool gas (essentially not expanding) having a Doppler velocity of ~1.1 km s^{-1} with respect to the star and a northern offset at arcsecond scale. Moreover, as the $\sum_{dir}$ distribution (Figure 3.20 right) suggests the presence of two components, it is therefore preferable to use the spike velocity rather than the star velocity as pivot to produce mirror spectra. The resulting map is displayed in Figure 3.22. What is done to obtain it is to calculate for each pair of (y, z) and $(-y, -z)$ spectra the flux integrated over the [0.2 km s^{-1}, 2.2 km s^{-1}] interval and decompose it into a common value f_{sym} (the smaller of the two values) and an excess f_{exc} (the difference between the larger and the smaller), the latter being mapped in Figure 3.22 left. If we had kept the earlier definition of mirror spectra and compared the spike interval at (y, z) with the mirror interval [−2.2 km s^{-1},−0.2 km s^{-1}] at $(-y, z)$ the result would have been qualitatively unchanged.

We have modified the standard model to include a sphere of cool gas meant to mimic the northern excess observed in the CO(1-0) data. Its Doppler velocity is redshifted by 1.1 km s^{-1} with respect to the star velocity. Its centre, (y_{excess}, z_{excess}) and its density are adjusted to best fit the data. The latter has a Gaussian dependence on radius with a value ρ_{excess} at the centre and a σ value R_{excess}. The temperature of the gas is taken to be 20 K and the velocity distribution is smeared with a Gaussian having a σ of 0.5 km s^{-1}. The parameters of the standard wind model are fixed at the standard model best fit values except for the fluxes of matter that are varied. The inclusion of the cool gas sphere is found to achieve a ~10% reduction of the best fit χ^2 with (y_{excess}, z_{excess})~(0.8″ E, 2.1″ N), approximately where the star was ~50 years ago), R_{excess}~2″ and ρ_{excess}~1800 H cm^3 (for a CO/H ratio of 4 10^{-4}), typically 2/3 of the average density probed by CO emission. The mass-loss rate of the star decreases by ~10%. The map of the northern excess predicted by the modified model is displayed in the right panel of Figure 3.22 and the velocity distribution of the relative excess in the northern and southern halves of the sky are compared with the data in Figure 3.23. The model gives a good qualitative description of the data but the predicted spike is only half of that observed.

The presence of non-expanding gas at small Doppler velocities with respect to the star has been previously noted, suggesting the existence of a companion source located ~0.98″ West and ~0.63″ North of the main source and accreting gas from its wind. While the main source is seen on both line and continuum maps, the companion source is not seen in the continuum but only on the line (Figure 3.11). Its possible role is discussed in Section 3.6.3.

3.5.4 CO(2-1) asymmetry

It was remarked earlier (Libert et al. 2010b; Hoai et al. 2014) that the CO(1-0) and CO(2-1) profiles appear to be centred on different values of the star velocity, the latter being shifted by ~0.5 km s^{-1} with respect to the former. In order to clarify this point, we make a direct, model independent comparison between the CO(1-0) and CO(2-1) velocity spectra. Four parameters a, b, c and a velocity offset ΔV between the two scales are adjusted to have the ratio CO(2-1)/CO(1-0) best fit a form $a + b(y^2 + z^2) + cz$

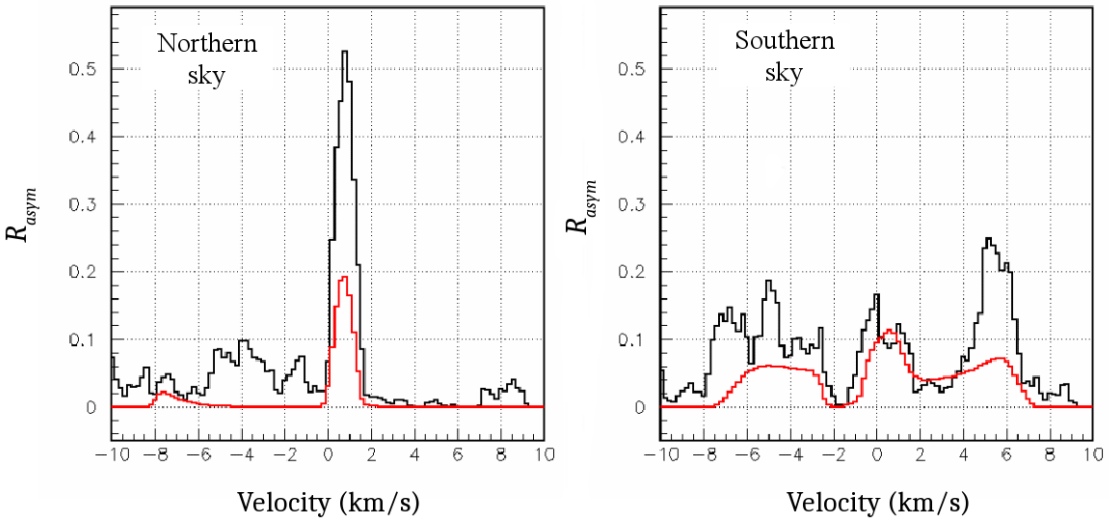

Figure 3.23: Distributions of R_{asym} summed over the 21 northern (left) and 21 southern (right) spectra of the CO(1-0) data (black line). The prediction (red) is shown for a modified standard model including a sphere of cool gas (see text).

in each of the 49 central (y, z) spectra. Here, a and b are meant to account for the different flux and radial distributions, the CO(2-1) data probing warmer regions, therefore smaller radii, than the CO(1-0) data. Parameter c allows for a possibly different North-South asymmetry in the CO(2-1) data than in the CO(1-0) data. Indeed, while the former were collected in November 2004-April 2005 exclusively, the latter are the result of a merging with 2011 data. The displacement of the star with respect to the centre of the set of velocity spectra is therefore half for the CO(2-1) data as it is for the more recent CO(1-0) data. The results of the best fit are: $\Delta V = 0.50$ km s^{-1}, $a = 8.45$, $b = -0.20$ and $c = -0.36$. Using an uncertainty of 0.12 Jy/beam in each channel of the CO(2-1) data gives a χ^2 value of $\sim$1 per degree of freedom and very small uncertainties on the parameters, well below the systematic uncertainties that can be reasonably expected at the few percent level. Setting ΔV to zero (and readjusting the other parameters) multiplies the χ^2 value by a factor 1.5 and, similarly, setting b and c to zero multiplies the χ^2 value by a factor 1.6, giving evidence for the strong significance of the effects described by these parameters. The values of b and c correspond to effects of respectively 21% and 13% at an angular distance of 3″ north of the star, and 85% and 26% for 6″ north: they are important. Figure 3.24 displays the 49 CO(2-1) central spectra compared with the results to the above best fit. We noted that the velocity offset between the CO(1-0) and CO(2-1) data is the same whether one uses the 2005 data or the 2011 data for CO(1-0): it is already present in the 2005 Pico Veleta data and would mean a non-linearity of the frequency scale at the ppm level if it were of instrumental origin. However, it was soon discovered that the CO(1-0) frequency used in the reduction of the data was 115271.0 MHz instead of 115271.2 MHz, meaning a velocity shift of 0.52 km s^{-1} and explaining the effect.

Figure 3.25 displays the velocity distributions of $\sum_{dir}$, Δ_{dir}, $\sum_{mir}$ and Δ_{mir}, evaluated over the northern half (24 spectra) of the CO(2-1) data as was done in Figure 3.20 for the CO(1-0) data. The star velocity used as pivot to define the mirror spectra is now 7.1 km s^{-1}, 0.5 km s^{-1} higher than for the CO(1-0) data. Significant asymmetries are again observed. However, at variance with the CO(1-0) case, Δ_{mir} is always negative, meaning that the excess is confined to the southern part of the sky, the northern

spike excess having no equivalent in the CO(2-1) data. This is more explicitly illustrated in Figure 3.26 that shows a map of the absolute excess integrated over the whole velocity range. It is compared with the prediction of the standard model, using a star velocity of 7.1 km s^{-1} as pivot and offsets in right ascension and declination twice as small as for the CO(1-0) data (to account for the fact that the data were taken only five years instead of ten after epoch 2000.0).

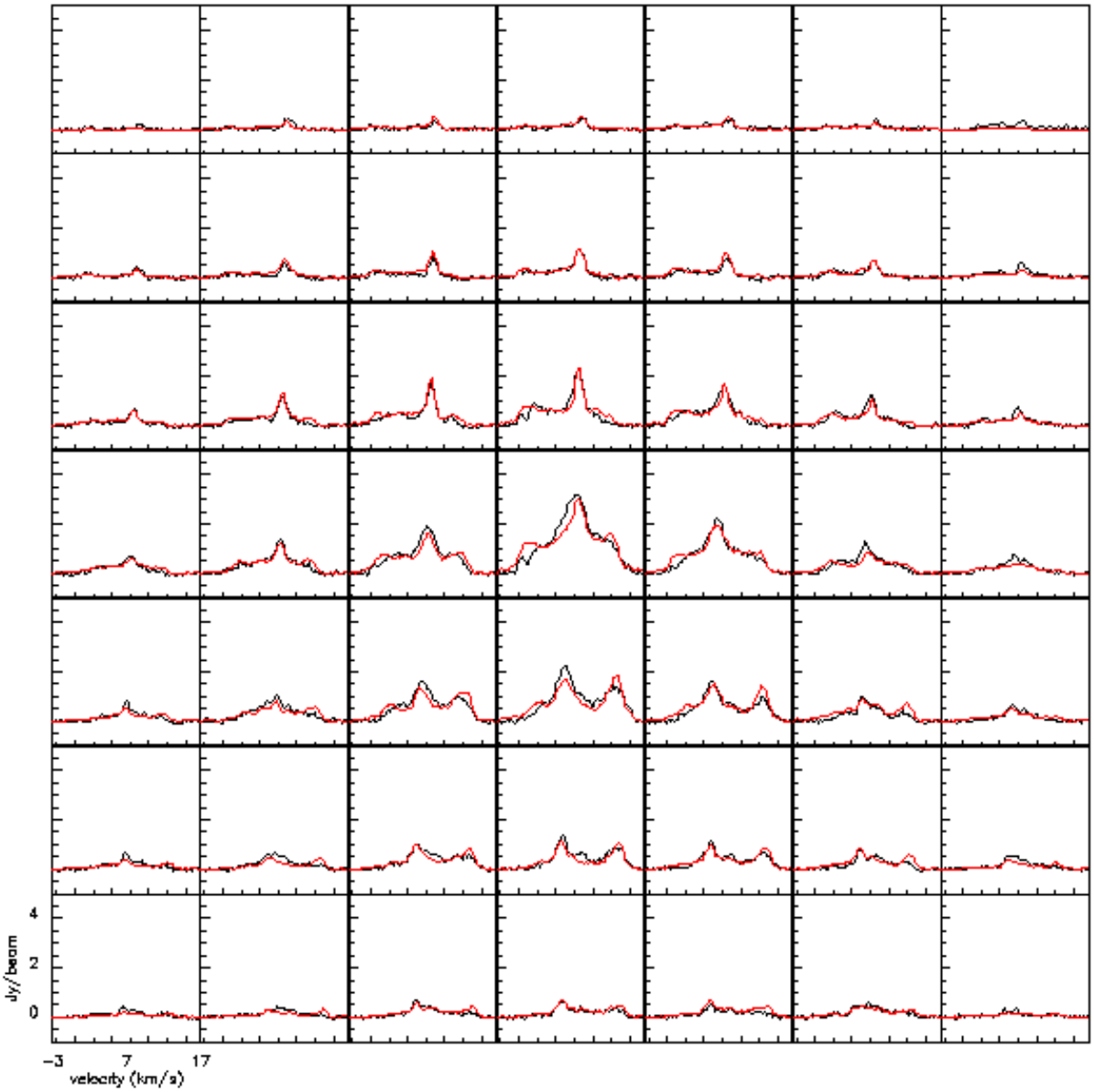

Figure 3.24: CO(2-1) channel maps (black) compared with the form $[a + b(y^2 + z^2) + cz]$CO(1-0) (red) where a, b and c take the best fit values of 8.3, −0.20 and −0.37 respectively.

The excess predicted by this same model is displayed in Figure 3.27 together with the prediction obtained by setting the right ascension and declination offsets to zero. In this latter case, absorption is the only source of central asymmetry and its effect is seen to be negligible. However, the excess predicted by the model is too low by a factor ∼5 with respect to the data: although the model predicts an

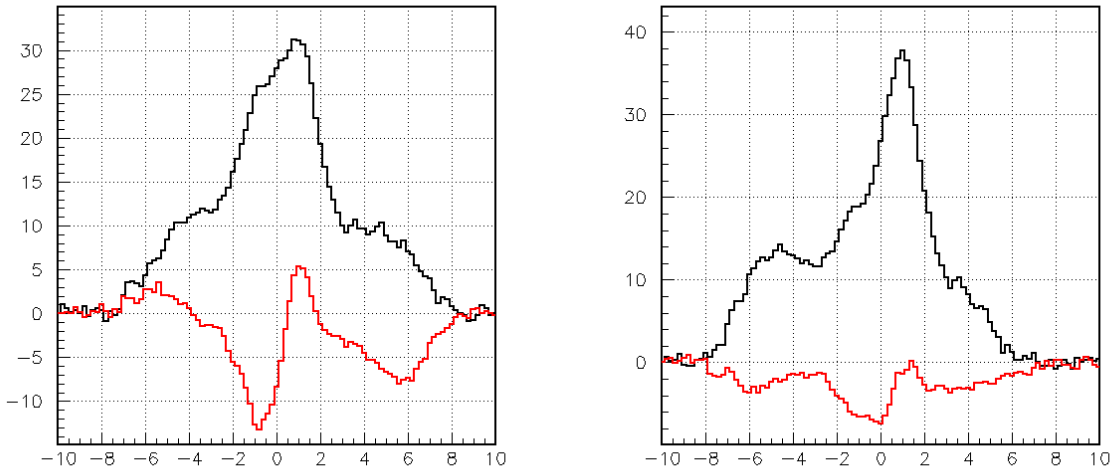

Figure 3.25: Same as Figure 3.20 for the CO(2-1) data, using a star velocity of 7.1 km s^{-1} as pivot to define mirror quantities. Left: Δ_{dir} (red) and $\sum_{dir}$ (black). Right: Δ_{mir} (red) and $\sum_{mir}$ (black).

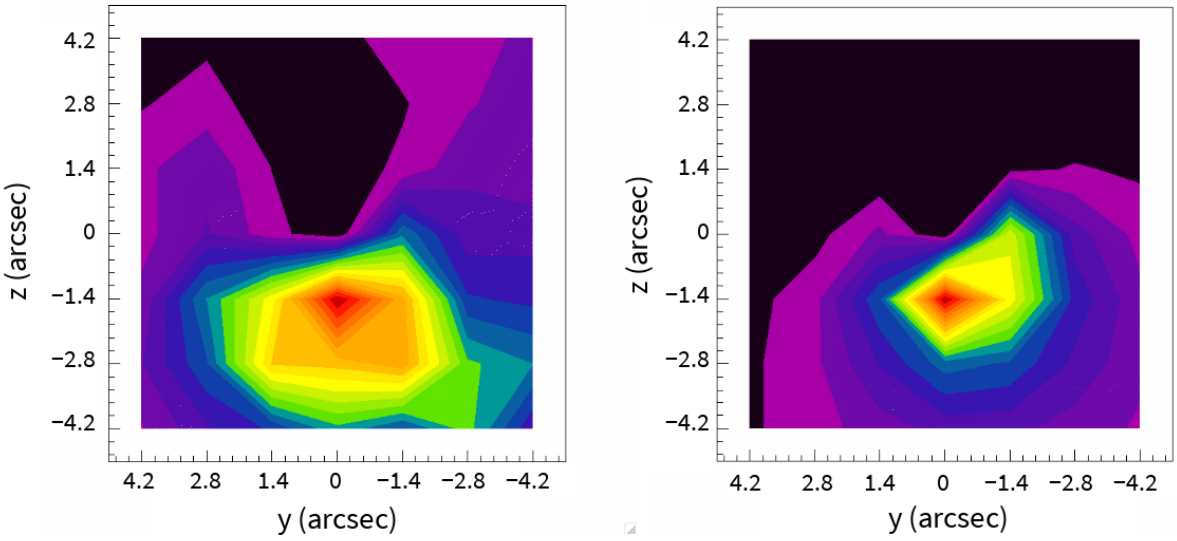

Figure 3.26: Mapping the excess in the CO(2-1) data (left panel) and standard model (right panel).

excess confined to the southern part of the sky and covering a broad velocity range, it fails to reproduce quantitatively the central asymmetry resulting from the expected offset values.

3.6 Reprocessed data and global analysis [1]

The asymmetries introduced by the proper motion of the star between year 2000 and the times at which observations were made (2004-2005 and 2011) having been found to introduce small but significant

[1]The content of this section has been published (Nhung et al. 2015a)

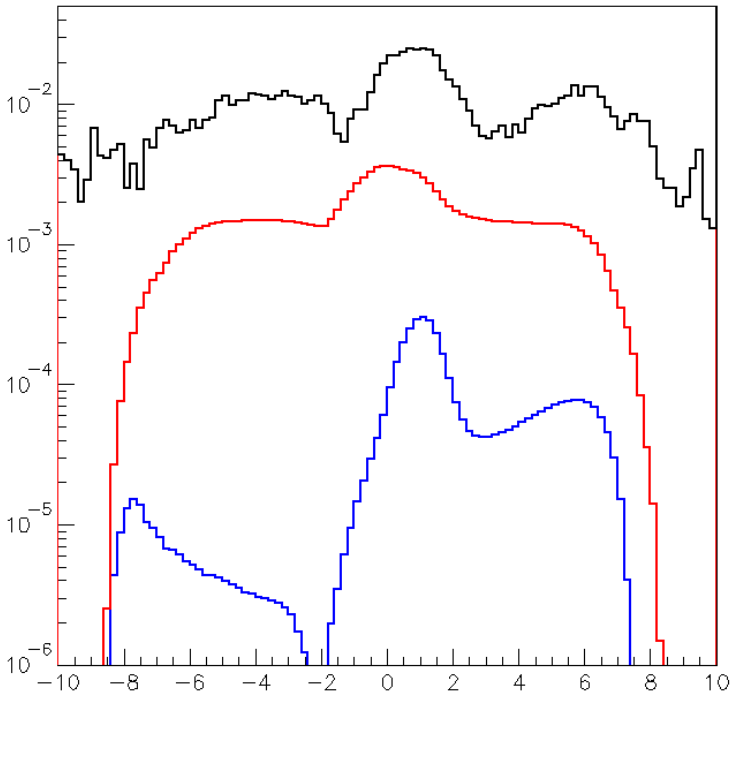

Figure 3.27: Velocity distribution (log scale) of the excess observed in the CO(2-1) data (black curve) when using 7.1 km s^{-1} as pivot for the mirror spectra. The red line shows the model prediction when using offsets in right ascension and declination twice as small as for the CO(1-0) data. The blue curve shows the model prediction when the offsets are set to zero, in which case absorption is the only source of central asymmetry. The excess is summed over the 48 central spectra (the central spectrum being excluded) and normalized to the total flux over the associated area.

central asymmetries, the data were reprocessed using the position of the star at the time of observations as centre of the spectral maps. Moreover, the 0.5 km s^{-1} velocity offset between the CO(1-0) and CO(2-1) data was also corrected, the reprocessed observations being therefore expected to be bias-free from the point of view of central symmetry. The standard model is centrally symmetric with respect to the star, except for a small absorption, which, however, induces negligible asymmetries. In what follows, the χ^2 minimization procedure uses uncertainties combining a 9% (8%) error with a 14 mJy (116 mJy) for CO(1-0) (CO(2-1)) respectively, adjusted to have for each set of observations a value close to the number of degrees of freedom.

3.6.1 Description of CO(1-0) and CO(2-1) emissions using a centrally symmetric model

A major difference between the CO(1-0) and CO(2-1) observations is the larger extension of the former with respect to the latter (Libert et al. 2010b, Figure 3). Figure 3.28 compares the R_{yz} distributions

observed for CO(1-0) and CO(2-1) emissions with the best fit results of the standard model (see below). Here, R_{yz} is the angular distance in the plane of the sky between the centre of the star and the central line of sight of each of the 49 velocity spectra (the impact parameter). For each value of R_{yz} (0″, 1.4″, 2.0″, 2.8″, etc.) there are a number of spectra (1, 4 or 8) over which the flux densities are averaged to obtain <CO(1-0)> and <CO(2-1)>. The error bars are the root mean square deviations from the mean for each of the R_{yz} values. They give an upper limit of the uncertainties attached to the data, which we estimate not to exceed 5%.

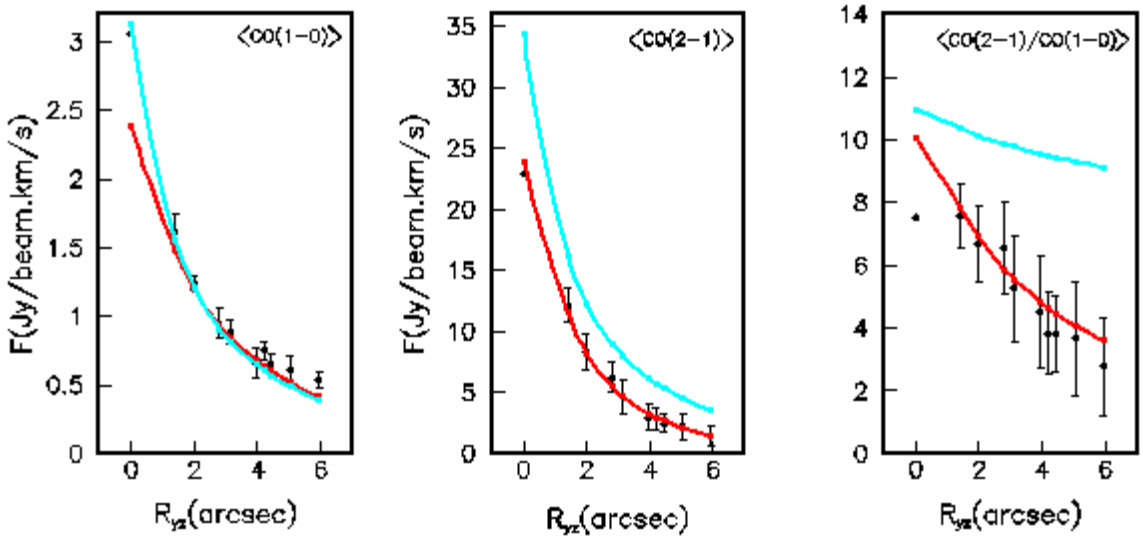

Figure 3.28: R_{yz} distributions of <CO(1-0)> (left panel) and <CO(2-1)> (middle panel) as observed (black symbols) and obtained from the standard model in its present version (red curves) or in the version used in Hoai et al. (2014) (cyan curves). Right panel: R_{yz} dependence of the <CO(2-1)>/<CO(1-0)> ratio as observed (black symbols) and obtained from the model (red and blue curves). The best fit results of the standard model (shown here) are essentially identical to those of its modified asymmetric version. The error bars show root mean square deviations with respect to the mean (not defined at $r = 0$ where a single cell contributes).

In the standard model, the assumption that the winds are stationary implies that the r-dependence of the gas density is uniquely determined by the velocity gradients and does not leave freedom to fit separately their contributions to the velocity and radial distributions. This is an obvious oversimplification of reality. Indeed, the flux of matter and wind velocities are parameterized at each value of the sine of the star latitude, γ, in the form $f_{\dot{M}}(\gamma) = f_{\dot{M}_1} F(\gamma) + f_{\dot{M}_2}$ and $V(\gamma, r) = V_1 F(\gamma)(1 - \lambda_1 \exp(-\frac{r}{2.5''})) + V_2(1 - \lambda_2 \exp(-\frac{r}{2.5''}))$. Here, $f_{\dot{M}_1}$, $f_{\dot{M}_2}$, V_1, V_2, λ_1 and λ_2 are six adjustable parameters and the function $F(\gamma)$ uses Gaussian profiles centred at the poles, $F(\gamma) = \exp[-\frac{(\gamma-1)^2}{2\sigma^2}] + \exp[-\frac{(\gamma+1)^2}{2\sigma^2}]$, where a seventh parameter σ measures the angular aperture of the bipolar flow. Two additional angles are necessary to fix its orientation in space, making a total of nine adjustable parameters. The density $\rho(\gamma, r)$ is then defined at any point from the relation $f_{\dot{M}}(\gamma) = r^2 V(\gamma, r)\rho(\gamma, r)$ and its r-dependence is exclusively controlled by the parameters λ_1 and λ_2 that define the velocity gradients.

The wind is supposed to be purely radial, free of turbulences and in local thermal equilibrium. Moreover, it is supposed to have been in such a regime for long enough a time, such that the radial

extension of the gas volume, in the 10″ ball park, is governed exclusively by the UV dissociation of the CO molecules from the ISM and does not keep any track of the star history.

In comparison with Hoai et al. (2014), two minor modifications have been introduced in the standard model, one related to the velocity gradients and the other to the radial distribution of the gas temperature. The aim is not to find the best possible analytic forms of $V(\gamma, r)$ and $T(r)$, but to have enough flexibility in the parameterization to understand how strongly the data constrain these quantities in different regions of r.

For the velocity gradients, the use of a power law in Hoai et al. (2014) has the disadvantage of suggesting that velocities keep increasing indefinitely, which is unphysical. Of course, such a suggestion is unfounded, the parameterization applying only to the region probed by the data, typically 0.2″ to 10″ (see lower panel of Figure 3.26). The form adopted here, an exponentially decreasing gradient, with velocities reaching a plateau, was preferred for this reason. It does not introduce additional parameters, simply replacing two power law indices by two exponential amplitudes, λ_1 and λ_2. Attempts to make the velocities reach a plateau at reasonable distances from the star, not exceeding 1″, have failed. As it is difficult to imagine a mechanism that would make it possible to maintain acceleration at large distances from the star, this result is probably the manner by which the model is able to best mimic a more complex reality. For example, simply artificially smearing the velocity distributions can remove the need for extended velocity gradients. Smearing in the model combines a thermal broadening of $0.02\sqrt{T}$ km s^{-1} and an ad hoc instrumental smearing of 0.2 km s^{-1}; we see no justification to increase it significantly.

For the temperature, the approach in Hoai et al. (2014) was simply to use the radial dependence proposed by Schöier & Olofsson (2001) from simple radiative transfer Monte Carlo simulations of spherical expanding shells, and to scale it down by a factor ∼2 to match the known effective temperature of RS Cnc, ∼3226 K (Dumm & Schild 1998; Dyck et al. 1996; Perrin et al. 1998). Here, by giving particular attention to the radial dependence of the ratio of the CO(2-1) and CO(1-0) emissions, we aim at a better understanding of the constraint imposed by the data on $T(r)$. In principle, both the velocity gradients and the radial dependence of the temperature control the R_{yz} dependence of the ratio of CO(2-1) and CO(1-0) emissions. In practice, however, the velocity gradients are strongly constrained by the wind velocities, leaving the temperature as the main handle to best fit the R_{yz} dependence of the emission ratio. Several possible parameterizations of $T(r)$ have been tried and found adequate but none was able to improve the quality of the fit at r =0 (Figure 3.25). The ∼25% disagreement between model and observations in the centre of the spectral map, while probably significant, has therefore another cause than a wrong temperature.

Figure 3.29 displays the r-dependence of the gas temperature as obtained from the standard model best fit together with the form proposed by Schöier & Olofsson (2001) and that used in Hoai et al. (2014). The standard model result uses as parameterization a power law $T(r) = T(1'')r^{-\alpha}$ with $T(1'')$ and α being two adjustable parameters. Many different parameterizations have been explored with the aim of understanding what the data impose on $T(r)$. The result of this exploration can be summarized as follows. The temperature must reach a low value of ∼10±2 K at r = 10″. The temperature gradient may then be small in absolute value at larger values of r, corresponding to a power law index of −0.7 or even less in absolute value. However, as soon as r decreases, the temperature gradient must increase in absolute value and the r-dependence of the temperature must become accordingly steeper, with a power

law index reaching values of the order of −1 at r ∼2″ to 5″ and of −1.1±0.1 at r = 0.1″. The low value of the gas temperature at r∼10″ is a cause of concern as the detection of H I at larger values of r (Hoai et al. 2014) implies temperatures well in excess of 10 K. The radiative transfer calculation of Schöier & Olofsson (2001) is expected to be more reliable at large values of r than near the star, suggesting a power law radial dependence of the temperature with index ∼ −0.7 beyond 10″. In the absence of reheating between 10″ and 30″, one would then expect the gas temperature at r∼10″ to be above 30 K or so. Evidence against higher temperatures is given in Figure 3.28 (right panel) where the r-dependence used in Hoai et al. (2014) is seen to imply too high a <CO(2-1)>/<CO(1-0)> ratio. We note that large values of R_{yz} receive contributions from large values of r exclusively while small values of R_{yz} receive contributions from the whole spectrum of the r distribution. As the dependence on temperature of the ratio of the populations of the J =2 and J = 1 states is maximal around 10 K, it is not surprising that the data constrain $T(r)$ in the large r region, where the temperature takes values in such a range. At small values of r, anyhow, the temperature is large enough for both rotational levels to be maximally populated. This implies that even at small R_{yz} values the <CO(2-1)>/<CO(1-0)> ratio is mostly governed by the temperatures reached at large r values.

Figure 3.30 displays the dependence over star latitude of the wind velocity, density and flux of matter as well as the r dependence of the wind velocity.

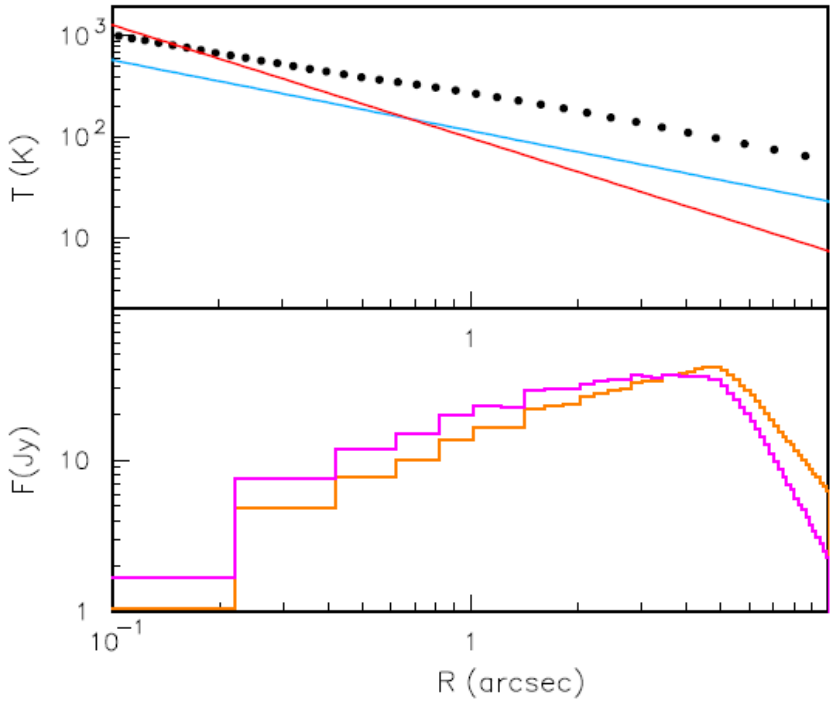

Figure 3.29: Dependence on r of the gas temperature (upper panel) and of the detected flux density obtained from the model (Jy per bin of 0.2 arcsec, lower panel), in log-log scales. Temperatures are displayed for the present version of the standard model (red), the version used in Hoai et al. (2014), (cyan line) and the radiative transfer calculations of Schöier & Olofsson (2001), (black dotted line). The flux densities are shown for CO(1-0) (orange) and CO(2-1) (magenta, divided by 10) separately. The restriction of the study to the 49 central cells implies an effective progressive truncation of the r distribution from ∼5″ onward.

3.6.2 Deviation from central symmetry in CO(1-0) and CO(2-1) emission

Having now adjusted the parameters of the standard model to best fit the set of reprocessed data, we are in a position to study to which extent they obey central symmetry. In the standard model, the only source of central asymmetry is the presence of absorption, which is found to have a nearly negligible effect. The velocity distributions of $\sum_{dir}$, Δ_{dir}, $\sum_{mir}$, Δ_{mir}, evaluated over the northern half (24 spectra) of the CO(1-0) and CO(2-1) data are displayed separately in Figure 3.31. Significant asymmetries are evidenced with $2\Delta_{mir}/\sum_{mir}$ reaching up to ∼30% in some cases but being usually well below a few percent. They display important regularities that can be schematically summarized as a dominance of two features: a narrow low velocity spike between ∼0 and ∼2 km s^{-1} in the northern part of the sky (meaning positive values of Δ_{mir}), particularly strong in the CO(1-0) data; and a broad velocity span in the southern part (meaning negative values of Δ_{mir}), particularly strong in the CO(2-1) data. As expected, the asymmetries calculated in the standard model (resulting from absorption exclusively) are seen to be negligible. We also note that the asymmetries associated with the proper motion of the star between year 2000 and the times where observations were made amount to typically a tenth of the asymmetries observed in the reprocessed data (from which they are absent).

In order to improve the agreement between observations and best fit results of the model, the latter must be modified to make room for the observed central asymmetries. How to do so is somewhat arbitrary. A possibility that has been explored is to assume the presence of a cold cloud in the northern part of the sky that mimics the northern excess observed in the CO(1-0) data. Here we prefer to retain a more phenomenological approach, which does not presume of the physics nature of the effect. As we need to have a northern excess confined to a low velocity spike and a southern excess covering a broad velocity range, we simply replace the parameters $f_{\dot{M}_1}$, $f_{\dot{M}_2}$, V_1 and V_2, by $(1 + \varepsilon f_{\dot{M}_1}\gamma)f_{\dot{M}_1}$, $(1 + \varepsilon f_{\dot{M}_2}\gamma)f_{\dot{M}_2}$, $(1 + \varepsilon V_1\gamma)V_1$ and $(1 + \varepsilon V_2\gamma)V_2$. The result is a significant decrease of the value of χ^2 with important asymmetries introduced in the γ dependences of the parameters, as displayed in Figure 3.30. The values taken by the former parameters do not change much (Table 3.3) but the values obtained for the ε asymmetry parameters are $_{\dot{M}_1} = -0.96$, $_{\dot{M}_2} = 0.95$, $\varepsilon V_1 = -0.40$ and $\varepsilon V_2 = 0.70$.

The asymmetries obtained from the modified model are illustrated in Figure 3.31. While qualitatively in good agreement with observations, they fail to reproduce them quantitatively. However, lacking a clear physical interpretation of the observed asymmetries, we did not attempt fine tuning the model in order to improve the agreement with observations. Model and observations are compared in Figures 3.32 and 3.33. We have checked that the new asymmetric model, using the values of the parameters optimized on the 49 central spectra, gives also good fits when extending the spectral maps to the 9×9=81 central spectra.

3.6.3 Conclusion

The detailed study of CO(1-0) and CO(2-1) emission from the circumstellar envelope of the AGB star RS Cnc has revealed departures from central symmetry that turned out to be efficient tools for the exploration of some of its properties. In a first phase, they provided evidence for offsets in velocity, declination and right ascension that were inherent to the procedure of data reduction and were causing small biases in

Table 3.3: Best fit model parameters with and without explicit asymmetries. The optimisation uses uncertainties combining a 9% [8%] error with a 14 mJy [116 mJy] noise for CO(1-0) [CO(2-1)] respectively, adjusted to have for each set of observations a value close to the number of degrees of freedom. Values in parentheses display the last digits corresponding to an increase of χ^2 of 1% when the parameter is varied with the others kept constant. The distance to the star is taken to be 143 pc (van Leeuwen 2007).

Parameter	Best fit value symmetric (standard model)	Best fit value asymmetric (modified standard model)
$AI(^\circ)$	52 (2)	53 (2)
$PA(^\circ)$	9 (6)	8 (5)
σ	0.33 (2)	0.33 (2)
V_1 (km s^{-1})	4.91 (15)	4.83 (11)
V_2 (km s^{-1})	2.56 (9)	2.58 (9)
λ_1	0.36 (11)	0.33 (10)
λ_2	0.62 (7)	0.66 (7)
$f_{\dot{M}_1}$ (10^{-8}M$_\odot$ yr^{-1} sr^{-1})	0.87 (10)	0.85 (9)
$f_{\dot{M}_2}$ (10^{-8}M$_\odot$ yr^{-1} sr^{-1})	0.49 (4)	0.51 (4)
T (1″) (K)	98 (6)	99 (6)
α	1.12 (5)	1.11 (5)
$\varepsilon_{\dot{M}_1}$	0	−0.96 (15)
$\varepsilon_{\dot{M}_2}$	0	0.95 (16)
ε_{V_1}	0	−0.40 (3)
ε_{V_2}	0	0.70 (6)
χ^2/dof	1.240	1.137

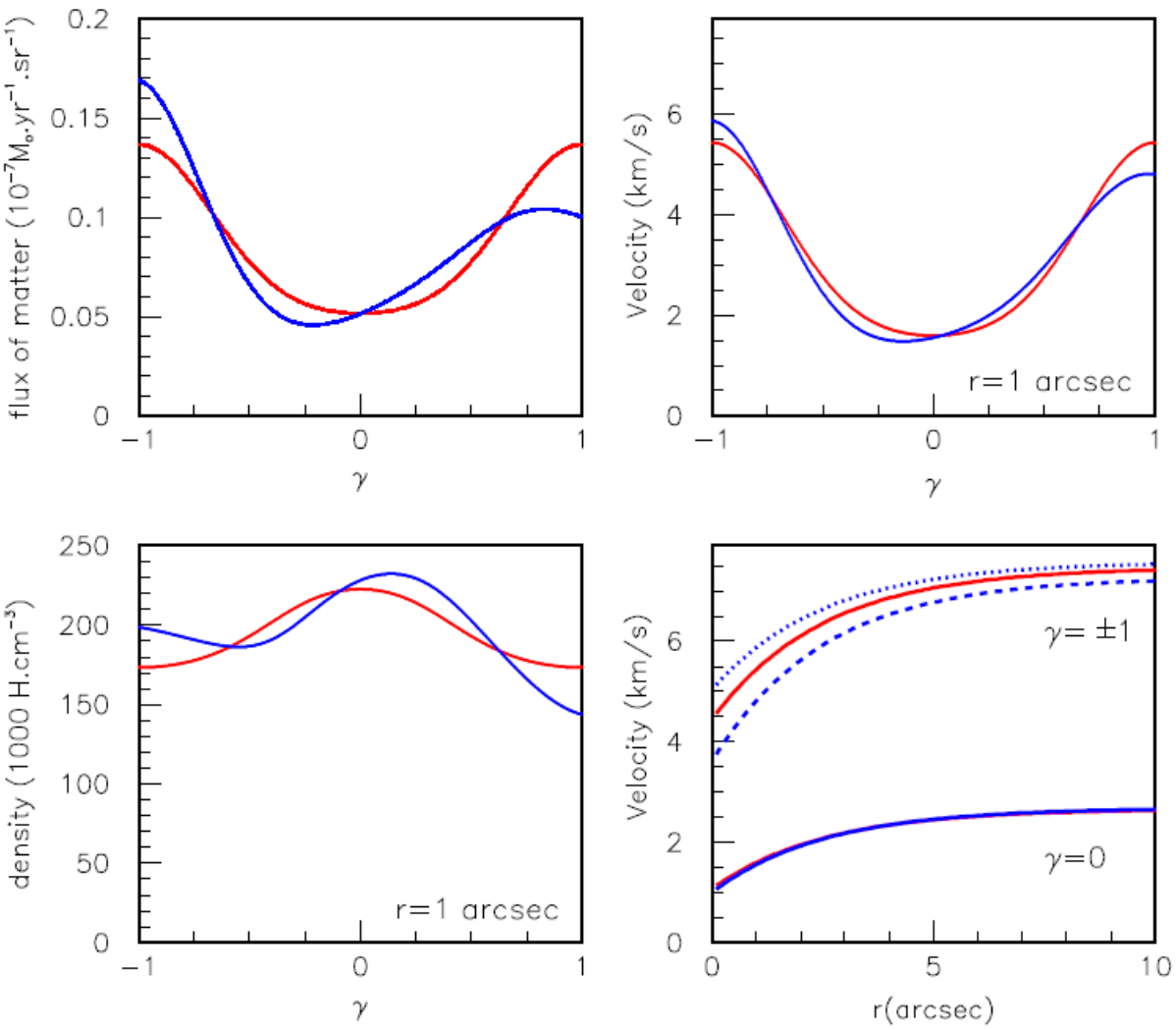

Figure 3.30: Dependence on the sine of the star latitude, γ, of the flux of matter (up-left), of the wind velocity at $r = 1''$ (up-right) and of the gas density at $r = 1''$ (down-left). Down-right: r-dependence of the equatorial (lower curves) and polar (upper curves) velocities. The best fit results of the symmetric model are shown in red and those of its modified asymmetric version in blue. The dashed curve is for $\gamma = 1$ (north) and the dotted curve for $\gamma = -1$ (south).

the data. These have been removed by reprocessing the data with the spectral map centred on the star position at the time when the observations were made and the velocity spectra centred on the star Doppler velocity.

I have developed a modelling of the emission in the CO(2-1) and (1-0) lines which provides a good fit to the spectral maps. The modelling assumes local thermal equilibrium for the population of the 3 first rotational levels of the CO molecule. This hypothesis is valid for the high densities found in the inner region of the circumstellar shell, but may break down in the outer region when the hydrogen density becomes lower than $\sim 10^4$ cm^{-3}. The same remark will apply for the other sources discussed in this thesis.

The study of the central asymmetry of the wind morphology and kinematics has revealed the pres-

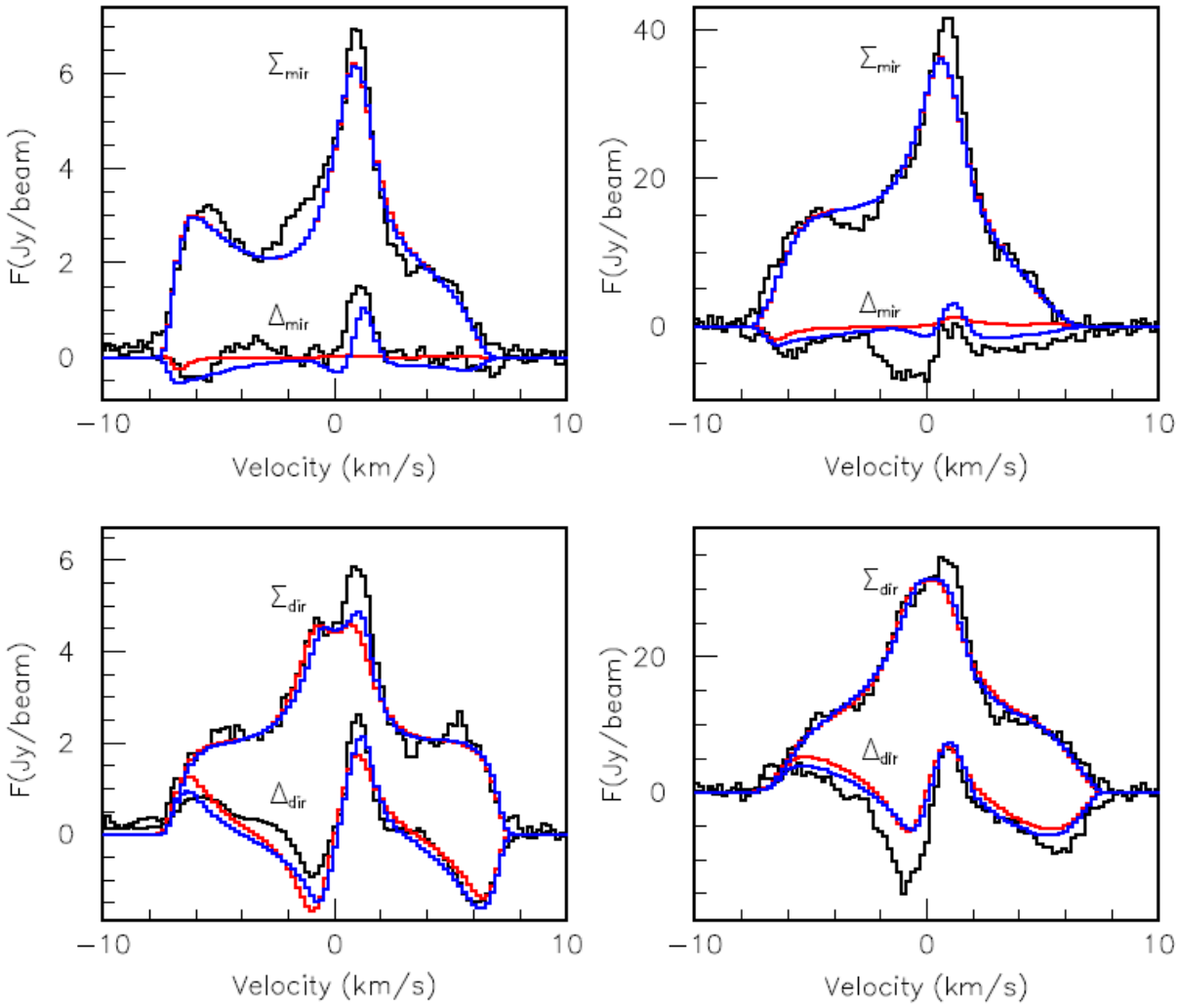

Figure 3.31: Velocity distributions of $\sum_{dir}$, Δ_{dir}, $\sum_{mir}$, Δ_{mir}, evaluated over the 24 pairs of diametrically opposite spectra of the CO(1-0) (left) and CO(2-1) (right) spectral maps. The upper panels are for mirror quantities and the lower panels for direct quantities. In each case, the data are shown in black, the best fit results of the standard model in red and of its modified asymmetric version in blue. The reference velocity is 7.25 km s^{-1}, the CO(1-0) data of Libert et al. (2010b) and Hoai et al. (2014) having been corrected by +0.5 km s^{-1}.

ence of significant central asymmetries that can be schematically summarized as a northern excess confined to a narrow spike of low velocity, mostly in CO(1-0) data, and a southern excess covering a broad velocity range, mostly in CO(2-1) data. A simple parameterization of the asymmetry has been suggested, providing a good qualitative description of the main features but failing to give a precise quantitative account. Lacking a clear physical interpretation of the observed asymmetries, we did not attempt refining the model. The observation of significant departures from central symmetry is in itself an interesting result in the context of the transition from the AGB to post-AGB and Planetary Nebulae phases that are known to display growing asymmetries, the origin of which is not clearly understood.

A possible source of central asymmetry is the suggested existence of a companion source located ~0.98″ West and ~0.63″ North of the main source and accreting gas from its wind (Hoai et al. 2014). At the present stage such an interpretation is only tentative, it is not even possible to discriminate between

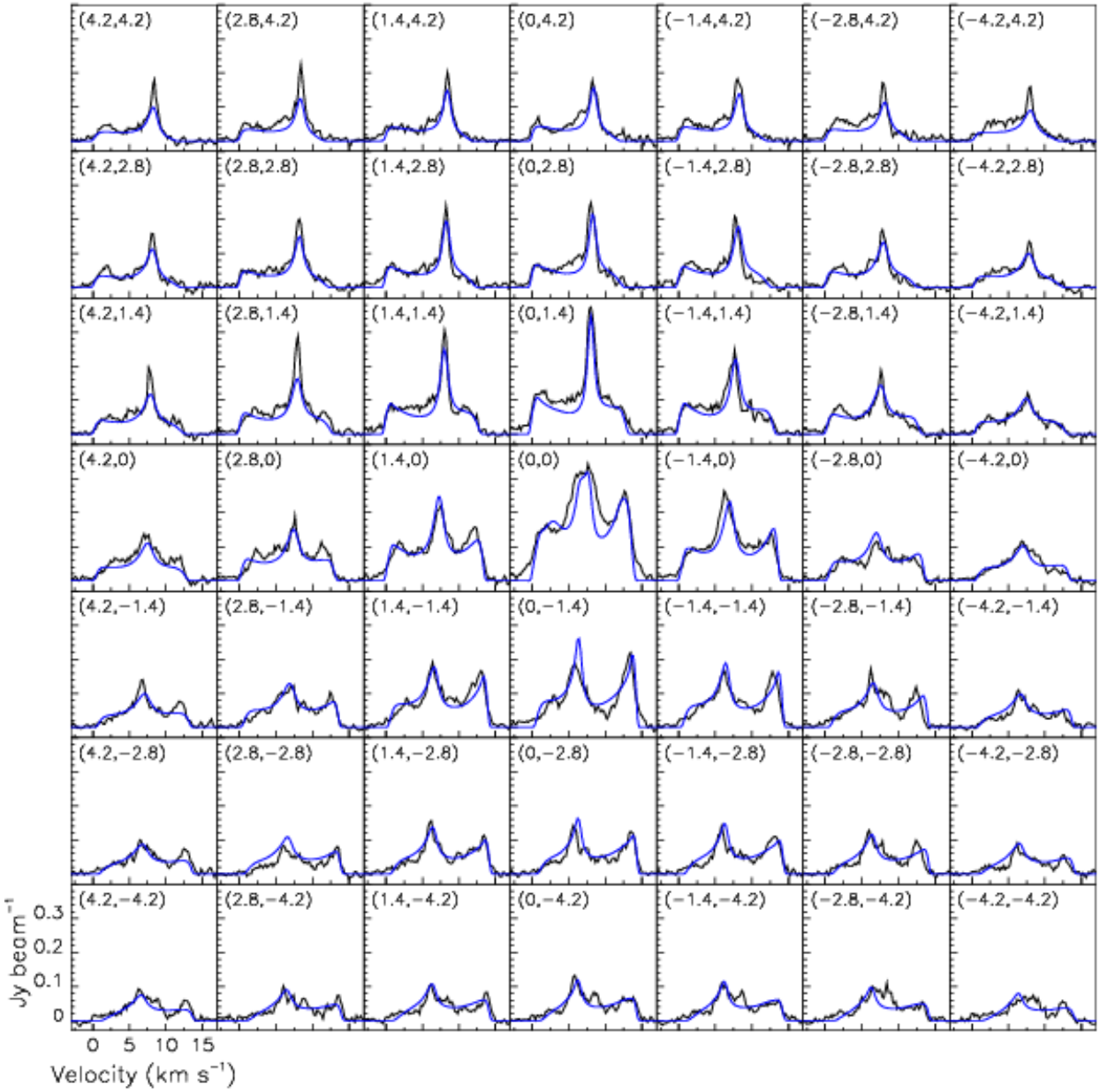

Figure 3.32: Spectral map centred on the star of the CO(1-0) observations (black) and best fit results of the modified asymmetric version of the standard model (blue). Steps in right ascension and declination are 1.4″. The synthesized beams are Gaussian with a full width at half maximum of 1.2″.

a compact source and a clump of gas. While the main source is seen on both line and continuum maps, the companion source is not seen in the continuum but only on the line. However, the large distance of the companion from the main star, ∼170 au (implying an orbital period of some 2200 years), makes it unlikely that it could play an important role in the shaping of the bipolar outflow. When binaries are invoked as triggers of the circumstellar envelope bipolar morphology, the companions are much closer with orbital periods of the order of a year (Jorissen et al. 2009; van Winckel et al. 2009). In the case of wide binaries, the companion plays a lesser role but is still likely to accrete gas and induce a weak asymmetry or produce structures such as spirals or detached shells (Maercker et al. 2012; Pérez-Sánchez

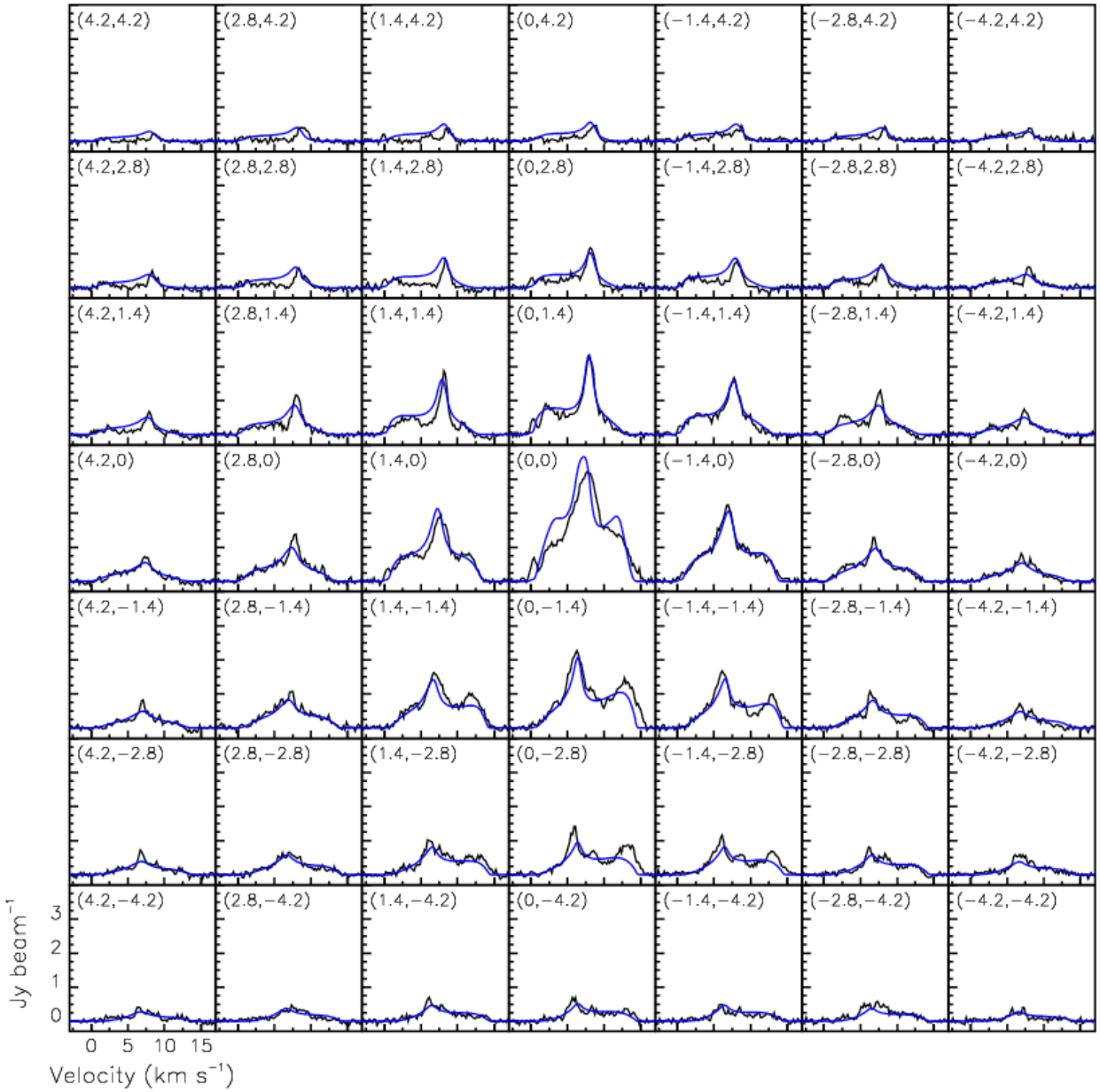

Figure 3.33: Spectral map centred on the star of the CO(2-1) observations (black) and best fit results of the modified asymmetric version of the standard model (blue). Steps in right ascension and declination are 1.4″. The synthesized beams are Gaussian with a full width at half maximum of 1.2″.

et al. 2013). Of course, one cannot exclude the presence of an unobserved close companion playing an important role in shaping the circumstellar envelope of RS Cnc, but this is of no relevance to the present discussion. Moreover, the interpretation of the observed morphology as due to a companion star is by no means certain as clumps and knotty jets have been observed in late AGB and post-AGB phases (for recent references, see Balick et al. 2013).

Chapter 4

CO EMISSION FROM EP Aqr [1]

4.1 Introduction

EP Aqr is an M-type (M8III) semi-regular variable (SRb) with a period of 55 days. It has a luminosity L $\approx$ 4800 $L_\odot$ (Winters et al. 2003), an initial mass M=1.7 $M_\odot$ and an effective temperature T=3236 K (Dumm & Schild 1998).

EP Aqr is one of the nearest mass losing AGB stars (van Leeuwen 2007, d=114 pc), and as such one of the best characterized objects of its class. The absence of technetium in the spectrum shows that it is still at the beginning of its evolution on the AGB. Yet Herschel has imaged a large scale (2′×4′) circumstellar shell at 70 μm and 160 μm (Cox et al. 2012, Figure 4.1) testifying for a relatively long duration of the mass loss (>10^4 years) and for interaction with the surrounding interstellar medium. The elongation of the FIR image is in a direction opposite to the EP Aqr space motion.

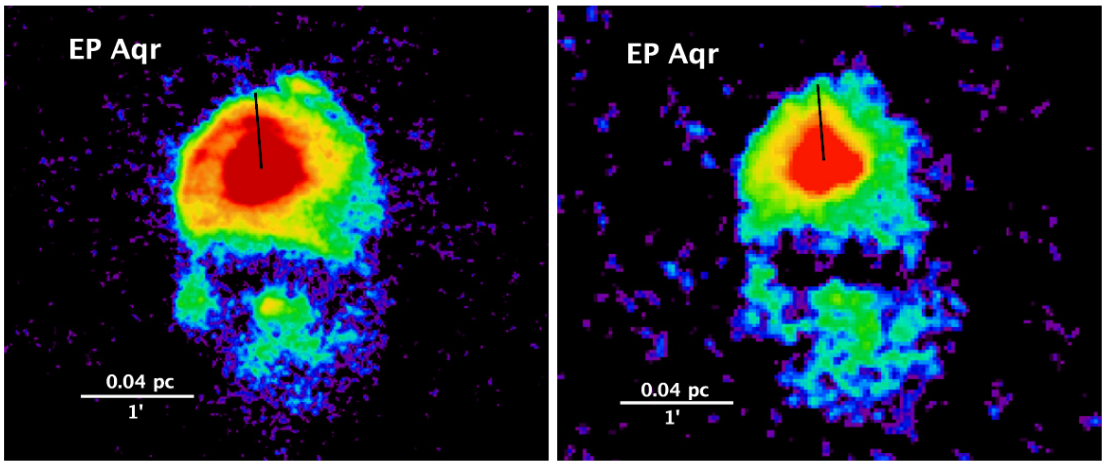

Figure 4.1: PACS image of EP Aqr at 70 μm (left) and 160 μm (right) (Cox et al. 2012).

EP Aqr has been detected in H I and SiO thermal emission lines. Their characteristics are shown in Table 4.1. The H I profile was obtained at NRT (Le Bertre & Gérard 2004) and appears to be complex,

[1] The content of this chapter has been published (Nhung et al. 2015b)

Table 4.1: The line profile features of EP Aqr

Line	V_{lsr}	V_{exp}	Ref*
SiO(3-2)	−31.9	7.9	(1)
SiO(2-1)	−31.9	8.2	(1)
CO(3-2)	−33.7	1.5	(2)
	−33.0	10.8	
CO(2-1)	−33.8	1.4	(2)
	−33.0	10.8	
	−34.0	1.0	(3)
	−34.0	11.0	
		FWHM (km s^{-1})	
H I	−31.1	13.3	(4)
	−26.4	2.6	
	−31.0	1.6	

References: (1) González Delgado et al. (2003); (2) Knapp et al. (1998); (3) Winters et al. (2003); (4) Le Bertre & Gérard (2004)

with a broad and a narrow components centred at $V_{lsr} \sim -31$ km s^{-1}and a prominent emission feature at $V_{lsr} \sim -26$ km s^{-1}(probably an artefact due to confusion).

The SiO thermal emission lines (2-1 and 3-2) (González et al. 2003) show only one component centred at −32 km s^{-1}. Interestingly the central velocities of these different lines differ by 1−2 km s^{-1}, with $V_{lsr} \sim -33.0$ to −34.0 for CO, −32.0 for SiO, and −31.0 for H I. Surprisingly, the narrow CO and H I features are different.

CO line spectra have been obtained by Knapp et al. (1998) and Nakashima (2006). They all show clear composite profiles of two main components with expansion velocities ∼2 and ∼10 km s^{-1}. This was then confirmed by combined observations obtained with the IRAM 30-m telescope and the Plateau-de-Bure Interferometer in ^{12}CO(1-0) and ^{12}CO(2-1) in 2003 and 2004. The spectra were analysed in terms of multiple isotropic winds (Winters et al. 2003, 2007). The interferometer data show an extended source of about 15″(FWHM), and evidence for a ring structure in CO(2-1).

The present study is revisiting the analysis of Winters et al. (2007), assuming instead a bipolar outflow approximately directed along the line of sight, taking advantage of the experience gained in similar studies of other stars, RS Cnc (preceding chapter, Hoai et al. 2014; Nhung et al. 2015a) and the Red Rectangle (following chapter, Tuan Anh et al. 2015).

The observations analysed here combine interferometer data obtained using the Plateau de Bure Interferometer with short-spacing data obtained using the Pico Veleta 30-m telescope. ^{12}CO(2-1) and ^{12}CO(1-0) emission data have been mapped with a spatial resolution of ∼1″ and ∼2″ respectively and a spectral resolution of 0.1 km s^{-1}. At such spatial resolution, the two spectral components seen in the single-dish line spectra are seen as coming from a same region. The images are virtually circularly symmetric and display smooth variations with velocity and projected distance from the star. The observed

spectra were interpreted by Winters et al. (2007) as a succession of spherically symmetric and short-spaced mass-loss events. They noted the presence of inhomogeneity in the spectral maps indicating a possible clumpiness of the morphology of the circumstellar envelope.

We have reprocessed the original data, correcting for an artifact introduced by a velocity shift of $0.52\,\mathrm{km\,s^{-1}}$ in the CO(1-0) data and recentering the maps on the position of the star at epoch 2004.0, correcting for its proper motion as determined by van Leeuwen (2007). The reprocessed channel maps are shown in Figures 4.2 and 4.3.

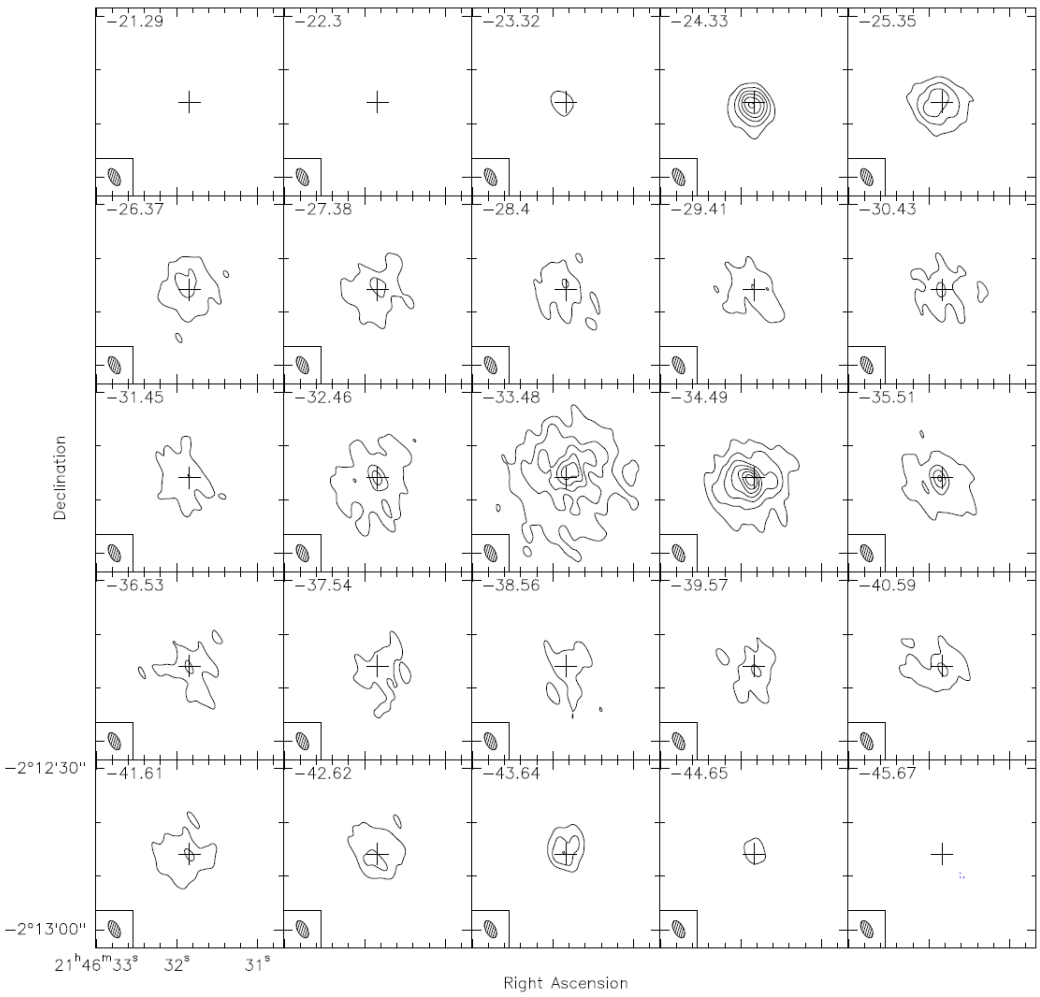

Figure 4.2: Channel maps in the ^{12}CO(J=1-0) line (smoothed to a width of $1\,\mathrm{km\,s^{-1}}$). Contours are plotted at 5, 10, 20, 30, 40 σ ($1\,\sigma = 14$ mJy/beam). The synthesized beam is indicated in the lower left.

The chapter is organised as follows: Section 4.2 introduces in an elementary way the main features of the peculiar geometry, with the star axis nearly parallel to the line of sight, mimicking spherical symmetry; it helps greatly the understanding of the following developments. Section 4.3 presents an analysis of the data using a simple bipolar outflow model that had been developed earlier for RS Cnc (preceding section, Hoai et al. 2014; Nhung et al. 2015a); the results of the best fit to the observations is used as a reference in the following sections. Section 4.4 presents a study of the CO(1-0) to CO(2-1) emission ratio, allowing for an evaluation of the temperature distribution nearly independent from the model

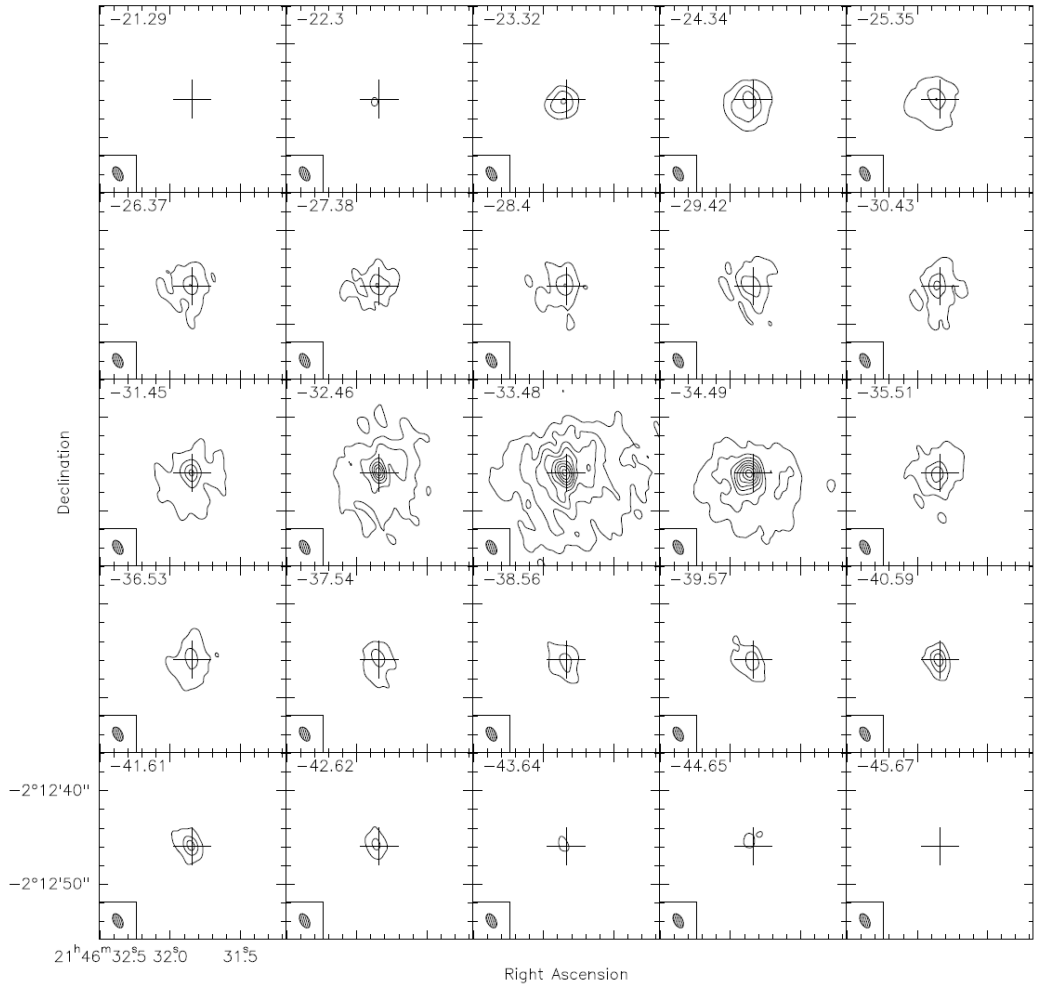

Figure 4.3: Channel maps in the ^{12}CO(J=2-1) line (smoothed to a width of 1 km s^{-1}). First contour is plotted at 10 σ, the following contours start at 20 σ and are plotted in 20 σ steps (1 σ = 16 mJy/beam). The synthesized beam is indicated in the lower left.

adopted for the description of the gas density and velocity. Section 4.5 uses the distribution of the gas velocity obtained in Section 4.3 to reconstruct directly in space the effective gas density, without making direct use of the parameterization of the mass-loss rate obtained in Section 4.3, and providing therefore a consistency check of the results of the model. Finally, Section 4.6 presents a detailed study of the variation across the sky map of the Doppler velocity of the narrow component, providing a sensitive check of the validity of the bipolar outflow hypothesis and of the effect of its small inclination with respect to the line of sight.

4.2 Observing a star along its symmetry axis

The high degree of azimuthal symmetry observed in the channel maps of both CO(1-0) and CO(2-1) emission (Winters et al. 2007) implies that a bipolar outflow, if present, should have its axis nearly parallel to the line of sight. In such a configuration, some simple relations apply between the space coordinates

and their projection on the sky plane. We review them briefly in order to ease further discussion. We use coordinates (Figure 4.4) centered on the star with x along the star axis, parallel to the line of sight, y pointing east and z pointing north. We assume rotation symmetry about the x axis and symmetry about the equatorial (y, z) plane of the star. Defining ρ the gas density, T the gas temperature and $\boldsymbol{V}$ the gas velocity in the star rest frame, having components V_x, V_y, V_z, the following relations apply at point (x, y, z): ρ and T are functions of $r = (x^2 + y^2 + z^2)^{\frac{1}{2}}$ and of $|\alpha|$ where $\alpha = \arctan(x/R)$ is the latitude in the star reference system, and $R = (y^2 + z^2)^{\frac{1}{2}}$ is the projection of r on the sky plane.

The velocity $\boldsymbol{V}$ takes a simple form when expressed in terms of meridian coordinates, $R = y\cos\omega + z\sin\omega$, x and $\eta = -y\sin\omega + z\cos\omega$, ω being the star longitude; its components are then functions of r and $|\alpha|$. In case of pure radial expansion, $V_\eta = 0$, $V_x = xV/r$ and $V_R = RV/r$ while in case of pure rotation $V_R = V_x = 0$.

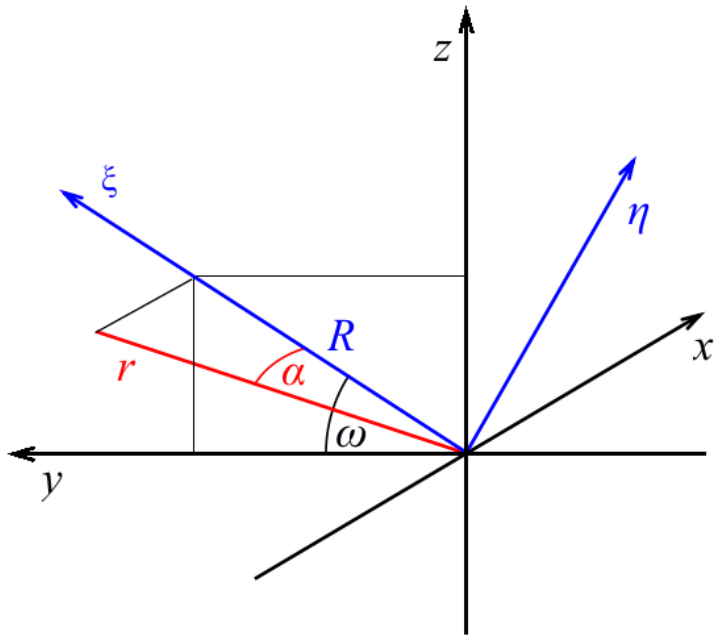

Figure 4.4: Definition of coordinates. The (ξ, η) coordinates are obtained from (y, z) coordinates by rotation of angle ω in the sky plane about the x axis (line of sight and star axis, cf. Sect. 4.2). In the sky plane, y is towards East, and z towards North.

In the case of pure radial expansion with a known radial dependence of the velocity, the flux density f measured in a pixel (y, z) at velocity V_x is associated with a well defined position in space, obtained from

$$x = rV_x/V = (x^2 + R^2)^{\frac{1}{2}} V_x/V = RV_x(V^2 - V_x^2)^{-\frac{1}{2}}. \tag{4.1}$$

Then, if one knows V, one can calculate V_x and therefore its derivative dV_x/dx at any point in space. Defining an effective density $\rho_{\rm eff}$ as $\rho_{\rm eff} = f dV_x/dx$, such that the observed flux in a given pixel be $\int f dV_x = \int \rho_{\rm eff} dx$, one is then able to calculate it at any point in space. The effective density, defined by this relation, is the product of the actual gas density and a factor accounting for the population of the emitting state, the emission probability and correcting for the effect of absorption.

We illustrate the above properties with a simple example, close to the reality of EP Aqr. We assume

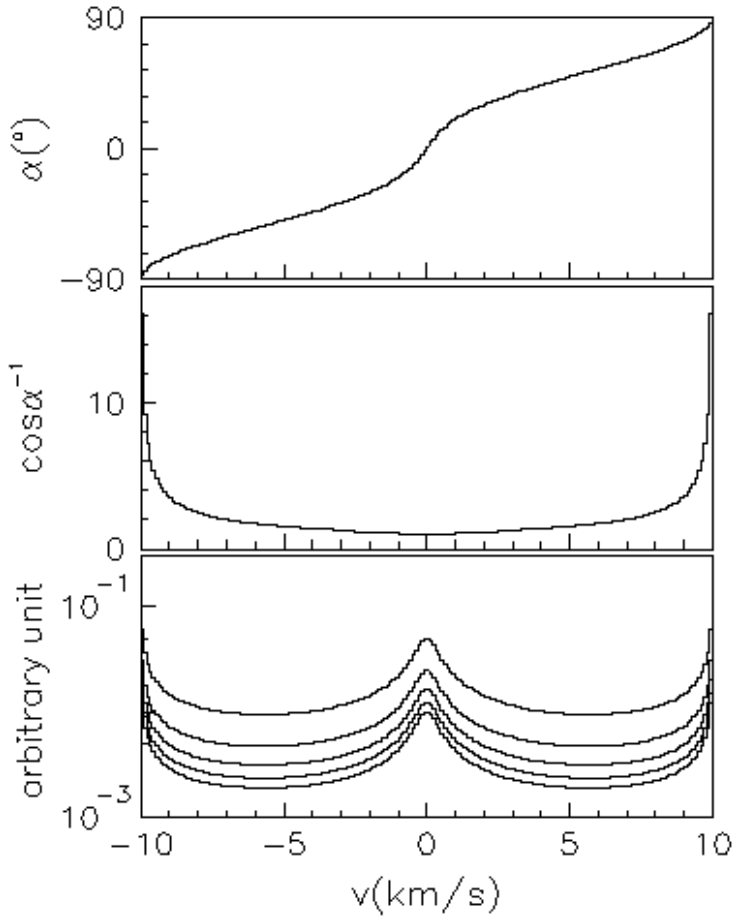

Figure 4.5: Relation between the Doppler velocity V_x and the star latitude α (cf. Eq. (4.2), upper panel), the ratio $r/R = 1/cos\alpha$ (middle panel) for the simple star model described in the text. Lower panel: velocity spectra obtained for the same model at R=1, 2, 3, 4 and 5 (running downward).

exact rotation invariance about the star axis (parallel to the line of sight), a purely radial wind with a velocity that only depends on α

$$V = V_0 + V_1 \sin^2\alpha \tag{4.2}$$

(V_0 at the equator and $V_0 + V_1$ at the poles) and an effective density (defined such that its integral over the line of sight measures the observed flux density) inversely proportional to r^2. From $V_x = V \sin\alpha$ and Eq. (4.2) we obtain $\sin^3\alpha + (V_0/V_1)\sin\alpha - (V_x/V_1) = 0$. This reduced cubic equation is explicitly solvable with $\sin\alpha = -(q-s)^{\frac{1}{3}} - (q+s)^{\frac{1}{3}}$, $s = (q^2+p^3)^{\frac{1}{2}}$, $p = \frac{1}{3}V_0/V_1$ and $q = -\frac{1}{2}V_x/V_1$. For a given value of the Doppler velocity V_x one can therefore calculate α independent of R: in any pixel, V_x and α are related in the same way, which is illustrated in Figure 4.5 (upper panel). Similarly, V_x and $r/R = 1/\cos\alpha$ are also related in a universal way, independent of R (Figure 4.5, middle panel). The resulting velocity spectra are displayed in Figure 4.5 (lower panel) for R=1, 2, 3, 4 and 5 (all quantities are in arbitrary units except for the velocities that are in $\mathrm{km\,s^{-1}}$ with $V_0 = 2\ \mathrm{km\,s^{-1}}$ and $V_1 = 8\ \mathrm{km\,s^{-1}}$). They simply scale as $1/R$, reflecting the $1/r^2$ dependence of the effective density. In such a simple model, the flux ratio between the CO(1-0) and CO(2-1) is a constant, independent of R and V_x.

4.3 Comparison of the observations with a bipolar outflow model

The spectral maps extracted from the reprocessed data are shown in Figure 4.6. The spectra are displayed in steps of 1″ in right ascension and declination. The synthesized beam is 3.53″ × 1.84″ (PA=28°) for CO(1-0), and 1.67″ × 0.94″ (PA=29°) for CO(2-1), respectively.

To describe EP Aqr, we use the model of Hoai et al. (2014), which assumes that the wind is purely radial, free of turbulence, and in local thermal equilibrium. For solving the radiative transfer, a ray-tracing method that takes absorption into account is used. Moreover, the wind is assumed to be stationary and is supposed to have been in such a regime for long enough a time, such that the radial extension of the gas volume is governed exclusively by the UV dissociation of the CO molecules by interstellar radiation (Mamon et al. 1988) and does not keep any trace of the star history. For EP Aqr the CO/H abundance ratio is taken as 2.5 10^{-4} (Knapp et al. 1998), a value representative for an M-type star. The temperature is parameterized by a power law of r, $T = T_0 r^{-n}$ but is independent of the stellar latitude α. The spectrum of flux densities in each pixel is calculated by integration along the line of sight, the temperature dependent contributions of emission and absorption being respectively added and subtracted at each step. The wind velocity V and the flux of matter f_M are smooth functions of $|\sin\alpha|$ and allowance is made for a radial velocity gradient described by parameters λ_1 at the poles and λ_2 at the equator. Assuming the wind to be stationary, the density ρ is then defined at any point by the relation $f_M(\alpha) = r^2\rho(\alpha, r)V(\alpha, r)$.

The bipolarity of the flow is parameterized as a function of $\sin\alpha$ using Gaussian forms centered at the poles:

$$G = \exp[-\frac{1}{2}(\sin\alpha - 1)^2/\sigma^2] + \exp[-\frac{1}{2}(\sin\alpha + 1)^2/\sigma^2], \tag{4.3}$$

where σ is a parameter to be adjusted. This function is used to define the $\sin\alpha$ dependence of both the wind velocity and the flux of matter:

$$V = V_1 G(1 - \lambda_1 e^{-r/2.5''}) + V_2(1 - \lambda_2 e^{-r/2.5''}) \tag{4.4}$$

and

$$f_M = f_{M_1} G + f_{M_2}. \tag{4.5}$$

The density then results from mass conservation:

$$\rho = r^{-2}(f_{M_1} G + f_{M_2})/[V_1 G(1 - \lambda_1 e^{-r/2.5''}) + V_2(1 - \lambda_2 e^{-r/2.5''})]. \tag{4.6}$$

For r-independent wind velocities, $\lambda_1 = \lambda_2 = 0$, the velocity and flux of matter are nearly $V_1 + V_2$ and $f_{M_1} + f_{M_2}$ at the poles and $\varepsilon V_1 + V_2$ and $\varepsilon f_{M_1} + f_{M_2}$ at the equator where ε is the small positive value taken by G at the equator.

A small inclination θ of the star axis with respect to the line of sight, with position angle ψ with respect to the north, is made allowance for. The relations quoted in Sect. 4.2 for $\theta = 0$ are modified

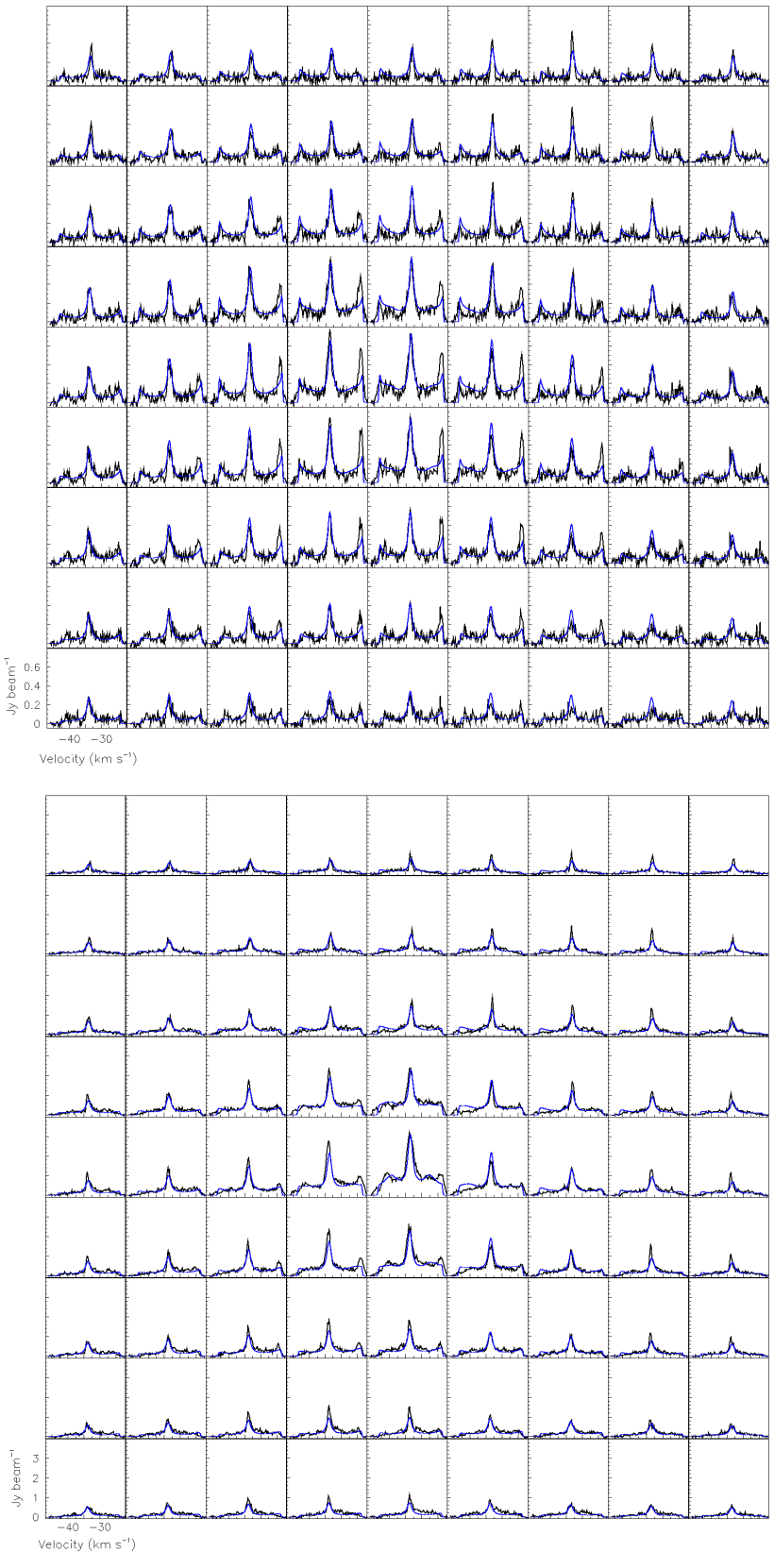

Figure 4.6: Spectral maps centered on the star of the CO observations (black) and the best-fit model (blue). The CO(1-0) map is shown in the upper panel, CO(2-1) in the lower panel. Steps in right ascension and declination are 1″.

Table 4.2: Best fit parameters obtained for the CO(1-0) and CO(2-1) data. A distance of 114 pc is adopted.

Parameter	Best fit value
θ	13°
ψ	144°
σ	0.3
V_1	8.0 km s^{-1}
V_2	2.0 km s^{-1}
f_{M_1}	1.26 10^{-8} M$_\odot$ yr^{-1}sr^{-1}
f_{M_2}	0.49 10^{-8} M$_\odot$ yr^{-1}sr^{-1}
λ_1	0.52
λ_2	0.38
T_0 ($r = 1''$)	116 K
n	0.77

accordingly. More precisely, the position of the star frame with respect to the sky plane and line of sight is now defined by angles θ and ψ and the polar coordinates in the star frame are the latitude α and the longitude ω defined in such a way as to conform with the definition given in Sect. 4.2 for $\theta = 0$. The star radial velocity as determined from the CO line profiles is -33.5 km s^{-1} in good agreement with the value of -34 km s^{-1} derived in Winters et al. (2003). The values taken by the parameters are obtained by a standard χ^2 minimization method. The best fit values of the parameters of the model to the joint CO(1-0) and CO(2-1) observations are listed in Table 4.2 and the quality of the fit is illustrated in Figure 4.6 where modeled velocity spectra are superimposed over observed ones.

This result shows that it is possible to describe the morphology and kinematics of the gas envelope of EP Aqr as the combination of a slow isotropic wind and a bipolar outflow, the wind velocities at the equator and at the poles being $\sim$2 km s^{-1} and $\sim$10 km s^{-1} respectively and the inclination of the star axis with respect to the line of sight, θ, being $\sim$13°. The flux of matter varies from 0.49 10^{-8} M$_\odot$ yr^{-1} sr^{-1} in the equatorial plane to 1.75 10^{-8} M$_\odot$ yr^{-1}sr^{-1} in the polar directions. The total mass-loss rate is 1.2 10^{-7} M$_\odot$ yr^{-1}. The angular aperture of the bipolar outflow, measured by the parameter $\sigma = 0.3$ in Eq. (4.3), corresponds to $\alpha = \arcsin(0.7) \sim 45°$.

Leaving for Sect. 4.6 a more detailed discussion of this result, we study in the next section the CO(1-0) to CO(2-1) flux ratio, which gives important information on the temperature distribution with only minimal dependence on the details of the model.

4.4 The CO(1-0) to CO(2-1) flux ratio

Comparing the fluxes associated with CO(1-0) and CO(2-1) emission provides information on the gas temperature nearly independently from the gas density and velocity, which are common to the two lines. In the optically thin limit and assuming local thermal equilibrium, the temperature T(K) is obtained from the ratio Q of the CO(1-0) to CO(2-1) fluxes as $T = 11.1/\ln(Q/0.063)$. However, the model presented in the preceding section does not reproduce well the observed flux ratio. In particular, we observe that Q is sometimes below the minimal value 0.063 allowed by the local thermal equilibrium hypothesis (when

$T = \infty$). This is illustrated in Figure 4.7, where the data have been averaged over concentric rings limited by circles having R=1″, 2″, 3″, 4″ and 5″ respectively.

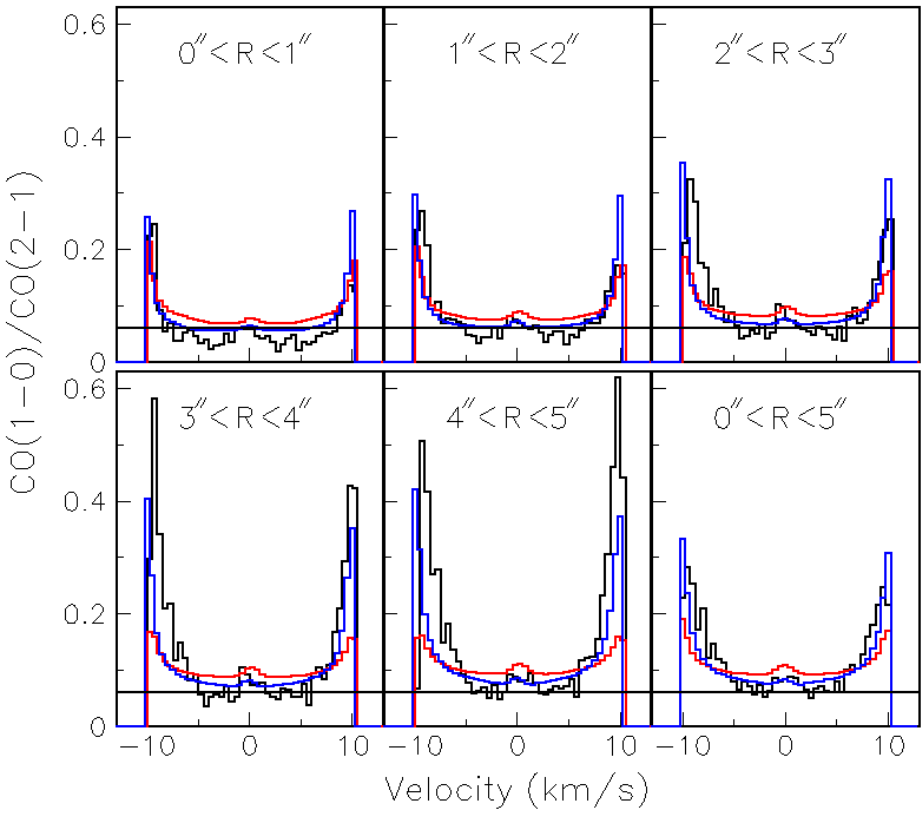

Figure 4.7: CO(1-0) to CO(2-1) flux ratio (black) where each of the CO(1-0) and CO(2-1) fluxes has been averaged over 5 successive velocity bins and over the concentric rings defined in the text. The lower right panel is for all pixels having $R < 5''$. The result of the best fit of the model described in Sect. 4.3 is shown in red and that of its modification described in Sect. 4.4 is shown in blue. The horizontal lines indicate the level (0.063) above which the data must be under the hypothesis of local thermal equilibrium.

Accordingly, we allow for a small difference of normalization between the CO(1-0) and CO(2-1) fluxes by multiplying the former by a factor $1 + \mu$ and the latter by a factor $1 - \mu$. This factor may account for a real difference in calibration as well as, in an *ad hoc* way, for any inadequacy of the model (assumption of local thermal equilibrium, absence of turbulence). Moreover, we see from Figure 4.7 that one needs to increase the ratio Q near the extremities of the velocity spectrum more than in the middle, meaning near the poles at large values of r more than near the equator at small values of r. Accordingly, we parameterize the temperature in the form

$$T = T_0(\sin^2\alpha + a\cos^2\alpha)(r/1'')^{-n} \tag{4.7}$$

with

$$n = n_1 + n_2\cos^2\alpha. \tag{4.8}$$

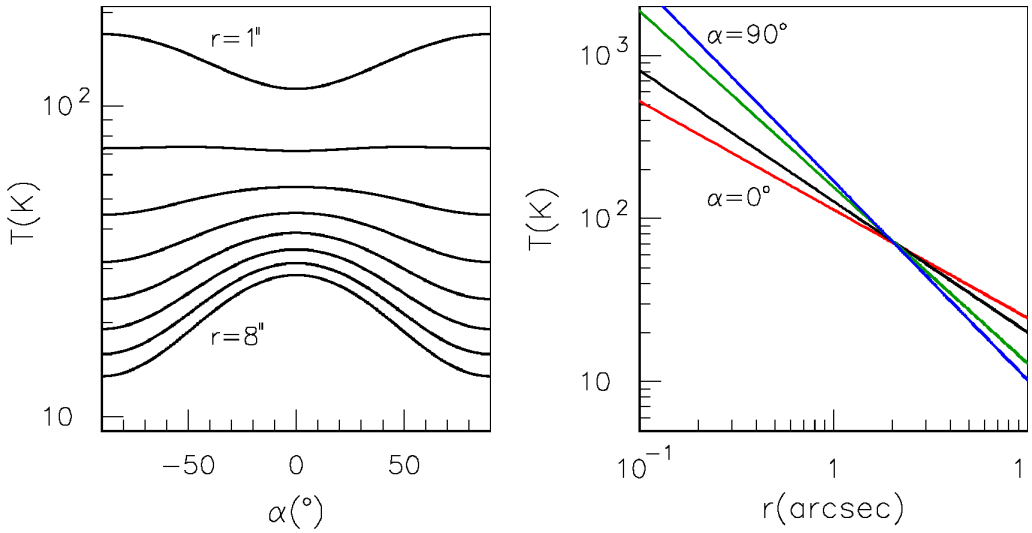

Figure 4.8: Distribution of the gas temperature. Left: as a function of α at distances from the star $r = 1''$ to $8''$ (from top to bottom) in steps of $1''$; right: as a function of r at latitudes $\alpha = 0°$ (red), 30° (black), 60° (green) and 90° (blue).

Table 4.3: Best fit parameters of the CO(2-1) to CO(1-0) ratio.

Parameter	T_0(K)	a	n_1	n_2	μ (%)	χ^2/dof
Best fit values	170	0.67	1.22	−0.55	9.0	1.14
Uncertainties	20	0.12	0.06	0.10	3.0	

At $r = 1''$, the temperature is T_0 at the poles and aT_0 at the equator. The power index describing the radial dependence of the temperature is n_1 at the poles and $n_1 + n_2$ at the equator.

The result is summarized in Table 4.3 and illustrated in Figure 4.7. The ratio between the values taken by the temperature at the equator and at the poles, ar^{-n_2}, varies from 0.70 at $r = 1''$ to 1.64 at $r = 5''$, crossing unity at $r \approx 2''$. As r/R is much larger near the poles than at the equator (it is equal to $1/\cos\alpha$ in the simple configuration studied in Sect. 4.2), the extremities of the velocity spectrum probe large r values, meaning low temperatures, as required by the measured Q values: both the values taken by n_2 and by a are determinant in increasing Q at the extremities of the velocity spectrum. For the same reason, the temperature increase obtained from the parameterization at small values of r and large values of α is not probed by any of the data, which makes its reliability uncertain.

The values of the temperature that we find close to the central star ($\sim$ 1000 K at $0.1''$) are consistent with those obtained by Cami et al. (2000) using infrared CO_2 lines.

The uncertainties listed in Table 4.3 are evaluated from the dependence of χ^2 over the values of the parameters, taking proper account of the correlations between them. However, they have been scaled up by a common factor such that the uncertainty on T_0 be 20 K. This somewhat arbitrary scaling is meant to cope with our lack of detailed control over systematic errors and the value of 20 K is evaluated from the robustness of the results against changes of different nature that have been made to the model finally adopted in the course of the study. While the quoted uncertainties give a good idea of the reliability of the result and of its sensitivity to the values taken by the parameters, both the quality of the data (in

particular the need for a μ-correction) and the crudeness of the model do not allow for a more serious quantitative evaluation.

We noted that the quality of the fits can be slightly improved by allowing for a temperature enhancement at mid-latitudes and small distances to the star; however, we were unable to establish the significance of this result with sufficient confidence.

The following two conclusions can then be retained:

- At large distances to the star, the temperature is significantly higher at the equator than at the poles, by typically 15 K at $r = 5''$;
- The temperature decreases with distance as $\sim r^{-1.2}$ at the poles and significantly less steeply at the equator, typically as $r^{-0.7}$.

4.5 Evaluation of the effective density in the star meridian plane

Under the hypotheses used to evaluate the model described in Sect. 4.3, one can associate to each data-triple (y, z, V_x) a point (r, α) in the meridian plane of the star. Indeed, x is a known function of r, α, and the star longitude ω, as is $V_x = Vx/r$. The former uses the values of θ and ψ and the latter the parameterization of V as a function of r and α that were obtained from the best fit. As one has three equations and three unknowns one obtains r, α and ω given V_x, y and z. The flux density f corresponding to a given data-triple can therefore be mapped as an effective density $\rho_{\rm eff} = f{\rm d}V_x/{\rm d}x$ in the meridian plane of the star, (i.e. each plane that contains the star's polar axis) with coordinates $r\cos\alpha$ and $r\sin\alpha$ (see Figure 4.4). Its evaluation uses the best fit parameterization of the wind velocity but not that of the flux of matter: it provides therefore a consistency check.

The validity of the procedure has been checked by replacing the data by the results of the model and verifying that the reconstructed effective density is identical to that used as input. The region of large $|\alpha|$ values is probed exclusively by the central pixels near the extremity of the spectrum and is therefore subject to large systematic uncertainties. Indeed, large $|\alpha|$ values mean large $|V_x|$ values, which in turn mean large r/R values, namely R much smaller than r. For this reason, on the basis of the result of the validity check, we restrict the space reconstruction to pixels having $R > 1''$. In addition, in order to avoid dealing with too low fluxes, we require R not to exceed $10''$. The resulting maps of $r^2\rho_{\rm eff}$ are displayed in Figure 4.9 for CO(1-0) and CO(2-1) separately and its averaged distributions as functions of r, α and ω in Figure 4.10.

All distributions display significant deviations with respect to the distributions generated by the model, which, however, reproduces well the general trends. In principle, one should be able to include in the model the result of the space reconstruction of $\rho_{\rm eff}$ and iterate the fitting procedure with a more realistic parameterization of the flux of matter and possibly a more sophisticated velocity model. However, the quality of the present data is insufficient to undertake such an ambitious programme. We shall be satisfied with simply taking note of the differences between the model of Sect. 4.3 and the image revealed by the space reconstruction, as long as they can be considered as being both reliable and significant.

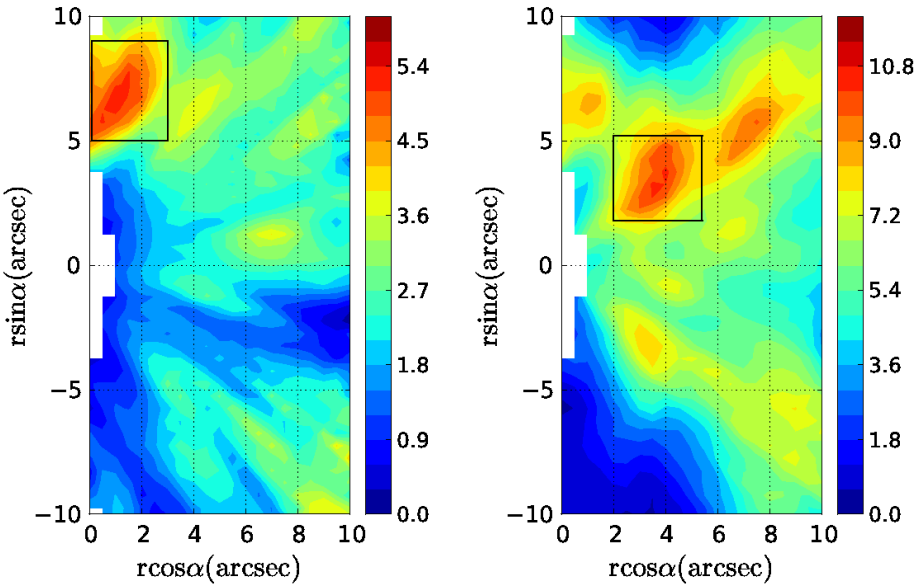

Figure 4.9: Reconstructed maps of the effective density, multiplied by r^2, in the star meridian plane under the assumption of a wind velocity having the form obtained from the best fit of the model of Sect. 4.3. The colour codes are such that the ratio between maximum and minimum values of ρr^2 are the same for CO(1-0) (left) and CO(2-1) (right). Units are Jy beam^{-1} km s^{-1} arcsec. The rectangles show the regions selected for displaying the ω distributions shown in Figure 4.11 (for CO(1-0), abscissa between 0″ and 3″, ordinate between 5″ and 9″; for CO(2-1), abscissa between 2.0″ and 5.4″, ordinate between 1.8″ and 5.2″).

The maps of Figure 4.9 and the α distributions of Figure 4.10 give evidence for a significant asymmetry between the northern and southern hemispheres of the star (defining north and south in the star coordinate system, north corresponding to $\alpha = \pi/2$, away from Earth, with a projection towards North in the sky plane). Indeed, a modification of the model allowing for an asymmetry of the same form as used in Nhung et al. (2015a) for RS Cnc, namely multiplying the flux of matter by a common factor $1 + \gamma \sin\alpha$, gives a 20% excess in the northern hemisphere of the star. Differentiating between the asymmetries of the two flux of matter terms, $f_{M_1} G$ and f_{M_2} reveals a strong correlation between them, the asymmetry of the first term being more efficient at improving the quality of the fit. Restricting the asymmetry to the first term results in a 37% excess in the northern hemisphere. The effect of absorption does not exceed ∼5% on average and cannot be invoked to explain such asymmetry. The fluctuations observed in the distributions of the effective density, as well as the differences observed between the CO(1-0) and CO(2-1) data, make it difficult to locate precisely the northern excess in space. Figure 4.11 displays the ω distributions of the effective density averaged over the $r - \alpha$ rectangles drawn in Figure 4.9 around the maxima of the meridian maps; they do not show an obvious enhancement, the maximum observed in CO(2-1) corresponding in fact to a minimum in CO(1-0). This suggests that the northern excess is distributed over the whole range of star longitudes rather than being confined to a particular region in space. This is confirmed by the (y, z) sky maps of the measured fluxes (integrated over Doppler velocity and multiplied by R) that are displayed in Figure 4.12 and show an enhancement at radii exceeding ∼3″. This enhancement, which was already noted by Winters et al. (2007) in the case of the narrow velocity component for CO(2-1), is also visible in the broad velocity component. A better space resolution would

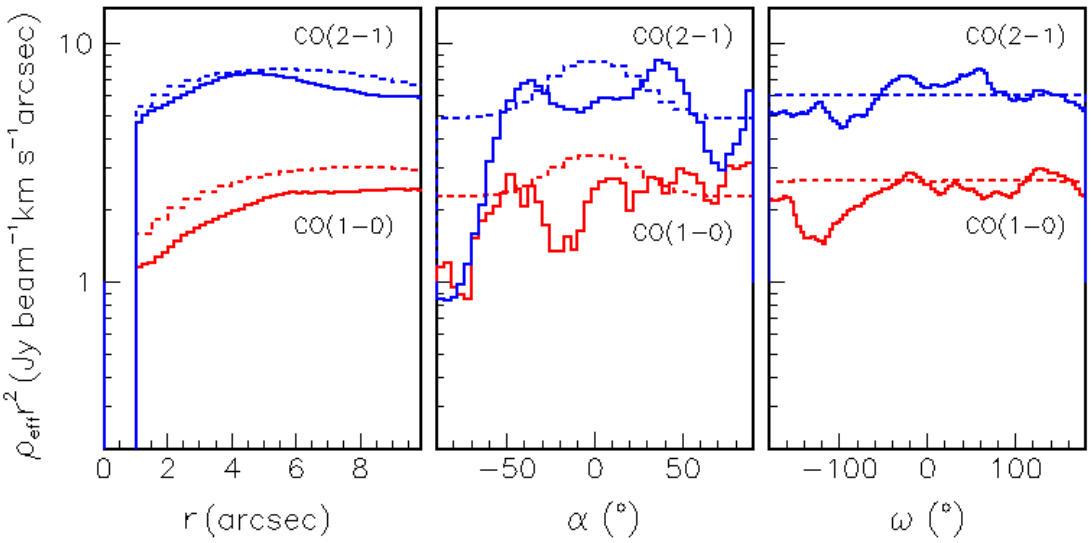

Figure 4.10: Distributions of the average effective density, multiplied by r^2, reconstructed in the meridian plane of the star for a wind velocity having the form obtained from the best fit of the model of Sect. 4.3. Note that the μ-correction has not been applied. left: radial dependence of $r^2\rho_{\rm eff}$, averaged over α and ω; middle: latitude dependence of $r^2\rho_{\rm eff}$, averaged over r and ω; right: longitude dependence of $r^2\rho_{\rm eff}$, averaged over r and α. In each panel, CO(1-0) results are shown in red and CO(2-1) results in blue. The dashed curves show the results of the model, ignoring absorption.

be necessary to make more quantitative statements concerning this excess, its precise location, morphology and velocity distribution. The present data allow for a qualitative description, retaining as likely the presence of a northern enhancement at distances from the star exceeding 3″ and distributed more or less uniformly in star longitude.

4.6 The mean Doppler velocity of the narrow line component

The centroid of the narrow component of the observed spectra moves across the sky map by $\sim\pm0.5$ km s^{-1} on either side of the average velocity. We measure its mean velocity Δv in each pixel after subtraction of the underlying broad component, interpolated from control regions spanning velocity intervals between 5.4 km s^{-1} and 2.6 km s^{-1} with respect to the average velocity (either blue-shifted or red-shifted). The procedure is illustrated in Figure 4.13 for the spectra summed over the 37×37=1369 pixels of the sky map (9.25″ × 9.25″). The resulting Δv distributions, measured in km s^{-1} with respect to the mean velocity measured for the whole maps, are shown in Figure 4.14 (left) and their maps in Figure 4.15. Both CO(1-0) and CO(2-1) data display very similar features, the narrow component being seen to be red-shifted in the north-west direction and blue-shifted in the south-east direction, nearly parallel to the direction of the projected star axis. This suggests that the inclination of the star axis with respect to the line of sight, measured by the angle $\theta\sim13°$, might be the cause of the effect.

In order to assess quantitatively the validity of this interpretation, we define a band running from south-east to north-west as shown in Figure 4.14. Calling ξ the sky coordinate running along the band,

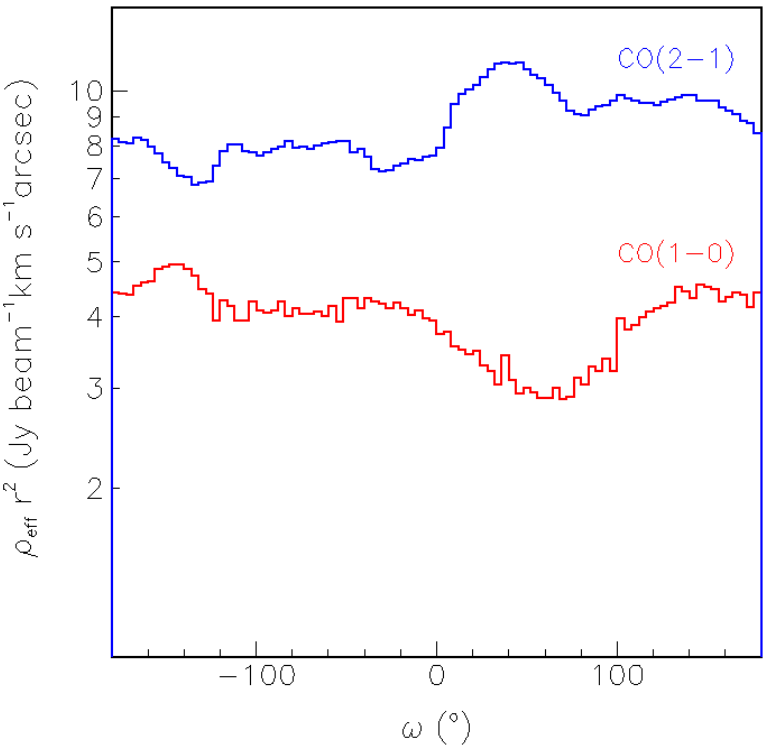

Figure 4.11: Distributions of the effective density, multiplied by r^2, as a function of star longitude ω for the annular regions delineated by the rectangles shown in Figure 4.9. CO(1-0) data are shown in red, CO(2-1) data in blue.

we display in Figure 4.13 (right) the dependence of Δv on ξ for pixels contained inside the band. It reveals a complex structure with successive bumps superimposed over a global increase, displaying remarkable similarities between CO(1-0) and CO(2-1), implying that it is likely to be real rather than an artifact of the analysis or instrumental. As a model, we use the best fit introduced in Sect. 4.3, however with the temperature distribution and the adjustment of the relative CO(1-0) to CO(2-1) normalization that were introduced in Sect. 4.4. As illustrated in Figs. 4.15 and 4.16, the adopted model reproduces correctly the main features of the observed distributions: the width of the Δv distribution and the amplitude of the Doppler shift when moving from south-east to north-west along the ξ axis. Again, as in the preceding section, observations are well reproduced by the model, not only qualitatively but also quantitatively in their general features. This is only achieved by the hypothesis of a bipolar wind structure and is inconsistent with the assumption of a spherical outflow.

4.7 Discussion

Applying a bipolar outflow model to analyze the spatially resolved CO(1-0) and CO(2-1) spectra from EP Aqr results in an excellent agreement of the model results with the observations. The peculiar geometry of the star orientation, with the symmetry axis nearly parallel to the line of sight, implies an

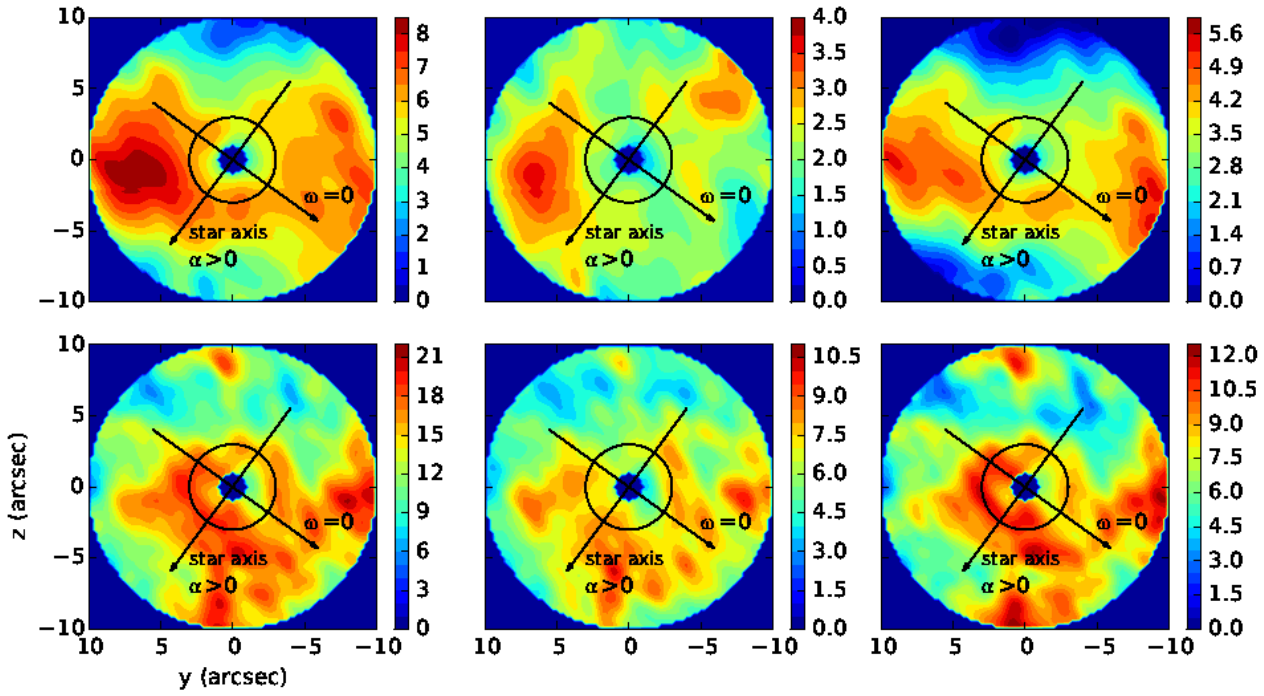

Figure 4.12: Sky maps of Rf for CO(1-0) (upper panels) and CO(2-1) (lower panels) observations. Units are Jy beam^{-1} km s^{-1} arcsec. From left to right: all velocities, $|V_x| < 2$ km s^{-1} and $|V_x| > 2$ km s^{-1}. The circles at $R = 3.5''$ correspond to the enhancement seen by Winters et al. (2007) in CO(2-1) data restricted to the narrow velocity component. The projection of the star axis on the sky plane (making an angle of 13° with the line of sight) and the axis from which the star longitude ω is measured (positive clockwise) are shown as black arrows.

approximate circular symmetry when projected on the sky and gives the illusion of a spherically symmetric gas distribution. However, when correlated with the Doppler velocity distributions, it allows for a transparent interpretation in terms of the spatial effective density, each data-triple being associated with a single point in space once the velocity of the radial wind is known. Under the hypotheses of pure radial expansion and of rotation invariance about the star axis, it is possible to reconstruct the space distribution of the effective density. As a first step, we have compared the observations with a simple bipolar outflow model that had been developed earlier to describe another AGB star, RS Cnc. A satisfactory description has been obtained by adjusting the model parameters to best fit the CO(1-0) and CO(2-1) data together. Several parameters defining the morphology and the kinematics of the gas volume surrounding EP Aqr have been evaluated this way with good confidence. Among these are the orientation of the star axis, making an angle of ∼13° with the line of sight and projected on the sky plane at ∼144° from north toward west. The velocity of the radial wind has been found to increase from ∼2 km s^{-1} at the star equator to ∼10 km s^{-1} at the poles. The flux of matter is also enhanced at the poles, however less than the radial wind, resulting in an effective density slightly enhanced in the equator region. This shows that an axi-symmetry such as that observed in EP Aqr (or RS Cnc, see figure 6 in Hoai et al. (2014) is more clearly revealed by velocity-resolved data. For instance infrared data obtained in the continuum, even at very high spatial resolution, could not reveal such an effect. Such a kind of morpho-kinematics could explain that asymmetries in AGB outflows are found preferentially through radio observations obtained at high spectral resolution (e.g. Castro-Carrizo et al. 2010). However, this characteristic of the model is partly arbitrary

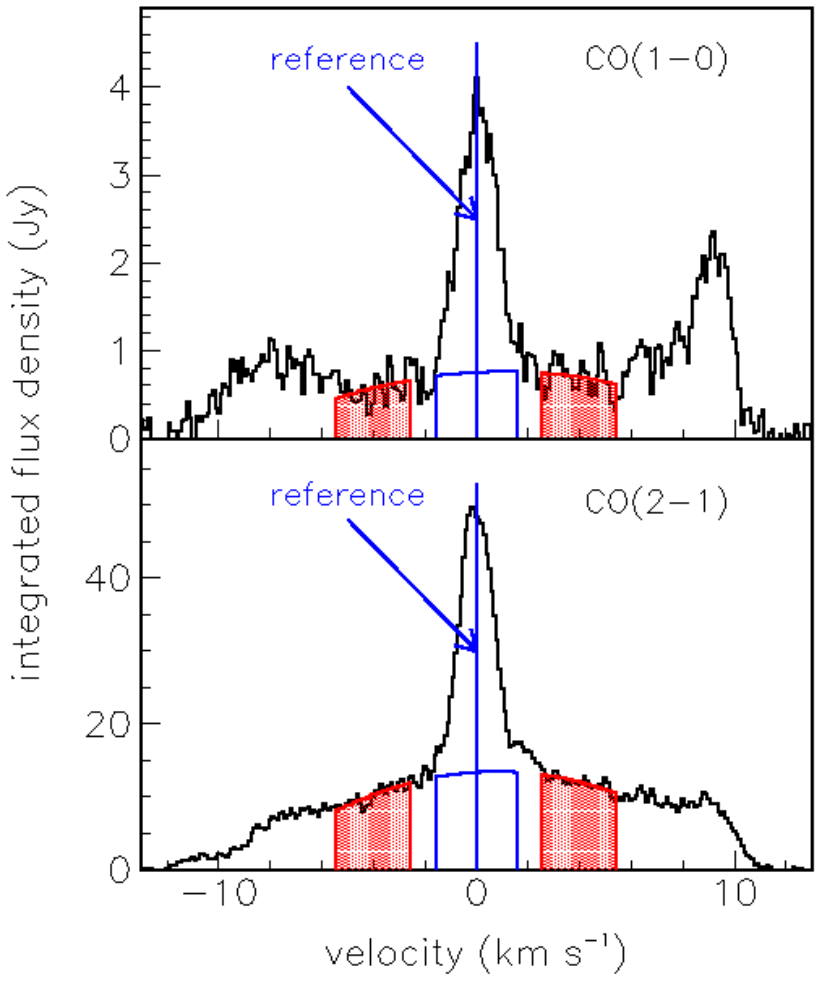

Figure 4.13: Illustration of the procedure used to evaluate the mean Doppler velocity Δv of the narrow component. The velocity spectra summed over the 1369 pixels of the map are shown in black for CO(1-0) (upper panel) and CO(2-1) (lower panel). The quadratic fit over the two control regions is shown in red and its interpolation below the narrow component in blue. The vertical blue lines show the mean Doppler velocities of the narrow component from which the interpolated broad component has been subtracted. They are used as reference for evaluating Δv in each pixel separately.

and its main justification is to give a good description of the observations. We do not claim that the form adopted in the proposed model is unique; on the contrary we are confident that other forms could have been chosen with similar success. In particular, the hypothesis of pure radial expansion retained in the model should not be taken as evidence for the absence of rotation of the gas volume about the star axis. Indeed, such rotation, if it were present, would be virtually undetectable as the resulting velocities, being nearly perpendicular to the line of sight, would not produce any significant Doppler shift.

The assumptions made in formulating the model are always approximations, some time very crude, of the reality. In particular, evidence has been obtained for significant departures from the symmetry with respect to the star equatorial plane assumed in the model, revealing an excess of emission at northern star latitudes over the whole longitudinal range at angular distances from the star exceeding $\sim 3''$. This

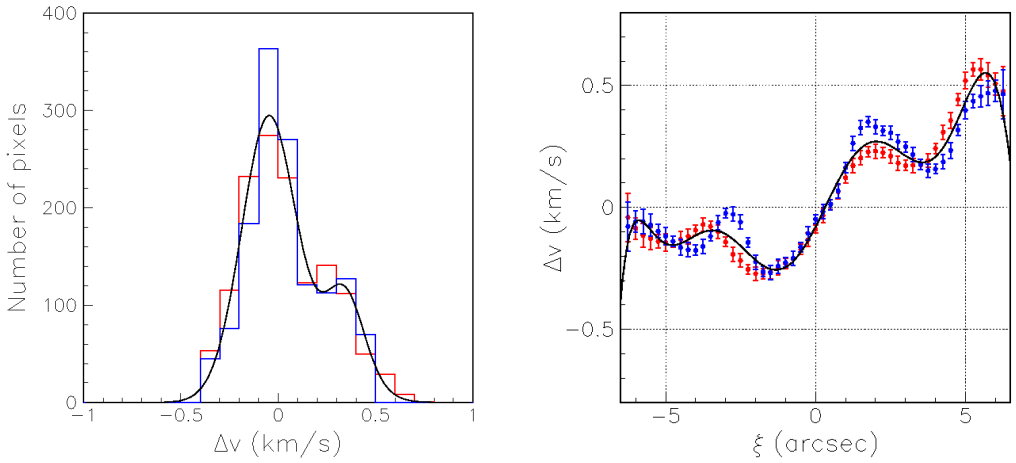

Figure 4.14: Left: distributions of the mean Doppler velocity Δv (km s^{-1}) measured with respect to its value averaged over the whole map (shown as "reference" in Figure 4.13). The black curve shows a two-Gaussian common fit to the two distributions. Right: dependence of the projection of the mean Doppler velocity Δv (km s^{-1}), averaged over pixels included in the bands shown in Figure 4.15, on coordinate ξ measured from south-east to north-west. The black curve shows a polynomial common fit to the two distributions. In both panels the CO(1-0) data are shown in red and the CO(2-1) data in blue.

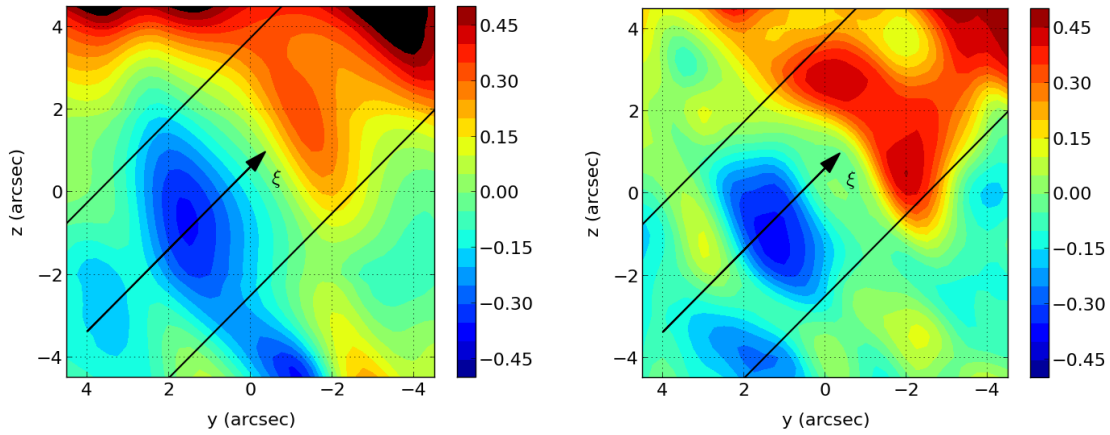

Figure 4.15: Sky maps of the mean Doppler velocity Δv (km s^{-1}) measured with respect to its value averaged over the whole map (shown as "reference" in Figure 4.13) for CO(1-0) (left) and CO(2-1) (right). The black lines limit the bands in which pixels are retained to evaluate the ξ dependence of Δv (Figure 4.14 right).

feature, at least part of it, had already been noted earlier (Winters et al. 2007) and thought to suggest the existence of successive mass loss events. In other words a succession of mass loss events can be mimicked by a latitudinal variation of the flux of matter.

In general, while the proposed model has been very efficient at describing the main features and general trends of the flux densities, some significant deviations with respect to the observations have also been found. The present data, in particular their spatial resolution, prevent a more detailed statement about the nature of these deviations. An important asset of the model is to illustrate the efficiency of

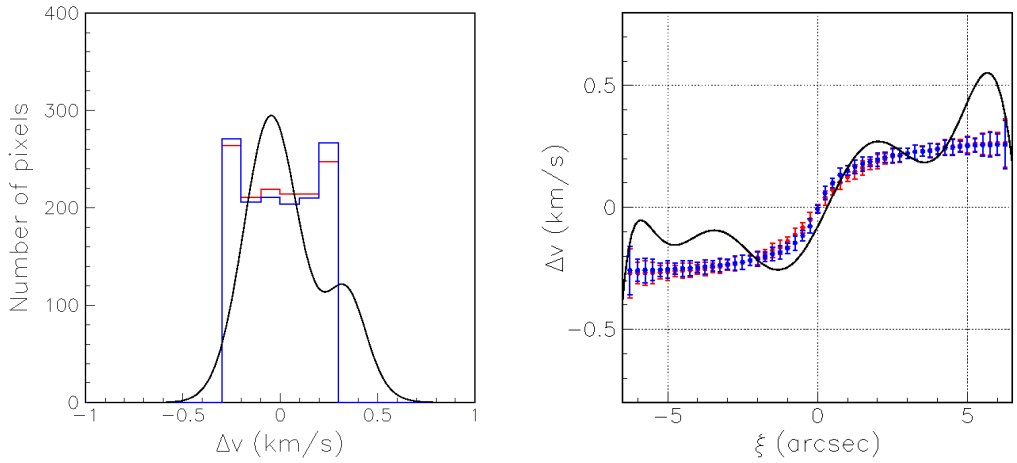

Figure 4.16: Results of the model introduced in Sect. 4.3 for the distributions displayed in Figure 4.14. The smooth curves are the results of the fits (respectively Gaussian and polynomial) made to the observations in Figure 4.14.

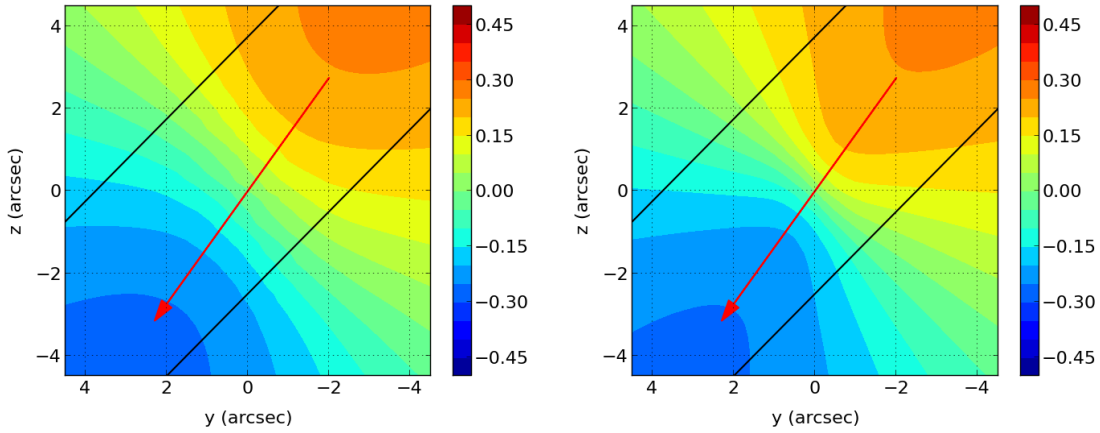

Figure 4.17: Results of the model introduced in Sect. 4.3 for the maps displayed in Figure 4.15. The red arrows indicate the projection of the star axis on the sky plane.

the method used to reconstruct the spatial morphology and kinematics of the gas envelope. Once data of a significantly better resolution will be available, e.g. from ALMA, using the same methodology will reveal many of such details with unprecedented reliability and precision.

The availability of measurements of the emission of two different rotation lines of the same gas is extremely precious and has been exploited as much as possible, based on the current data. The flux ratio of two lines allows to evaluate the temperature distribution of the gas in a region where the ratio between the populations and emission probabilities of the two states vary rapidly, which is the case for angular distances from the star probed by the present observations. Most of the details of the model are irrelevant to the value of the flux density ratio between the two lines, which depends mostly on temperature under reasonable approximations (local thermal equilibrium, absence of large turbulence, etc.). Through this

property, evidence was found for a significant enhancement of temperature at the star equator, therefore correlated with the orientation of the bipolar flow and at variance with the hypothesis of a pure radial dependence.

A method allowing iterating the wind velocity and the effective density in successive steps has been sketched. When data with significantly improved spatial resolution will be available, this will provide a very efficient analysis tool. The peculiar orientation of EP Aqr makes such an analysis much more transparent than in the general case where the star axis is neither parallel nor perpendicular to the sky plane.

Furthermore, the good spectral resolution of the present observations has made it possible to finely analyse the variations of the Doppler velocity of the narrow line component across the sky map, providing a sensitive test of the validity of the bipolar flow hypothesis and a quantitative check of the inclination of the star axis with respect to the line of sight.

The present work leads us to prefer a bipolar, stationary, wind model over the spherical, variable, scenario that was proposed earlier. AGB stars have traditionally been assumed to be surrounded by almost spherical circumstellar shells. Deviations, sometimes spectacular, from spherical symmetry are observed in planetary nebulae (PNs). Such deviations are also observed in post-AGB sources and it is generally considered that they arise during the phase of intense mass loss, after the central stars have evolved away from the AGB. However, it has also been recognized that the geometry of circumstellar shells around AGB stars may sometimes show an axi-symmetry (e.g. X Her, Kahane & Jura (1996); RS Cnc, Hoai et al. (2014)). The origin of this axi-symmetry has not been clearly identified: magnetic field, stellar rotation, or presence of a close binary companion may play a role. Recently, Kervella et al. (2015) reported the detection of a companion to L2 Pup, another M-type AGB star, with a disk seen almost edge-on. The case of EP Aqr is particularly interesting because, with no detected Tc and a $^{12}C/^{13}C$ ratio $\sim$ 10, it seems to be in a very early stage on the AGB. All these cases raise the interesting possibility that the deviations from sphericity observed in PNs and in post-AGB stars are rooted in their previous evolution on the AGB.

4.8 Conclusion

We have revisited the EP Aqr data obtained by Winters et al. (2007). We now interpret them in terms of an axi-symmetrical model similar to that developed for RS Cnc by Hoai et al. (2014). The expansion velocity varies smoothly with latitude, from $\sim$2 km s^{-1} in the equatorial plane to $\sim$10 km s^{-1} along the polar axis, which for EP Aqr is almost parallel to the line of sight. The mass loss rate is estimated to $\sim$1.2 10^{-7} M$_\odot$ yr^{-1}. The two stars look very similar, the differences in the observations being only an effect of the orientations of their polar axis with respect to the line of sight. There is evidence for a temperature enhancement near the star equator and a faster decrease along the polar axis than in the equatorial plane.

Both RS Cnc and EP Aqr show peculiar CO line emission whose profiles consist of two components (Knapp et al. 1998; Winters et al. 2003). This may suggest that the other sources with such composite CO line profiles (e.g. X Her, SV Psc, etc.) might also be interpreted with a similar model, rather than with successive winds of different characteristics as has been proposed earlier.

Chapter 5

CO EMISSION FROM THE RED RECTANGLE [1]

5.1 Introduction

The Red Rectangle was discovered by Cohen et al. (1975) and since then has been the target of many observations and the object of numerous modelling exercises. It owes its name to its appearance in the visible, as observed recently by Cohen et al. (2004) using the Hubble Space Telescope and shown in Figure 5.1. It is commonly accepted that this appearance is the result of a biconical structure with axis perpendicular to the line of sight. The star in the centre, HD 44179, is known to be a binary made of a post AGB star and a secondary star accreting the wind of the former in a disk perpendicular to the star axis and therefore to the sky plane. The binary is an unresolved spectroscopic binary, the main parameters of which are well known. The secondary star is usually considered to be a low mass main sequence star but some authors argue in favour of a white dwarf (see for example Men'shchikov et al. 2002). The general idea is that a fast jet normal to the accretion disk has dug a conical cavity in the slow wind of the post AGB star. The appearance at visible wavelengths is complicated by the fact that the light observed is the light emitted by the star and diffused on the walls of the conical cavities, direct light being prevented to reach the Earth by the presence of a dense dust torus around the star. Several authors have proposed models along such lines. Two recent examples from which earlier references can easily be traced are Koning et al. (2011) and Thomas (2012).

An open question is the nature of the bipolar outflow carving the conical cavities in the slowly expanding wind of the post-AGB star. While it is commonly accepted that it has a high velocity, in excess of 158 kms^{-1} according to Koning et al. (2011), its opening angle might be broad, typically at the scale of the conical cavity, or narrow but precessing around the star axis. A recent polarization measurement (Martínez González et al. 2015) pleads in favour of the second hypothesis.

Until recently, radio and millimetre wave observations of the Red Rectangle had insufficient spatial resolution to map the morphology of molecular gas emission. The only exception was a Plateau de Bure

[1] The content of this chapter has been published in Research in Astronomy and Astrophysics (Tuan Anh et al. 2015)

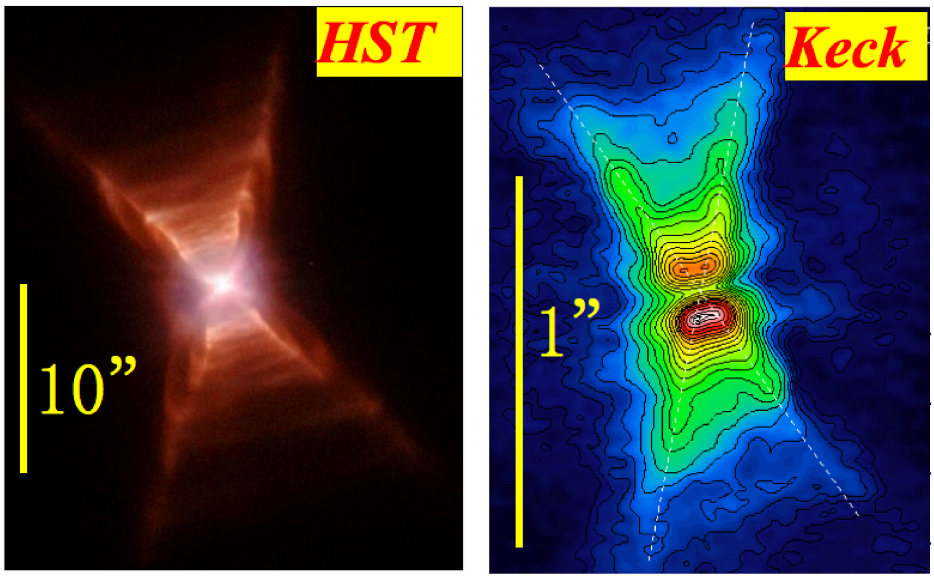

Figure 5.1: Left: HST wide field planetary camera 2 image of the Red Rectangle from Cohen et al. (2004). Right: Keck telescope near-infrared speckle image from Tuthill et al. (2002). North is up and East is left.

IRAM observation of CO(2-1) and CO(1-0) emission, with a resolution of ∼1″, sufficient to reveal the presence of a disk in rotation perpendicular to the star axis (Bujarrabal et al. 2005). Using the experience gained by observing other proto-planetary nebulae, the detailed study of the profiles of other rotational lines confirmed the presence of such a disk (Bujarrabal & Alcolea 2013; Bujarrabal et al. 2013a). Recently, ALMA observations in CO(6-5) and CO(3-2) with an order of magnitude better resolution (Bujarrabal et al. 2013b) have been made available. Their analysis is reported in the following sections.

5.2 Data

CO(3-2) and CO(6-5) ALMA data of the Red Rectangle have been recently released for public access (Project number 2011.0.00223.S). CO(3-2) data are available in the form of data-cubes of 360×360 pixels and 70 frequency bins, CO(6-5) data of 432×432 pixels and 43 frequency bins. For convenience, we have rearranged both CO(3-2) and CO(6-5) data in a common array of 50×50 pixels centred on the continuum emission of the star and covering a solid angle of 5″×5″, with Doppler velocity spectra covering from -7.2 kms^{-1} to 7.2 kms^{-1} in 36 bins of 0.40 kms^{-1} each.

The observed maps have been rotated by 13° clockwise for the new array to be aligned with the star axis. The value of 13° used for the position angle of the star axis is consistent with values found in the literature (between 10° and 15°) and with a preliminary analysis which we made of the data, giving as result 13° ± 2°. Both the sky maps and the velocity spectra associated with the new arrays are centred on the star, the former using the continuum data with a precision of ∼0.02″ and the latter such that the mean Doppler velocity evaluated over pixels distant by less than 2.5″ from the star cancels, with a precision of ∼0.1 kms^{-1}. The resulting sky maps, integrated over velocities, are illustrated in Figure 5.2. Details of data collection are given in Appendix A of Bujarrabal et al. (2013b) and do not need to be repeated here, where we use the data in the form provided by the ALMA staff, which are of a quality sufficient for the

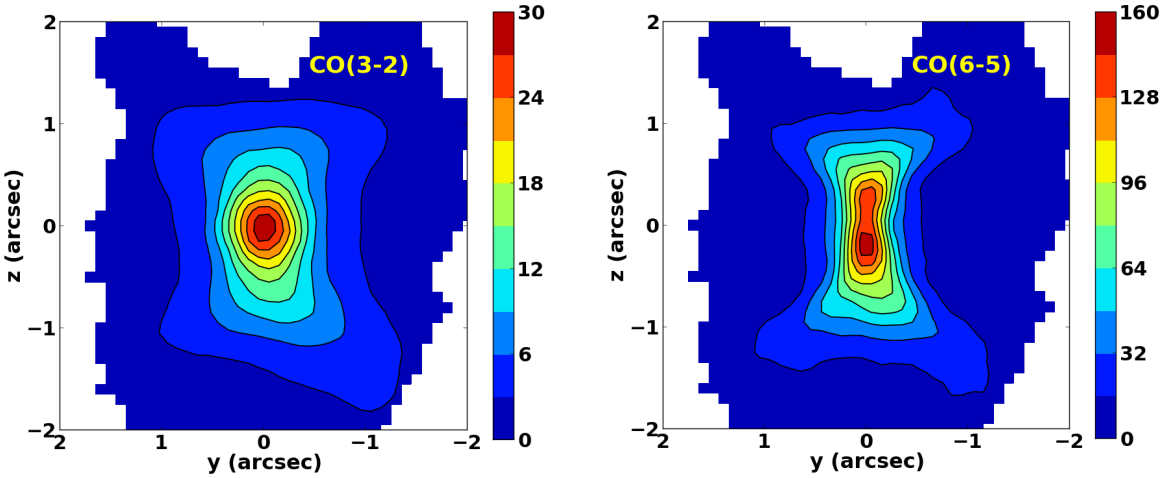

Figure 5.2: CO(3-2) (left) and CO(6-5) (right) images (4″×4″) rotated by 13° clockwise integrated over Doppler velocities from −7.2 kms^{-1} to 7.2 kms^{-1} (present work). Unit of color bars is Jy beam^{-1}km s^{-1}

purpose of the present study. The synthetic beam sizes are 0.50″×0.49″ and 0.27″×0.24″ for CO(3-2) and CO(6-5) respectively.

Figure 5.3 (left and middle) shows the projections of the continuum emission on the axes of the rotated array, used to centre the sky map; continuum emission is discussed in Section 8. Figure 5.3 (right) displays the lower ends of the line flux density distributions; after small adjustment of the empty sky baselines, Gaussian fits give rms values of 20 mJy/beam for CO(3-2) and 72 mJy/beam for CO(6-5), corresponding respectively to 0.082 and 1.11 Jy arcsec^{-2}. The image reprocessing made by Bujarrabal et al. (2013b) yields significantly lower values (respectively 7 and 30 mJy/beam) with the implication that most of the flux fluctuations observed here arise from imperfect deconvolution and/or calibration. As a consequence, the uncertainty attached to the sum of N data cubes is far from being equal to the above values multiplied by $\sqrt{N}$ and must be evaluated for each specific case separately. In particular, when integrating pixel flux densities over velocity spectra we find that reliable results are obtained by retaining only pixels containing more than 0.75 Jy km s^{-1} arcsec^{-2} in the CO(3-2) data sample and more than 3.0 Jy km s^{-1} arcsec^{-2} in the CO(6-5) data sample. The map covered by the retained pixels is illustrated in the upper left panel of Figure 5.4 and contains 1526 pixels (covering 15.3 arcsec^2). The restriction to such a region of the sky is conservative but sufficient for the purpose of the present study. However, improved deconvolution and calibration, such as made by Bujarrabal et al. (2013b), would allow for exploring finer details, in particular at large distance from the star.

^{13}CO data are also available from the same ALMA observations but have not been considered in the present work.

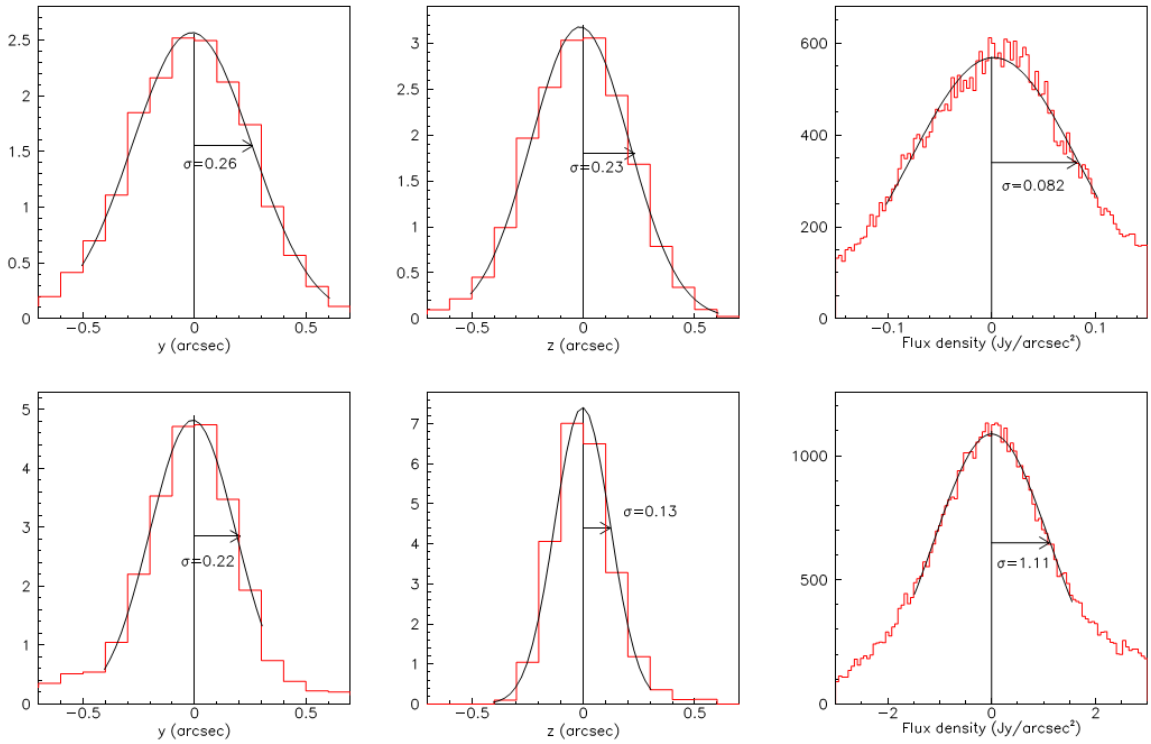

Figure 5.3: Projections on y (left) and z (middle) of the continuum emission (Jy/beam). Right: Empty sky contribution at low values of the line flux density distributions (Jy arcsec^{-2}). The upper panels are for CO(3-2) and the lower panels for CO(6-5). Gaussian fits are shown on the peaks.

5.3 Main features

We present below general information that can be obtained from the data without having recourse to a model. We pay particular attention to assessing the symmetries of the structure and to comparing CO(6-5) and CO(3-2) emissions (an indicator of the temperature when absorption can be neglected). Figure 5.2 shows the sky maps of CO(3-2) and CO(6-5) emissions integrated over the lines. They display the same symmetries as the visible and infrared maps.

We use coordinates x, y and z, respectively pointing away from Earth (along the line of sight), 13° south of East and 13° east of North (along the star axis), all measured as angular distances in arcseconds (the star is usually considered as being 710 pc away from Earth, see Men'shchikov et al. 2002). We define a space radius $r = \sqrt{x^2 + y^2 + z^2}$, a sky radius $R = \sqrt{y^2 + z^2}$ and an equatorial radius $\xi = \sqrt{x^2 + y^2}$. To a good approximation, the inclination angle of the star axis with respect to the sky plane, θ, is known to cancel. Under such an approximation, symmetry properties of the gas morphology and kinematics take remarkably simple forms in terms of the measured flux densities, $F(y, z, V_x)$, V_x being the Doppler velocity.

We define star cylindrical coordinates, (ξ, ω, z) with $\xi = x/\sin\omega$ and $\tan\omega = -x/y$. Introducing a coordinate $\eta = x\cos\omega + y\sin\omega$, normal to the meridian plane, the components V_ξ, V_η and V_z of the space velocity contribute respectively $V_\xi \sin\omega$, $V_\eta \cos\omega$ and 0 to the Doppler velocity. Moreover, relaxing the

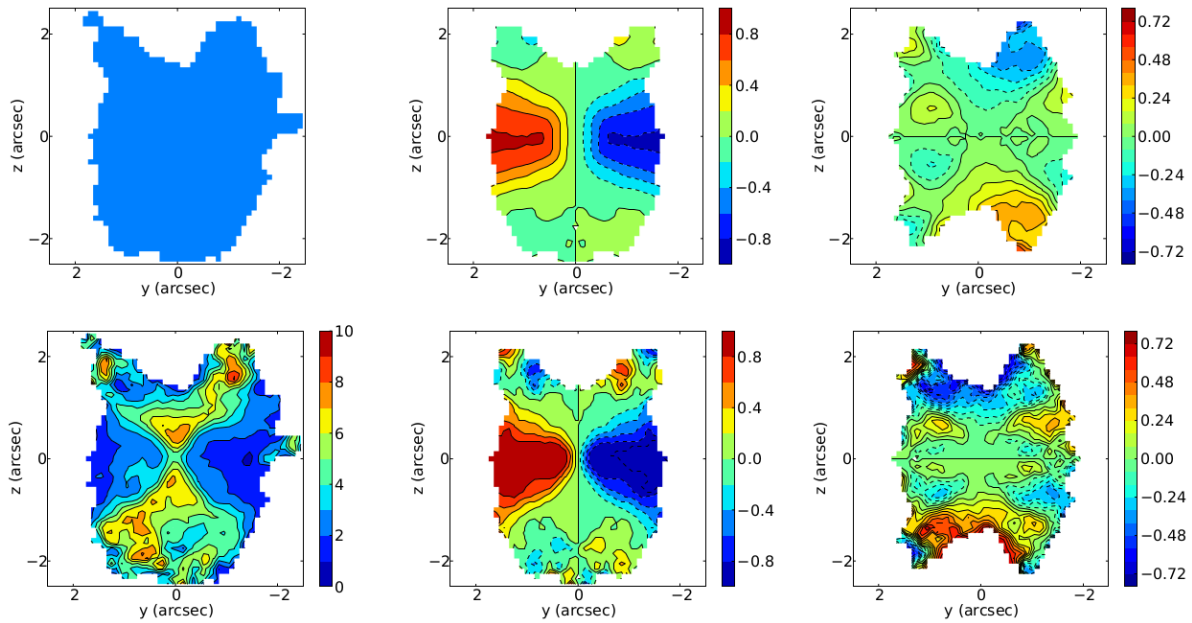

Figure 5.4: Left: the upper panel displays (in blue) the map of retained pixels and the lower panel that of A_T, the CO(6-5) to CO(3-2) flux ratio. Sky maps of A_η (middle) and A_z (right) are shown for CO(3-2) and CO(6-5) in the upper and lower panels respectively.

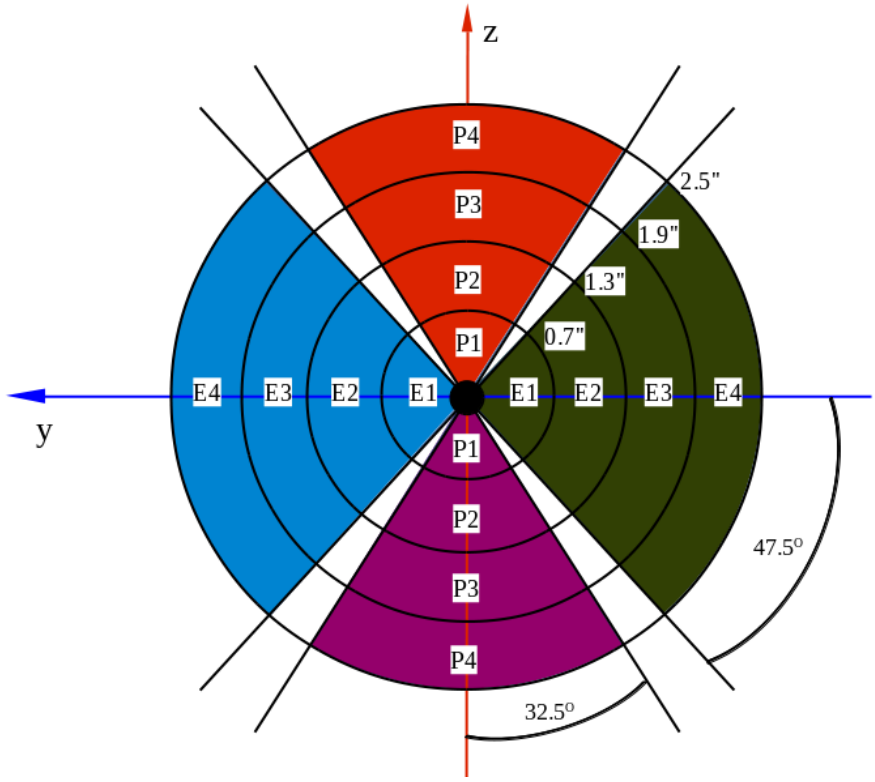

Figure 5.5: Sketch of sky regions having velocity spectra in Figure 5.6

condition θ=0 simply introduces, to first order in θ, a contribution θV_z. The Doppler velocity reads then:

$$V_x = (x/\xi)V_\xi - (y/\xi)V_\eta + \theta V_z \tag{5.1}$$

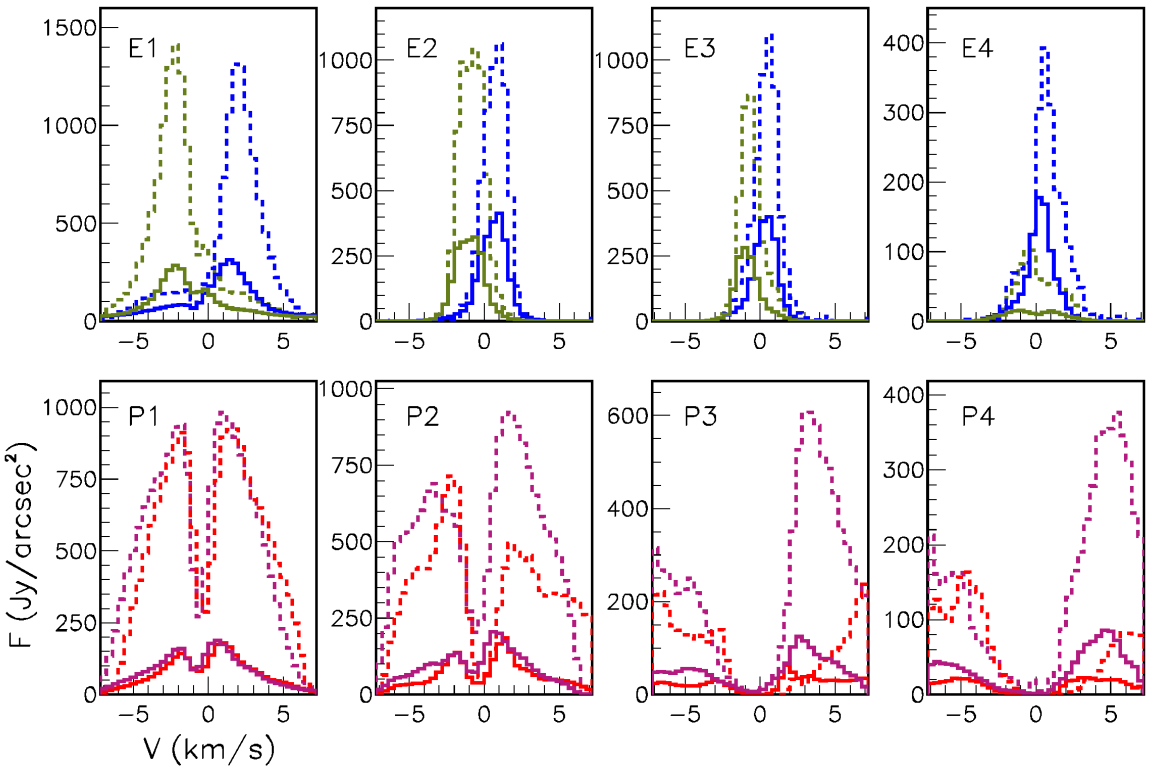

Figure 5.6: Velocity spectra integrated over sky regions defined in Figure 5.5. Dotted lines are for CO(6-5), solid lines for CO(3-2). P and E stand for polar and equatorial sectors respectively, followed by a digit labelling the radial rings from centre outward. Different colors correspond to different regions as defined in Figure 5.5.

It is convenient to introduce an effective density $\rho(x, y, z)$ such that the flux density integrated over Doppler velocities observed at a point (y, z) in the sky plane reads

$$F(y,z) = \int F(y,z,V_x)dV_x = \int \rho(x,y,z)dx \tag{5.2}$$

the second integral being taken along the line of sight. When discussing symmetries, it is also convenient to introduce blue shifted and red shifted components, B and R ($F = B + R$), with the the first integral running over $V_x < 0$ and $V_x > 0$ respectively. Under the hypothesis that the properties of the star are invariant by rotation about the star axis (namely independent from ω), at a given z, V_ξ contributes $R(y) = B(y) = R(-y) = B(-y)$ and V_η contributes $R(y) = B(-y), B(y) = R(-y)$. A good indicator of rotation about the star axis is therefore the quantity A_η $=[R(y) + B(-y) - R(-y) - B(y)]/[F(y) + F(-y)]$. Figure 5.4 displays maps on the sky plane of $A_T = F(CO[6-5])/F(CO[3-2])$, A_η and the North-South asymmetry, $A_z = [F(y,z) - F(y,-z)]/[F(y,z) + F(y,-z)]$.

The first of these quantities is sensitive to temperature. Indeed, in addition to the actual CO density, namely gas density multiplied by CO abundance, the effective density introduced in Relation 5.2 accounts for the population of the excited molecular level and the emission probability. Under the hypothesis of local thermal equilibrium, it depends therefore essentially on temperature. The assumption of rotational

invariance about the star axis implies in addition that absorption is negligible. Integrating the flux over the pixels that have been retained, we obtain respectively 142 Jy km s^{-1} and 615 Jy km s^{-1} for CO(3-2) and CO(6-5). Under the hypothesis of thermal equilibrium and neglecting absorption, their ratio, 4.3, corresponds to an average temperature of 63 K. A detailed discussion of the distribution of the gas temperature is given in Section 5. The A_T map reveals the biconical structure in a very clear way, providing evidence for a temperature distribution dominated by the morphology of the outflow down to small distances to the star. It also reveals inhomogeneities of the biconical outflow that are discussed in Section 7. The second quantity, A_η, reaches very high values and provides spectacular evidence for rotation over a broad angular range about the equator, the eastern part being red-shifted and the western part blue-shifted. There is no sign of a thin equatorial disk.

The third quantity, A_z, displays a significant north-south asymmetry of the bipolar outflow at large distances from the star, however much smaller than in the case of A_η.

A summary of the main features of the observed morphology and kinematics is presented in Figure 5.6 where each of the four quadrants of the sky plane, North-East, North-West, South-East and South-West, are folded together and segmented in four radial and two angular intervals (see Figure 5.5). The radial intervals (sky radius R) are 0.6″ wide starting at 0.1″. The angular regions are a polar sector for position angles inferior to 32.5° with respect to the star axis (z) and an equatorial sector for position angles inferior to 47.5° with respect to the equator (y). Figure 5.6 displays velocity spectra integrated over the eight regions defined by this ring and sector geometry. The equatorial region is dominated by rotation, with velocities decreasing with R from ∼2 kms^{-1} at R∼0.5″ to ∼0.7 kms^{-1} at R∼1.5″. The polar regions are instead dominated by an outflow, with Doppler velocities extending to, and even beyond, the limits of the spectra. The outflow velocity is seen to increase significantly with R. It may be due to the presence of a velocity gradient, the gas being accelerated continuously over the whole range of R explored here, or to an opening of the biconical cavity when R increases. As was already remarked in Figure 5.4, strong deviations from symmetry are present at large values of R, in particular in the CO(6-5) data.

5.4 Gas effective density

The complexity of the Red Rectangle morphology is an invitation to proceed by steps in the evaluation of its geometrical, kinematical and physical properties.

In a first step we evaluate the effective densities from the values taken by the measured flux densities integrated over the velocity spectra for CO(3-2) and CO(6-5) separately. We assume that the effective densities obey rotational symmetry about the star axis, namely that they are functions of ξ and z exclusively. The study of the effect of such an assumption is kept for the last step. The effective densities are obtained by simply solving the integral equation $F(y,z) = \int \rho(\xi,z)dx$ (Relation 2).

In a second step, retaining the assumption of rotational symmetry, we evaluate the field of gas velocities using the values of the effective densities obtained in the first step and fit the CO(3-2) and CO(6-5) data together with a same velocity distribution. Here, the ξ (expansion) and η (rotation) components of the velocity vectors need to be evaluated as functions of ξ and z, implying the adoption of a

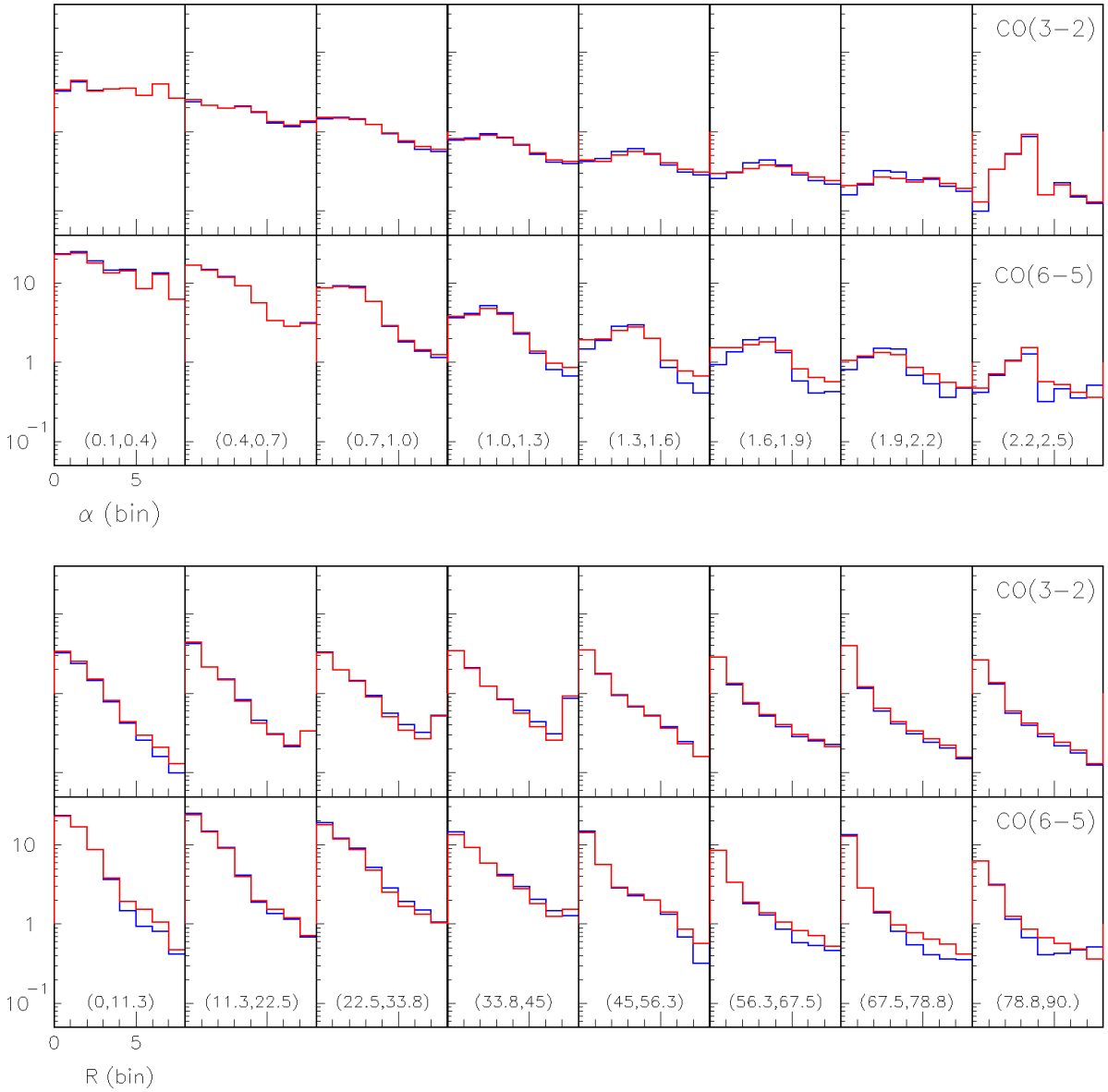

Figure 5.7: Measured flux densities (blue) averaged over (R,α) intervals of sizes (0.3″,11.25°) are compared with the result (red) of integrating over the line of sight the effective densities obtained by solving the integral equation. The upper panels display α distributions in eight successive R intervals, the lower panels display R distributions in eight successive α intervals. In each case, the upper row is for CO(3-2) and the lower row for CO(6-5). Panels are labelled with the corresponding interval, in arcseconds for R and degrees for α.

model, which we choose as simple as possible.

The last step studies the asymmetries that have been neglected in the first two steps and the implications of the assumptions that have been made.

The present section deals with the first of these three steps. The integral equation is solved by iteration, using as input the fluxes, integrated over Doppler velocities, measured in each of the 1526 pixels that have been retained. Integration along the line of sight is made in steps of x of 0.02″ with the

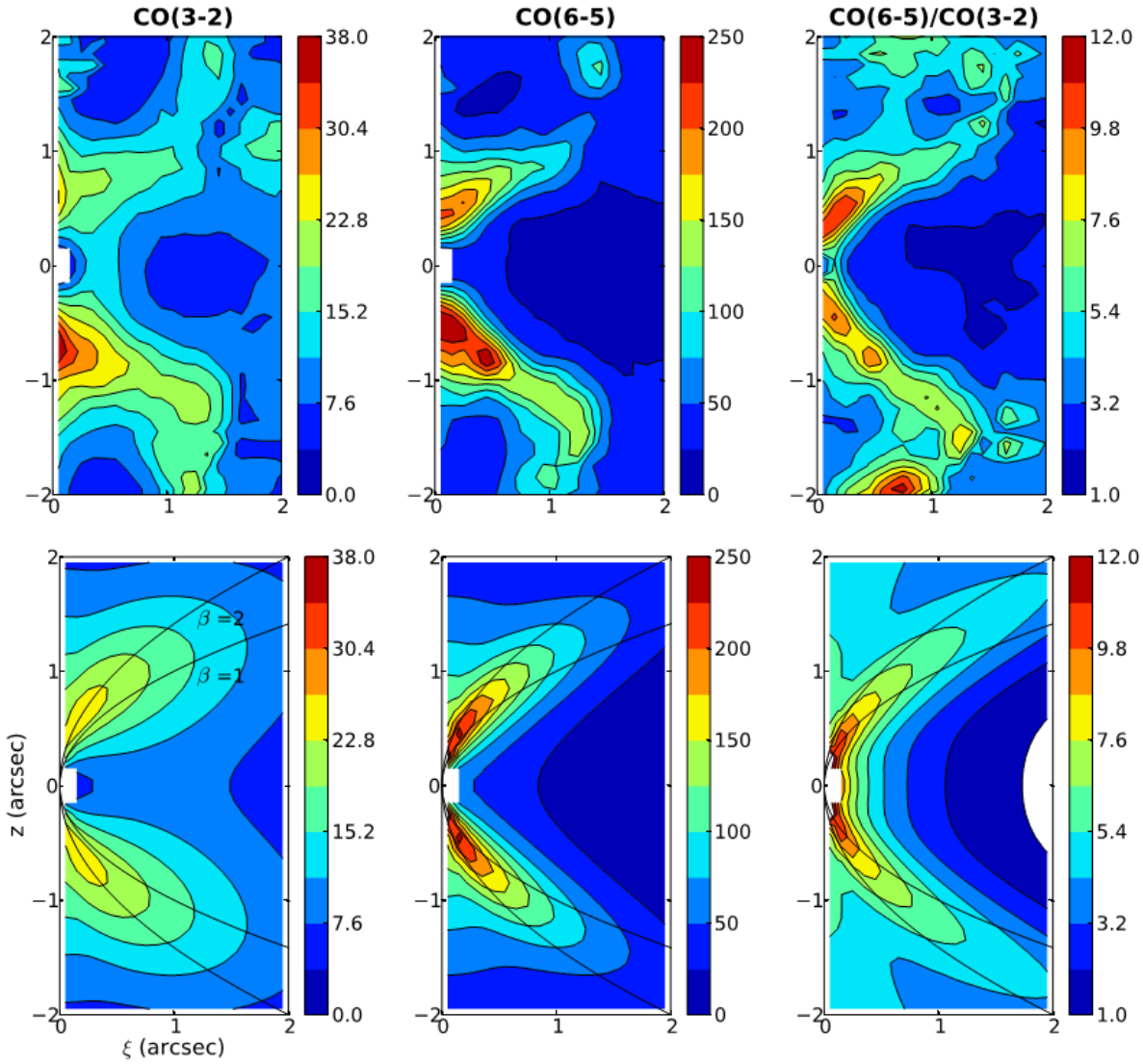

Figure 5.8: Distribution of the effective densities multiplied by r^2 in the (ξ,z) meridian half-plane of the Red Rectangle for CO(3-2) (left panel), CO(6-5) (middle panel) and the ratio CO(6-5)/CO(3-2) (right panel). The upper panels are for the solutions of the integral equation and the lower panels for the model described in the text. Parabolas corresponding to β=1 and β=2 are shown in the lower panels.

space radius r limited to the interval [0.1″, 3.5″]. The effective densities are defined on an array of 35 ξ bins and 50 z bins, each 0.1″ wide covering half a meridian plane of the star. The iterative process is stopped when the value of χ^2 used to measure the quality of the agreement between observations and fluxes obtained by integration of the effective densities along the line of sight reaches a constant value. Various reasonable estimates of the measurement uncertainties have been tried in the definition of χ^2, all giving very similar results. The uncertainties retained here are the quadratic sum of an absolute and a relative contributions, the former being 0.16 Jy arcsec^{-2} for CO(3-2) and 2.2 Jy arcsec^{-2} for CO(6-5) and the latter 20% for each. Ten iterations are amply sufficient to achieve convergence. In order to illustrate the quality of the numerical resolution of the integral equation, we compare in Figure 5.7 the observed flux densities with those obtained by integration of the effective densities along the line of

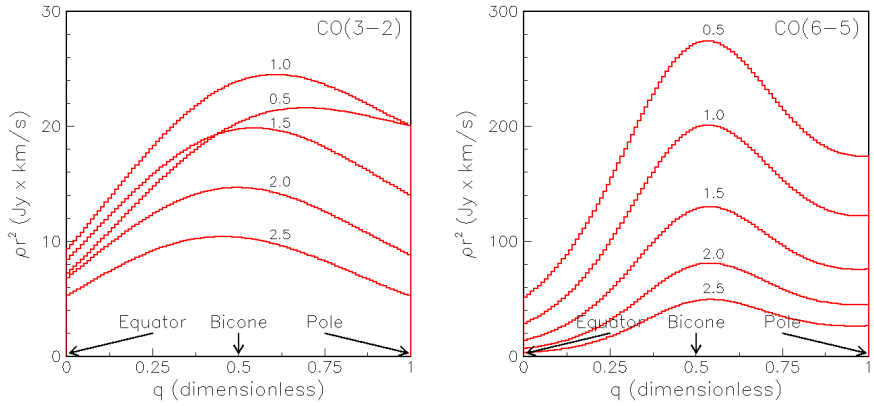

Figure 5.9: Dependence on $q = 1 - \exp(-\beta \ln 2/\beta_0)$ of the parameterized effective densities multiplied by r^2 for r=0.5″, 1.0″, 1.5″, 2.0″ and 2.5″ for CO(3-2) (upper panel) and CO(6-5) (lower panel).

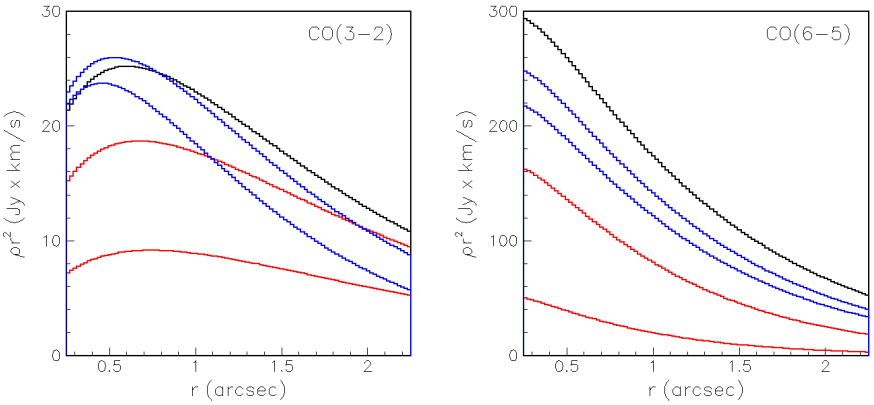

Figure 5.10: Dependence on r of the parameterized effective densities multiplied by r^2 for q values of 0 and 0.25 (equator, red), 0.5 (bicone, black) and 0.75 and 1 (poles, blue) for CO(3-2) (upper panel) and CO(6-5) (lower panel).

sight. To do so in a manageable way, we have grouped the data in 8 bins of R and 8 bins of the position angle measured from the star axis, $\alpha = \tan^{-1}(|y|/|z|)$. Figure 5.8 displays the distribution of the effective densities multiplied by r^2 in the meridian half-plane for CO(3-2), CO(6-5) and their ratio. As the integral equation does not mix different values of z, it consists in fact of 50 independent integral equations, one for each z bin, preventing a reliable evaluation of the effective density at large values of $|z|$, where the signal to noise ratio is low. For this reason, Figure 5.8 restricts $|z|$ and ξ to the [0, 2″] interval.

The observed morphology suggests introducing a parameter β having the dimension of an angular distance, defined as $\beta = z^2/\xi$. Constant values of β define parabolas having their axis in the equatorial plane and their summit at the star position. The region of large CO(6-5) to CO(3-2) ratio visible in the right panel of Figure 5.8 corresponds approximately to $\beta \sim 1$ to 2. At larger distances from the star, parabolic arcs are seen in the form of "wine glasses" (Cohen et al. 2004), with axes along the star axis; they have no relation with the parabolas defined here, which are suited to the description of the

Table 5.1: Best fit parameters to the CO(3-2) and CO(6-5) effective densities multiplied by r^2.

	β_0	n	σ_0	ρ_{eq}	ρ_p	ρ_{bic}	r_{eq}	r_p	r_{bic}
CO(3-2)	1.55	0.605	0.40	0.0655	0.534	0.593	1.21	0.737	0.025
CO(6-5)	1.36	0.215	0.207	0.334	1.26	1.27	0.60	0.84	0.19

gas envelope close to the equatorial torus. Indeed, beyond 2″ or so, the optimal description of the gas morphology has to evolve from an equator-dominated to a bipolar-dominated picture.

The present analysis does not require a parameterization of the effective densities, the following sections will use instead, for each data set, the array of numbers that has been obtained in the (ξ,z) meridian half-plane from the resolution of the integral equation. However, such a parameterization being useful to display the main features, we give a simple description of the effective densities in terms of the product of a function of β by a function of r. As β varies from zero at the equator to infinity at the pole, we use as variable the quantity $q = 1 - \exp(-\beta \ln 2/\beta_0)$, which varies smoothly from zero at the equator to 1 at the pole, taking the value $\frac{1}{2}$ for $\beta = \beta_0$. Similarly, in order to describe the r-dependence, we use as variable the quantity $\psi = (r/r_0)^n \exp(-r/r_0)$, which increases from zero at the origin to reach a maximum $n^n e^{-n}$ at $r = nr_0$ and then decreases exponentially to zero. Both r_0 and ρ are given a dependence on q in the form of a sum of a linear function and a Gaussian centred at 0.5 with a width σ_0. In summary, using the labels *eq* for the equator, *bic* for the bicone and *p* for the poles,

$$\rho = [\rho_{eq} + (\rho_p - \rho_{eq})q + \rho_{bic} g]\psi/r^2 \tag{5.3a}$$

$$q = 1 - \exp(-\beta \ln 2/\beta_0) \tag{5.3b}$$

$$\psi = (r/r_0)^n \exp(-r/r_0) \tag{5.3c}$$

$$r_0 = r_{eq} + (r_p - r_{eq})q + r_{bic} g \tag{5.3d}$$

$$g = \exp[-\frac{1}{2}(q - \frac{1}{2})^2/{\sigma_0}^2] \tag{5.3e}$$

The parameters have been adjusted to minimize the χ^2 describing the quality of the fit in the region (ξ<2″,|z| <2″) to the effective densities obtained above. The best fit values are listed in Table 5.1. We did not seek a parameterization giving a precise description of the effective densities in all details. Our ambition was only to give a description accounting for the main features and their most significant characteristics. Figure 5.8 (lower panels) displays the distribution of the parameterized effective densities multiplied by r^2 in the (ξ,z) meridian half-plane for CO(3-2), CO(6-5) and their ratio, as was done in the upper panels for the effective densities themselves. Figure 5.9 displays the dependence on β of the parameterized effective densities for different values of r and Figure 5.10 that on r for different values of β. They display broad latitudinal enhancements around the bicone, broader for CO(3-2) than for CO(6-5) and a steep decrease with radius. The enhancements are typically three times as wide as the beams and the difference between their appearances in CO(3-2) and CO(6-5) cannot be blamed on the different beam sizes used for the respective observations.

5.5 Temperature and density distributions

The preceding section studied the morphology of the CO envelope of the Red Rectangle without paying particular attention to the absolute values taken by the effective density and the implication on the actual gas density and temperature. We address this issue in the present section.

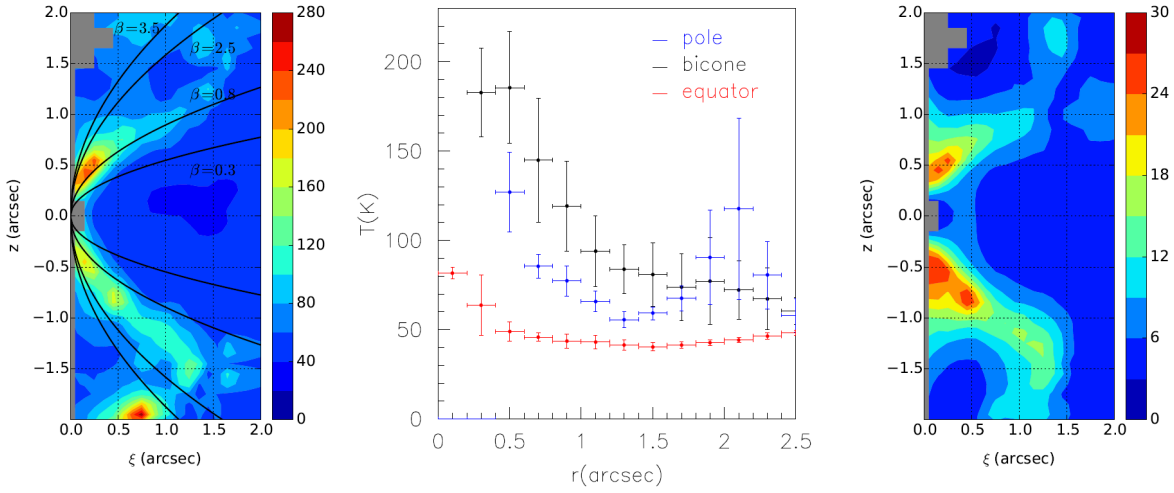

Figure 5.11: Left: Map of temperatures in the half-meridian plane of the star obtained from the effective densities using Relation 4. The parabolas are for β=0.3, 0.8, 2.5 and 3.5 and define the sectors illustrated in the central panel. Middle: r-distribution of the gas temperature averaged over the three angular sectors delineated in the left panel: the red points are for the equatorial region (inside the β = 0.3 parabola), the black points are on the bicone (between the β = 0.8 and β = 2.5 parabolas) and the blue points are for the polar region (outside the β = 3.5 parabola). Error bars show the dispersion within each r bin. Right: CO density (in molecules per cm^3) multiplied by r^2 (in arcsec^2).

In a regime of thermal equilibrium, and in the absence of significant absorption, the effective density is the product of three factors: the actual gas density, which is the same for CO(3-2) and CO(6-5); the population of the emitting rotational states (with angular momenta J=3 and 6 respectively); the emission probability. To a good approximation, the product of the second and third factors depends on temperature T as $\frac{1}{T}\exp(-\frac{E_J}{k_BT})$ with E_J the energy of the emitting state and k_B the Boltzmann constant. Therefore, the ratio R_T of the effective densities obtained in the preceding section for CO(6-5) and CO(3-2) separately obeys the relation $R_T \exp(-\frac{E_3}{k_BT})$=$C\exp(-\frac{E_6}{k_BT})$, with C a known constant depending only on the values of J, 6 and 3 respectively. Hence $\ln(R_T/C)$=$\frac{E_3}{k_BT} - \frac{E_6}{k_BT}$ and

$$k_BT = \frac{E_6 - E_3}{\ln(C/R_T)} \tag{5.4}$$

In principle, Relation 4 provides a mean to evaluate the gas temperature at any point in space once the value of R_T is known. In practice, however, dT/T being proportional to $dR_T/[R_T \ln(R_T/C)]$, namely to TdR_T/R_T, the uncertainty attached to the measurement of T increases as T^2, making higher temperatures increasingly difficult to evaluate. In particular, when R_T approaches C, T diverges, while when R_T approaches 0, T cancels. In the present case, $(E_6 - E_3)/k_B$=82.5 K and C=15.6. The map

Table 5.2: Best fit parameters P of the joint fit to the CO(3-2) and CO(6-5) spectral maps. Also listed are the values of Δ^+ and Δ^- measuring the sensitivity of the value of χ^2 to small deviations of the parameter from its best fit value (see text).

	β_0 ($''$)	V_{rot} (kms^{-1})	k	V_{out} (kms^{-1})	V_{rad} (kms^{-1})	θ ($^\circ$)	σ_p (kms^{-1})	σ_{eq} (kms^{-1})
P	0.81	−0.99	1.03	6.3	1.56	−8	1.4	1.0
Δ^+	0.15	0.15	0.10	0.8	0.26	8	0.7	0.3
Δ^-	0.09	0.14	0.18	0.7	0.26	8	0.5	0.2

of temperatures evaluated in this manner in the meridian half-plane of the Red Rectangle is displayed in Figure 5.11. While the temperature of the equatorial region decreases slowly from ~60 K at r=0.3$''$ to ~50 K at r=2$''$, the temperature of the outflow takes much higher values at short distance to the star, typically 200 K at r=0.3$''$, and decreases steeply with distance to reach some 80 K at r=1.5$''$. In comparison, the dust temperature quoted by Men'shchikov et al. (2002) decreases from ~80 K at r=1$''$ to ~60 K at r=2.5$''$. A hot spot at z~−2$''$ reaches a value of ~270 K.

The CO density, multiplied by r^2, is displayed in the right panel of Figure 5.11. It is in good agreement with a model (Men'shchikov et al. 2002) assuming a dust over gas ratio of 1% and a CO to H ratio of 2 10^{-3}.

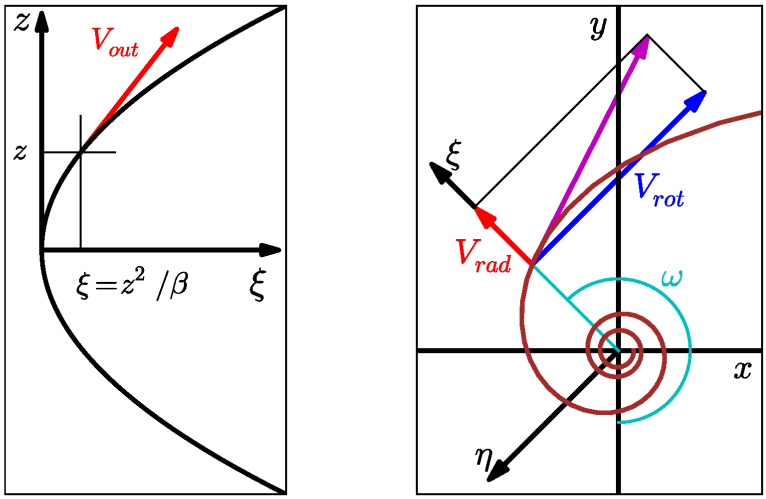

Figure 5.12: Left: In the polar region ($\beta > \beta_0$) the gas velocity V_{out} is confined to meridian planes (ξ,z) and tangent to parabolas of equation $z^2 = \beta\xi$. Right: In the equatorial region ($\beta < \beta_0$) the gas velocity is confined to planes parallel to the equatorial plane and tangent to hyperbolic spirals with a constant radial component V_{rad} and a rotation velocity V_{rot} proportional to r^{-k}.

5.6 Gas velocity

We use Relation (1) $V_x=(x/\xi)V_\xi - (y/\xi)V_\eta + \theta V_z$ to evaluate the gas velocity components V_ξ and V_η, the last term providing an evaluation of the small tilt θ once a value is assumed for V_z. We use the results of the preceding sections to compare the data with a simple model (Figure 5.12) allowing for rotation about the star axis in the equatorial region and for a polar outflow, the parabolic separation between them being defined by a first parameter, β_0, expected to be of the order of 0.8″. In the equatorial region, we adopt as model $V_\eta=V_{rot}r^{-k}$, with $k\sim0.5$ for a Keplerian motion, and allow for a constant radial expansion, normal to the star axis, $V_\xi=V_{rad}$, $V_z=0$. In the polar region, on the contrary, we take $V_\eta=0$ and velocities in the meridian plane tangent to the parabolas associated with constant β values, $V_\xi=2V_{out}z/\sqrt{\beta^2+4z^2}$ and $V_z=V_{out}\beta/\sqrt{\beta^2+4z^2}$. Here, $V_{out}=\sqrt{V_\xi^2+V_z^2}$. Moreover, we allow for a small tilt θ of the star axis with respect to the sky plane, producing a velocity θV_z along the line of sight.

As the gas velocities are the same for CO(3-2) and CO(6-5) emission, we fit both sets of data jointly, each set being given the effective densities obtained in the preceding section. The six model parameters are adjusted by minimizing the value of χ^2 that measures the quality of the fit to the velocity spectra associated with each pixel of each of the two data sets. We require R to be in the interval [0.2″, 2.5″] and r in the interval [0.2″, 3.5″]. We find that the fits are significantly improved when allowing for some Gaussian smearing of the velocity distributions, the best values of their σ's being σ_p=1.4 kms^{-1} in the polar region and σ_{eq}=1.0 kms^{-1} in the equatorial region. Such large values are likely to account for imperfections of the model rather than for a physical dispersion of the space velocities. Setting them to zero deteriorates the quality of the fit but does not alter the values taken by the other parameters. The best fit values of the adjusted model parameters are listed in Table 2 together with quantities Δ^+ and Δ^- measuring the sensitivity of the value of χ^2 to small deviations of the model parameters from their best fit values. They are defined such that when a parameter having best fit value P varies in the interval [$P-\Delta^-$,$P+\Delta^+$], χ^2 does not exceed its minimal value by more than 5%. The quality of the fit is surprisingly good in view of the crudeness of the model. It is illustrated in Figure 5.13 for CO(3-2) and CO(6-5) separately. While each of the 1526 velocity spectra associated to the pixels that have been retained contributes separately to the value of χ^2, they have been grouped for convenience into only 36 spectra in Figure 5.13, each group covering a square of 7×7=49 pixels.

Allowing for additional parameters trivially improves the quality of the fit, but we have been unable to think of a simple specific addition that would do so very significantly. In particular, allowing for a transition region between the polar outflow and the equatorial rotating torus does not bring much improvement, the data being satisfied with a sharp transition. Similarly when allowing for variations of the parameters V_{rot}, V_{out} and V_{rad} across the regions where they operate. It is difficult to give precise evaluations of the uncertainties attached to the parameters: the quality of the data, the validity of the approximations made and the crudeness of the model prevent doing it reliably. However, a few general results can be safely stated:

1) Two regions, equatorial and polar, coexist, hosting very different velocity fields. To a good approximation, they are separated in the meridian half-plane by a parabola of equation z^2/ξ=0.81″.

2) The evidence for rotation of the equatorial torus, with velocity of ∼1 kms^{-1} at r =1″, is over-

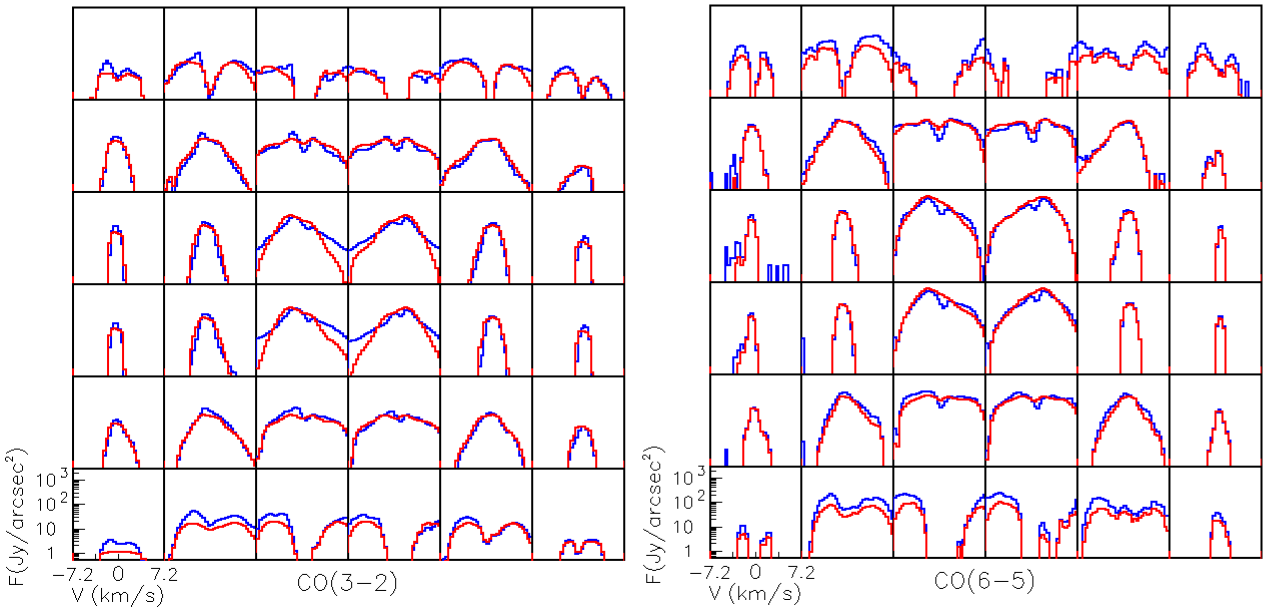

Figure 5.13: CO(3-2) (left) and CO(6-5) (right) velocity spectra for data (blue) and model (red) averaged over groups of 49 pixels, each group covering 0.7″×0.7″, the whole map covering 4.2″ ×4.2″.

whelming and its r-dependence requires a power index k of order unity. Both density and rotation velocity are homogeneously distributed across the torus rather than on a thin disk. The need for radial expansion, at the level of ∼1.6 kms^{-1}, arises from the clear separation between positive and negative velocities at small values of y. Lacking such a component implies the presence of a peak at very low velocities.

3) The evidence for a polar outflow is equally overwhelming. The choice made here of a parabolic flow in the meridian plane cannot be claimed to be unique. However, it gives significantly better results than a radial outflow, in addition to being more sensible from a pure hydrodynamic point of view once a parabolic separation is adopted between torus and polar outflow. Moreover, it implies an r-dependence of the Doppler velocity that fits well the data, making the introduction of a velocity gradient unnecessary.

4) With respect to the sky plane, the star axis is inclined by ∼8° from the North toward the Earth.

5.7 Asymmetries

In the preceding sections, it was usually assumed that the gas effective density was invariant by rotation about the star axis and even, in several occasions, by symmetry with respect to the star equatorial plane. It was already remarked that these were crude approximations from which important deviations were present at large distances from the star. We map these in Figure 5.14 as deviations from $< F(y,z) >= \frac{1}{4}[F(y,z)+F(-y,z)+F(y,-z)+F(-y,-z)]$. More precisely, the quantity displayed is $[F(y,z) - < F(y,z) >]R$ where the factor R gives a better balance between deviations at short distances and large distances from the star. Indeed, it would be the proper factor to be used if the effective densities would decrease with R as R^{-2} and if the uncertainties were purely statistical. The main feature is an important south-east excess, particularly enhanced in the region of the bicone where it reaches ∼70%. This observation addresses

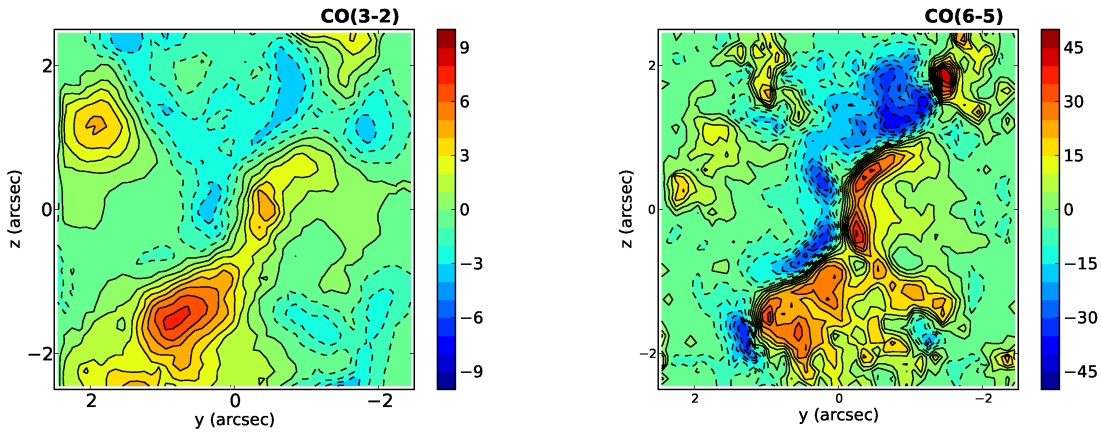

Figure 5.14: Sky maps of the deviation from full symmetry (see text) multiplied by R of the measured fluxes for CO(3-2) (left panel) and CO(6-5) (right panel). Units are Jy km s^{-1} arcsec^{-2}. The south-eastern excess reaches ∼70% of the symmetric value at maximum.

several questions: how reliable is it? which effect does it have on the results of the preceding sections? and which physics interpretation does it suggest?

The presence of an excess on the eastern limb of the bicone, larger in the southern than in the northern region, can be safely asserted. We have checked its robustness by varying the parameters used in reducing the data, such as centring the sky maps or adjusting the baselines. Moreover, its presence in both the CO(3-2) and CO(6-5) data makes it unlikely that it could be blamed on imperfections of the calibration and/or imaging. However, to take seriously the finer details visible at large distances from the star, such as the fluctuations observed in the north-western part of the CO(6-5) map, would require reprocessing the images as done by Bujarrabal et al. (2013b).

The effect of such an excess −and other deviations from symmetry− on the results of the preceding sections is simply to deteriorate the quality of the fits that have been performed but not to alter the results which have been stated in the approximation of rotation symmetry and/or north-south symmetry. As the magnitude of the excess is commensurate with that of the symmetric model, its contribution to χ^2 is important and prevents attempting more detailed modelling than presented in the preceding sections without first accounting for the observed asymmetries.

We are unable to state whether the observed excess is the result of temperature or of actual gas density, or both. A detailed study of its properties would probably allow for a reliable physics interpretation and provide very valuable information toward a better understanding of the Red Rectangle.

5.8 Continuum and dust

The space resolution and the sensitivity of the interferometer for the observation of the continuum are not sufficient to allow for a detailed study of the dust morphology. The projections of the flux density distributions on the y and z axes, displayed in Figure 5.3, are well described by Gaussians having the following σ values: at 345 GHz, σ_y=0.26″ and σ_z=0.23″ and at 690 GHz, σ_y=0.22″ and σ_z=0.13″. The

ratio σ_z/σ_y takes values of 0.88 and 0.60 at 345 GHz and 690 GHz respectively, revealing an elongation of the dust along the y axis, at variance with the distribution of the line, which reveals an elongation of the gas along the z axis. This is consistent with dust being concentrated in the equatorial region. The values of σ_y and σ_z are dominated by the beam size, twice as large at 345 GHz as at 690 GHz, consistent with a source concentrated at short distance to the star (Men'shchikov et al. 2002). The integrated fluxes are 0.66±0.10 Jy at 345 GHz and 4.0±0.6 Jy at 690 GHz, with a 690 GHz to 345 GHz ratio of 6.0 compared with a ratio of ∼5 corresponding to the measured SED (see Men'shchikov et al. 2002).

5.9 Discussion

Bujarrabal et al. (2005) have presented a detailed model of the morphology and kinematics of the Red Rectangle based on CO(1-0) and CO(2-1) data obtained from Plateau de Bure Interferometer and on the study of a number of evolved stars, in particular of the associated line profiles. Our approach is different in the sense that we have not presented any model but tried to describe as simply and exactly as possible CO(6-5) and CO(3-2) emission observations from ALMA. These ALMA data have been also considered by Bujarrabal et al. (2013b) in a letter to A&A where they present channel maps but postpone a detailed analysis to a later publication, which has not yet appeared. It is therefore interesting to compare the ALMA data, as presented in our analysis, with the predictions of the model elaborated by Bujarrabal et al. (2005). In general, the main features of the model are qualitatively verified by the ALMA data: presence of a conical bipolar outflow and of an equatorial rotating gas volume, with expansion and rotation velocities of the correct magnitude. Much of the results presented in our analysis rest on the assumption of rotational invariance about the star axis, which cannot be verified by the data and is also an assumption inherent to the model. Part of the results of our analysis, those concerning temperature and density, are obtained under the hypothesis of local thermal equilibrium, which cannot be strictly valid in the case of the Red Rectangle: however, as stated in our text, this is a useful hypothesis to obtain a zero order approximation of the underlying physics; in particular, the ratio of the flux densities measured on the two lines reveals a close relation with the biconical morphology, which is interesting in itself.

Bujarrabal et al. (2005) found a rotating disk about an axis of symmetry having an inclination angle of 5° with respect to the plane of the sky and a position angle of 11° from north. Their values are close to ours, 8° and 13° respectively. On the other hand, they assume a thin disk (∼1.4″) with an inner region (R <∼0.8″) in purely Keplerian rotation and an outer region (R >∼0.8″) mixing rotation and expansion. At 0.8″, the rotation and expansion velocities are 1.65 km s^{-1} and 1.6 km s^{-1} respectively followed by a decrease in $1/r$ for the rotation. In our analysis, we found a clear evidence for rotation of the equatorial torus. The velocity are found ∼1 km s^{-1} at 1″ and decreasing in $1/r$ for the rotation and at the level of 1.6 km s^{-1} for the expansion. Moreover, the polar region is well described by parabolic meridian trajectories joining smoothly between the torus and the star axis with a constant wind velocity of the order of 6 to 7 km s^{-1}.

In our approach, under the assumption of local thermal equilibrium, the excitation temperature is measured from the flux ratio of CO(6-5) and CO(3-2) and found higher in the polar direction than in the equatorial plane. It decreases with the distance to the star centre from ∼200 K at 0.3″ to ∼80 K at 1.5″ in

the polar region and from ∼60 K at 0.3″ to ∼50 K at 2″ in the equatorial region. Though these absolute values will change when taking into account the effect of non-LTE and absorption, which we plan to study in detail, they are qualitatively not far from reality. Bujarrabal et al. (2005) assume an isotropic temperature and find that it decreases with distance as $1/r^{0.7}$ and has a value of ∼140 K at 0.3″ and ∼40 K at 2″.

Men'shchikov et al. (2002) made a detailed study of the Red Rectangle using high spacial resolution data obtained in the infrared range. They cannot constrain the kinematic but they find a morphology similar to that inferred in our work.

5.10 Summary and conclusions

ALMA observations of the CO emission of the Red Rectangle, of an unprecedented quality, have been analysed with the aim to reveal the main features of the morphology and kinematics of the gas envelope. The analysis was performed in a spirit of simplicity, with limited ambitions in terms of precision and sensitivity: it used the image processing provided by the ALMA staff while the reprocessing performed by Bujarrabal et al. (2013b) should allow for the exploration of finer details than was possible in the present work.

The effective density, combining actual density and temperature, was reconstructed in space under the hypothesis of rotation symmetry about the star axis and assuming that absorption is negligible. Both are very crude approximations that limit the scope of the study. In principle, ^{13}CO observations available in the ALMA data set should shed light on the validity of the optically thin approximation; however, the weakness of the line would require reprocessing the image in order to obtain reliable results. The effective density was observed to decrease with distance faster than r^{-2}, requiring an additional exponential factor with characteristic length at the arcsecond level, and to vary smoothly as a function of star latitude, reaching a maximum at latitudes between 45° and 60° typically. Comparison between the CO(3-2) and CO(6-5) effective densities provides an evaluation of the gas temperature, observed to decrease slowly with distance in the equatorial region, from ∼60 K at 0.3″ to ∼50 K at 2″. In the polar region, the temperature takes much higher values at short distance to the star, typically 200 K at 0.3″, and decreases steeply with distance to reach some 80 K at 1.5″. A crude model of the calculated effective densities has been presented.

The study of the gas kinematics has revealed a sharp separation between the equatorial and polar regions. To a good approximation, the former is a parabolic torus in rotation about the star axis and expansion outward from it. The rotation velocity is of the order of 1 kms^{-1} at a distance of 1″ and decreases with distance with a power index of order unity. The expansion velocity is constant across the torus, at ∼1.6 kms^{-1}. The polar regions host outflows that are well described by parabolic meridian trajectories joining smoothly between the torus and the star axis with a constant wind velocity of the order of 6 to 7 kms^{-1}. A very simple model has been proposed, giving quite a good description of the measured Doppler velocities.

The position angle of the star axis is ∼13° east from north and its inclination angle with respect to the sky plane is ∼8°, both in good agreement with values obtained by studies made of visible and infrared

observations.

Important deviations from a fully symmetric model have been revealed: an excess of the effective density has been observed in both CO(3-2) and CO(6-5) data on the eastern limb of the bicone, particularly strong in the south-east direction. No obvious physics interpretation could be given. The continuum observations are consistent with a compact dust source elongated along the equator and with the SED values available in the literature.

Existing models of the Red Rectangle, such as proposed by Koning et al. (2011) or Men'shchikov et al. (2002), are essentially based on the dust properties and leave much freedom for the gas morphology and kinematics. Yet, the observations presented here are in qualitative agreement with the general picture proposed by Men'shchikov et al. (2002).

The observations analysed in the present work were done in an early phase of ALMA operation, with only 21 to 24 active antennas in a configuration that extended up to only 380 m. New observations using the complete array and a broader bandwidth would obviously very much improve the quality of the data and their significance for the understanding of the morphology and kinematics of the gas surrounding the Red Rectangle.

Chapter 6

CO EMISSION OF OTHER STARS

6.1 X Her and RX Boo

X Her is a semi-regular variable (SRb) with a period of 95.0 days (General Catalogue of Variable Stars). Light variations are small (~ 0±0.5 mag in the visible) and irregular. It has a variable spectral type, from M6 to M8. The stellar effective temperature is ~3200 K (Dumm & Schild 1998; Dyck et al. 1996). According to Glassgold & Huggins (1983), atomic hydrogen should be the dominant species in the stellar atmosphere. The distance to the Sun is 137 pc (van Leeuwen 2007) and the luminosity is around 4800 $L_{\odot}$.

RX Boo is an oxygen-rich M-type semi-regular variable (SRb) with a period of 162 days. Its magnitude varies between 8.6 and 11.3 and its spectral class between M6.5 and M8. The effective temperature is 3010 K, the luminosity 8912 $L_{\odot}$ (De Beck et al. 2010) and the distance to the Sun d=191 pc (van Leeuwen 2007).

X Her and RX Boo have been claimed to have bipolar structures (Kahane & Jura 1996; Castro-Carrizo et al. 2010). Like EP Aqr, X Her and RX Boo are AGB stars at the beginning of the thermal pulsing phase (no dredge up) with no presence of technetium in their spectra (Lebzelter & Hron 2003). Their properties are compared in Table 6.1 with those of EP Aqr. All three sources were observed by Knapp et al. (1998) using the 10.4 m telescope of the Caltech Sub-millimetre Observatory (Hawaii) in 1996-1997. The observations were made in CO(2-1) and CO(3-2) for EP Aqr and X Her and in CO(3-2) for RX Boo. The integrated profiles of EP Aqr and X Her in both lines present two components of different widths (10.8 and 1.4 km s^{-1} for EP Aqr and 8.7 and 3.3 km s^{-1} for X Her in average) centred at approximately the same velocity.

X Her was first claimed to display an axi-symmetric circumstellar shell by Kahane & Jura (1996). From spatially resolved CO(2-1) line profiles obtained using the IRAM 30-m telescope, they identified a bipolar flow inclined with respect to the line of sight (making an angle AI of ~60° with the sky plane and having a projection on the sky plane making an angle PA of ~45° to the north). A composite profile has also been observed in SiO (2-1) thermal emission (González et al. 2003).

Recently, Castro-Carrizo et al. (2010) observed X Her in February and March 2005 using both the

Table 6.1: The properties of stars: EP Aqr, X Her and RX Boo

	EP Aqr	X Her	RX Boo	
Distance (pc)	114	137	191	Hipparcos (vL2007)
Spectral type	M8III	M6e	M6.5e-M8IIIe	GCVS
Period (day)	55.0	95.0	162.3	GCVS
V_* (km s^{-1})	−33.0	−73.0[a]	1.5	K1998
V_{exp} (km s^{-1})	10.8	8.7[a]	9.6	K1998 (broad)
	1.4	3.3[a]	–	K1998 (narrow)
$\dot{M}$ (10^{-7} M$_\odot$ yr^{-1}) corrected for distance	1.6	1.1	4.5	K1998 (broad)
	0.12	0.34	–	K1998 (narrow)

[a]: average, K1998: Knapp et al. (1998), vL2007: van Leeuwen (2007)
GCVS: General Catalogue of Variable Stars (version 2013-04-30)

PdB interferometer and the IRAM 30 m single dish. In Figure 10 of their paper, they show a position-velocity diagram of X Her similar to that obtained on RS Cnc by Libert et al. (2010b).

RX Boo shows only one component in the CO(3-2) profile obtained by Knapp et al. (1998). Nevertheless, we also selected this source because Castro-Carrizo et al. (2010) claim evidence for an axi-symmetric structure with PA∼50° and AI∼ −30° in its circumstellar envelope. They show a position-velocity diagram where the highest velocity does not occur along the symmetry axis as expected for the spherical case (their Figure 8).

In this chapter, the CO model developed in the preceding chapters for RS Cnc and EP Aqr is used to study the morphologies and kinematic features of two sources X Her and RX Boo. The data were obtained in the COSAS project and have been presented in Castro-Carrizo et al. (2010).

6.2 Results

We use the standard model developed for RS Cnc and EP Aqr, accounting for the field of view by multiplying the calculated flux at position (y, z) on the sky plane with a factor $f_{beam} = \exp(-\frac{y^2+z^2}{2\sigma^2_{beam}})$ where σ_{beam} is the RMS width of the primary beam (σ_{beam} ≈FWHM/2.35). The same He abundance of 1/9 (meaning that hydrogen accounts for $^9/_{13}$ ∼70% of the total mass) as in RS Cnc is used for these stars. As they are in an earlier phase of their evolution than RS Cnc (S-type), the CO abundance is taken to be 2.5 10^{-4} (Knapp et al. 1998, for oxygen-rich stars) instead of 4×10^{-4}. The photo-dissociation of CO molecules follows the results of Mamon et al. (1988) for spherical stars.

6.2.1 X Her

The observations of X Her used in the present analysis were obtained in the COSAS project and have been presented in Castro-Carrizo et al. (2010). They consist in two images in CO(1-0) and CO(2-1) lines

with a spectral resolution of 2km s^{-1}. The synthesized beams are 1.99″×1.56″ with a position angle PA = 68° for CO(1-0) and 1.11″×0.875″ with PA = 49° for CO(2-1). We extracted from the observed data two sets of 15×15 velocity spectra, one for each line, covering 30″×30″ with a spacing of 2″. The rms noise in the resulting maps is 9.6 mJy/beam and 16 mJy/beam in 2 km s^{-1} spectral channels at 2.6 mm and at 1.3 mm respectively.

The CO(1-0) and CO(2-1) emissions as a function of the angular distance (R_{yz}) are shown in Figure 6.1 together with results of an attempt to fit the standard model to the observed data. However, the simple model does not succeed to simultaneously reproduce the radial distributions of <CO(1-0)> and <CO(2-1)>. As recovering short-spacings was difficult in some channels of the CO(2-1) map (Castro-Carrizo et al. 2010), we restrict the analysis to the CO(1-0) data.

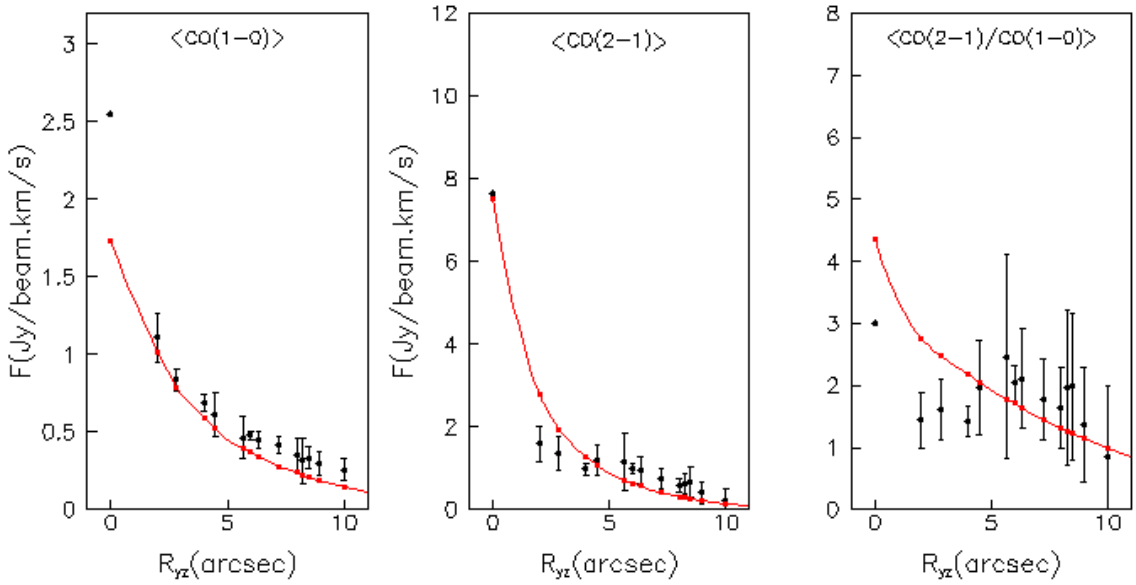

Figure 6.1: Angular distance distributions from the star centre of <CO(1-0)>, <CO(2-1)> and $<\frac{\text{CO(2-1)}}{\text{CO(1-0)}}>$ as observed (black) and obtained from the model (red).

The parameters of the model have been adjusted to obtain the best fit to the 81 CO(1-0) spectra (covering 18″×18″). The best-fit values of the parameters are given in Table 6.2. The dependence over star latitude of the wind velocity, density and flux of matter as well as the r-dependence of the wind velocity are displayed in Figure 6.2. The best-fit model and observations are compared in Figure 6.3. We obtain reasonable agreement in the central part of the map. However the model produces too low profiles in the outer part, particularly in the direction perpendicular to the symmetry axis (South East-North West).

We have modified the standard model in a simple way to account for a possible disk-like structure suspected in the central channel of the CO(1-0) map (Figure 9 of Castro-Carrizo et al. (2010)). The flux of matter and wind velocity parameterization are modified as $f_{\dot{M}}(\gamma) = f_{\dot{M}_1}F(\gamma) + f_{\dot{M}_2}[1 - F(\gamma)]$ and $V(\gamma, r) = V_1F(\gamma)[1 - \lambda_1 \exp(-\frac{r}{2.5''})] + V_2[1 - F(\gamma)][1 - \lambda_2 \exp(-\frac{r}{2.5''})]$, where the function $F(\gamma)$ uses Gaussian profiles centred at the poles (i.e. we replaced the spherical component by an oblate component). The best-fit results of the modified model to the data are given in Table 6.2 and displayed in

Figures 6.2 and 6.3. It only slightly improves a few central spectra. We have made several attempts, including different forms of the function $F(\gamma)$ to describe a disk-like structure, of the radial distribution temperature, and also a possible asymmetry in the axis direction, but none of them improves the quality of the fit significantly (the decrease of χ^2 never exceeds 3%). We need observations with higher spatial and spectral resolutions to better constrain the parameters of the model.

Table 6.2: Best fit values of the parameters of the standard model and the modified model.

Parameter	X Her Best fit value standard model	X Her Best fit value modified model
AI (°)	−40	−40
PA (°)	56	56
σ	0.40	0.41
V_1 (km s^{-1})	5.89	8.37
V_2 (km s^{-1})	2.63	3.19
λ_1	0	0.03
λ_2	1.0	1.0
$f_{\dot{M}_1}$ (10^{-8} M$_\odot$ yr^{-1}sr^{-1})	1.72	2.26
$f_{\dot{M}_2}$ (10^{-8} M$_\odot$ yr^{-1}sr^{-1})	0.20	0.35
T (1″) (K)	115	141
α	1.07	0.87

6.2.2 RX Boo

The data are from the observations of Castro-Carrizo et al. (2010) in June and November 2004. They include OTF observation with the 30m telescope and the PdBI array in its most compact configuration. The data were merged and reduced with a 2 km s^{-1} spectral resolution. The restoring beam of CO(1-0) is 3.43″×2.63″ with PA=41° and of CO(2-1) is 1.47″×1.03″ with PA=24°. The noise levels are 16 mJy/beam for CO(1-0) and 29 mJy/beam for CO(2-1). The primary beam attenuation is quite high in particular in CO(2-1) (Castro-Carrizo et al. 2010, Figure 27) and is not corrected in the data. This effect is included in the model.

We extracted 7×7 spectral maps with a grid spacing of 2″ for both CO(1-0) and CO(2-1), meaning a size of 14″×14″. Each spectrum has 30 velocity bins with a size of 2km s^{-1}. The $r_{1/2}$, the distance at which 50% of CO molecules are dissociated, is 16″ (4.5 10^{16} cm) corresponding to the value of Mamon et al. (1988) for V=7.5km s^{-1} and $\dot{M} \sim 4-5\ 10^{-7}$ M$_\odot$ yr^{-1}. We adopt an uncertainty of 31 mJy/beam for both CO(1-0) and CO(2-1).

We started with a spherical model. The best fit results for CO(1-0) and CO(2-1) separately are listed in the second and third columns of Table 6.3, where V is the expansion velocity of the wind, $\dot{M}$

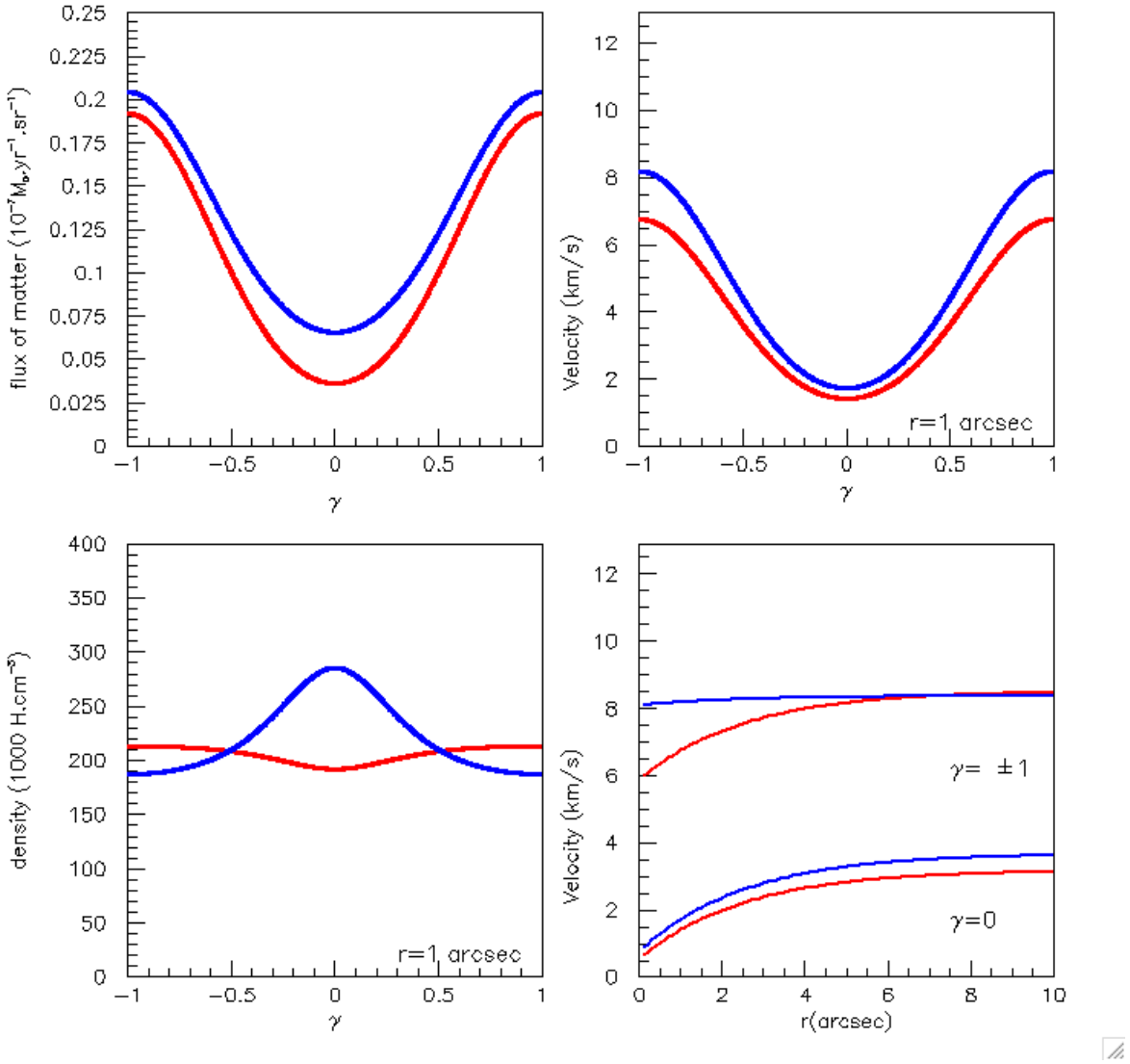

Figure 6.2: X Her. Dependence on the sine of the star latitude, γ, of the flux of matter (up-left), of the wind velocity at $r = 1''$ (up-right) and of the gas density at $r = 1''$ (down-left). Down-right: r-dependence of the equatorial (lower curves) and polar (upper curves) velocities. The results of the standard model are in red and its modified model in blue.

is the mass loss rate (over 4π steradians), the density being $n(r) = \frac{\dot{M}}{4\pi V r^2}$. Spectral maps obtained from the best fit are compared with observations in Figure 6.4. The velocity of the wind is ~7.7 km s^{-1}, the temperature is $\sim 245 r^{-1.07}$ (K) and not too different (<15%) between CO(1-0) and CO(2-1) but the mass-loss rates are completely different, twice smaller in CO(1-0) than in CO(2-1). The velocity gradient is insignificant and is ignored.

The results of a simultaneous fit to CO(1-0) and CO(2-1) observations are listed in the fourth column of Table 6.3. The radial dependence of temperature is steepened in order to compromise between the mass-loss rates obtained in the separated fits. However this is not enough to obtain a good fit. Figure 6.5 displays the dependence of the integrated flux of CO(1-0) and CO(2-1) and their ratio on the distance to the central star. The results of the separated fits (red) match very well the data while the results of the

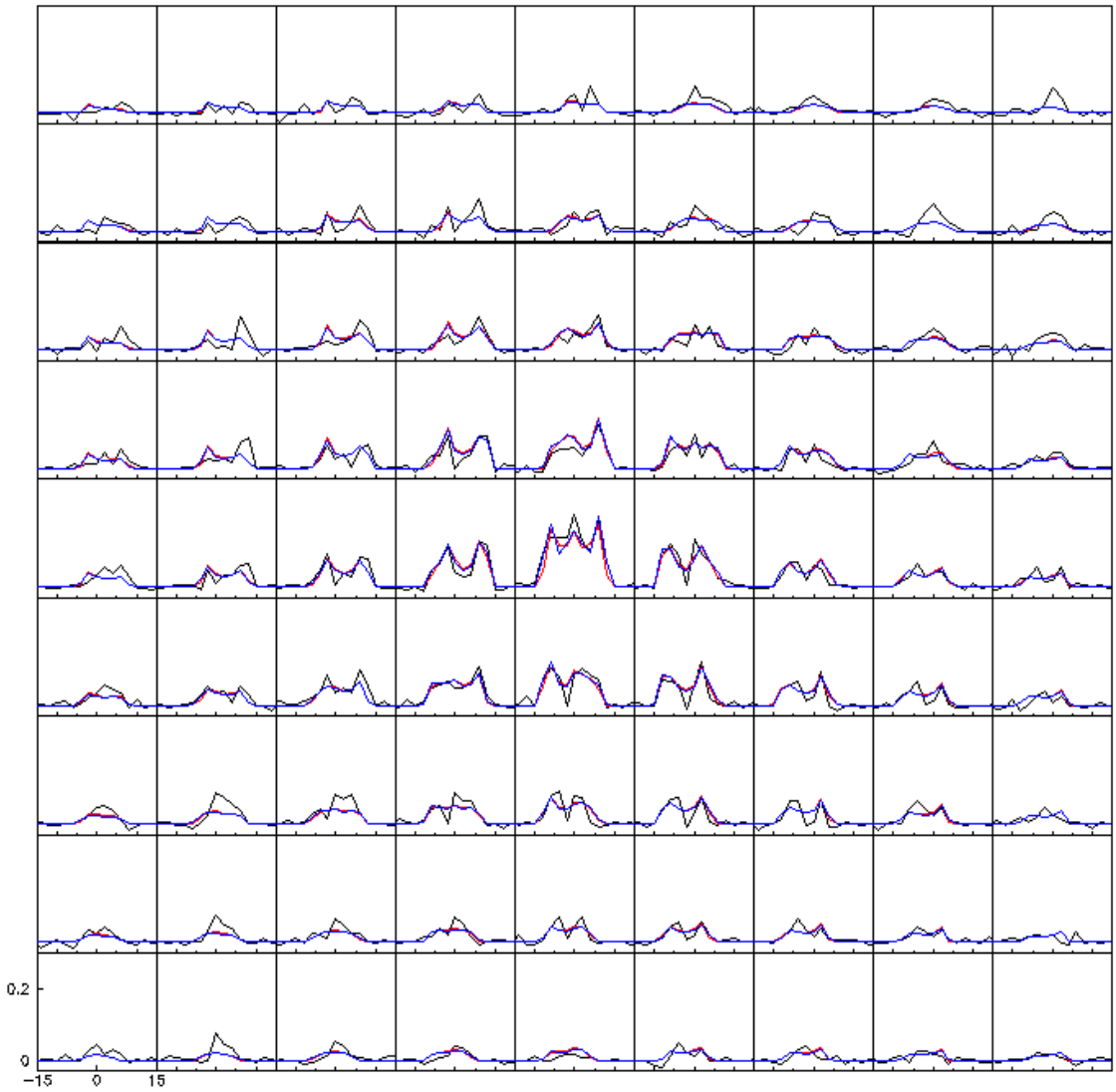

Figure 6.3: X Her. Spectral map centred on the star of the CO(1-0) observations (black), the best-fit standard model (red) and the modified model (blue). Steps in right ascension and declination are 2″.

Table 6.3: Best fit values of spherical model for RX Boo

	CO(1-0)	CO(2-1)	CO(1-0)& CO(2-1)
V (km s^{-1})	7.9	7.5	7.9
$\dot{M}$ (10^{-7} M$_\odot$ yr^{-1})	6.6	2.9	3.7
$T(1'')$ (K)	281	209	241
α	1.13	1.01	1.44
χ^2 (d.o.f^{-1})	0.96	1.24	1.53

combined fit (blue) do not. The ratio of CO(2-1) to CO(1-0) fluxes is too low to be reproduced by the model.

The residuals (data−model) show a bipolar structure in CO(1-0). Figure 6.6 displays their maps

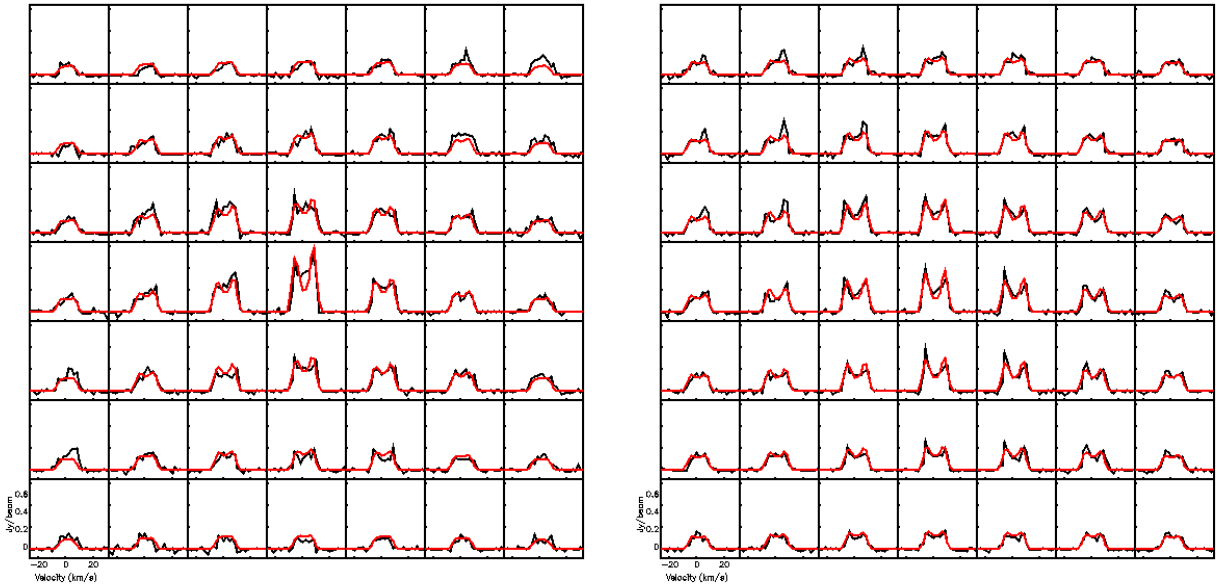

Figure 6.4: RX Boo. Spectral maps for CO(1-0) (left) and CO(2-1) (right) observations of RX Boo as observed (black) and described by the model (red).

over red-shifted velocities (from 6 to 8 km s^{-1}) (left) and over blue-shifted velocities (from −6 to −4 km s^{-1}) (right). The spherical model is missing a red-shifted flux in the north-east direction and a blue-shifted flux in the south-west direction. However, such structure is not visible in CO(2-1).

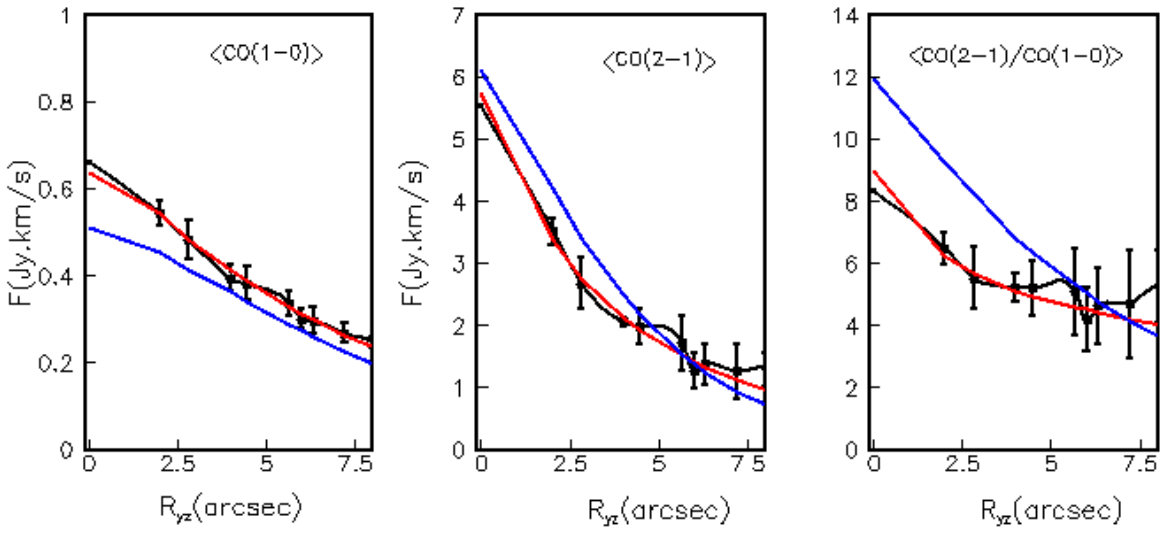

Figure 6.5: RX Boo. Dependence on R_{yz} of the averaged integrated fluxes in CO(1-0) (left), CO(2-1) (middle) and their ratio (right). The data are shown in black, the model predictions in red for the separated fits and in blue for the combined fit.

Including a bipolar outflow into the model for CO(1-0), the quality of the fit improves by ∼10%. The best fit parameters are shown in Table 6.4. The axis orientation is defined by AI=−13° and PA= 54°. The bipolar outflows are very narrow and dense (1.5 times denser than that at the equator). The aperture

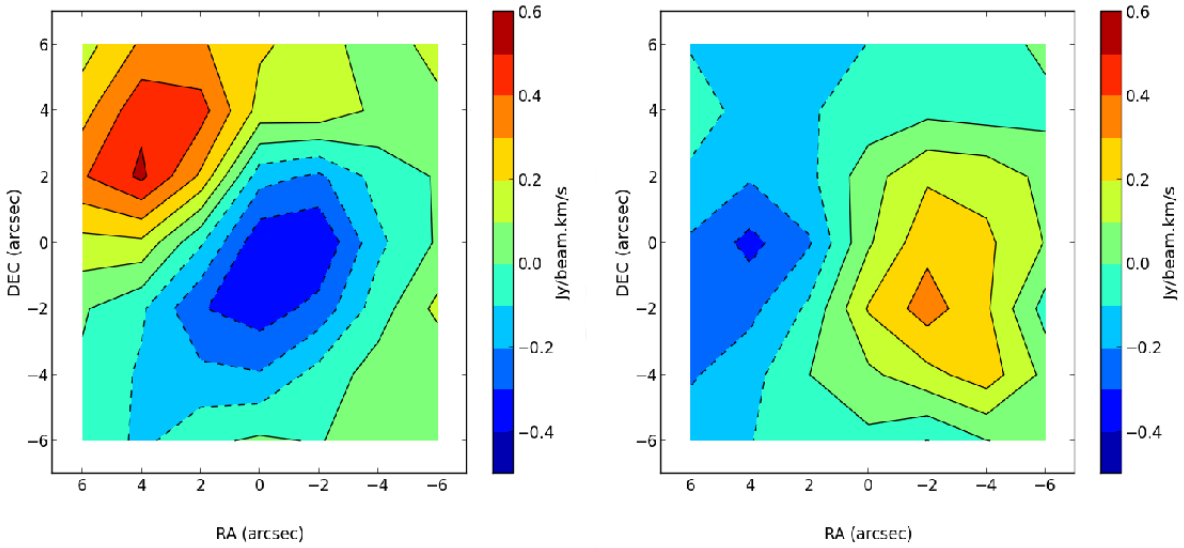

Figure 6.6: RX Boo. Integrated missing flux of the spherical model over the red-shifted velocity range (6 to 8 km s^{-1}) (left) and over the blue-shifted velocity range (−6 to −4 km s^{-1}) (right).

(rms width) of the polar cones is ∼24°. The velocities in the polar direction are 20% higher than that at the equator. The dependence on the sine of the latitude of the wind velocity, flux of matter and density obtained from the best fit in CO(1-0) with bipolar structure are shown in Figure 6.7.

Table 6.4: Best fit results to the CO(1-0) emission of RX Boo with a bipolar outflow.

	CO(1-0)
AI (°)	−13
PA (°)	54
σ	0.09
V_1 (km s^{-1})	2.1
V_2 (km s^{-1})	8.0
λ_1	0
λ_2	1.0
$f_{\dot{M}_1}$ (10^{-8} M$_\odot$ yr^{-1}sr^{-1})	5.4
$f_{\dot{M}_2}$ (10^{-8} M$_\odot$ yr^{-1}sr^{-1})	5.1
T (1″) (K)	282
α	1.13
χ^2 (d.o.f^{-1})	0.88

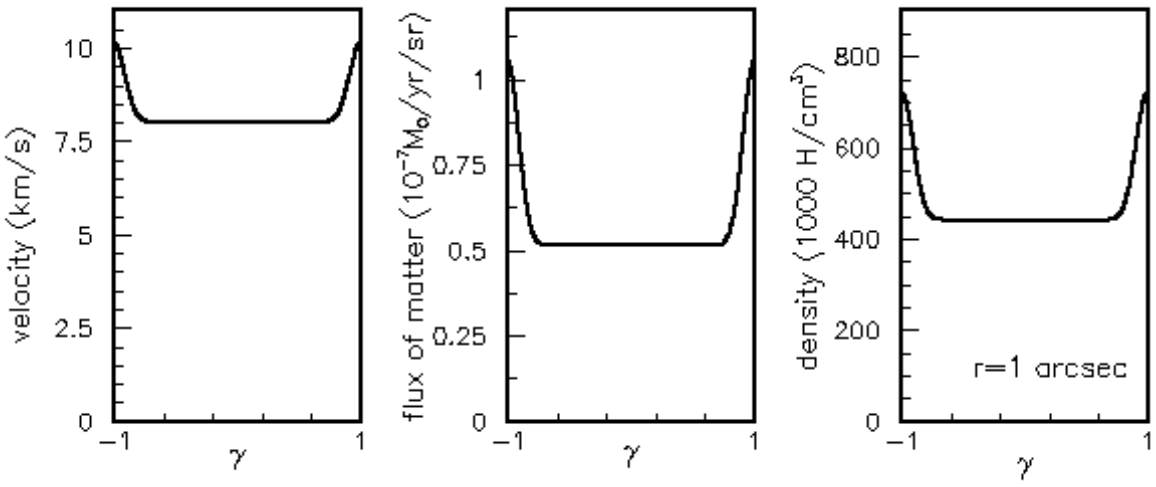

Figure 6.7: The best fit parameters of CO(1-0) with bipolar structure.

6.3 Summing up

In the present and previous chapters, we attempted to describe the morphology and kinematics of the gas envelopes surrounding AGB stars at different stages of their evolution. The aim has been to reconstruct the spatial distribution of their density, temperature and velocity from the observed spectral maps. In general, this is not possible without making additional hypotheses. Of these, the most important is the hypothesis of rotation invariance about an axis. We have always assumed its validity, the justification for it being its relative success in describing the data, even if we have been able to show its limitations by giving evidence for occasional but important deviations. In all cases that have been studied, the importance of absorption has been found sufficiently small to be able to take advantage of this spatial symmetry from the study of the measured fluxes, namely after integration over the line of sight, crossing regions where the absorption has different effects.

Two stars, the Red Rectangle and EP Aqr, have peculiar orientations that have been found to ease the analysis significantly: the former has its axis nearly parallel to the sky plane and the latter nearly perpendicular. In the case of the Red Rectangle, we have been able to reconstruct the effective density in the meridian plane of the star with no need for additional hypotheses; in the case of EP Aqr, this could be done only by assuming a model for the wind velocities. In both cases, the power and the limitations of the method were clearly illustrated.

While the quality of the data in terms of spectral resolution was usually sufficient, the need for as good as possible spatial resolution and high sensitivity was overwhelming. In this sense, ALMA opens a new era in terms of the reliability and precision being now at hand. It marks the transition from a phase where most of the analyses were largely qualitative, based on the inspection of channel maps and position-velocity (P-V) diagrams, to a phase where quantitative evaluations, based on spectral maps, are becoming possible. It opens the door to analyses where the uncertainties on the data can be evaluated reliably, allowing for χ^2 values being translated in terms of quantitative confidence levels for a given

model, probably requiring to work in the uv plane.

A particularly useful quantity is the ratio between the flux densities measured from the emission of two different lines of the same gas, here CO. In such cases, one has direct access to an effective temperature distribution that is very close to the real temperature distribution under some reasonable assumptions, in particular thermal equilibrium and optical thinness. In the case of the Red Rectangle and EP Aqr, where such analyses could be performed reliably, evidence was found for a latitudinal dependence of the temperature, superimposed on the standard power law decrease that is present in all stars. The power of the method is limited to distances from the central star where the ratio between the two emissions is neither too small nor too large: at high temperatures, both emissions saturate, at low temperatures, both emissions cancel.

RS Cnc was the first star to be studied and was used to develop a simple model of radial bipolar outflow (no rotation) with the wind velocity and the mass loss rate having a same latitudinal dependence. Under such hypothesis, it was found necessary to allow for a radial dependence of the wind velocity in terms of simple velocity gradients. Both the quality of the data available and the complexity of the RS Cnc geometry (the star axis is at 52° from the sky plane) prevented claiming that the proposed model is unique. On the contrary, we expressed our confidence that other choices could have been made. However, our analysis has shown that the spatial resolution reachable at ALMA will allow for identifying the main features of the gas properties in terms of a unique model offering reliable descriptions of the reality.

The origin of the bipolar outflow is still unclear, however. Such morphology seems to be a widespread phenomenon in nature. It addresses the question of what is shaping bipolar PNs and, more generally, what is shaping PNs at large. Is there a link between axi-symmetrical AGB CSs and axi-symmetrical PNs? Is the axi-symmetry intrinsic to the stellar system, or does it appear during the evolution of the star?

Chapter 7

H I OBSERVATIONS OF THE WIND-ISM INTERACTION

7.1 H I observations

Far away from the star, carbon monoxide and other molecules are photo-dissociated by the interstellar radiation field. Observations at large distance, in particular of the wind-ISM interaction region, require the use of other tracers, such as dust or atomic species. Dust, at low temperature, is emitting in the infrared and is a very good tracer of the wind-ISM interaction. Infrared images are mostly observed by space telescopes such as IRAS, ISO, Spitzer, Akari and Herschel in the wavelength range of 50−200 μm. The best images have been obtained by Herschel (Cox et al. 2012) with a spatial resolution of 6 arcsec at 70 μm. They display a great variety of features, such as arcs, rings, "eyes", trailing tails... which can be described as resulting from the interaction of the wind with the ISM. In some cases such as IRC +10216 (Sahai & Chronopoulos 2010), and Mira (Martin et al. 2007), this region is also observed in NUV which is most likely due to the dust scattering of the interstellar radiation field and in FUV coming from molecular hydrogen, excited by electrons of ∼30 eV which are produced in the bow shock, and which are de-excited by emission in lines of the Werner or Lyman bands. However, these observations, being associated with continuous frequency distributions or having not good enough spectral resolution, does not provide information on kinematics. For this, we need other observations which give a good velocity resolution. Such is the case of H I observations obtained recently.

The emission of neutral atomic hydrogen at 21 cm (H I line) is due to the spin-flip of the electron in the ground state of the atom. This line is an important tracer of circumstellar shells at large distance from the central star because it is essentially unaffected by the interstellar radiation field. It offers a measurement of the gas Doppler velocity with excellent spectral resolution, thereby providing unique insight into its kinematics.

Observing H I emission from the circumstellar envelopes of AGB stars is difficult in practice because of the strong ISM H I emission: even for the nearest AGB stars, the H I signal is quite weak, and often coincident, in particular at low galactic latitudes, with strong galactic foreground and background emission, both in position and in frequency. Indeed, initial efforts to detect H I associated with evolved

stars were unsuccessful. Until recently, the combined result of these studies (Zuckerman et al. 1980; Knapp & Bowers 1983; Bowers & Knapp 1987, 1988) included a single 21-cm line detection (Bowers & Knapp 1988) of a genuine AGB star, *o* Ceti (Mira). The same authors detected H I around Betelgeuse (α Ori), a red supergiant (Bowers & Knapp 1987). These results have often been interpreted as implying that the material lost from AGB stars must be primarily molecular (e.g., Zuckerman et al. 1980; Knapp & Bowers 1983), although in many cases, the derived H I upper limits are not sufficiently sensitive to rule out atomic hydrogen as an important constituent of the circumstellar envelope.

Successful observation of H I line emission from AGB stars was recently reported. Using the upgraded Nançay Radio Telescope, T. Le Bertre, E. Gérard, and coworkers have detected H I around some two dozens of AGB and similar stars. These include semi-regular variables such as RS Cnc, EP Aqr, and X Her (Gérard & Le Bertre 2003; Le Bertre & Gérard 2004; Gardan et al. 2006) and the carbon-rich semi-regular variable Y CVn (Le Bertre & Gérard 2004). These first successful observations were followed by a more extensive survey covering a variety of AGB stars and planetary nebulae (Gérard & Le Bertre 2006). These results show that a significant fraction of the gas in the circumstellar envelopes of many evolved stars is atomic, and that it is feasible to use H I emission as a diagnosis probe of the late stages of stellar evolution.

Indeed, the observation of H I emission up to distances of the order of 2 pc from the star confirms that H I probes regions well beyond those probed by CO or other molecular tracers. The observed line profiles are typically narrower (3-5 km s^{-1}) than produced by the winds close to the star (~10 km s^{-1} for CO emission), suggesting that the outflows are slowing down with time, while interacting with the ISM. The observation of H I emission allows therefore for the study of the mass-loss properties up to times of the order of 10^5 yr, at the scale of the time separating two successive thermal pulses. The VLA images of different stars observed in H I by Matthews et al. (2013) often show extended shells trailing away from the proper motion of the star (Figure 7.1. These images also reveal a systematic velocity gradient, particularly apparent across the H I envelope of X Her where it reaches ~6.5 km s^{-1}.

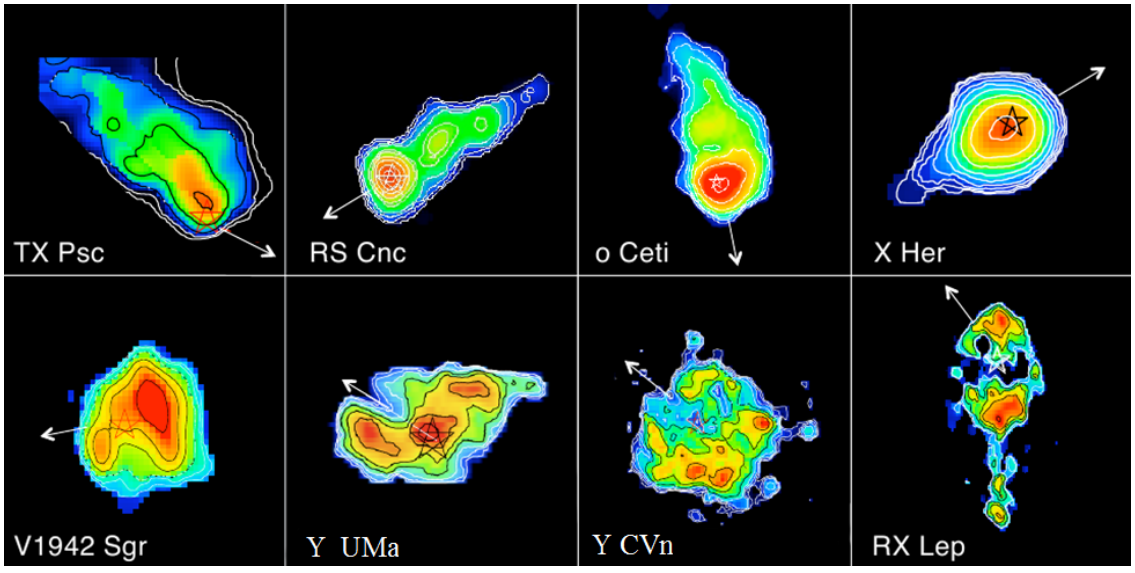

Figure 7.1: VLA images of AGB stars. The arrow shows the space motion direction of the star (adapted from Matthews et al. 2008, 2011, 2013)

The H I map of RS Cnc (Figure 7.1 and Figure 3.2 (right)) shows a 6′-long tail, in a direction opposite to the space motion of the star, and a compact structure of size ∼75″×40″ approximately centered on the star, the "head"; it is elongated in the direction of the bipolar outflow observed in CO at shorter distances, up to ∼10″, showing that H I is tracing an extension of the molecular outflow, interacting with the local interstellar medium, beyond the CO dissociation radius. However, the width of the H I line (which has a negligible intrinsic width) is significantly smaller than that observed in CO, suggesting either that the atomic hydrogen has been slowed down in its interaction with the interstellar medium or that it was emitted at an earlier epoch when the bipolar outflow was not yet important. The velocity-integrated H I flux density is measured as 1.14±0.03 Jy km s^{-1} implying a mass of ∼5.5 10^{-3} solar masses.

There is no velocity gradient detected along the RS Cnc tail. However, evidence for a complex structure of the velocity field is revealed by the presence of important inhomogeneity.

While a clear H I signal was detected around EP Aqr by the Nançay Radio Telescope, subsequent observations using the VLA revealed the presence of multiple clumps red shifted with respect to the star (while CO emission is well centered), shedding doubt on the identification of the H I signal as being associated with the star. Added together, their peak flux density reaches ∼24 mJy. In summary, the quality of the presently available data does not allow for an unambiguous identification of the observed H I emission with EP Aqr mass-loss, a possible confusion with galactic sources along the line of sight cannot be excluded.

H I emission from post-AGB and high mass-loss rate AGB stars is mostly undetected. It has been thought that molecular hydrogen, but not atomic hydrogen, dominates the stellar envelope. However, this explanation is not entirely satisfactory for at least two reasons. First, molecular hydrogen is expected to be photo-dissociated by UV photons from the interstellar radiation field (ISRF) in the external parts of circumstellar shells (Morris & Jura 1983). Secondly, the mass-loss rate of AGB stars is expected to vary with time (e.g. Vassiliadis & Wood 1993), so that a given star should be surrounded by interacting shells, originating from different episodes of mass-loss at different rates, from 10^{-8} M$_\odot$ yr^{-1} upwards, and different velocities (Villaver et al. 2002), with probably a mix of atomic and molecular hydrogen.

Another possibility is that radiative transfer effects weaken 21-cm emission, thus making the detection of H I difficult. The narrowness of the line profiles could increase the optical depth at particular frequencies, thus exacerbating self-absorption. The presence of an intense background at 21 cm may also play a role (Levinson & Brown 1980). In the following section, I present a simple model simulation, in the spirit of that used to describe CO emission, with the aim of studying the effect of background absorption and optical thickness on H I detection.

7.2 H I model

Hydrodynamical models of dust-forming long-period variable stars can describe outflows with mass-loss rates ranging from ∼10^{-8} to 10^{-4} M$_\odot$ yr^{-1}, and expansion velocities ranging from a few to 40 km s^{-1}(Winters et al. 2000). Close to the central star, the density is much larger than in the interstellar medium (ISM), and the wind expands freely. We hereafter refer to the case where the wind expands freely as scenario 1. However, at some point, the stellar wind is slowed down by the ambient medium,

and a structure develops in which both circumstellar and interstellar matter accumulates. Such structures were discovered with IRAS from the detection of spatially resolved 60 μm continuum emission (Young et al. 1993) and are referred to as "detached shells". Subsequently, the H I line was detected in the direction of several resolved IRAS sources (Le Bertre & Gérard 2004; Gérard & Le Bertre 2006) but the spatial resolution of the data does not allow for revealing detached shells.

Libert et al. (2007) developed a model of a detached shell (hereafter scenario 2) adapted to the H I emission from the prototypical case of Y CVn. In this model, a double-shock structure develops, with a termination shock, facing the central star, where the supersonic stellar wind is abruptly slowed down, and a leading shock (i.e. outward facing shock) where interstellar matter is compressed and integrated in the detached shell. These two limits define the detached shell which is thus composed of circumstellar and interstellar matter separated by a contact discontinuity. The circumstellar matter is decelerated, by a factor ~4, when it crosses the termination shock, and heated. It then cools down, while the expansion velocity further decreases and the density increases until the contact discontinuity. The model assumes spherical symmetry and stationarity. Adopting an arbitrary temperature profile, the equation of motion is solved numerically between the two limits of the detached shell. The H I line profile is then calculated assuming that the emission is optically thin.

Libert et al. (2007) could reproduce the H I line profile observed in Y CVn and generalize the model to other cases of sources with mass-loss rates of about $10^{-7}\,M_{\odot}\,yr^{-1}$ (e.g. Libert et al. 2010b). However, as discussed by Matthews et al. (2013), although this model is effective in reproducing spatially integrated line profiles, it faces some difficulties in reproducing the spatial distribution of the H I emission. Namely, at small radii, it seems to predict too much flux in both the shell component and the freely expanding wind component of the spectral profile. The mass-loss variations with time and the interaction between consecutive shells may need to be taken into account (see Villaver et al. 2002). The more elaborate numerical modelling performed by Villaver et al. follows the mass-loss and velocity variations of the stellar winds of thermally pulsing AGB (TP-AGB) stars, and describes self-consistently the formation and development of circumstellar shells embedded in the ISM (hereafter scenario 3). They show that large regions (up to 2.5 pc) of neutral gas may be formed around AGB stars.

In this work, we simulate the H I line profiles expected for the three scenarios and examine how they compare with presently available observations, adapting from the ray-tracing code developed for CO with absorption and emission taken into account (section 2.8). We assume that, in each cell, the gas is in equilibrium and that the distribution of the velocities is Maxwellian. In all cases, stars are taken spherical. We explore the line profiles for a source that is not resolved spatially by the telescope, and assume a uniform response in the telescope beam (boxcar response, cf. Gardan et al. 2006). We also assume that the line profiles can be extracted from position-switched observations, i.e. that there is no spatial variation of the background. The flux densities are expressed in the units of Jansky. We performed various tests in order to evaluate the accuracy of the simulations, found to depend mainly on the mass-loss rate of the star.

7.2.1 Freely expanding wind (scenario 1)

We consider a spherical wind in free expansion at V_{exp} =10 km s^{-1}. We measure distances in arc minutes, fixing the distance between observer and star equal to 200 pc. The mass-loss rate is varied from 10^{-7} to 10^{-4} M$_\odot$ yr^{-1}. We assume that the gas is composed, in number of atoms, of 90% atomic hydrogen and 10% ^{4}He. We assume a radial dependence of the temperature of the form $r^{-0.7}$, r being the distance to the central star, for r<0.17 pc where the temperature reaches 5K. This probably underestimates the real value of the temperature at this distance; indeed, the photoelectric heating by grains absorbing UV photons is expected to raise the temperature of the gas in the cool external layers of shells around stars having a high mass-loss rate (Schöier & Olofsson 2001). Yet, temperatures as low as 2.8 K, just above the CMB temperature, have been reported in some high mass-loss rate sources (e.g. U Cam; Sahai 1990). Such low temperatures are only expected in the freely expanding regions of the circumstellar shells.

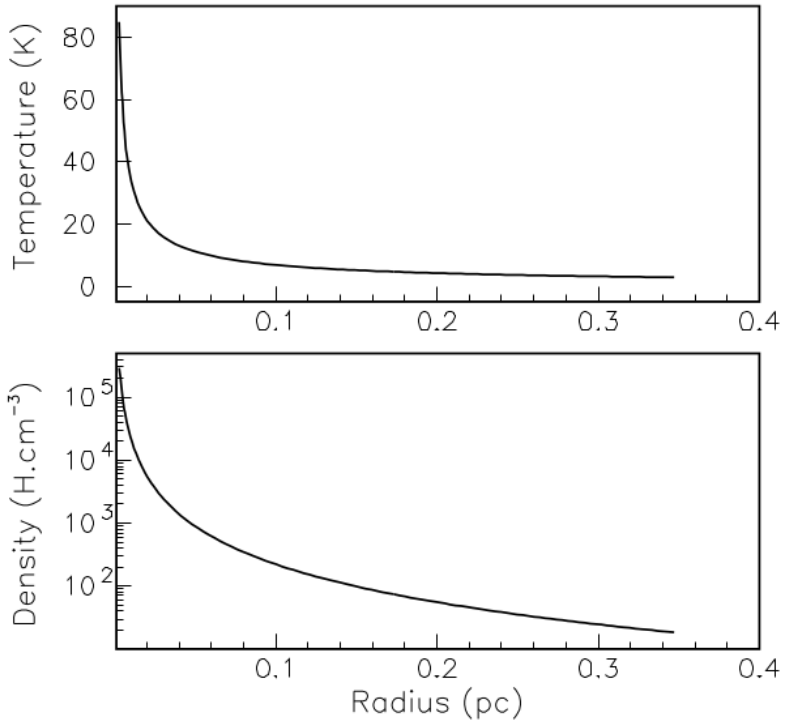

Figure 7.2: Density and temperature profiles for an outflow in uniform expansion (scenario 1, V_{exp} = 10 km s^{-1}, $\dot{M}$ = 10^{-5} M$_\odot$ yr^{-1}).

The density and temperature profiles obtained from the model are illustrated in Figure 7.2 for the 10^{-5} M$_\odot$ yr^{-1}case. In a first set of simulations (Figure 7.3), we integrate the emission within a sphere of diameter φ_{max}= 6 arcmin in the absence of background, in order to estimate the effect of self-absorption. The background is expected to have a minimum brightness temperature of 3 K. Self-absorption starts to play a significant role when the mass-loss rate reaches 10^{-6} M$_\odot$ yr^{-1}, reducing the intensity of H I detection and altering the shape of the line profile from almost rectangular to parabolic. In the case of molecular emission from expanding circumstellar envelopes (Morris et al. 1985) a slight asymmetry of the line profile is present, with more absorption on the blue side; here, however, it is so small that it can

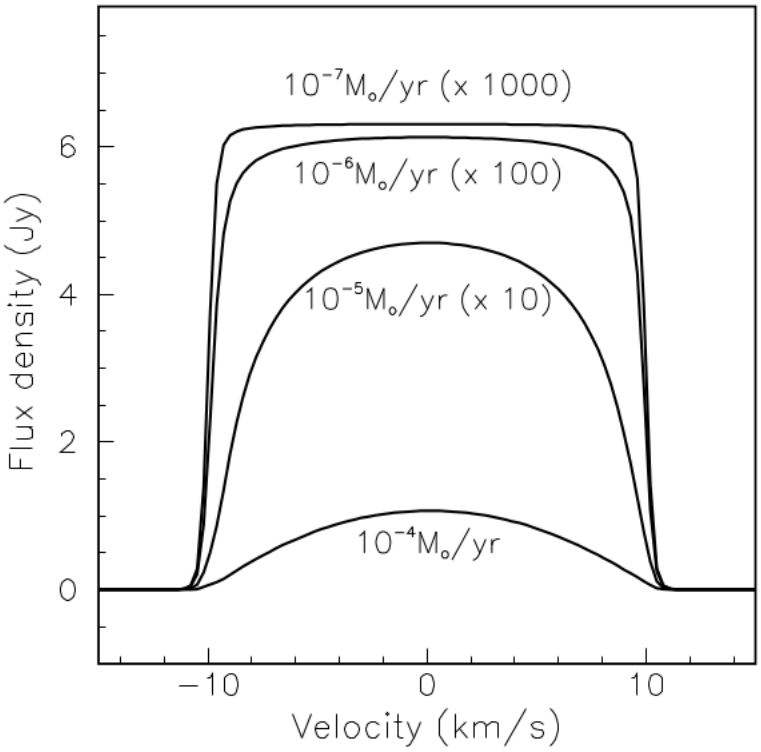

Figure 7.3: H I line profiles of shells in free expansion for various mass-loss rates with no background. The profiles for 10^{-7}, 10^{-6}, 10^{-5} $M_\odot\,yr^{-1}$are scaled by factors 1000, 100, and 10, respectively. The distance is set at 200 pc.

be completely neglected.

In a second set of simulations, the mass-loss rate is kept at 10^{-5} $M_\odot\,yr^{-1}$, and the background is varied up to 10 K (Figure 7.4). The effects noted previously are amplified by the background, in particular with an absorption developing on the blue side of the profile, and then extending to the complete spectral domain when the background temperature reaches 10K.

Adopting a radial dependence of the temperature shallower than $r^{-0.7}$, would increase it in the outer layers of the circumstellar shell and thus reduce the effects of self-absorption, as well as the absorption of the background radiation. An external source of heating (e.g. by photoelectric heating) would have the same influence.

7.2.2 Single detached shell (scenario 2)

We adopt the model developed by Libert et al. (2007). It has been shown to provide good spectral fits of the H I observations obtained on sources with mass-loss rates $\sim 10^{-7}$ $M_\odot\,yr^{-1}$. As in the preceding section, we assume a spatially unresolved source at 200 pc distance having a mass-loss rate of 10^{-7} $M_\odot\,yr^{-1}$. The internal radius of the detached shell is set at 2.5 arcmin (or 0.15 pc) and its external radius at 5.5 arcmin. We examine the dependence of the line profile for models with various masses of the detached

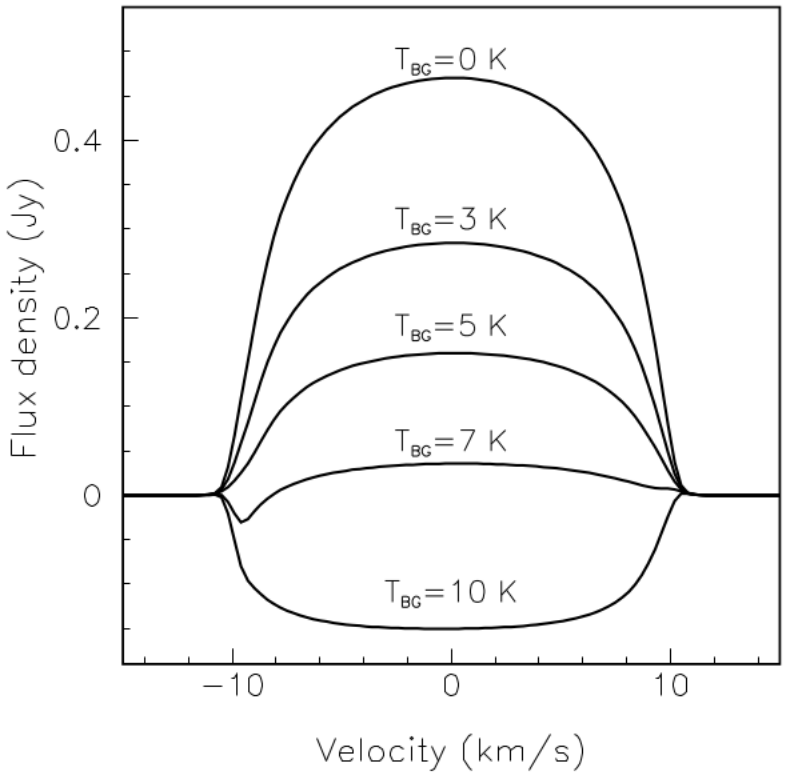

Figure 7.4: H I line profiles of a shell in free expansion for $\dot{M}$=10^{-5} $M_\odot$ yr^{-1}, and for various background levels (T_{BG} = 0, 3, 5, 7, 10 K).

shell (MDT, CS) and various background levels (Figure 7.5 and 7.6). The parameters of the four cases illustrated in Figure 7.5 are given in Table 7.1. The free-wind expansion velocity is taken to be V_{exp} = 8 km s^{-1}. At the termination shock the downstream temperature is given by $T_f \sim \frac{3\mu m_H}{16k} V_{exp}^2 \sim 1800$ K (equation 6.58 in Dyson & Williams 1997) with m_H being the mass of the hydrogen atom and μ the mean molecular weight. For the temperature profile inside the detached shell we use the expression 9 in Libert et al. (2007) with a temperature index, $a = -6.0$. The temperature is thus decreasing from ∼1800 K, to T_f, at the interface with the ISM, r_f. The density, velocity and temperature profiles are illustrated in Figure 7.7 for case D.

Self-absorption within the detached shell has a limited effect, with a reduction ranging from 1% (model A) to 20% (model D), as compared to the optically thin approximation (Figure 7.5). However, taking into account the background introduces a much larger effect (Figure 7.6).

The results depend on the values adopted for the model parameters (mainly internal radius, expansion velocity and age). Smaller internal radii and expansion velocities, and/or longer ages would lower the average temperature in the detached shell. This would increase the effect of self-absorption, as well as that of the background absorption. The line profiles simulated in the A and B cases displayed in Figure 7.5 provide a good approximation to several observed H I line profiles (Libert et al. 2007, 2010a; Matthews et al. 2013).

Table 7.1: Model parameters (scenario 2), d =200 pc, V_{exp} = 8 km s^{-1} and $\dot{M}$ = 10^{-7} M$_\odot$ yr^{-1}.

Case	Age (yr)	r$_f$ (arcmin)	T$_f$ (K)	M$_{DT,CS}$ (M$_\odot$)
A	5×10^5	3.85	135	0.05
B	10^6	4.14	87	0.1
C	2×10^6	4.47	55	0.2
D	4×10^6	4.83	35	0.4

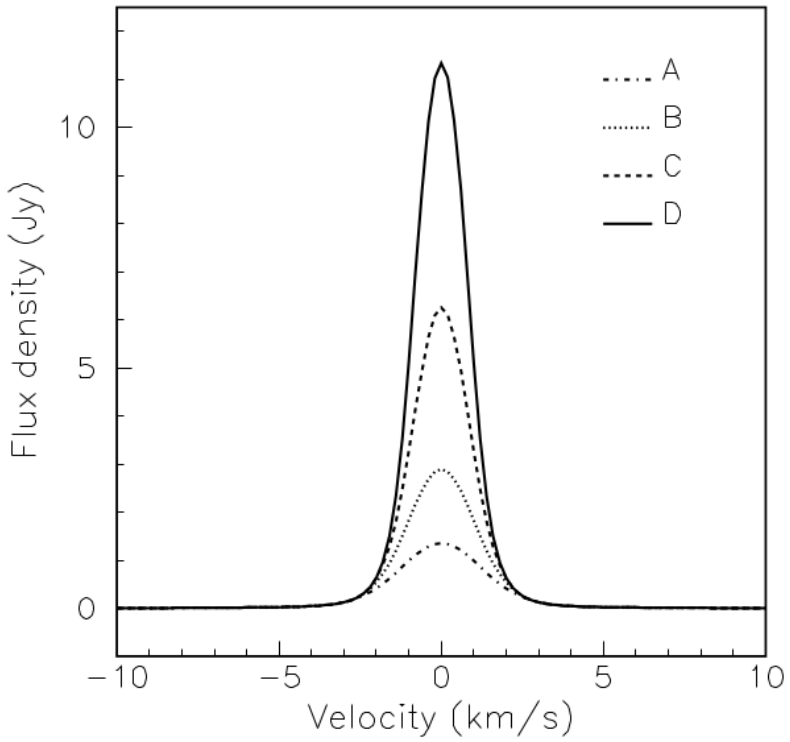

Figure 7.5: H I line profiles of single detached shells for various circumstellar masses (A: 0.05 M$_\odot$, B: 0.1 M$_\odot$, C: 0.2 M$_\odot$, D: 0.4 M$_\odot$,), in the absence of background.

As an illustration, we compare in Figure 7.8 the spatially integrated profile of Y CVn observed by Libert et al. (2007) with the model prediction. In this case, a distance of 321 pc (van Leeuwen 2007), a mass-loss rate of 1.3×10^{-7} M$_\odot$ yr^{-1}, and a duration of 7×10^5 yr have been adopted. These parameters differ from those adopted by Matthews et al. (2013), who assumed 1.7×10^{-7} M$_\odot$ yr^{-1}and a distance of 272 pc (Knapp et al. 2003). However, by adopting a lower mass-loss rate, and conversely, a longer duration, we can fit the spatially resolved spectra obtained by the VLA (Figure 7.9. Table 7.2 shows the values of the model parameters.

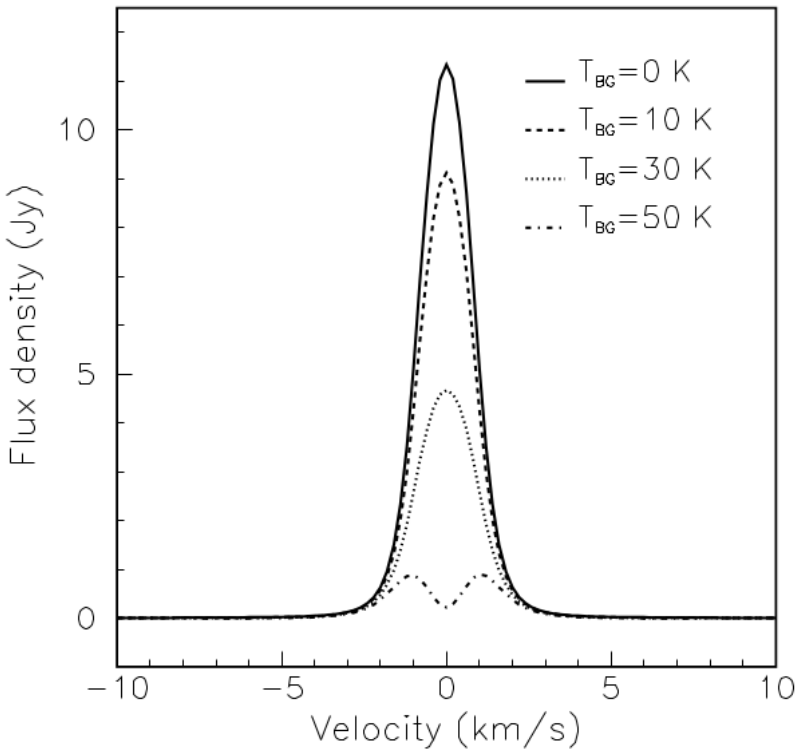

Figure 7.6: H I line profiles of a single detached shell (scenario 2, case D) for various background levels (T_{BG} = 0, 10, 30, 50 K).

Table 7.2: Model parameters of Y CVn

Parameters	Values
d (pc)	321
$\dot{M}(10^{-7}\,M_{\odot}\,yr^{-1})$	1.3
V_{exp} (km s^{-1})	8
r_{in} (arcmin)	2.8
r_{f} (arcmin)	4.0
r_{out} (arcmin)	5.1
Temperature index a	−6.0
Detached shell age (yr)	7×10^{5}

7.2.3 Villaver et al. model (scenario 3)

Villaver et al. (2002) have modelled the dynamical evolution of circumstellar shells around AGB stars. The time dependence of the stellar wind is taken from the stellar evolutionary model of Vassiliadis & Wood (1993).

For our H I simulations, we use the 1.5 $M_{\odot}$ circumstellar shell model of Villaver et al. (2002)

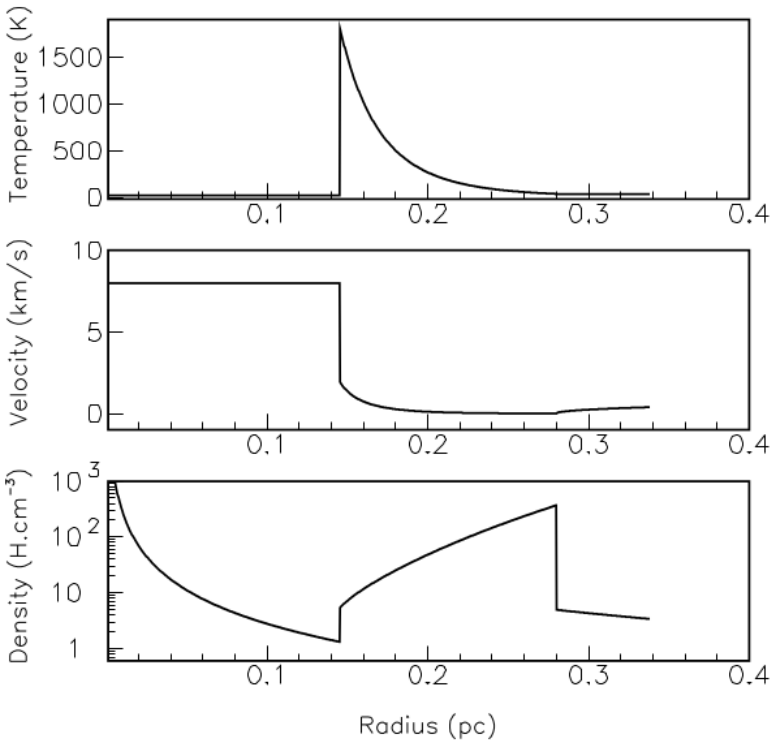

Figure 7.7: Density, velocity and temperature profiles for a detached shell model (scenario 2, case D).

at various times of the TP-AGB evolution. We select the epochs at 5.0, 6.5 and 8.0×10^5 yr, which correspond to the end of the first two thermal pulses, and then to the end of the fifth (and last) thermal pulse. The density, velocity and temperature profiles are illustrated in Figure 7.10. Here, where the external radius may reach large values (0.75, 1.66 and 2.5 pc, respectively), we adopt a distance to the star of 1 kpc (implying a diameter of up to 17 arcmin). The results are shown in Figure 7.11. In this scenario, the temperature in the circumstellar environment is maintained at high values due to the interactions between the successive shells (Figure 7.10). The shape of the line profile is thus dominated by thermal broadening, and does not depend much on the epoch which is considered (although the intensity of the emission depends strongly on time, together with the quantity of matter expelled by the star). For the same reason, these results do not depend much on background (<5% for T_{BG} = 100 K). Indeed in the models the temperature of the gas in the circumstellar shell always stays at a high level (>10^3 K, except close to the central star in the freely expanding region).

The predictions obtained with this scenario, in which wind-wind interactions are taken into account, differ clearly from those obtained with the previous scenario, in which the detached shell is assumed to result from a long-duration stationary process; the main difference is a much larger line width (FWHM $\sim$ 16 km s^{-1}). In summary, for scenario 3, the large line is essentially the result of thermal broadening, with a lesser contribution from kinematic broadening (cf. Figure 7.10).

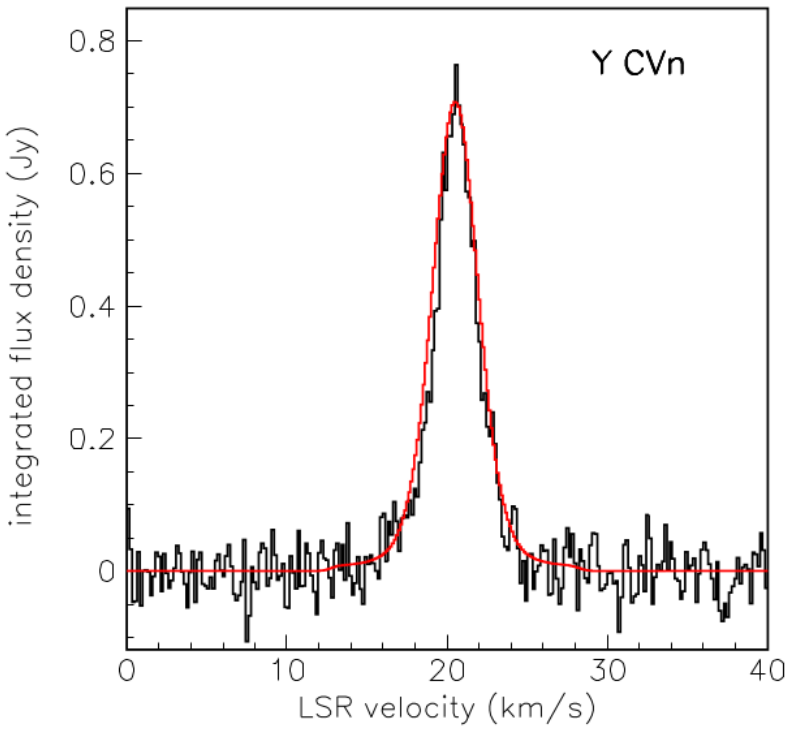

Figure 7.8: Y CVn integrated spectrum (Libert et al. 2007) and best fit result using scenario 2 (d = 321 pc, $\dot{M}$ = 1.3× 10^{-7} $M_\odot$ yr^{-1}, age = 7×10^5 yr).

7.3 Discussion

7.3.1 Optically thin approximation

If absorption can be neglected, the intensity becomes proportional to the column density of hydrogen. For a source at a distance d, the mass of atomic hydrogen (M_{HI}) can be derived from the integrated flux density through the standard relation (e.g. Knapp & Bowers 1983):

$$M_{HI} = 2.36 \times 10^{-7} \int d^2 S_{HI} dV \tag{7.1}$$

where d is expressed in pc, V in km s^{-1}, S_{HI} in Jy and M_{HI} in solar masses ($M_\odot$).

The calculations allow us to estimate the error in the derived H I mass of circumstellar envelopes that is incurred from the assumption that the emission is optically thin and not affected by the background. As an example, Figure 7.12 displays the ratio between the estimated mass (using the standard relation) and the exact mass of atomic hydrogen. The case without background illustrates the effect of self-absorption within the circumstellar shell for different mass-loss rates. We adopt a freely expanding wind with a temperature profile of the form $r^{-0.7}$, with r expressed in arcminutes, or a constant temperature (5 K, 10 K, 20 K). The ratio clearly decreases with decreasing temperature in the circumstellar shell, increasing mass-loss rate and increasing background temperature.

Figure 7.9: H I spectral maps of Y CVn from VLA data (black) and from the detached shell model (blue).

In the constant temperature case with T = 5 K and T_{BG} =5 K, the line profiles should be flat, at a level of zero flux density, and thus the estimated masses should exactly cancel.

The standard relation used for estimating the mass of atomic hydrogen should obviously be handled with caution in the case of scenario 1 (freely expanding wind). However, our calculations show that the deviation is much smaller for the two other scenarios (and basically negligible for scenario 3). This is mainly an effect of the high temperature in the detached shells resulting from the wind-wind interaction.

7.3.2 Spectral variations of the background

The H I absorption produced by cold galactic gas in the foreground of bright background emission shifts the line centroid velocity up or down depending on their respective temperatures (cf. Levinson & Brown

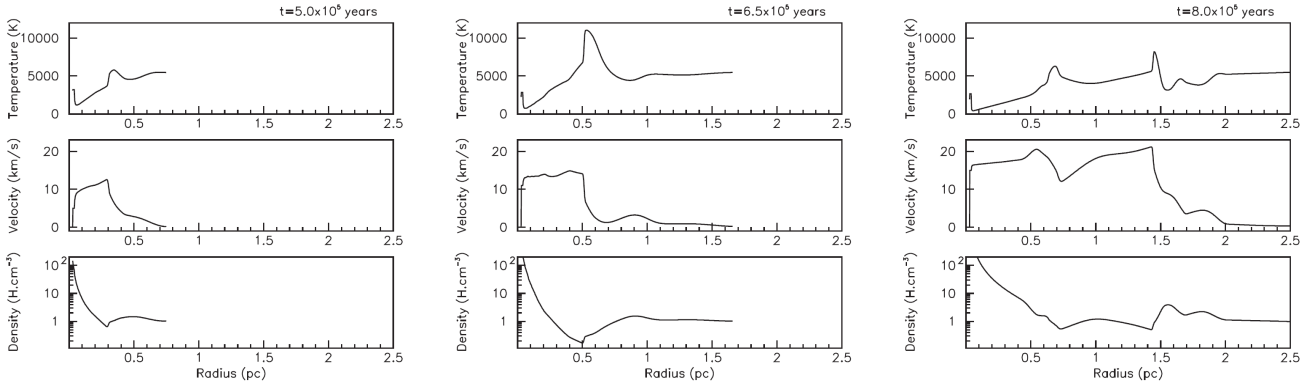

Figure 7.10: Density, velocity and temperature profiles for the Villaver et al. (2002) model at three different epochs [5.0×10^5 yr (left), 6.5×10^5 yr (centre), 8.0×10^5 yr (right)].

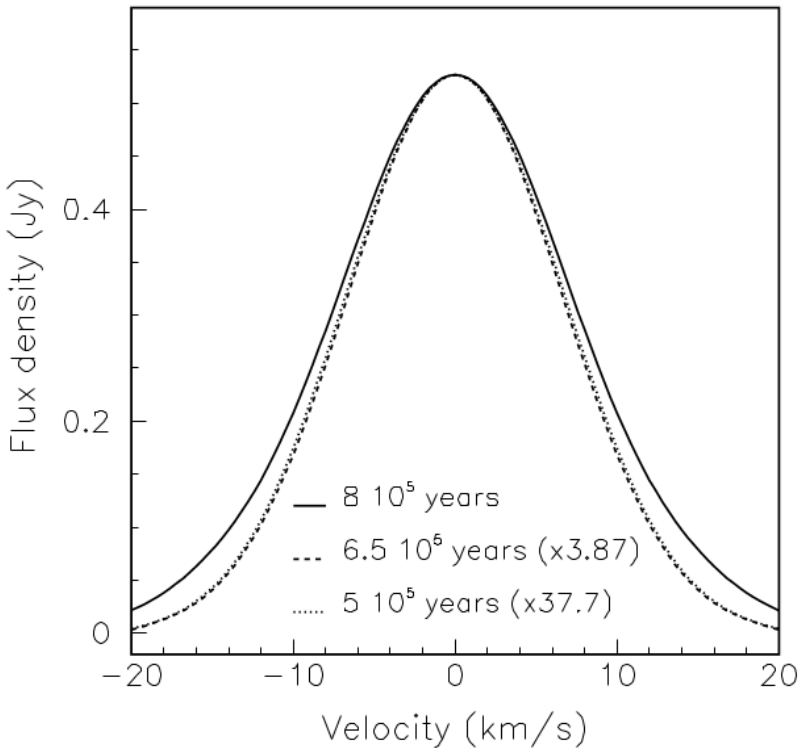

Figure 7.11: H I line profiles of a circumstellar shell model around a 1.5 $M_\odot$ star during the evolution on the TP-AGB phase (5.0, 6.5, 8.0×10^5 yr; Villaver et al. (2002), in the absence of background. The distance is set at 1000 pc. The first two profiles, scaled by up by factors of 37.7 and 3.87 respectively, in order to help the comparison, are virtually indistinguishable.

1980). We illustrate this effect in the case of scenario 1 in Figure 7.13 for a 10^{-5} $M_\odot\,yr^{-1}$ mass-loss rate, and a background temperature varying linearly between 10 K at -10 km s^{-1}, and 5 K at $+10$ km s^{-1}. The absorption is clearly shifted towards velocities with higher background and the emission towards velocities with lower background.

In the case of an intense and spectrally structured background, some care should be taken when

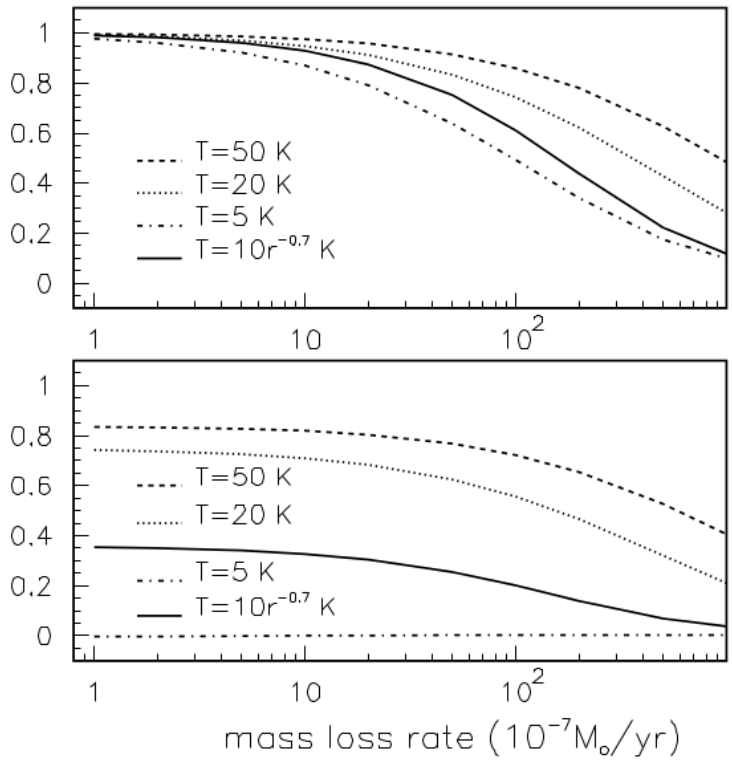

Figure 7.12: Ratio between the estimated and real values of the mass of atomic hydrogen for scenario 1 (freely expanding wind) with mass-loss rates ranging from 10^{-7} $M_\odot$ yr^{-1} to 10^{-4} $M_\odot$ yr^{-1} (see Section 7.3.1) and different cases of temperature dependence (see text). Upper panel: no background. Lower panel: with a 5 K background.

comparing the H I line centroids with the velocities determined from other lines.

7.3.3 Comparison with observations

Freely expanding winds have been clearly detected in the H I line of only two red giants: Y CVn (Le Bertre & Gérard 2004) and Betelgeuse (Bowers & Knapp 1987). The emission is relatively weak and difficult to detect. Data obtained at high spatial resolution reveal a double-horn profile (e.g. Bowers & Knapp 1987). It is worth noting that a high-velocity expanding wind ($V_{exp} \sim 35$ km s^{-1}) has also been detected around Cepheid δ Cep (Matthews et al. 2012). The presence of a pedestal is suspected in a few H I line profiles, which could have its source in the freely expanding region (Gérard & Le Bertre 2006; Matthews et al. 2013). Scenario 1 is likely to be well suited for the description of sources in their early phase of mass-loss, or sources at large galactic latitudes, embedded in a low-pressure ISM.

In general, sources that have been detected in H I up to now show quasi-Gaussian line profiles of FWHM $\sim$ 2-5 km s^{-1} (Gérard & Le Bertre 2006; Matthews et al. 2013), revealing slowing-down detached shells. Such profiles are well described by scenario 2 assuming mass-loss rates of a few 10^{-7} $M_\odot$ yr^{-1}, and durations of a few 10^5 yr. In particular, for Y CVn and Betelgeuse, the main H I component has a narrow line profile (~ 3 km s^{-1}) and is well described by such simulation (Libert et al. 2007; Le Bertre et al. 2012).

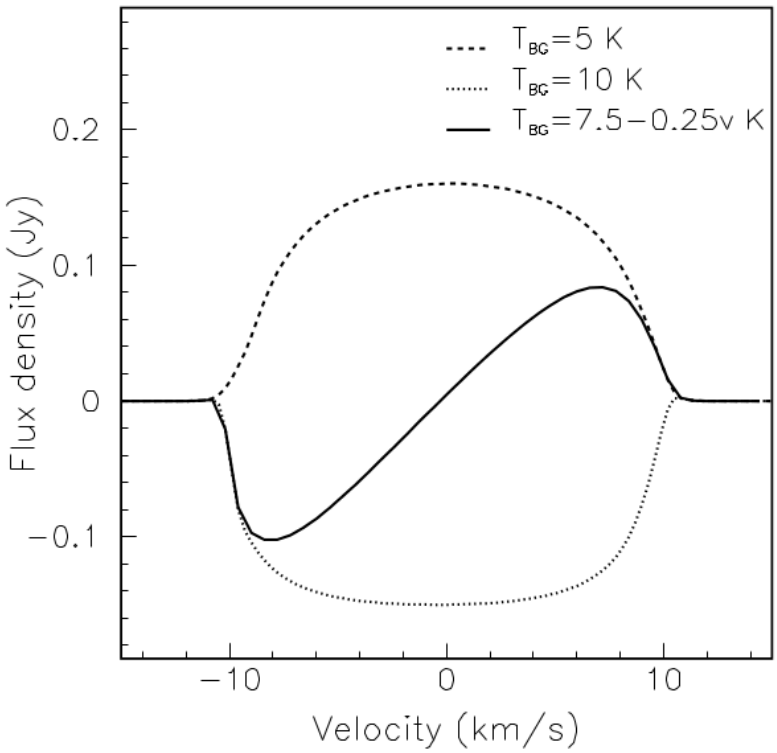

Figure 7.13: Effect of a background intensity varying linearly from 10 K to 5 K across the line profile for scenario 1 with $\dot{M} = 10^{-5}\mathrm{M}_{\odot}\,\mathrm{yr}^{-1}$. The curves labelled "$T_{BG}$ =5 K", and "T_{BG} =10 K", are taken from Figure 7.4.

Sources with large mass-loss rates ($\geq 5{\times}10^{-7}\,\mathrm{M}_{\odot}\,\mathrm{yr}^{-1}$) have rarely been detected (with the notable exceptions of IRC +10216 and AFGL 3068, see below). The simulations presented in Section 7.2.3 show the line profiles, such as those predicted by Villaver et al. (2002), that such sources should display at the end of the thermal-pulse phase, when interacting with the ISM. In the Villaver et al. model, which accounts for the evolution of the central star, the circumstellar envelopes include both interacting shells and swept-up ISM matter. Shocks between successive shells maintain a high gas temperature (~4000 K). In such cases, the calculated line profiles are not seriously affected by the background level, and the flux densities are large enough for allowing H I detection up to a few kpc. For instance, in the GALFA-H I survey (Peek et al. 2011), the 3σ detection limit for a point source in a 1 km s^{-1} channel is ~30 mJy. Saul et al. (2012) have detected many compact isolated sources in this survey. However, at the present stage, none could be associated with an evolved star (Begum et al. 2010).

Furthermore, several sources with high mass-loss rates, such as IRC +10011 (WX Psc), IK Tau (NML Tau) or AFGL 3099 (IZ Peg), which are observed at high galactic latitude with an expected low interstellar H I background, remain undetected (Gérard & Le Bertre 2006; Matthews et al. 2013). The simulations that we have performed based on the three different scenarios considered in this work cannot account for such a result. It seems therefore that, in sources with large mass-loss rates ($\geq 5{\times}$ $10^{-7}\,\mathrm{M}_{\odot}\,\mathrm{yr}^{-1}$), hydrogen is generally not in atomic, but rather in molecular form.

Glassgold & Huggins (1983) have discussed the H/H_2 ratio in the atmospheres of red giants. They find that for stars with photospheric temperature $T \geq 2500$ K, most of the hydrogen should be in atomic

form, and the reverse for $T \leq 2500$ K. Winters et al. (2000) find that there is an anti-correlation between T and the mass-loss experienced by long period variables. It seems likely that, generally, stars having a mass-loss rate larger than a few $10^{-7}\,M_\odot\,yr^{-1}$ have also a low photospheric temperature, $T \leq 2500$ K, and thus a wind in which hydrogen is mostly molecular.

Recently, Matthews et al. (2015) have reported the detection of atomic hydrogen in the circumstellar environment of IRC +10216, a typical mass-losing AGB star at the end of its evolution with $\dot{M} \sim 2 \times 10^{-5}\,M_\odot\,yr^{-1}$. The observed morphology, with a complete ring of emission, is in agreement with the predictions of Villaver et al. (2002, 2012). They find that atomic hydrogen represents only a small fraction of the expected mass of the circumstellar environment (<1%), supporting a composition dominated by molecular hydrogen. Unfortunately, a reliable line profile could not be extracted due to the low level of the emission and to a patchy background. The detection of H I over a spectral range $\sim$10 km s^{-1} suggests a line width larger than commonly observed in evolved stars, which would make it compatible with scenario 3. Gérard & Le Bertre (2006) have reported the possible detection of AFGL 3068, another carbon star with high mass-loss rate ($\sim 10^{-4}\,M_\odot\,yr^{-1}$). In this case also, the line width ($\sim$30 km s^{-1}) is larger than expected for scenario 2, and might be better described by scenario 3. Another possibility for this source, which is at a large galactic latitude, would be that we are mostly detecting a freely expanding wind not slowed down by its local ISM (i.e. scenario 1).

If atomic hydrogen is of atmospheric origin (a fraction of 1% is expected for a star with an effective temperature of 2200 K; Glassgold & Huggins (1983)), its abundance should correspondingly be scaled down in our radiative transfer simulations. The effect of the optical depth on the line profiles could be considerably reduced in such a case. For stars with lower effective temperature ($T \leq 2200$ K), atomic hydrogen might also be present in the external regions of circumstellar envelopes as a result of the photodissociation of molecular hydrogen by UV photons from the ISRF (Morris & Jura 1983).

7.4 Prospects

We have simulated H I line profiles for mass-losing AGB stars using three different scenarios assuming spherical symmetry. However, AGB sources are moving through the ISM and their shells may be partially stripped by ram pressure (Villaver et al. 2003, 2012). As a consequence of the interaction a bow-shock shape appears in the direction of the movement, but also a cometary tail is formed which is fed directly from the stellar wind and from material stripped away from the bow shock. The cooling function and the temperature assumed for the wind have an important effect on the formation of the tail as shown by Villaver et al. (2012). Higher density regions formed behind the star will cool more efficiently and will collapse against the ISM pressure, allowing the formation of narrow tails.

Gérard & Le Bertre (2006) have reported shifts of the H I emission in velocity as well as in position for several sources. Matthews et al. (2008) have reported a shift in velocity for different positions along the tail of Mira (see also X Her, Matthews et al. 2011). These effects can also affect the H I line profiles, and thus the detectability. In addition, material lost by the AGB star should be spread along a tail that may reach a length of 4 pc, as in the exceptional case of Mira. On the other hand, Villaver et al. (2012) show that for sources with large mass-loss rates at the end of their evolution, dense shells could still be

found close to the present star position.

In our simulations, we have used backgrounds of uniform brightness. This applies only to the CMB and, to a lesser extent, to the galactic continuum emission. It does not apply to the galactic H I emission which may show spatial structures of various kinds, resulting in more complex morphologies than simulated in Section 7.2. For instance, an absorption line could form preferentially at the position of a peak of galactic H I emission (a radiative transfer effect). Such a phenomenon may affect the predictions presented in Section 7.3.4. Therefore, a good description of the background is in principle needed to model the observed line profiles. Such input may be obtained from frequency-switched observations for the galactic H I component, and from available surveys for the continuum at 21 cm.

It must be noted that, in the position-switched mode of observation, the intrinsic line profile of the stellar source can also be spoiled by the patchiness of the galactic background emission (observational artefact). The main source of confusion is the galactic H I emission which is structured spatially and spectrally. The classical position-switched mode of observation is not always efficient to correct the 21-cm spectra from the emission that is not directly associated with the star and 2D mapping may be necessary for subtracting the contaminating emission in such cases. Interferometry observations have the advantage of filtering out the large-scale galactic emission; however, in general, a compact circumstellar emission is not subtracted. Also, artefacts may arise from incomplete spatial sampling of the large-scale emission, as illustrated by the case of TX Psc Matthews et al. (2013). If feasible, an excellent u-v coverage combined with maps from a single-dish telescope providing small spacings has to be obtained. Moreover, for circumstellar shells angularly larger than the primary beam of the interferometer, mosaicked observations combined with single-dish maps are required.

A final caveat is that, when the distance to the source becomes larger, the foreground ISM material may play the role of an absorbing layer of growing importance (Zuckerman et al. 1980). The circumstellar shell line profile may thus be distorted by absorption due to the foreground cold material that shares the same radial velocity range. Sources with high mass-loss rate ($\sim 10^{-6} - 10^{-5}$ $M_\odot\,yr^{-1}$) tend to be concentrated towards the galactic plane. They are expected to dominate the contribution of AGB stars to the replenishment of the ISM (Le Bertre et al. 2003). The recent detection of IRC +10216 by Matthews et al. (2015) shows that atomic hydrogen should be present in these sources and that the H I line can be used to probe the morphology and the kinematics of stellar matter decelerated at large distance from the central star. However, as discussed above, when the background is large, a proper modelling of the line profiles is necessary.

Chapter 8

CONCLUSION AND PERSPECTIVES

The work presented in the thesis has used observations of the CO and H I emissions of the circumstellar envelopes of evolved stars to illustrate the methods of analysis of such data, the assets and limitations of the models that can be conceived and the main features of the underlying physics. The emphasis has been on reconstructing the morphology and kinematics of the gas envelope of evolved stars observed using telescopes and interferometer arrays at Pico Veleta, Nançay, Plateau de Bure (PdBI), Atacama Large Millimeter-sub-millimeter Array (ALMA), Very Large Array (VLA), etc.

The joint study of CO and H I emissions has made it possible to explore the circumstellar envelopes at both short distance from the star, using the former, and large distance from the star, using the latter. CO observations are of the emission, at millimetre wavelengths, from rotational states of the carbon monoxide molecule; they explore regions where the temperature varies over two orders of magnitude between typically thousand Kelvins and ten Kelvins.H I observations, at 21 cm wavelength, explore larger radial distances, where molecules are dissociated by the interstellar UV radiation; they tell us about the interaction between the gas envelope of the star and the interstellar medium. The complementarity between these two modes of observation has been amply demonstrated by the examples that have been presented.

This work is a step toward improved modelling of the circumstellar shells of evolved stars, at a time when the excellent observing conditions offered by ALMA, with unprecedented sensitivity and spatial and spectral resolutions, ask for more quantitative analyses than was previously possible.

8.1 CO observations

Five evolved stars have been studied using CO data from IRAM telescopes (PdBI array and Pico Veleta single dish) and from ALMA. Three of these were studied in much detail: RS Cnc, EP Aqr and the Red Rectangle. They are representative of three different stages of evolution. EP Aqr, from the absence of Technetium in its circumstellar envelope, is identified as a young AGB star; RS Cnc, being in its thermal pulsing phase and fourth dredge up episode, is well advanced on the AGB; the Red Rectangle is a post-AGB star in the process of becoming a Planetary Nebula. All three stars display approximate rotational

invariance about an axis having different orientations with respect to the sky plane: nearly perpendicular for EP Aqr, at about 45° for RS Cnc and nearly parallel for the Red Rectangle.

The basic quantities available from observations for further analysis are flux densities $f(y, z, V_x)$ that depend on three variables: the sky coordinates, y and z, and the Doppler velocity V_x measured along the line of sight. Analyses were presented taking into account the emission probability of the detected radiation, its absorption in the foreground gas and the population of the emitting quantum state. However, much use has been made of a more direct and simpler quantity, the effective density ρ_{eff}, defined as $\rho_{eff}(x, y, z)dx = f(y, z, V_x)dV_x$. Under the approximation of thermal equilibrium and negligible absorption the effective density can be related simply to the density and temperature of the gas.

In the case of the Red Rectangle, under the hypothesis of rotational invariance about the star axis, the effective density can be reconstructed in space by simply solving the integral equation $F(y, z) = \sum \rho_{eff}(x, y, z)dx$. This equation, in the approximation of a star axis exactly parallel to the sky plane, does not mix different z values and therefore effectively splits in as many equations as there are measured values of z. For each of these, $\rho_{eff}(x, y, z)$ depends exclusively on $\xi = \sqrt{x^2 + y^2}$ and the integral equation is easily solved.

The situation is very different in the case of EP Aqr. In that case, in the approximation of a star axis exactly perpendicular to the sky plane, rotational invariance about the star axis results simply in circular symmetry on the sky plane and does not help with the solution of the integral equation: radial and latitudinal dependences of the effective density are mixed. Indeed, there is no way to distinguish between spherical symmetry and axial symmetry about an axis parallel to the line of sight when considering the effective density alone. It is then necessary to use the information contained in the velocity measurement and to make assumptions about the nature of the wind: for each measured flux density, in pixel (y, z), writing $R = \sqrt{y^2 + z^2}$ and assuming the wind to be purely radial with velocity V, the relation $x/R = V_x/\sqrt{V^2 - V_x^2}$ provides a direct measurement of x once V is known. One may then assume a smooth dependence of V on the star latitude, from a value Veq at the equator to a value V_{pole} at the poles, and be able to reconstruct the effective density in space. However, one may as well assume isotropic expansion and obtain a spherical model of the star with density and wind velocity depending on the radial distance to the star. Both assumptions have been made, with a slight preference for the former.

We see from these two extreme examples that an intermediate situation, such as that of RS Cnc, requires the preliminary elaboration of a model specifying the form of the space dependence of the effective density and wind velocity. The model adopted in the thesis assumes that the wind is purely radial, free of turbulences and in local thermal equilibrium. Moreover, it is supposed to have been in such a regime for long enough a time, such that the radial extension of the gas volume is limited exclusively by the UV dissociation of CO molecules by interstellar radiation and does not keep any trace of the star history. The temperature is parameterized as a power of $r = \sqrt{x^2 + y^2 + z^2}$ but independent of latitude. The spectrum of flux densities in each pixel is calculated by integration along the line of sight, the temperature dependent contributions of emission and absorption being respectively added and subtracted at each step. The wind velocity V and the mass-loss rate $\dot{M}$ are smooth functions of the latitude and allowance is made for velocity gradients. The bipolarity of the flow is parameterized as a function of latitude using Gaussian forms of standard deviation σ centred at the poles, used to describe both the wind velocity and the mass-loss rate. A satisfactory description of the observed flux densities is

obtained this way.

Measurements are available on two rotation lines in each case, CO(2-1) and CO(1-0) for EP Aqr and RS Cnc, CO(6-5) and CO(3-2) for the Red Rectangle. Their ratio, being independent from gas density and velocity, provides invaluable information on the physical properties of the gas, in particular its temperature. Indeed, under the simplifying hypothesis of thermal equilibrium, the flux ratio is a simple function of temperature, rising from zero to maximum in a range of radial distances from the star where CO observations are available. If the temperature were independent of latitude and would display a pure radial dependence, for example such as proposed by Schöier & Olofsson (2001), the flux density ratio between two different lines would be independent of latitude. In both EP Aqr and RS Cnc, evidence is obtained for the temperature to be significantly larger at low latitudes than near the poles. On the contrary, the gas surrounding the Red Rectangle is warmer in the bipolar outflow and particularly on its rather sharp interface with the cooler equatorial gas torus.

For both RS Cnc and EP Aqr, the model described above provides a satisfactory description of the observed flux densities by adjusting the model parameters to best fit CO(1-0) and CO(2-1) emissions together. However, the assumption of a same latitudinal dependence of the wind velocity and mass-loss rate, resulting in a density nearly independent of the star latitude, is somewhat arbitrary: its only justification is its ability to reproduce the data. Moreover, in both cases, important deviations from rotational invariance and central symmetry have been observed and analysed in detail, giving evidence for significant lumps of excess density randomly distributed. The spatial resolution of the data is not sufficient to claim that the form adopted in the model is unique; on the contrary, we are confident that other forms could have been chosen with as much success and the assumptions retained in the model are but crude approximations of reality. The gain that can be obtained by the availability of data of higher spatial resolution than presently available, as ALMA makes it possible, is immense. ALMA data will open a new chapter in the study of evolved stars and we have submitted a proposal to observe EP Aqr. At the same time, a request for observation time at NOEMA aimed at observing the CO(2-1) emission of RS Cnc with data of a better quality than presently available, has been accepted.

The case of the Red Rectangle is different; the higher spatial resolution of the data allows for a more detailed description of the morphology and kinematics, with evidence for a clear separation between a rotating equatorial gas volume and conical polar outflows. Moreover, at variance with EP Aqr and RS Cnc, the integrated flux, far from being spherically distributed, displays an axial symmetry that strongly deviates from isotropy. The mass-loss rates measured for EP Aqr and RS Cnc are both at the level of 10^{-7} $M_{\odot}$ yr^{-1}, insufficient for having significantly modified the morphology of the circumstellar envelope. On the contrary, the Red Rectangle displays a spectacular X shape, usually interpreted as resulting from a strong bipolar wind having carved two conical cavities in the gas envelope at the end of the AGB phase. While no evidence for such a strong wind is presently available, it must be remarked that a purely axial wind, being perpendicular to the line of sight, would produce no Doppler effect and consequently be unobserved. Similarly, in the case of EP Aqr, an equatorial rotating volume would also be undetected, for the same reason.

The limitations of the proposed models have been amply discussed. In particular, the presence of important deviations from rotational invariance and/or central symmetry has been studied in much detail, implying important restrictions on the validity of the models that have been used. In the future,

the availability of ALMA and NOEMA data will make it possible to deal with these issues in a much more reliable and quantitative way than presently possible.

The adequacy of a bipolar outflow model for the description of evolved stars at very different stages of their evolution calls for some additional comments. To some extent, one might say that it is natural to describe the deviation from a spherical shape to first order by an elongation along an axis and that the adequacy of such a description is not surprising.

There is more to it, however, in particular the surprising similarity of the bipolar wind velocities, at the 10 km s^{-1} scale, in stars such as EP Aqr, RS Cnc and the Red Rectangle, at very different stages of their evolution. In particular, in the case of the Red Rectangle, and at variance with the other two stars, a significant mass loss has already occurred, having shaped the gas envelope in a shape strongly deviating from spherical. The terminal velocity measured here (a hint at the presence of a bipolar outflow of such a magnitude had been given by Bujarrabal & Alcolea (2013) from an analysis of far-infrared CO Herschel observations) is much too low to explain the observed morphology of the Red Rectangle. This has led different authors to devise models in which a high mass-loss episode occurred thousand or so years ago (Koning et al. 2011; Soker 2000; Thomas 2012; Martínez González et al. 2015) either at a single time or in a succession of events. Moreover, the kinematic configuration displays a very clear discontinuity between a rotating torus and the expanding polar cones, of which there is no indication in the two other stars. One is then tempted to assume that the observed similarity of the outflow velocities between the Red Rectangle and the other two AGB stars is accidental. Yet, it remains that EP Aqr and RS Cnc, in spite of the very different durations of their presence on the asymptotic giant branch, have both similar mass loss rates and outflow wind velocities. This may be, for example, the result of a tight correlation between the two quantities, or evidence for an AGB population spending a major fraction of its life on the branch with nearly constant properties of the bipolar outflow. A comparative study of a large number of AGB stars would shed new light on this issue and contribute significant progress to the understanding of the mechanism governing their evolution. Better access to archived IRAM data would considerably ease such investigations.

Evaluations of the gas temperature have been made for each of the three stars under the assumption of thermal equilibrium and optical thinness. Optical thinness was shown to apply in the case of RS Cnc and EP Aqr but was not explicitly discussed in the case of the Red Rectangle. The reason is that in the cases of the former stars, a detailed modelling was performed, accounting for both emission and absorption of the radiation, providing direct evidence for the low contribution of absorption. In the case of the Red Rectangle, the good spatial resolution and the peculiar geometry (with the star axis nearly parallel to the sky plane) made it possible to extract most of the relevant physical quantities directly from observations, without having recourse to a model. The relatively low values obtained for the gas temperature, not exceeding 200 K in the explored range (see Figure 5.11), cannot be used as a proof for the validity of the optical thinness assumption. While both EP Aqr and RS Cnc display a significant temperature enhancement near the equator, the Red Rectangle requires the temperature to be lower in the equatorial torus than in the expanding cones, while being strongly enhanced at the interface between the two regimes. Dorfi & Höfner (1996) have studied the effect of a slow rotation of the gas envelope on the mass loss mechanism and argue that an enhancement of the mass loss rate and of the terminal velocity is expected in the equatorial region as a result of the influence on the dust driven winds of the

dust forming time scales. It seems therefore that the winds of both RS Cnc and EP Aqr, which have a small mass-loss rate deficit in the equatorial region, and for which there exists no evidence for rotation (at least in the case of RS Cnc, in the case of EP Aqr rotation is difficult to detect) are not driven by the mechanism considered by Dorfi & Höfner (1996). Indeed, several authors assume the radial wind to be spherically symmetric during the whole duration of the presence of the star on the asymtotic giant branch, keeping the development of an asymmetric wind for the post AGB phase. The present results obtained for RS Cnc and EP Aqr provide clear evidence for the contrary, with the presence of a bipolar wind on the AGB, even at an early phase of it in the case of EP Aqr. In the case of the Red Rectangle, the spiralling observed in the equatorial region is consistent with naive expectation but the behaviour at the abrupt interface with the expanding cones is of a less obvious nature, even if shear effects between the two volumes may play a role.

Finally, a feature common to the three stars is the presence of very important inhomogeneities of the gas density, introducing significant deviations from central and axial symmetries and seriously limiting the ability of simple models to describe the morphology of the gas envelope with sufficient precision. Such inhomogeneities are present at a very early stage of the red giant phase and are understood as convective cells appearing during the expansion of the gas envelope. As early as 1975, Schwarzschild had already suggested that convective cells at the surface of red giants should be very large and that their number should be nearly independent of the size of the envelope and in the ballpark of a hundred. Recent 3d hydrodynamical simulations have confirmed this prediction Freytag & Chiavassa (2013); Chiavassa et al. (2013). We have not attempted, in the present study, to give a detailed description of such inhomogeneities but, in the future, the availibility of high spatial resolution data from ALMA will probably make it necessary to subtract their contribution in order to describe more precisely the global evolution of the gas envelope.

8.2 H I observations

The observation of the hydrogen line is made very difficult by the presence of a strong interstellar emission in both the foreground and background, particularly important at low galactic latitudes. It took indeed a long time before the first significant observations of the H I emission of evolved stars could be obtained at the Nançay radio telescope. They made it clear that hydrogen is also present in atomic form in the circumstellar envelopes of evolved stars, and not only in molecular form as had been previously assumed to explain the absence of H I observations. Their observation, in addition to simply probing a region where molecular species have been dissociated by the interstellar UV background, provide information on the interaction between the gas envelope of the star and the interstellar medium. It results in trailing tails often displaying a significant velocity gradient.

The model that was developed for CO emission has been adapted to handle the case of H I emission at 21 cm wavelength. The simulations show the effects of self-absorption and of the background radiation on the line profiles for various cases of stellar winds. They also include the Libert et al. (2007) model, and apply it successfully to the case of Y CVn, which has been recently observed at VLA with a spatial resolution of 1′ (Matthews et al. 2013). The new Y CVn model presented here can account for the

previous high signal-to-noise ratio spectroscopic observations obtained with the Nançay radio telescope, as well as for the recent VLA spectral map. In the near future we expect to interpret more spectral maps obtained at the VLA with this model and a more elaborate version of it.

We have also included results of hydrodynamical models developed by Villaver et al. (2002) applied to the case of a mass losing Red Giant. The resulting H I profiles display too large line widths, incompatible with observations. We suspect that the cooling law adopted in the models for the material that has crossed the termination shock needs to be revised.

Finally, the simulations show that self-absorption and absorption of the background radiation cannot explain the non-detection of many cool Red Giants displaying high mass-losses. In these sources, hydrogen should be mainly in molecular, rather than in atomic, form. Nevertheless, the high sensitivity observations of IRC+10216 presented by Matthews et al. (2015) show that hydrogen might still be present in such sources at a level of 1%. Therefore, the H I line at 21 cm can still be used as a probe of the external regions of these circumstellar shells, albeit with a requirement for high sensitivity. In this respect, the FAST radiotelescope, to be operated in nearby China at the end of 2016, will be perfectly suited for the detection of H I in AGB stars with high mass-losses. As they tend to be concentrated close to the Galactic Plane, we have included in the simulations the effect of a strong background, and demonstrated that taking it in proper account will be needed to interpret the results on AGB stars from H I surveys of the Galactic Plane.

The H I image of RS Cnc using the VLA is the best available today. It shows a clear "head-tail" morphology that has been reported already in several Red Giants such as Mira (Matthews et al. 2008). The H I head is dominated by slowed down material. It shows an elongation that is consistent with the orientation of the bipolar flow revealed by CO observations, suggesting that the gap between CO and H I imaging is nearly closed.

The H I image of RS Cnc shows also a tail, likely resulting from ram-stripping of the circumstellar material by the local medium through which the star and its quasi-stationary shell are moving. The new data presented in the thesis show also clumps of material that are reminiscent of the vortices predicted by some hydrodynamical models of interaction between a stellar wind and the flowing local medium (Wareing et al. 2007). This suggests that the circumstellar matter might be injected in the ISM through vortices associated with stellar tails.

To obtain an image of higher spatial resolution is presently out of reach. It would require the combination of a large collecting area and long baselines that will be available only with the Square Kilometre Array (SKA).

8.3 Future prospects

While data obtained at the PdBI or VLA, as used in the present thesis, have made it possible to make spectacular progress in the study of evolved stars, the reliability and accuracy of the conclusions that can be drawn are still essentially limited by the sensitivity and spatial resolution of the data. In the near future the availability of NOEMA and ALMA observations at molecular wavelengths and of JVLA and

FAST observations on the hydrogen line will allow for another major step forward.

ALMA is the world-largest ground-based facility for observations at millimetre and sub-millimetre wavelengths. It is located in northern Chile on the Chajnantor plateau, 5000 metres in altitude. It includes a giant array of fifty 12-m antennas, which can be configured to achieve baselines up to 16 km. It is equipped with state-of-the-art receivers that cover all the atmospheric windows up to 1 THz. An additional compact array of 7-m and 12-m antennas enhances ALMA's ability to image extended sources. Its construction was completed in 2014. Before completion of the array at full observing power, a period of Early Science allows for an early exploitation of the facility. It is operated by an international partnership of the European Organisation for Astronomical Research in the Southern Hemisphere (ESO), the U.S. National Science Foundation (NSF) and the National Institutes of Natural Sciences (NINS) of Japan in cooperation with the Republic of Chile. A Science Portal, with which we are familiar, contains all the information and software necessary to prepare observing proposals, access data through the Science Archive and reduce ALMA data and a help-desk is available to assist the user community. Observations are available for public access one year after completion, an invaluable feature for small research teams in developing countries such as ours.

FAST, standing for Five-hundred-meter Aperture Spherical Telescope, is a gigantic fixed antenna under construction in nearby China. Its design is based on the same principle as the Arecibo antenna in Porto Rico: it rests on ground, following the natural shape of a broad basin in the mountain and the receivers are located at the focus, hanging from cables supported by high towers. It is located in Guizhou province, at some six hundred kilometres from Ha Noi. The project was initiated in the early nineties and officially approved in 2008. The construction started in 2011 and first light is expected in September 2016. It includes some 4500 moveable triangular mirror panels, made of aluminium, 10 square metres in area and weighing 500 kilograms each. They cover a spherical cap, 500 metres in diameter. The orientation of the panels can be individually tuned to form parabolas pointing to adjustable directions, resulting in an effective single dish 300 metres in diameter. FAST can cover an angular field of view reaching up to 40° from zenith. The working frequency is 0.3-3.0 GHz and the pointing accuracy is 8 arcseconds. A multi-beam receiver (19 beams) will be eventually available; however, in the early science phase (until the end of 2017), observations will be exclusively in single beam mode.

We have expressed interest for both ALMA and FAST, for ALMA by having submitted a proposal to observe EP Aqr and for FAST by having established close contacts with the science coordinator.

Appendix A

A&A 565, A54 (2014)
DOI: 10.1051/0004-6361/201423529

Astronomy & Astrophysics

The multi-scale environment of RS Cancri from CO and H I observations⋆

D. T. Hoai[1,2], L. D. Matthews[3], J. M. Winters[4], P. T. Nhung[1,2], E. Gérard[5], Y. Libert[1,4], and T. Le Bertre[1]

[1] LERMA, UMR 8112, CNRS & Observatoire de Paris, 61 av. de l'Observatoire, 75014 Paris, France
e-mail: Thibaut.LeBertre@obspm.fr
[2] VATLY/INST, 179 Hoang Quoc Viet, Cau Giay, Ha Noi, Vietnam
[3] MIT Haystack Observatory, off Route 40, Westford MA 01886, USA
[4] IRAM, 300 rue de la Piscine, Domaine Universitaire, 38406 St. Martin d'Hères, France
[5] GEPI, UMR 8111, CNRS & Observatoire de Paris, 5 place J. Janssen, 92195 Meudon Cedex, France

Received 29 January 2014 / Accepted 7 March 2014

ABSTRACT

We present a detailed study of the circumstellar gas distribution and kinematics of the semi-regular variable star RS Cnc on spatial scales ranging from ∼1″ (∼150 AU) to ∼6′ (∼0.25 pc). Our study utilizes new CO1−0 data from the Plateau de Bure Interferometer and new H I 21 cm line observations from the Jansky Very Large Array (JVLA), in combination with previous observations. New modeling of CO1−0 and CO2−1 imaging observations leads to a revised characterization of RS Cnc's previously identified axisymmetric molecular outflow. Rather than a simple disk-outflow picture, we find that a gradient in velocity as a function of latitude is needed to fit the spatially resolved spectra, and in our preferred model, the density and the velocity vary smoothly from the equatorial plane to the polar axis. In terms of density, the source appears quasi-spherical, whereas in terms of velocity the source is axisymmetric with a low expansion velocity in the equatorial plane and faster outflows in the polar directions. The flux of matter is also larger in the polar directions than in the equatorial plane. An implication of our model is that the stellar wind is still accelerated at radii larger than a few hundred AU, well beyond the radius where the terminal velocity is thought to be reached in an asymptotic giant branch star. The JVLA H I data show the previously detected head-tail morphology, and also supply additional details about the atomic gas distribution and kinematics. We confirm that the head seen in H I is elongated in a direction consistent with the polar axis of the molecular outflow, suggesting that we are tracing an extension of the molecular outflow well beyond the molecular dissociation radius (up to ∼0.05 pc). The 6′-long H I tail is oriented at a PA of 305°, consistent with the space motion of the star. The tail is resolved into several clumps that may result from hydrodynamic effects linked to the interaction with the local interstellar medium. We measure a total mass of atomic hydrogen $M_{\rm HI} \approx 0.0055\ M_{\odot}$ and estimate a lower limit to the timescale for the formation of the tail to be $\sim 6.4 \times 10^4$ years.

Key words. stars: AGB and post-AGB – circumstellar matter – stars: individual: RS Cnc – stars: mass-loss – radio lines: stars – radio lines: ISM

1. Introduction

Asymptotic giant branch (AGB) stars undergo mass loss at a high rate. One of the best tracers of AGB outflows are the rotational lines of carbon monoxide (CO). From the modeling of the line profiles it has been possible to derive reliable expansion velocities and mass loss rates (Ramstedt et al. 2008). In addition imaging at high spatial resolution allows us to describe the geometry and the kinematics of these outflows in the inner circumstellar regions where the winds emerge and where their main characteristics get established (Neri et al. 1998).

High quality observations of CO line emissions at high spectral resolution have shown that some profiles are composite, with a narrow component superimposed on a broader one, revealing the presence of two winds with different expansion velocities (Knapp et al. 1998; Winters et al. 2003). Using high spatial resolution data obtained in the CO1−0 and 2−1 lines, Libert et al. (2010) have suggested that the composite line-profiles of the semi-regular AGB star RS Cnc probably originate from an axisymmetrical geometry with a slowly expanding equatorial disk and a faster perpendicular bipolar outflow. Other cases of AGB stars with axisymmetrical expanding shells have been identified in a CO mapping survey of AGB stars by Castro-Carrizo et al. (2010). It shows that the axisymmetry which is often observed in post-AGB stars (e.g., Sahai et al. 2007) may develop earlier when the stars are still on the AGB.

Although extremely useful, CO as a tracer is limited to the inner parts of the circumstellar shells because, at a distance of typically $\sim 10^{17}$ cm, it is photo-dissociated by the interstellar radiation field (ISRF). At larger distances, it is necessary to use other tracers, such as dust or atomic species. The H I line at 21 cm has proved to be an excellent spatio-kinematic tracer of the external regions of circumstellar shells (e.g., Gérard & Le Bertre 2006; Matthews & Reid 2007). In particular, the H I map of RS Cnc presented by Matthews & Reid shows a 6′-long tail, in a direction opposite to the space motion of the central star, and clearly different from that of the bipolar flow observed in CO at shorter distances (2–10″) by Libert et al. (2010). In such a case the shaping mechanism is thought to be due to the motion of the star relative to the local interstellar medium (Libert et al. 2008; Matthews et al. 2013).

Thus, RS Cnc is an ideal target to study, in the same source, the two main effects that are expected to shape circumstellar environments and to evaluate their respective roles. In this paper, we revisit RS Cnc with new high spatial resolution data obtained

⋆ Based on observations carried out with the IRAM Plateau de Bure Interferometer and the IRAM 30 m telescope. IRAM is supported by INSU/CNRS (France), MPG (Germany) and IGN (Spain).

Table 1. Properties of RS Cnc.

Parameter	Value	Ref.
Distance	143 pc	1
MK Spectral type	M6eIb-II(S)	2
Variability type	SRc:	2
Pulsation periods	122 and 248 days	3
Effective temperature	3226 K	4
Radius	225 $R_\odot$	4
Luminosity	4945 $L_\odot$	4
LSR radial velocity ($V_\star$)	6.75 km s^{-1}	5
Expansion velocity	2.4/8.0 km s^{-1}	5
Mass loss rate	1.7×10^{-7} $M_\odot$ yr^{-1}	6
3D space velocity; PA	15 km s^{-1}; 155°	this work

References. (1) HIPPARCOS (van Leeuwen 2007); (2) GCVS (General Catalogue of Variable Stars); (3) Adelman & Dennis (2005); (4) Dumm & Schild (1998); (5) Libert et al. (2010); (6) Knapp et al. (1998).

in CO at 2.6 mm and in H I at 21 cm. Our goal is to combine observations in these two complementary tracers, in order to describe the spatio-kinematic structure of the circumstellar shell from its center to the interstellar medium (ISM). The stellar properties of RS Cnc are summarized in Table 1.

Until recently, a distance of 122 pc was adopted from the parallax measured using HIPPARCOS (Perryman et al. 1997). However, new analyses of the HIPPARCOS data have led to somewhat larger estimates of the distance, 129^{+16}_{-16} pc (Famaey et al. 2005) and 143^{+12}_{-10} pc (van Leeuwen 2007). In the present work, we adopt the improved values of the parallax and proper motions by van Leeuwen, and scale the published results with the new estimate of the distance. We also adopt the peculiar solar motion from Schönrich et al. (2010). RS Cnc is an S-type star (CSS 589, in Stephenson's 1984 catalog) in the Thermally-Pulsing AGB phase of evolution: Lebzelter & Hron (1999) reported the presence of Tc lines in its spectrum.

2. CO observations

2.1. Summary of previous data

RS Cnc was imaged in the CO1−0 and 2−1 lines by Libert et al. (2010). An on-the-fly (OTF) map covering a region of 100″ × 100″ with steps of 4″ in RA and 5″ in Dec was obtained at the IRAM 30 m telescope. Interferometric data were obtained with the Plateau de Bure Interferometer (PdBI) in three configurations, B, C, and D, i.e., with baselines ranging from 24 m to 330 m. All sets of observations were obtained with a spectral resolution corresponding to 0.1 km s^{-1}. The data from the 30 m telescope and the PdBI were merged and images in 1−0, with a field of view (fov) of 44″ and a spatial resolution of ∼2.3″, and in 2−1, with a fov of 22″ and a spatial resolution of ∼1.2″, were produced. Libert et al. presented the corresponding channel maps with a spectral resolution of 0.4 km s^{-1}.

These maps show clearly that the broad and narrow spectral components reported by Knapp et al. (1998) originate from two different regions that Libert et al. (2010) described as a slowly expanding (∼2 km s^{-1}) equatorial disk/waist and a faster (∼8 km s^{-1}) bipolar outflow. Libert et al. estimated that the polar axis lies at an inclination of ∼45° with respect to the plane of the sky and is projected almost north-south, along a position angle (PA) of ∼10°.

2.2. New data

In January and February 2011, we obtained new data in the CO1−0 line with the PdBI array in configurations A and B, increasing the baseline coverage up to 760 m.

The new data were obtained in dual polarizations and covered a bandwidth of 3.6 GHz centered at 115.271 GHz, the nominal frequency of the CO1−0 line. Two units of the narrow band correlator were set up to cover the CO line with a spectral resolution of 39 kHz over a bandwidth of 20 MHz, and the adjacent continuum was observed by the wideband correlator WideX (Wideband Express) with a channel spacing of 1.95 MHz.

These observations resulted in 12 h of on-source integration time with the six-element array and reach a 1σ thermal noise level of 12 mJy/beam in 0.2 km s^{-1} channels. The synthesized beam is 0.92″ × 0.78″ at a position angle PA = 62°.

2.3. Continuum

We used the new WideX data to produce a continuum image of RS Cnc at 115 GHz. The data were integrated over a 2 GHz band, excluding the high frequency portion of the band that is affected by atmospheric absorption. A single point source is clearly detected. The source is unresolved, and there is no evidence of a companion. It has a flux density of 5.4 ± 0.3 mJy, which is consistent with the flux density reported by Libert et al. (2010). It is slightly offset southwest with respect to the center of phase because we used the coordinates at epoch 2000.0 from HIPPARCOS. The offset (–0.15″ in RA and –0.37″ in Dec) is consistent with the proper motion reported by HIPPARCOS (−11.12 mas yr^{-1} in RA and –33.42 mas yr^{-1} in Dec, van Leeuwen 2007).

2.4. Channel maps in CO1–0

The channel maps obtained in 2011 across the CO1−0 line are dominated by a compact central source. However, at 6.6 km s^{-1} (Fig. 2), we observe a companion source at ∼1″ west-northwest (PA ∼ 300°). This source is detected from 5.8 km s^{-1} to 6.8 km s^{-1}, but not outside this range. In the channel map at 6.6 km s^{-1}, in which it is most clearly separated, it has an integrated flux of 93 ± 6 mJy, compared to 300 ± 20 mJy for the central source. This secondary source is clearly not at the origin of the bipolar outflow, which is aligned on the central source. Within errors, the central source coincides with the continuum source discussed in the previous section.

2.5. Merging (CO1–0)

Finally, the new data (observed in the extended A and B configurations) were merged with the old data already presented by Libert et al. (2010). These were obtained in the previous B, C, and D configurations and combined with short spacing observations obtained on the IRAM 30 m telescope. The final combined data set now covers a spectral bandwidth of 580 MHz, resampled to a spectral resolution of 0.2 km s^{-1}. The 1 σ thermal noise in the combined data cube is 8.7 mJy/beam (for a channel width of 0.2 km s^{-1}) and the synthesized beam is 1.15″ ×0.96″ at PA = 67°, similar to the resolution already obtained on CO2−1 (Libert et al. 2010).

In Fig. 3, we present the resulting spectral map that we derived by using a circular restoring beam with a Gaussian profile of $FWHM = 1.2''$. The line profiles are composed of three components whose relative intensities depend on the position

in the map. We also note that the two extreme components, at ~ 2 km s^{-1} and ~ 12 km s^{-1}, tend to deviate more from the central component as the distance to the central source increases. In Fig. 4, three spectra obtained in the south of the central position are overlaid. We note a shift in velocity of the red peaks, which correspond to the southern polar outflow at $\sim 12-14$ km s^{-1}, relative to the central peaks at $\sim 5-8$ km s^{-1}, which correspond to the emission close to the equatorial plane, with distance to the central source.

3. CO model

3.1. Description

In order to constrain the spatio-kinematic structure of RS Cnc, we have constructed a model of CO emission adapted to any geometry and based on a code already developed by Gardan et al. (2006). A ray-tracing approach, taking into account the velocity-dependent emission and absorption of each element along a line of sight, allows us to reconstruct the flux obtained, within an arbitrary beam, from a source with an arbitrary geometry. The density, the excitation temperature, and the velocity are defined at each point of the circumstellar shell. The code can then produce synthetic spectral maps that can be compared to the observed ones.

The populations of the rotational levels of the CO molecules are calculated assuming local thermodynamic equilibrium. The temperature profile is assumed to vary as $r^{-0.7}$, where r is the distance from the center of the star, and is scaled to models kindly provided by Schöier & Olofsson (2010, priv. comm.; Fig. 5). These profiles were obtained using the radiative transfer code developed in spherical geometry by Schöier & Olofsson (2001). The same temperatures are adopted to calculate for each element the thermal Doppler broadening, assuming a Maxwellian distribution of the velocities.

3.2. Application to RS Cnc

Following Libert et al. (2010) the source is defined by an equatorial plane and a polar axis. It is thus axisymmetric and we need only two angles, which for instance define the orientation of the polar axis. For simplicity, we will use the angle of inclination of this axis over the plane of the sky (AI), and the position angle of the projection on the plane of the sky of this axis of symmetry (PA).

We assume that the velocities are radial and that the outflows are stationary. Thus, the product $v \times n \times r^2$ (where v is the velocity, n the density, and r the distance to the center) is kept constant along every radial direction. In order to account for the velocity gradient observed in the line profiles (Fig. 4), we adopt a dependence of the velocity in r^{α}, α being the logarithmic velocity gradient (Nguyen-Q-Rieu et al. 1979).

We adopt a stellar CO/H abundance ratio of 4.0×10^{-4} (all carbon in CO, Smith & Lambert 1986). Then we take a dependence of the CO abundance ratio with r from the photodissociation model of Mamon et al. (1988) for a mass loss rate of 1.0×10^{-7} $M_{\odot}$ yr^{-1} (see below). The external limit is set at $20''$ ($\sim 4.3 \times 10^{16}$ cm). In addition, we assume an He/H abundance ratio of 1/9. The star is offset from the center of the map by the amount measured on the continuum map (Fig. 1). Finally, we adopt a stellar radial velocity $V_{\rm lsr} = 6.75$ km s^{-1} (see Table 1).

In our preferred model of RS Cnc, the density and the velocity vary smoothly from the equatorial plane to the polar

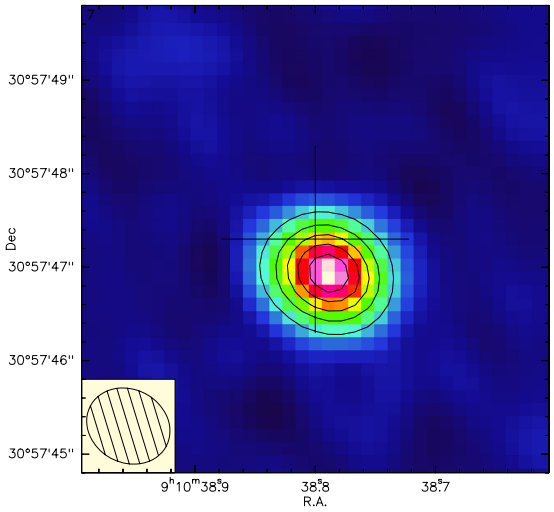

Fig. 1. Continuum map at 115 GHz of RS Cnc (A+B configuration data obtained in 2011). The cross corresponds to the 2000.0 position of the star (RA 09:10:38.800, Dec 30:57:47.30). The contour levels are separated by steps of 0.90mJy/beam ($\equiv 20\sigma$). The beam is $0.92'' \times 0.78''$ (PA = 62°).

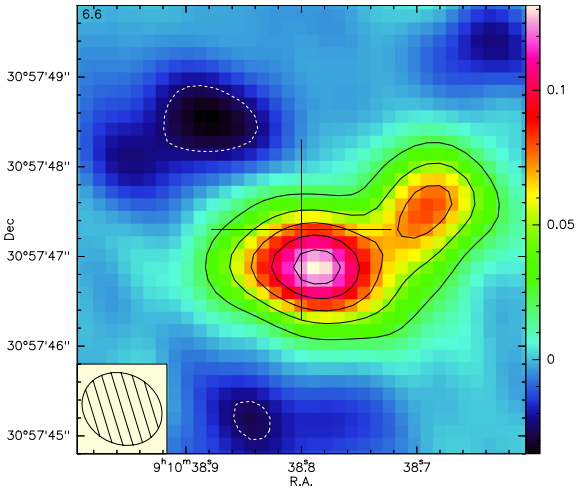

Fig. 2. Continuum subtracted CO1−0 channel map at 6.6 km s^{-1} (A+B configuration data obtained in 2011). The contour levels are separated by steps of 24 mJy/beam ($\equiv 2\sigma$). The negative contours are in dashed lines.

axis. The profiles of the density and the velocity are shown in Figs. 6 and 7, respectively. The latitude (θ, $\mu = \sin\theta$) dependence was obtained by a combination of exponential functions of μ. In order to adjust the parameters of the model we used the MINUIT package from the CERN program library (James & Roos 1975), which minimizes the sum of the square of the deviations (i.e., modeled minus observed intensities). The minimization is obtained on the CO1−0 spectral map, which has the best quality, and the same parameters are applied for the CO2−1 map. The flux of matter varies from 0.53×10^{-8} $M_{\odot}$ yr^{-1} sr^{-1} in the equatorial plane to 1.59×10^{-8} $M_{\odot}$ yr^{-1} sr^{-1} in the polar directions

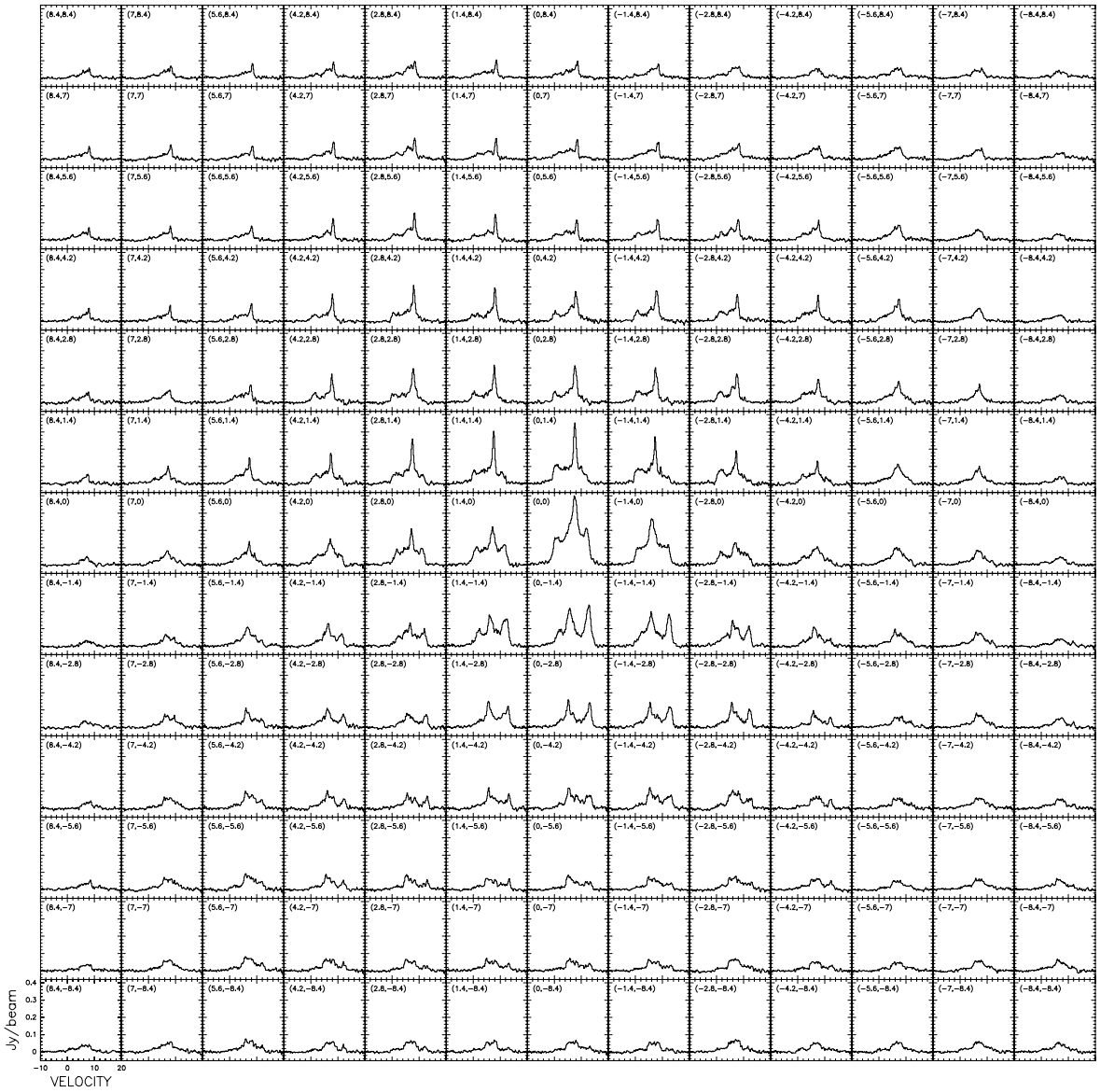

Fig. 3. CO1−0 spectral map of RS Cnc obtained with a restoring beam of 1.2″. The offsets with respect to the center of phase are given in the upper-left corner of each panel (step = 1.4″). North is up, and east is to the left.

(Fig. 8). The total mass loss rate is $1.24 \times 10^{-7}\ M_{\odot}\,\mathrm{yr}^{-1}$. The mass loss rate integrated within the two polar cones ($|\mu| > 0.5$) is $0.83 \times 10^{-7}\ M_{\odot}\,\mathrm{yr}^{-1}$. The exponent in the velocity profile varies from $\alpha = 0.13$ in the equatorial plane, to $\alpha = 0.16$ in the polar directions (Fig. 9).

In Figs. 10 and 11, we present a comparison of the spectra obtained in CO1−0 and CO2−1 together with the results of the model. We obtain a good compromise between the 2−1 and 1−0 data and the model, although with a slight excess of the model in 2−1 in particular in the central part of the map. The orientation of the source obtained with the minimization algorithm is defined by AI = 52° (angle of inclination of the polar axis over the plane of the sky), and PA = 10° (position angle of the projection of this axis over the plane of the sky).

4. VLA and JVLA observations

H I imaging observations of RS Cnc obtained with the Very Large Array (VLA) [1] in its D configuration (0.035−1.03 km baselines) were previously presented by Matthews & Reid (2007; see also Libert et al. 2010). These data were acquired

[1] The VLA of the National Radio Astronomy Observatory (NRAO) is operated by Associated Universities, Inc., under cooperative agreement with the National Science Foundation.

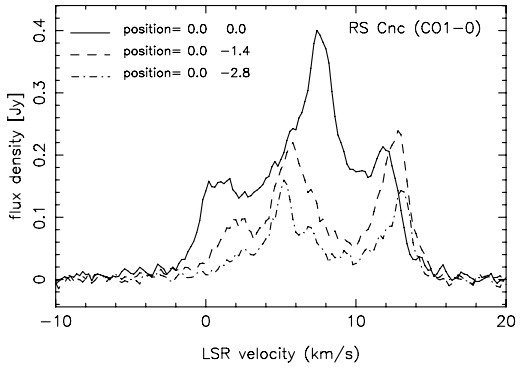

Fig. 4. Spectra obtained at different positions (center, 1.4″ south, 2.8″ south) in a beam of 1.2″ (cf. Fig. 3).

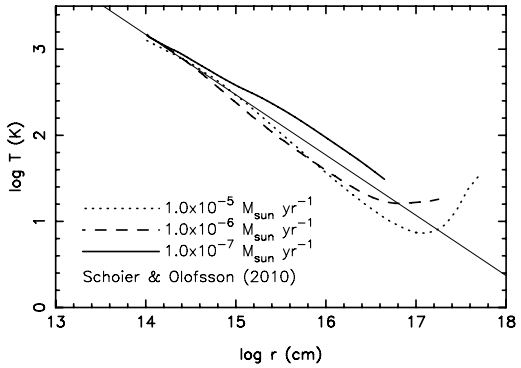

Fig. 5. Temperature profiles for different mass loss rates from Schöier & Olofsson (2010, priv. comm.). The thin line represents the temperature profile adopted here.

using dual circular polarizations and a 0.77 MHz bandpass. On-line Hanning smoothing was applied in the VLA correlator, yielding a data set with 127 spectral channels and a channel spacing of 6.1 kHz (~1.29 km s^{-1}). Further details can be found in Matthews & Reid.

For the present analysis, the VLA D configuration data were combined with new H I 21 cm line observations of RS Cnc obtained using the Jansky Very Large Array (JVLA; Perley et al. 2011) in its C configuration (0.035−3.4 km baselines). The motivation for the new observations was to obtain information on the structure and kinematics of the H I emission on finer spatial scales than afforded by the D configuration data alone, thereby enabling a more detailed comparison between the H I and CO emission (see Sect. 2).

The JVLA C configuration observations of RS Cnc were obtained during observing sessions on 2012 March 2 and 2012 April 19. A total of 4.8 h was spent on-source. Observations of RS Cnc were interspersed with observations of the phase calibrator J0854+2006 approximately every 20 minutes. We observed 3C286 (1331+305) as bandpass and absolute flux calibrator.

The JVLA WIDAR correlator was configured with eight subbands across each of two independent basebands, both of which measured dual circular polarizations. Only data from the first baseband pair (A0/C0) were used for the present analysis. Each subband had a bandwidth of 0.25 MHz with 128 spectral channels, providing a channel spacing of 1.95 kHz (~0.41 km s^{-1}).

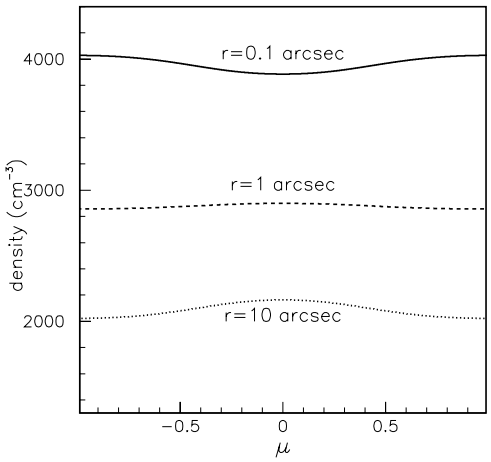

Fig. 6. Density profiles (in hydrogen atom number) in our preferred model as a function of μ (≡sin θ, θ being the angle with respect to the equator) and for various distances from the central star. The profile for r = 1 arcsec (r = 0.1 arcsec) is scaled by a factor of 1/100 (1/10 000).

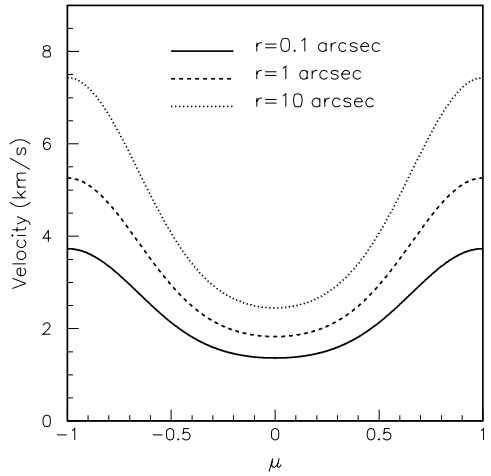

Fig. 7. Same as in Fig. 6, but for the velocity.

The eight subbands were tuned to contiguously cover a total bandwidth of 2 MHz.

The bulk of the JVLA data were taken with the central baseband frequency slightly offset from the LSR velocity of the star. However, additional observations of the phase and bandpass calibrators were made with the frequency center shifted by −1.5 MHz and +1.5 MHz, respectively, to eliminate contamination from Galactic H I emission in the band and thus permit a robust bandpass calibration and more accurate bootstrapping of the flux density scale.

Data processing was performed using the Astronomical Image Processing System (AIPS; Greisen 2003). Data were loaded into AIPS directly from archival science data model (ASDM) format files using the BDFIn program available in the Obit software package (Cotton 2008). This permitted the creation of tables containing on-line flags and system power measurements.

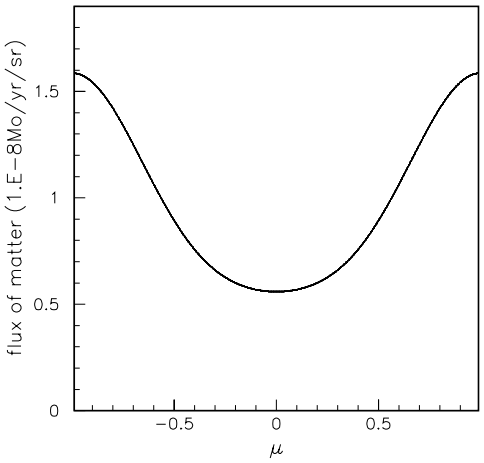

Fig. 8. Flux of matter as a function of μ.

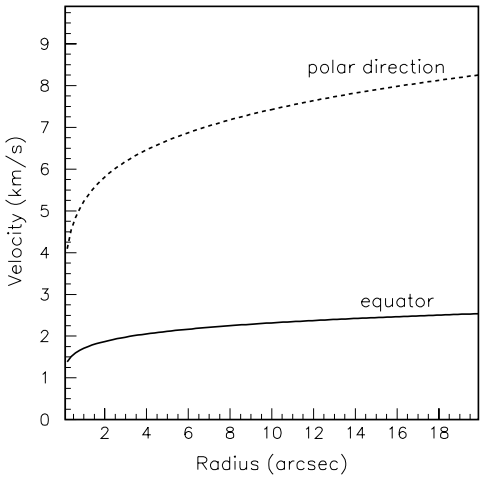

Fig. 9. Velocity profiles in the equatorial plane (μ = 0) and along the polar axis (μ = ± 1).

After updating the antenna positions and flagging corrupted data, an initial calibration of the visibility data was performed using the AIPS task TYAPL, which makes use of the system power measurements to provide optimized data weights (Perley 2010). Calibration of the bandpass and the frequency-independent portion of the complex gains was subsequently performed using standard techniques, taking into account the special considerations for JVLA data detailed in Appendix E of the AIPS Cookbook[2]. The gain solutions for the fifth subband were interpolated from the adjacent subbands because of line contamination. Following these steps, time-dependent frequency shifts were applied to the data to compensate for the Earth's motion.

4.1. Imaging the continuum

An image of the 21 cm continuum emission within a ∼50′ region centered on the position of RS Cnc was produced using only the C configuration data. After excluding the first and last two channels of each subband and the portion of the band containing line emission, the effective bandwidth was ∼1.7 MHz in two polarizations.

Robust +1 weighting (as implemented in AIPS) was used to create the continuum image, producing a synthesized beam of 17.″4 × 14.″3. The rms noise in the resulting image was ∼0.11 mJy beam^{-1}.

The brightest continuum source within the ∼30′ JVLA primary beam was located ∼12.″6 northwest of RS Cnc, with a

[2] http://www.aips.nrao.edu/cook.html

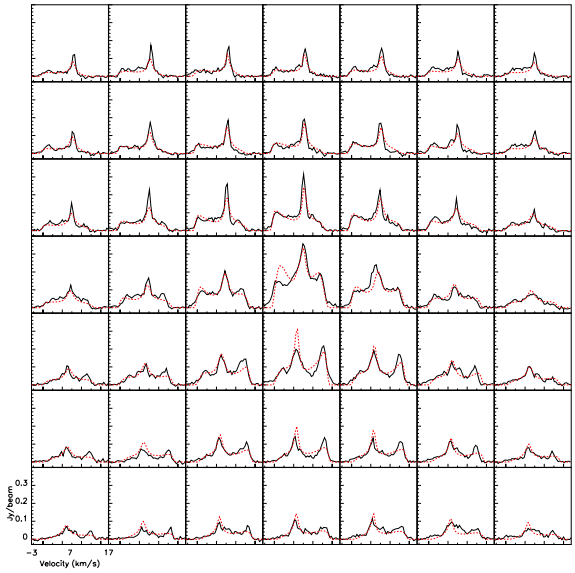

Fig. 10. Central part of the CO1−0 spectral map of RS Cnc together with the fits (dotted lines, in red in the electronic version) obtained in Sect. 3.2.

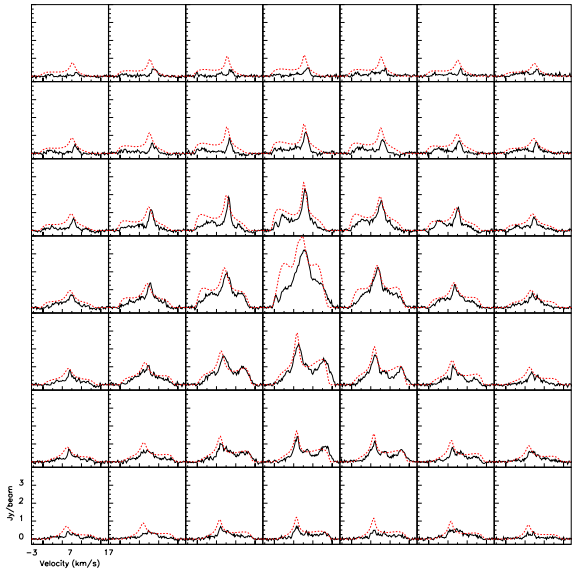

Fig. 11. Same as in Fig. 10, but for CO2−1. The original Libert et al. (2010) data have been resampled to 0.2 km s^{-1}.

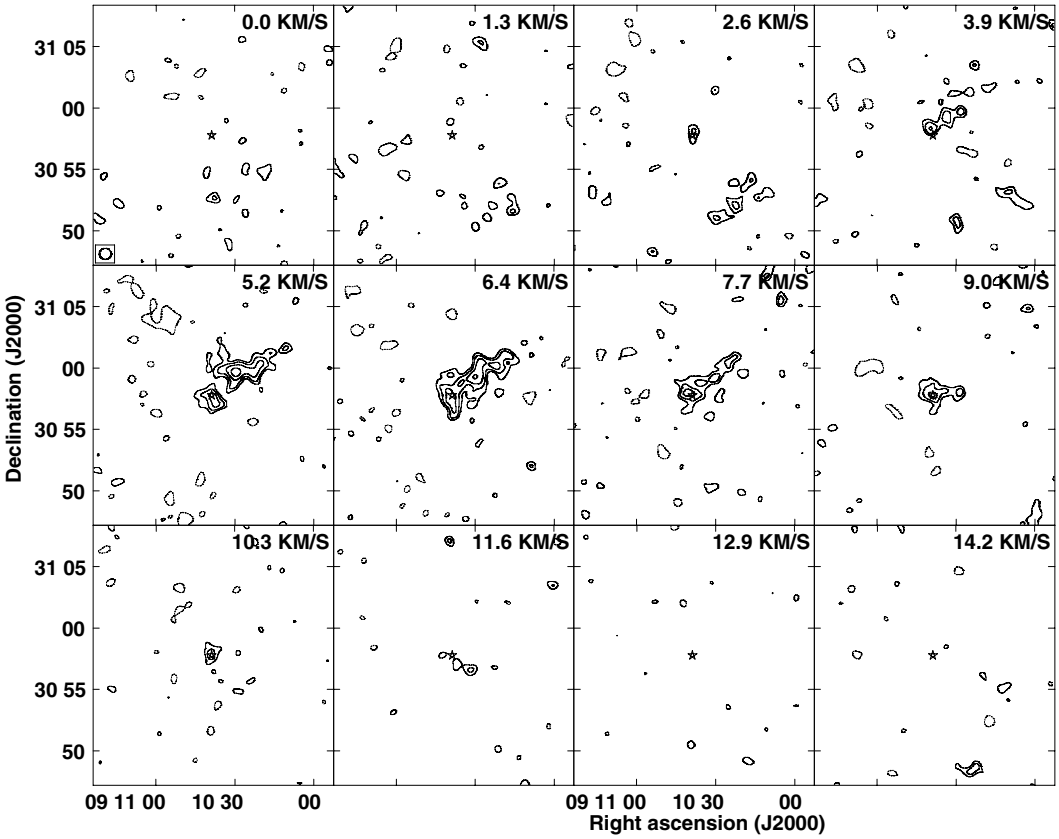

Fig. 12. H I channel images of RS Cnc obtained from combined (J)VLA C and D configuration data. Contour levels are (−6[absent], −4.2, −3, 3, 4.2, 6, 8.5) × 1.4 mJy beam^{-1}. A *u-v* tapering of 4kλ (see Sect. 4.2) was used to produce these images. The lowest contour is ∼3σ. The synthesized beam size is 57.″9 × 54.″2. The star symbol marks the stellar position of RS Cnc from HIPPARCOS.

flux density of 110 ± 1 mJy. No continuum emission was detected from RS Cnc itself, and we place a 3σ upper limit on the 21 cm continuum emission at the position of the star within a single synthesized beam to be <0.33 mJy. Using Gaussian fits, we compared the measured flux densities of the six brightest sources in the primary beam with those measured from the NRAO VLA Sky Survey (Condon et al. 1998), and found the respective flux densities to be consistent to within formal measurement uncertainties.

4.2. Imaging the HI line emission

Because the C and D configuration observations of RS Cnc were obtained with different spectral resolutions, prior to combining them the C configuration data were boxcar smoothed and then resampled to match the channel spacing of VLA D configuration data. Subsequently, the C and D configuration data sets were combined using weights that reflected their respective gridding weight sums as reported by the AIPS task IMAGR. The combined data set contained 127 spectral channels with a channel spacing of 6.1 kHz and spanned the LSR velocity range from +81.2 km s^{-1} to −81.2 km s^{-1}. Before imaging the line emission, the continuum was subtracted from the combined data set using a first order fit to the real and imaginary parts of the visibilities in the line-free portions of the band (taken to be spectral channels 10−50 and 77−188).

Three different H I spectral line image cubes were produced for the present analysis. The first used natural weighting of the visibilities, resulting in a synthesized beam size of 36.″2 × 31.″6 at a position angle (PA) of 87° and an rms noise of ∼1.1 mJy beam^{-1} per channel. For the second image cube, the visibility data were tapered using a Gaussian function with a width at the 30% level of 4 kλ in the u and v directions. This resulted in a synthesized beam of 57.″9 × 54.″1 at PA = −88° and an rms noise level of ∼1.4 mJy beam^{-1} per channel. The third data cube used Gaussian tapering of 6 kλ, resulting in a synthesized beam of 49.″5 × 44.″8 at PA = 89° and rms noise of ∼1.3 mJy beam^{-1} per channel.

5. H I imaging results

5.1. Morphology of the H I emission

Figure 12 shows H I channel images obtained from the combined (J)VLA C+D configuration data. Statistically significant emission (≥4σ) is detected at or near the stellar position over the range of LSR velocities from 2.6 to 11.6 km s^{-1}. The bulk of this emission appears to be associated with the circumstellar wake of RS Cnc. This can be seen even more clearly in Fig. 13, where we present an H I total intensity map of RS Cnc derived by summing the emission over the above velocity range.

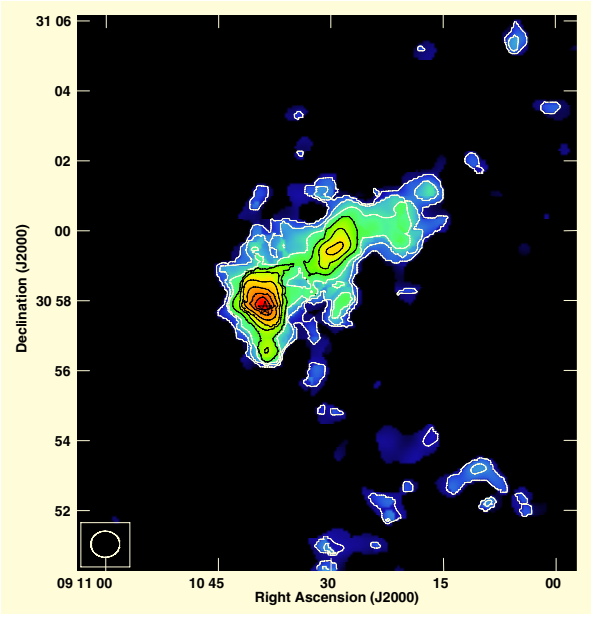

Fig. 13. H I total intensity map, derived from data with 6 kλ tapering (see Sect. 4.2). Contour levels are (1,2,3...9) × 6.6 Jy beam^{-1} m s^{-1}. This image was derived by summing the emission over the velocity range from 2.6 km s^{-1} to 11.6 km s^{-1}; to minimize the noise contribution to the map, data that did not exceed a 2σ threshold after smoothing the data spatially and spectrally by a factor of 3 were blanked. The star symbol marks the stellar position of RS Cnc.

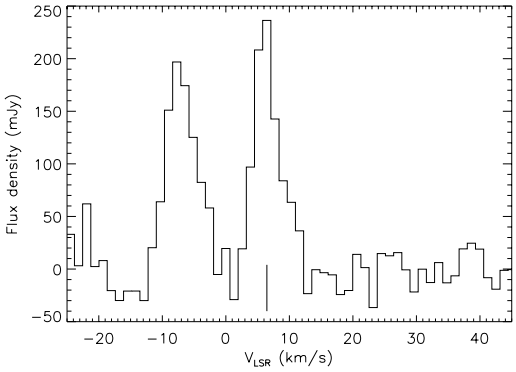

Fig. 14. Spatially integrated H I spectrum of RS Cnc derived from naturally weighted (J)VLA C+D configuration data. The vertical bar indicates the stellar systemic velocity derived from CO observations. The spectral feature centered near the stellar systemic velocity is circumstellar in origin, while the second peak near $V_{LSR} = -7$ km s^{-1} results from interstellar contamination within the measurement aperture.

As previously reported by Matthews & Reid (2007), the H I associated with RS Cnc comprises two components: a compact structure centered close to the stellar position (known as the head), of size 75″ × 40″, and an extended wake of material that is known to trail directly opposite the direction of space motion of the star (known as the tail). The tail has a measured extent of ∼6′ (∼0.25 pc) in the plane of the sky. Based on Fig. 13, we find the peak H I column density within the head of RS Cnc, ∼16″ north of RS Cnc (i.e., offset from the stellar position by roughly half a synthesized beam).

Our new H I data clearly confirm the previous suggestions that the H I emission surrounding the position of RS Cnc is elongated and that the position angle of this elongation is consistent with the CO outflow described above (see Matthews & Reid 2007; Libert et al. 2010). This is evident in the H I total intensity map (Fig. 13) and in the channel image centered at $V_{LSR} = 6.4$ km s^{-1} (Fig. 12). Figure 13 also shows evidence of two lobes of emission, extending north and south, respectively, from the more compact head of the H I emission structure. Each of these lobes extends to ∼100″ from the stellar position. The correspondence between the elongation of the H I emission in RS Cnc's head and the position angle of the molecular outflow traced in CO immediately suggest the possibility that the H I is tracing an extension of the molecular outflow beyond the molecular dissociation radius. An examination of the gas kinematics seems to reaffirm this picture (see Sect. 5.3).

5.2. Global H I spectrum and total H I mass

An integrated H I spectrum of RS Cnc is shown in Fig. 14. The narrow, roughly Gaussian shape of the line profile is typical of many of the other AGB stars detected in H I (e.g., Gérard & Le Bertre 2006; Matthews et al. 2013), but it contrasts with the two-component CO line profile of RS Cnc (Fig. 3). The H I line centroid is also slightly offset from the stellar systemic velocity derived from the CO spectra (see Table 1), and as already seen from Fig. 12, the velocity range of the detected H I emission is significantly smaller than that of the CO emission. This suggests either that the atomic hydrogen has been slowed down by its interaction with the surrounding medium and/or that the material we detect in H I emission originated during an earlier epoch of mass loss during which the maximum outflow speeds were lower.

We have derived the velocity-integrated H I flux density for RS Cnc by integrating the emission in each spectral channel in the range 2.6−11.6 km s^{-1} within a 6.′8 × 6.′4 rectangular aperture centered at the middle of the tail ($\alpha_{J2000} = 9^h10^m29.8^s$, $\delta_{J2000} = 30°58'47''.3$). We use the naturally weighted data cube for this measurement, after correcting for the attenuation of the primary beam. Using this approach, we measure an integrated H I flux density $\int S_{HI} dV = 1.14 \pm 0.03$ Jy km s^{-1}. At our adopted distance to RS Cnc, this translates to an H I mass of 5.5×10^{-3} $M_\odot$, where we have used the standard relation $M_{HI} = 2.36 \times 10^{-7} d^2 \int S_{HI} dV$. Here d is the distance in parsecs, V is the velocity in km s^{-1}, and the units of M_{HI} are solar masses.

The integrated H I flux density that we derive for RS Cnc is a factor of ∼2.5 times higher than reported previously by Matthews & Reid (2007). We attribute this difference to a combination of three factors. First, the improved sensitivity and short spacing u-v coverage of our combined C+D configuration data improves our ability to recover weak, extended emission. Second, Matthews & Reid measured the integrated emission within a series of irregularly shaped blotches in each spectral channel, defined by their outer 2σ contours. While this approach minimizes the noise contribution to each measurement, it can also exclude weak, extended emission or noncontiguous emission features from the sum. Last, Matthews & Reid measured their integrated flux density from a tapered image cube. Based on the original VLA data alone, we found that for our presently adopted measurement aperture, this results in an integrated flux density that is ∼40% lower compared with a measurement from

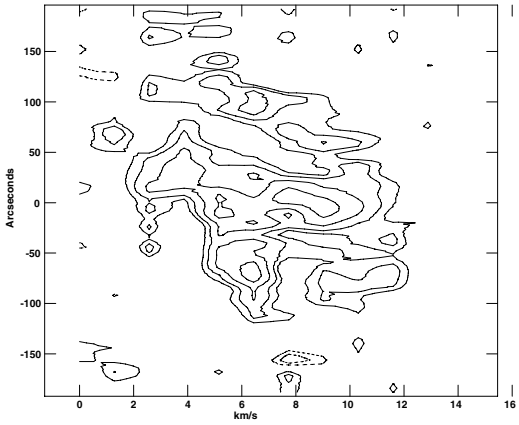

Fig. 15. H I position−velocity plot derived from naturally weighted data along PA = 10° and centered on the position of RS Cnc. Contour levels are $(-5.6[\text{absent}], -4, -2.8, -2, 2...5.6) \times 1.1$ mJy beam^{-1}. The lowest contour level is $\sim 2\sigma$. The origin of the y-axis is the stellar position.

a naturally weighted data cube. Although our new H I mass estimate is higher than the previous value reported from VLA measurements, it is significantly less than reported by Libert et al. (2010) from NRT measurements ($M_{\rm HI} \approx 0.04\ M_\odot$). We now suspect that the NRT measurement suffered from local confusion around 7 km s^{-1}.

5.3. Kinematics of the H I emission

One of the main advantages of H I 21 cm line observations for the study of circumstellar ejecta is that they provide valuable kinematic information on material at large distances from the star. For example, for the AGB stars Mira and X Her, both of which have trailing H I wakes analogous to RS Cnc, Matthews et al. (2008) and Matthews et al. (2011), respectively, measured systematic velocity gradients along the length of the circumstellar wakes and used this information to constrain the timescale of the stellar mass-loss history (see also Raga & Cantó 2008). Interestingly, RS Cnc shows no clear evidence of a velocity gradient along the length of its wake. This can be seen simply from inspection of the channel maps in Fig. 12. RS Cnc also contrasts with the other stars known to have trailing H I wakes in that its space velocity is much lower, $\sim$15 km s^{-1} compared with $V_{\rm space} \gtrsim 57$ km s^{-1} (see Matthews et al. 2013).

While no velocity gradient is seen along the tail of RS Cnc, the morphology of the tail gas reveals evidence of the importance of hydrodynamical effects. For example, a wavy structure is evident along the length of the tail in the channel image centered at $V_{\rm LSR} = 6.4$ km s^{-1} (Fig. 12). Additionally, the H I total intensity image in Fig. 13 shows a region of enhanced column density approximately half way along the length of this tail. A narrow stream of gas appears to connect this "presque isle" to the head of RS Cnc.

To facilitate comparison between the kinematics of the H I and CO emission in the CSE of RS Cnc, we present in Fig. 15 an H I position−velocity plot extracted along PA = 10° – i.e., the position angle of the CO outflow described above. This plot shows that the kinematics of the atomic gas in the head of RS Cnc are rather complex.

We see that the central region of the head ($r \lesssim \pm 50''$) contains emission spanning from $\sim$2 to 12 km s^{-1}– i.e., the full velocity range over which H I has been detected. However, all of the gas blueward of $\sim$4 km s^{-1} lies north of the stellar position. This is suggestive of a relation to the high-velocity CO outflow, in which blueshifted emission is seen north of the star. Furthermore, the velocity spread of the emission is smaller than seen in the molecular gas.

At distances of $>\pm 50''$ from RS Cnc, the gas kinematics appear different on the northern and southern sides of the head. In the south, we see evidence of H I emission near $V_{\rm LSR} \approx 6$ km s^{-1} and $V_{\rm LSR} \approx 10$ km s^{-1} extending to $\sim 100''$ from the stellar position. These features may represent the atomic counterparts to the south polar and equatorial molecular outflows, respectively. In the north, the high-latitude emission is dominated by a plume of gas whose velocity decreases from $\sim$9 km s^{-1} at $\sim 50''$ north to $\sim$6 km s^{-1} (close to the stellar systemic velocity) at $\sim 125''$ north. In Fig. 13 we see that the morphology and position angle of the emission at this location are suggestive of this being the extended northern counterpart to high-speed polar CO outflow. Alternatively, it could be material stripped from the equatorial regions.

6. Discussion

6.1. CO model

In Sect. 3.2, we presented our preferred CO model, with a continuous density distribution from the equatorial plane to the poles. However, we tried several other configurations before selecting this model. Our first trial consisted in using the model proposed by Libert et al. (2010) of a bipolar flow and of an equatorial disk, separated by a gap, and with no velocity gradient in the outflows. The calculated spectra showed spikes at $V_\star \pm 2$ km s^{-1} and $V_\star \pm 6$ km s^{-1}, corresponding to the velocities selected in the model (projected to the line of sight), whereas the observations reveal much smoother spectra. In addition, the drifts in the velocities seen in the spectral maps were not reproduced.

In a second series, we introduced a gradient in the velocities in order to reproduce these drifts, all other parameters being kept identical. The agreement was generally improved, except for the central spectra. We have thus been led to subdivide the equatorial disk, introducing an inner part (±15° of the equatorial plane) where the velocity is kept slow, and an outer part (from 30 to 45° and from –30 to –45°) where the velocity is increased. Finally, as the gap between the equatorial disk and the polar outflows does not seem physically justified, we introduced smooth functions of the latitude to describe the velocity and the density, and obtained the results presented in Sect. 3.2. With this final step, the improvement on the sum of the square of the residuals was at least of a factor of 2.

One of the conclusions of these exercises is that the notion of a disk as a separate entity is perhaps misleading. The data are consistent with a low velocity outflow that extends in latitude far from the equatorial plane. On the other hand, a high velocity outflow along the polar direction is clearly needed. Although we cannot assert that our model is a unique representation of the close environment of RS Cnc, it is the simplest that we could find and that gives an approximate reproduction of the spectral maps available in CO1−0 and 2−1. The position−velocity diagrams with two S-shaped features in opposition are often taken as evidence of disk/outflow structures (Nakashima 2005; Libert et al. 2010). In Fig. 16, we present the position (Dec)-velocity diagram in CO1−0 obtained with our preferred model. The two S-shaped features are reproduced with the correct sizes

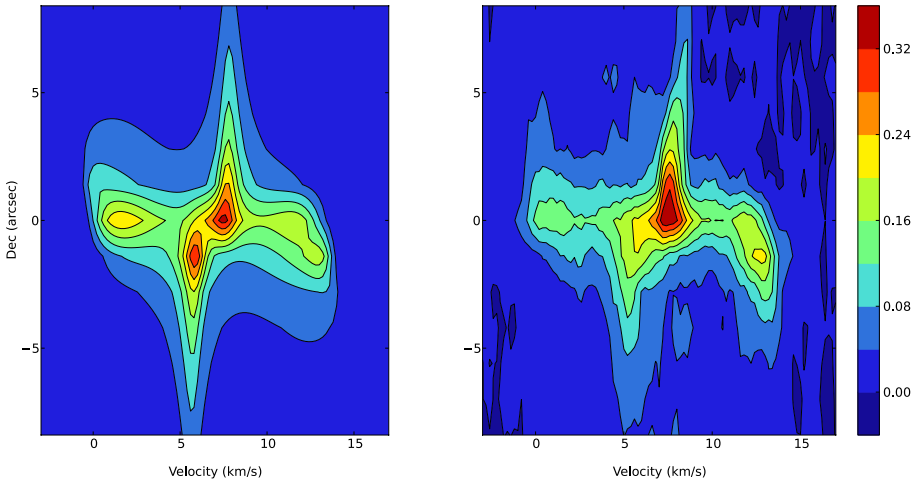

Fig. 16. *Left panel*: synthetic position−velocity diagram (offset in declination, from the 2000.0 HIPPARCOS position, against velocity) in CO1−0, obtained for our preferred model. The scale is in Jy/beam, and the channel width is 0.2 km s^{-1}. *Right panel*: observed position–velocity diagram with same conditions.

and velocity amplitudes. It illustrates that our model can also account for this kind of diagram.

The estimate of the mass loss rate that we obtain through our modeling agrees with that of Knapp et al. (1998, see Table 1), but not with that of Libert et al. (2010, $7.3 \times 10^{-7}\,M_{\odot}\,\mathrm{yr}^{-1}$ at 143 pc). The latter assumed an optically thick wind in CO1−0, which, from the present work, appears unlikely. As discussed in Winters et al. (2003), this hypothesis may lead to an overestimate of the mass loss rate by a factor of ∼3.5. We investigated the effect of the optical depth in our model, and found that self-absorption becomes effective only in the central part of the circumstellar shell in CO2−1. Furthermore, the CO2−1 and 3−2 spatially integrated spectra obtained by Knapp et al. are fitted satisfactorily by our model.

The simultaneous fit to the CO1−0, 2−1, and 3−2 data supports the temperature profiles adopted from Schöier & Olofsson (2010). However, we note that a steeper temperature profile would improve the quality of line-profile fits in the 2−1 spectral map, with almost no effect in 1−0. This is probably related to the fact that the 2−1 line starts to be optically thick for the lines of sight close to the central star. Clumpiness in the outflow could also affect the 2−1 data more than the 1−0 ones.

An intriguing feature of the modeling is the need of a velocity gradient inside the CO shell. It is needed in order to reproduce the shifts in velocity of the blue and red peaks with distance to the central star. In a stationary case, it means that the outflow is still accelerated at distances larger than a few hundred AU (a few 10^{15} cm). This is surprising because in models of dust-driven winds a terminal velocity is reached at a distance of ∼20 stellar radii (a few 10^{14} cm, e.g., Winters et al. 2000). Other acceleration processes should probably be considered, for instance the radiation force on molecules (Jørgensen & Johnson 1992), which may play a role in low mass loss rate winds.

On the other hand, evidence of accelerating outflows has been obtained in some bipolar pre-planetary nebulae. Recently Sahai et al. (2013) found a velocity gradient of 4 km s^{-1} from $\sim 4 \times 10^{16}$ to 10^{17} cm in the waist of the low-luminosity ($300\,L_{\odot}$) central star of the Boomerang Nebula (IRAS 12419–5414). Finally, although ad hoc, we cannot exclude that the flow is not stationary, and that we are witnessing a decrease with time of the expansion velocity.

In other CO models, such as that of Schöier & Olofsson (2001), the expansion velocity is assumed to be constant throughout the CO shell. It is noteworthy that in these models the goal is to reproduce the spatially integrated spectra, and that turbulence is invoked with a typical value of ∼0.5 km s^{-1} throughout the entire flow. In our modeling, we do not need to invoke turbulence.

6.2. Binarity

The presence of Tc lines in its optical spectrum shows that RS Cnc is evolving on the TP-AGB, and that it has already undergone several thermal pulses and dredge-up events. Busso & Trippella (2013, priv. comm.), using recent prescriptions for mass loss (Cristallo et al. 2011) and the revision of the s-process element production by Maiorca et al. (2012), fitted the abundances and ^{12}C/^{13}C ratio determined by Smith & Lambert (1986) with a stellar evolution model of a 1.6 $M_{\odot}$ star in its fourth dredge-up episode. RS Cnc is clearly an intrinsic S-type star that does not owe its peculiar abundances to a mass transfer from a more evolved companion (Van Eck & Jorissen 1999).

The energy distribution of RS Cnc is presented in Fig. 17. It combines UV data from GALEX (at ∼154 and 232 nm), optical data from Mermilliod (1986), near-infrared data from 2MASS, far-infrared data from IRAS, and mm data from our work. There is no clear evidence of an UV excess that might reveal the presence of a warm companion. In addition, we have found no evidence of a companion in the continuum map (Sect. 2.3). The CO structure at 6.6 km s^{-1} (see Fig. 2) may hint at the presence of a companion that might be surrounded by a disk accreting material from the wind that would be seen only in a narrow range of velocities. In that case we would have a less evolved star, probably still on the main sequence, for instance a dwarf of less than 1.6 $M_{\odot}$. However, presently, we cannot discriminate between a clump in the outflow and a cloud around a companion.

In the course of the modeling process described in Sect. 6.1, we also introduced a disk in Keplerian rotation around the central star. There was no improvement of the quality of the fits and we did not include the rotating disk in our preferred model. It means that, presently, there is no evidence in the data of such a structure. However, we cannot exclude that new data with a better spatial resolution ($\leq 1''$) would bring it into evidence. Such a structure has been invoked for X Her, another semi-regular AGB star with composite CO line-profiles, by Nakashima (2005), although it could not be confirmed by Castro-Carrizo et al. (2010).

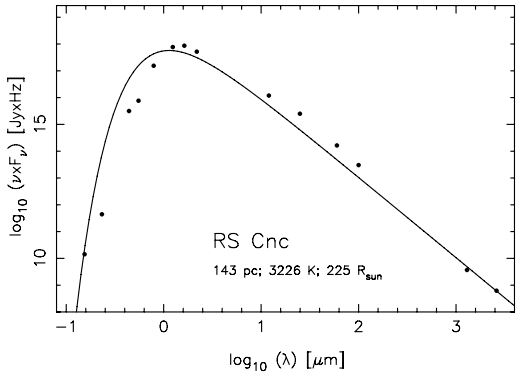

Fig. 17. Energy distribution of RS Cnc. The continuous line corresponds to a blackbody with size and temperature determined by Dumm & Schild (1998, see also Table 1).

The absence of evidence of a companion or a disk is puzzling. Another possibility to explain the axisymmetry in the outflow might be the rotation of the central star. Evidence of rotating cores in giant stars has recently been obtained by the satellites CoRoT and *Kepler* (e.g., Beck et al. 2012). These rotating cores might have an influence on the late mass loss of evolved stars when most of the stellar envelope has been removed. However, hydrodynamical models of stellar winds from rotating AGB stars predict a higher mass loss rate in the equatorial plane than in the polar directions (Dorfi & Höfner 1996; Reimers et al. 2000), which does not agree with our findings for RS Cnc (see Fig. 8). Finally, magnetic fields have been invoked to produce equatorial disks in AGB stars (e.g., Matt et al. 2010). These models also result in higher densities in the equatorial plane than in the polar directions, something that we do not observe.

6.3. Head and tail in HI

The head-tail structure revealed by the first observations of Matthews & Reid (2007) has been reaffirmed. The global shape agrees with the triangular-shaped image obtained by *Spitzer* at 70 μm (Geise 2011), although the length of the IR tail (∼4′) appears smaller than that in H I. This might be an effect of the temperature of the dust which is decreasing with distance to the central star, whereas the H I emission should not depend on temperature, and is thus a better tracer of morphology. Matthews et al. (2013) have classified the structures observed in H I around evolved stars in three categories. RS Cnc clearly belongs to their Category 1 of *"extended wakes, trailing the motions of the stars through space"*, and resulting from the dynamical interaction between stellar winds and their local ISM.

Our new JVLA data show additional detail that makes RS Cnc the best observed case. The head is elongated in a direction consistent with the polar direction determined by the CO modeling. It corresponds to the direction in which the mass loss rate is maximum. However, the velocity in H I is clearly lower than in CO, which means that the outflow has been slowed down. Nevertheless, there is presently no observational evidence of a termination shock that would mark the external limit of the freely expanding wind (Libert et al. 2007). If it really exists it must be located between 20″ (or 4×10^{16} cm, the external limit of the CO wind), and 30″ (our spatial resolution at 21 cm).

The new data show also substructures in the tail that seem to be distributed in two groups, at ∼2.5′ and 5′ from the star, that share the same elongated global shape as that of the head. They could trace past episodes of enhanced mass loss. However, the hydrodynamical models of the interaction between stellar outflows from evolved stars and the ISM tend to show that the wind variations do not remain recorded in the density or velocity structure of the gas (e.g., Villaver et al. 2002, 2012). In addition the substructures observed in the tail are evocative of the vortices suggested by numerical simulations (Wareing et al. 2007). The presence of a latitude dependence of the stellar outflow may help to develop such substructures (Raga et al. 2008).

A particularity of RS Cnc tail, as compared to the other objects in Category 1, is that there is no observed velocity gradient. It means that the tail of RS Cnc lies in the plane of the sky. This could be an effect of the small value of the stellar radial velocity. It also suggests that the local ISM shares the same radial velocity as RS Cnc. This hypothesis is supported by the ISM confusion which peaks at $\sim$7 km s^{-1} (see Figs. 11 to 13 in Libert et al. 2010, and Sect. 5.2). If this is correct it would mean that the velocity of RS Cnc relative to its surrounding medium is still smaller than its space velocity (15 km s^{-1}).

The mass in atomic hydrogen is now estimated at 0.0055 $M_\odot$. Assuming 10% of the matter in He, it translates to 0.008 $M_\odot$. This does not account for a possible component of the head-tail in molecular hydrogen and/or ionized hydrogen. Given the effective temperature of RS Cnc ($T_{\rm eff}$ = 3226 K, Table 1), the presence of the former is unlikely (Glassgold & Huggins 1983).

Adopting the present mass loss rate estimated from the CO modeling, 1.24×10^{-7} $M_\odot$ yr^{-1}, we obtain a timescale of 64×10^3 years for the formation of the head-tail structure. This estimate should be used with caution, as we observe structures in the tail that might be due to episodes of enhanced mass loss. Furthermore, models of stellar evolution generally predict a mass loss rate that increases with time.

The proper motions, corrected for solar motion (8 mas/yr in RA and 17 mas/yr in Dec), would translate to a crossing time of $\sim 2 \times 10^4$ years for a 6′ structure, a factor of 3 less than the previous estimate. Therefore, the matter in the tail appears to follow the star in its motion through space, an effect that has already been observed in the other stars of Category 1 (e.g., Mira Matthews et al. 2008).

Finally, the narrow linewidth ($\sim$4 km s^{-1}, Fig. 14) that is observed in H I can be used to constrain the temperature of the gas in the tail of RS Cnc. Assuming a Maxwellian distribution of the velocities and an optically thin emission, an H I line shows a Gaussian profile with a $FWHM = 0.214 \times T^{1/2}$. We can thus estimate the average temperature in the tail at $\lesssim$350 K. As discussed above there is no global kinematics broadening of the H I line, because the tail lies in the plane of the sky, but there might be a contribution from vortices.

6.4. Multi-scale environment of RS Cnc

It is now possible to describe the RS Cnc outflow from ∼100 AU to its interface with the ISM at distances of tens of thousands of AU from the star. In the central part, the outflow exhibits an axisymmetric morphology centered on the red giant. This structure develops on a scale ≥2000 AU, as probed by the CO lines. Our modeling shows that the flow is faster and more massive along the polar directions than in the equatorial plane. However, our present spatial resolution does not allow us to uncover the physical mechanism that shapes the outflow close to the mass losing star, nor to evaluate the nature and the role of the substructure observed at 1″ northwest around 6.6 km s^{-1}.

The H I line at 21 cm enables us to trace the outflow beyond the molecular photodissociation radius. The flow is observed to

be slowed down, and to keep the same preferential orientation, as observed in CO, over a distance of ~8000 AU (~0.04 pc). Farther away (from 0.04 pc to 0.25 pc) the flow is distorted by the motion relative to the local ISM. It takes the shape of a tail that narrows down stream, and shows substructures (~0.01 pc) that can be interpreted as vortices resulting from instabilities initiated at the level of a bow shock (Wareing et al. 2007). However, the present spatial resolution is insufficient to observe the transition between the free-flowing stellar wind and the slowed-down flow in interaction with the ISM. In addition, we do not observe the bow shock directly, perhaps because hydrogen from the ISM is ionized when crossing this interface (Libert et al. 2008).

Recent hydrodynamic models predict that tails similar to the one observed around RS Cnc may develop in the early phase of mass loss from AGB stars (Villaver et al. 2003, 2012). However, they seem to be found preferentially in stars moving rapidly through the ISM ($\geq$50 km s^{-1}). The axisymmetry of the central flow might also play a role in the development of red giant tails, as other stars which have a composite line-profile in CO also show an H I-tail (Matthews et al. 2008, 2011). The proximity of RS Cnc, the favorable observing conditions, and the well documented parameters of the system should allow us to perform a detailed comparison between observations and models.

7. Conclusions

New PdBI CO1−0 and JVLA H I interferometric data with higher spatial resolution have been obtained on the mass-losing semi-regular variable RS Cnc. These data, combined with previous information, allow us to study with unprecedented detail the flow of gas from the central star to a distance of ~10^{18} cm.

The previous CO observations of RS Cnc have been interpreted with a model consisting of an equatorial disk and a bipolar outflow. However, we find now that a better fit to the data can be obtained by invoking continuous axisymmetric distributions of the density and the velocity, in which matter is flowing faster along the polar axis than in the equatorial plane. The polar axis is oriented at a position angle (PA) of 10°, and an inclination angle (from the plane of the sky) of 52°. It is aligned on the central AGB star. The mass loss rate is ~1.24×10^{-7} $M_\odot$ yr^{-1}, with a flux of matter larger in the polar directions than in the equatorial plane. The axisymmetry appears mainly in the velocity field and not in the density distribution. This probably implies that both stellar rotation and magnetic field are not the cause of the axisymmetry. We also find that an acceleration of the outflow is possibly still at play at distances as large as 2×10^{16} cm from the central star.

The H I data obtained at 21 cm with the (J)VLA show a head-tail morphology. The head is elongated in a direction consistent with the polar axis observed in the CO lines. The emission peaks close to the star with, at the present stage, no direct evidence of a termination shock. The 6′-long tail is oriented at a PA of 305°, consistent with the proper motion of the star. It is resolved in several clumps that might develop from hydrodynamic effects linked to the interaction with the local interstellar medium. We derive a mass of atomic hydrogen of ~0.0055 $M_\odot$, and the timescale for the formation of the tail ~64×10^3 years, or more.

Acknowledgements. We acknowledge fruitful discussions with Pierre Darriulat, and are grateful for his continuous support. We are grateful to Maurizio Busso and to Oscar Trippella for their new determination of the evolutionary status of RS Cnc. We are grateful also to Hans Olofsson and to Fredrik Schöier for providing their temperature structures of AGB circumstellar shells. We thank Eric Greisen for updates to AIPS tasks that were used for this work. We thank the LIA FVPPL, the PCMI, and the ASA (CNRS) for financial support. LDM gratefully acknowledges financial support from the National Science Foundation through award AST-1310930. Financial and/or material support from the Institute for Nuclear Science and Technology, Vietnam National Foundation for Science and Technology Development (NAFOSTED) under grant number 103.08-2012.34 and World Laboratory is gratefully acknowledged. The (J)VLA data used for this project were obtained as part of programs AM798 and AM1126. This research has made use of the SIMBAD and ADS databases.

References

Adelman, S. J., & Dennis, J. W. 2005, Baltic Astron., 14, 41
Beck, P. G., Montalban, J., Kallinger, T., et al. 2012, Nature, 481, 55
Castro-Carrizo, A., Quintana-Lacaci, G., Neri, R., et al. 2010, A&A, 523, A59
Condon, J. J., Cotton, W. D., Greisen, E. W., et al. 1998, AJ, 115, 1693
Cotton, W. D. 2008, PASP, 120, 439
Cristallo, S., Piersanti, L., Straniero, O., et al. 2011, ApJS, 197, 17
Dorfi, E. A., & Höfner, S. 1996, A&A, 313, 605
Dumm, T., & Schild, H. 1998, New Astron., 3, 137
Famaey, B., Jorissen, A., Luri, X., et al. 2005, A&A, 430, 165
Gardan, E., Gérard, E., & Le Bertre, T. 2006, MNRAS, 365, 245
Geise, K. M. 2011, Master's Thesis, University of Denver, USA
Gérard, E., & Le Bertre, T. 2006, AJ, 132, 2566
Glassgold, A. E., & Huggins, P. J. 1983, MNRAS, 203, 517
Greisen, E. W. 2003, in Information Handling in Astronomy-Historical Vistas, ed. A. Heck (Dordrecht: Kluwer), 109
James, F., & Roos, M. 1975, Comput. Phys. Commun., 10, 343
Jørgensen, U. G., & Johnson, H. R. 1992, A&A, 265, 168
Knapp, G. R., Young, K., Lee, E., & Jorissen, A. 1998, ApJS, 117, 209
Lebzelter, T., & Hron, J. 1999, A&A, 351, 533
Libert, Y., Gérard, E., & Le Bertre, T. 2007, MNRAS, 380, 1161
Libert, Y., Le Bertre, T., Gérard, E., & Winters, J. M. 2008, Proc. SF2A-2008, eds. C. Charbonnel, F. Combes, & R. Samadi, 317
Libert, Y., Winters, J. M., Le Bertre, T., Gérard, E., & Matthews, L. D. 2010, A&A, 515, A112
Maiorca, E., Magrini, L., Busso, M., et al. 2012, ApJ, 747, 53
Mamon, G. A., Glassgold, A. E., & Huggins, P. J. 1988, ApJ, 328, 797
Matt, S., Balick, B., Winglee, R., & Goodson, A. 2010, ApJ, 545, 965
Matthews, L. D., & Reid, M. J. 2007, AJ, 133, 2291
Matthews, L. D., Libert, Y., Gérard, E., Le Bertre, T., & Reid, M. J. 2008, ApJ, 684, 603
Matthews, L. D., Le Bertre, T., Gérard, E., Johnson, M. C., & Dame, T. M. 2011, AJ, 141, 60
Matthews, L. D., Le Bertre, T., Gérard, E., & Johnson, M. C. 2013, AJ, 145, 97
Mermilliod, J.-C. 1986, Catalogue of Eggen's UBV data
Nakashima, J. 2005, ApJ, 620, 943
Neri, R., Kahane, C., Lucas, R., Bujarrabal, V., & Loup, C. 1998, A&AS, 130, 1
Nguyen-Q-Rieu, Laury-Micoulaut, C., Winnberg, A., & Schultz, G. V. 1979, A&A, 75, 351
Perley, R. A. 2010, EVLA Memo 145, http://www.aoc.nrao.edu/evla/geninfo/memoseries/evlamemo145.pdf
Perley, R. A., Chandler, C. J., Butler, B. J., & Wrobel, J. M. 2011, ApJ, 739, L1
Perryman, M. A. C., Lindegren, L., Kovalevsky, J., et al. 1997, A&A, 323, L49
Raga, A. C., & Cantó, J. 2008, ApJ, 685, L141
Raga, A. C., Cantó, J., De Colle, F., et al. 2008, ApJ, 680, L45
Ramstedt, S., Schöier, F. L., Olofsson, H., & Lundgren, A. A., 2008, A&A, 487, 645
Reimers, C., Dorfi, E. A., & Höfner, S. 2000, A&A, 354, 573
Sahai, R., Morris, M., Sánchez Contreras, C., & Claussen, M. 2007, AJ, 134, 2200
Sahai, R., Vlemmings, W. H. T., Huggins, P. J., Nyman, L.-Å., & Gonidakis, I. 2013, ApJ, 777, 92
Schöier, F. L., & Olofsson, H. 2001, A&A, 368, 969
Schönrich, R., Binney, J., & Dehnen, W. 2010, MNRAS, 403, 1829
Smith, V. V., & Lambert, D. L. 1986, ApJ, 311, 843
Stephenson, C. B. 1984, Publ. Warner & Swasey Obs., 3, 1
Van Eck, S., & Jorissen, A. 1999, A&A, 345, 127
van Leeuwen, F. 2007, HIPPARCOS, the New Reduction of the Raw Data (Springer), Astrophysics and Space Science Library, 350
Villaver, E., García-Segura, G., & Manchado, A. 2002, ApJ, 571, 880
Villaver, E., García-Segura, G., & Manchado, A. 2003, ApJ, 585, L49
Villaver, E., Manchado, A., & García-Segura, G. 2012, ApJ, 748, 94
Wareing, C. J., Zijlstra, A. A., & O'Brien, T. J. 2007, ApJ, 660, L129
Winters, J. M., Le Bertre, T., Jeong, K. S., Helling, C., & Sedlmayr, E. 2000, A&A, 361, 641
Winters, J. M., Le Bertre, T., Jeong, K. S., Nyman, L.-Å., & Epchtein, N. 2003, A&A, 409, 715

Appendix B

Monthly Notices of the ROYAL ASTRONOMICAL SOCIETY

MNRAS **449,** 2386–2395 (2015) doi:10.1093/mnras/stv486

Modelling the H I 21-cm line profile from circumstellar shells around red giants

D. T. Hoai,[1,2] P. T. Nhung,[1,2] E. Gérard,[3] L. D. Matthews,[4] E. Villaver[5] and T. Le Bertre[1]★

[1]*LERMA, UMR 8112, CNRS & Observatoire de Paris/PSL, 61 av. de l'Observatoire, F-75014 Paris, France*
[2]*VNSC/VAST, 18 Hoang Quoc Viet, Cau Giay, 10000 Hanoi, Vietnam*
[3]*GEPI, UMR 8111, CNRS & Observatoire de Paris/PSL, 5 place J. Janssen, F-92195 Meudon Cedex, France*
[4]*MIT Haystack Observatory, Off Route 40, Westford, MA 01886, USA*
[5]*Departamento de Física Teórica, Universidad Autónoma de Madrid, Cantoblanco 28049 Madrid, Spain*

Accepted 2015 March 3. Received 2015 March 3; in original form 2015 February 2

ABSTRACT

We present H I line profiles for various models of circumstellar shells around red giants. In the calculations we take into account the effect of the background at 21 cm, and show that in some circumstances it may have an important effect on the shape and intensity of the observed line profiles. We show that self-absorption should also be considered depending on the mass-loss rate and the temperature reached by circumstellar gas. H I emission from circumstellar shells has been mostly reported from stars with mass-loss rates around 10^{-7} $M_\odot$ yr^{-1}. We discuss the possible reasons for the non-detection of many sources with larger mass-loss rates that are hallmarks of the end of the asymptotic giant branch (AGB) phase. Although radiative transfer effects may weaken the line emission, they cannot alone account for this effect. Therefore, it seems likely that molecular hydrogen, rather than atomic hydrogen, dominates the composition of matter expelled by stars at the end of their evolution on the AGB. However sensitive H I observations can still yield important information on the kinematics and physical properties of the circumstellar material at large distances from central stars with heavy mass-loss, despite the low abundance of atomic hydrogen.

Key words: stars: AGB and post-AGB – circumstellar matter – stars: individual: Y CVn – stars: mass-loss – radio lines: stars.

1 INTRODUCTION

Asymptotic giant branch (AGB) stars are undergoing mass-loss via slow stellar winds (Olofsson 1999). They get surrounded by expanding circumstellar shells that are well characterized by CO emission lines in the millimetre range (Knapp & Morris 1985; Loup et al. 1993). From the modelling of the CO line profiles, expansion velocities are derived to be in the range from a few to 40 km s^{-1}, and mass-loss rates, from $\sim 10^{-7}$ to a few 10^{-4} $M_\odot$ yr^{-1}.

Most of the matter in circumstellar shells should be in hydrogen ($\sim$70 per cent in mass). Early searches for 21-cm line emission from atomic hydrogen were mostly unsuccessful (Zuckerman, Terzian & Silverglate 1980; Knapp & Bowers 1983) leading to the conclusion that hydrogen in stellar envelopes is molecular rather than atomic. However, more recently, the H I line at 21 cm has been detected from several AGB stars (Gérard & Le Bertre 2006). A number of the detected stars have also been imaged in H I with the Very Large Array (VLA; Matthews & Reid 2007; Matthews et al. 2008, Matthews et al. 2011, 2013). In general, the detected sources have mass-loss rates $\sim 10^{-7}$ $M_\odot$ yr^{-1}, and they show a narrow H I line profile (3–5 km s^{-1}). On the other hand, many sources with large mass-loss rate ($\geq 10^{-6}$ $M_\odot$ yr^{-1}) remain undetected.

Again, a possible explanation could be that hydrogen in sources with large mass-loss rates is mostly in molecular form. However, this is not entirely satisfactory for at least two reasons. First, molecular hydrogen is expected to be photodissociated by UV photons from the interstellar radiation field (ISRF) in the external parts of circumstellar shells (Morris & Jura 1983). Secondly, the mass-loss rate from AGB stars is supposed to be highly variable (e.g. Vassiliadis & Wood 1993), so that a given star should be surrounded by interacting shells, originating from different episodes of mass-loss at different rates, from 10^{-8} $M_\odot$ yr^{-1} upwards, and different velocities (Villaver, García-Segura & Manchado 2002), with probably a mix of atomic and molecular hydrogen.

Another possibility is that radiative transfer effects are weakening the 21-cm line emission, thus rendering difficult the detection of H I. The narrowness of the line profiles could increase the optical depth

★ E-mail: thibaut.lebertre@obspm.fr

at particular frequencies, thus exacerbating self-absorption. The presence of an intense background at 21 cm may also play a role (Levinson & Brown 1980). In this paper, we examine the formation of the H I line in circumstellar shells around AGB stars, taking into account these effects.

2 CONTEXT

Hydrodynamical models of dust-forming long-period variable stars reproduce outflows with mass-loss rate ranging from $\sim 10^{-8}$ to 10^{-4} $M_\odot$ yr^{-1}, and expansion velocity ranging from a few to 40 km s^{-1} (Winters et al. 2000). Close to the central star, the density is much larger than in the interstellar medium (ISM), and the wind expands freely (freely expanding wind). We hereafter refer to the case where the wind expands freely as scenario 1. However, at some point, the stellar wind is slowed down by the ambient medium, and a structure develops in which both circumstellar and interstellar matter accumulates. Such structures were discovered with *IRAS* owing to the presence of spatially resolved 60-μm continuum emission (Young, Phillips & Knapp 1993) and are referred to as 'detached shells'.[1]

Subsequently, the H I line at 21 cm was detected in the direction of several resolved *IRAS* sources (Le Bertre & Gérard 2004; Gérard & Le Bertre 2006). The H I emission is more extended than the CO emission and generally corresponds with the far-infrared size. Also the main components of the H I line are narrower than the CO line profiles, thus demonstrating that stellar outflows are slowed down by an external medium, and that the H I line profiles can be used to probe the kinematics in the external regions of circumstellar shells. Imaging obtained with the VLA has revealed detached H I shells with narrow-line profiles, sometimes associated with extended tails (Matthews et al. 2013).

Libert, Gérard & Le Bertre (2007) developed a model of a detached shell (hereafter scenario 2) adapted to the H I emission from the prototypical case of Y CVn. In this model, a double-shock structure develops, with a termination shock, facing the central star, where the supersonic stellar wind is abruptly slowed down, and a leading shock (i.e. outward facing shock) where interstellar matter is compressed and integrated in the detached shell. These two limits define the detached shell which is thus composed of circumstellar and interstellar matter separated by a contact discontinuity. The circumstellar matter is decelerated, by a factor ∼4, when it crosses the termination shock, and heated. It then cools down, while the expansion velocity further decreases and the density increases until the contact discontinuity. The model assumes spherical symmetry and stationarity. Adopting an arbitrary temperature profile, the equation of motion is solved numerically between the two limits of the detached shell. The H I line profile is then calculated assuming that the emission is optically thin.

Libert et al. (2007) could reproduce the H I line profile observed in Y CVn and generalize the model to other cases of sources with mass-loss rates of about 10^{-7} $M_\odot$ yr^{-1} (e.g. Libert et al. 2010). However, as discussed in Matthews et al. (2013), although this model is effective in reproducing spatially integrated line profiles, it faces some difficulties in reproducing the spatial distribution of the H I emission. Namely, at small radii, it seems to predict too much flux in both the shell component and the freely expanding wind component of the spectral profile. The mass-loss variations with time and the interaction between consecutive shells may need to be taken into account (see Villaver et al. 2002). The more elaborate numerical modelling performed by Villaver et al. follows the mass-loss and velocity variations of the stellar winds of thermally pulsing AGB (TP-AGB) stars, and describes self-consistently the formation and development of circumstellar shells embedded in the ISM (hereafter scenario 3). They show that large regions (up to 2.5 pc) of neutral gas may be formed around AGB stars.

In this work, we will simulate the H I line profiles that would be expected for these three kinds of scenarios and examine how they compare with observations presently available.

[1] This designation has also been used for shells resulting from an outburst of mass-loss and observed in CO molecular lines (Olofsson et al. 2000). In this paper, we adopt to the definition of Young et al.

3 GENERAL COMMENTS ON THE FORMATION OF THE H I LINE PROFILE

The H I line at 21 cm is produced by a transition between two levels of the ground state of hydrogen. The rest frequency, ν_0, corresponds to 1420.4 MHz, and the transition probability, A_{21}, to 2.87 10^{-15} s^{-1}. As the transition probability between the two levels is very low, the natural width of the line is extremely small, and the frequency dependence of the absorption and emission coefficients are entirely defined by the atomic hydrogen velocity. This is determined by the bulk motion of the gas (including, if present, turbulence), and the hydrogen kinetic temperature (T). We assume local thermal equilibrium. Also, in general, as the frequencies are small, one may replace $\exp(h\nu/kT) - 1$, by $h\nu/kT$ ($h\nu/k \sim 0.07$ K).

The intensity emitted, at a frequency ν, along an element ds, dI_ν, is given by

$$\frac{\mathrm{d}I_\nu}{\mathrm{d}s} = \frac{h\nu}{4\pi} n_2(v) A_{21}, \tag{1}$$

where $n_2(v)$ is the number density of hydrogen atoms in the upper level with a velocity along the line of sight corresponding to ν.

Similarly the absorption part is given by

$$\frac{\mathrm{d}I_\nu}{\mathrm{d}s} = -\kappa(\nu) I_\nu, \tag{2}$$

with the absorption coefficient, $\kappa(\nu)$, given by

$$\kappa(\nu) = \frac{c^2 n_1(v) g_2}{8\pi {\nu_0}^2 g_1} A_{21} \frac{h\nu}{kT} \tag{3}$$

(cf. equation 3.14 in Lequeux 2005). g_2 and g_1 are the statistical weights of the upper and lower levels, respectively, and $n_1(v)$ is the number density of hydrogen atoms in the lower level with a velocity along the line of sight corresponding to ν. It is interesting to note that, in general, the absorption coefficient varies as $1/T$.

For the H I line at 21 cm: $g_1 = 1$, $g_2 = 3$, and for a population in statistical equilibrium, $n_1 = 1/4\, n_\mathrm{H}$, and $n_2 = 3/4\, n_\mathrm{H}$, where n_H is the total number density of hydrogen atoms in the ground state ($n_\mathrm{H} = n_1 + n_2$), and assuming $\exp(h\nu/kT) = 1$ for the Boltzmann factor.

In practice, spectra are represented as a function of the velocity, V. We may thus replace $n_1(v)$ by $1/4\, n_\mathrm{H}(V)$ and $n_2(v)$ by $3/4\, n_\mathrm{H}(V)$. With this convention, the absorption coefficient can be rewritten as

$$\kappa(V) = \frac{3c^2 n_\mathrm{H}(V)}{32\pi\nu_0} A_{21} \frac{h}{kT}. \tag{4}$$

Finally, the radiative transfer equation is written as

$$\frac{\mathrm{d}I(V)}{\mathrm{d}s} = \frac{3\,h\nu_0}{16\pi} n_\mathrm{H}(V) A_{21} - \frac{3c^2 n_\mathrm{H}(V)}{32\pi\nu_0} A_{21} \frac{h}{kT} I(V). \tag{5}$$

At radio frequencies, it is usual to express the intensity in terms of the equivalent temperature of a blackbody that would give the same intensity in the same spectral domain. With this convention, the boundary condition can be defined through a background brightness temperature, $T_{\rm BG}$

$$I^{+}(V) = \frac{2k\nu_0^2}{c^2} T_{\rm BG}(V), \quad (6)$$

I^{+} referring to the incoming intensity on the rear side of the shell. The background is the sum of the 3-K cosmic emission, the synchrotron emission from the Galaxy and the H I emission from the ISM located beyond the circumstellar shell with respect to the observer. The first component is a continuum emission, which is smooth, angularly and spectrally. The second component is also smooth spectrally, but it presents a strong dependence with galactic latitude, and shows also some substructures. The sum of these two components has been mapped with a spatial resolution of 0.°6 by Reich (1982), Reich & Reich (1986) and Reich, Testori & Reich (2001). The third component (H I emission from the ISM) shows both strong spatial and spectral dependences, which make it a serious source of confusion. It has been mapped with a spatial resolution of 0.°6 and a spectral resolution of 1.3 km s^{-1} by Kalberla et al. (2005; Leiden–Argentina–Bonn, LAB, survey). Surveys of selected regions of the sky, in particular along the Galactic plane, have been obtained at a resolution down to 1 arcmin, and show spatial structures, like filaments or clouds, at all sizes (e.g. Stil et al. 2006).

Away from the Galactic plane, typical values range from $T_{\rm BG} \sim$ 3–5 K, outside the range of interstellar H I emission, to $T_{\rm BG} \sim$ 10–20 K inside an interstellar H I emission. Close to the Galactic plane, the continuum may reach $T_{\rm BG} \sim$ 10–20 K, and, including the interstellar H I emission, the background may reach $T_{\rm BG} \sim$ 100 K. Note that the background temperature, $T_{\rm BG}$, is not directly related to the kinetic temperature of the surrounding ISM.

In addition, in some cases, a radio source may be seen in the direction of a circumstellar shell. In such a case, we have an unresolved continuum emission (see e.g. Matthews et al. 2008). Such a source may be useful to probe the physical conditions within the circumstellar shell in a pencil-beam mode.

4 SIMULATIONS

For this work, we adapted the code developed by Hoai et al. (2014). It is a ray-tracing code that takes into account absorption and emission in the line profile. It can handle any kind of geometry, but for the purpose of this paper we restricted our simulations to circumstellar shells with a spherical geometry as described in Section 2. We assume that, in each cell, the gas is in equilibrium and that the distribution of the velocities is Maxwellian.

In this section, we explore the line profiles for a source that is not resolved spatially by the telescope, and assume a uniform response in the telescope beam (boxcar response, cf. Gardan, Gérard & Le Bertre 2006). We also assume that the line profiles can be extracted from position-switched observations, i.e. that there is no spatial variation of the background. The flux densities are expressed in the units of Jansky (Karl Jansky), where 1 Jy = 10^{-26} W m^{-2} Hz^{-1}.

We performed various tests in order to evaluate the accuracy of the simulations. It depends mainly on the mass-loss rate of the central source and on the size of the geometrical steps adopted in the calculations. For the results presented in this section, the relative error on the line profile ranges from $\sim 10^{-6}$, for mass-loss rates of 10^{-7} M$_\odot$ yr^{-1}, to a few 10^{-3}, for mass-loss rates of 10^{-4} M$_\odot$ yr^{-1}.

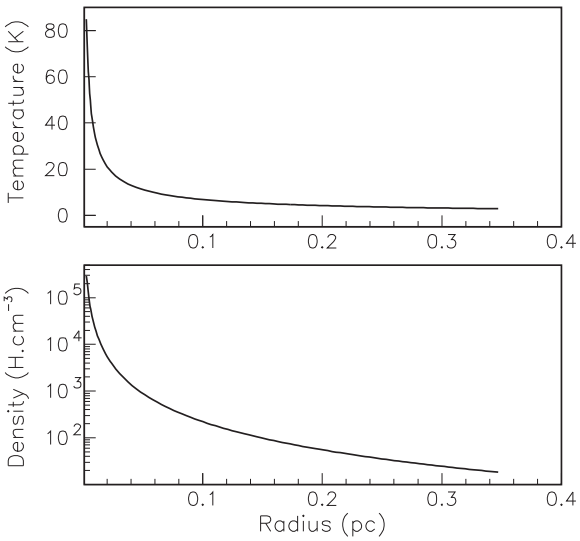

Figure 1. Density and temperature profiles for an outflow in uniform expansion (scenario 1, $V_{\rm exp} = 10$ km s^{-1}, $\dot{M} = 10^{-5}$ M$_\odot$ yr^{-1}).

4.1 Freely expanding wind (scenario 1)

We consider a spherical wind in free expansion at $V_{\rm exp}$=10 km s^{-1}. The distance is set at 200 pc, and the mass-loss rate is varied from 10^{-7} to 10^{-4} M$_\odot$ yr^{-1}. We assume that the gas is composed, in number, of 90 per cent atomic hydrogen and 10 per cent ^{4}He. We assume a temperature dependence proportional to $r^{-0.7}$, r being the distance to the central star, out to the external boundary (0.17 pc) where the temperature drops to 5 K. This temperature of 5 K is probably underestimated as the photoelectric heating by grains absorbing UV photons is expected to raise the temperature of the gas in the cool external layers of shells around stars with high mass-loss rate (Schöier & Olofsson 2001). On the other hand, temperatures as low as 2.8 K have been reported in some high mass-loss rate sources (e.g. U Cam; Sahai 1990). Such low temperatures are only expected in the freely expanding regions of the circumstellar shells. The density and temperature profiles are illustrated in Fig. 1 for the 10^{-5} M$_\odot$ yr^{-1} case.

In a first set of simulations (Fig. 2), we calculate the integrated emission (within a diameter, $\phi = 6$ arcmin) with no background, in order to estimate the effect of self-absorption (in fact the background should have a minimum brightness temperature of 3 K, cf. Section 3). Self-absorption starts to play a clear role for 10^{-6} M$_\odot$ yr^{-1}, with an intensity that is reduced, and a profile that changes its shape from almost rectangular to parabolic. A slight asymmetry of the line profile is also present (although not discernible by eye in the figure), with more absorption on the blue side, due to the outwardly decreasing temperature, an effect which has already been described in the case of molecular emission from expanding circumstellar envelopes (Morris, Lucas & Omont 1985).

In a second set of simulations, the mass-loss rate is kept at 10^{-5} M$_\odot$ yr^{-1}, and the background is varied from 0 K (as above) to 10 K (Fig. 3). The effects noted previously are amplified by the background, in particular with an absorption developing on the blue side of the profile, and then extending to the complete spectral domain when the background temperature reaches 10 K.

We adopted a temperature dependence proportional to $r^{-0.7}$ which fits the results obtained with a radiative transfer model by

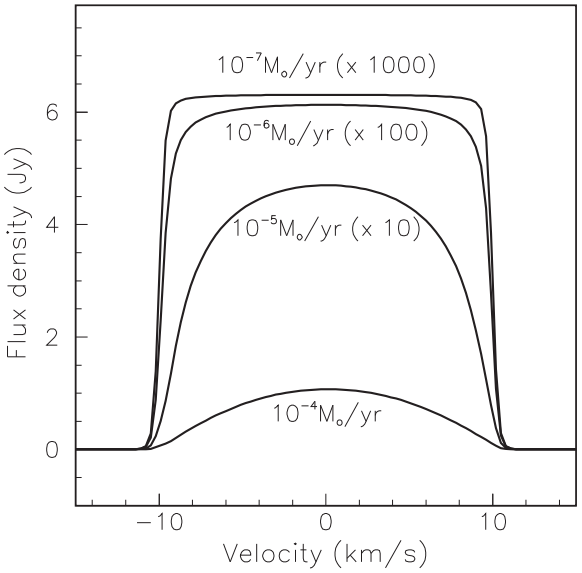

Figure 2. H I line profiles of shells in free expansion for various mass-loss rates with no background. The profiles for 10^{-7}, 10^{-6} and 10^{-5} $M_\odot$ yr^{-1} are scaled by factors 1000, 100, and 10, respectively. The distance is set at 200 pc.

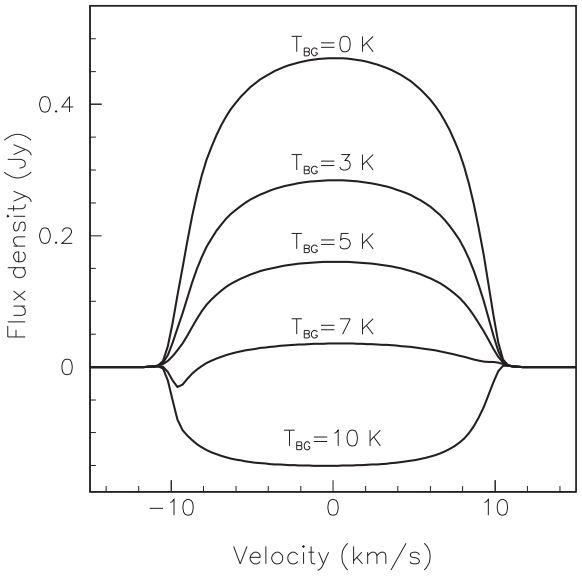

Figure 3. H I line profiles of a shell in free expansion for $\dot{M}$ = 10^{-5} $M_\odot$ yr^{-1}, and for various background levels (T_{BG} = 0, 3, 5, 7, 10 K).

Schöier & Olofsson (2001). A shallower dependence would increase the temperature in the outer layers of the circumstellar shell and thus reduce the effects of self-absorption, as well as the absorption of the background radiation. An external source of heating (e.g. by photoelectric heating) would have the same influence.

4.2 Single detached shell (scenario 2)

We adopt the model developed by Libert et al. (2007). It has been shown to provide good spectral fits of the H I observations obtained on sources with mass-loss rates $\sim 10^{-7}$ $M_\odot$ yr^{-1} (cf. Section 2).

As in Section 4.1, we assume a spatially unresolved source at 200 pc with a mass-loss rate of 10^{-7} $M_\odot$ yr^{-1}. The internal radius of the detached shell is set at 2.5 arcmin (or 0.15 pc). Similarly, we examine the dependence of the line profile for models with various masses in the detached shell ($M_{DT,\,CS}$) and various background levels (Figs 4 and 5). The parameters of the four cases illustrated in Fig. 4 are given in Table 1. The free-wind expansion velocity is taken to be V_{exp}= 8 km s^{-1}. At the termination shock the downstream

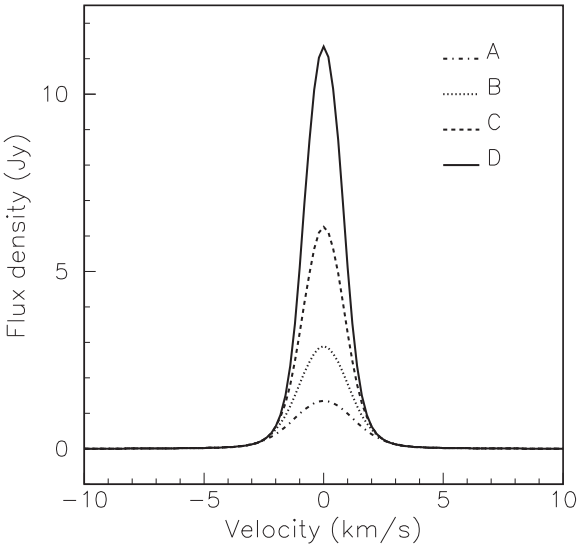

Figure 4. H I line profiles of single detached shells for various circumstellar masses (A: 0.05 $M_\odot$, B: 0.1 $M_\odot$, C: 0.2 $M_\odot$, D: 0.4 $M_\odot$,), no background.

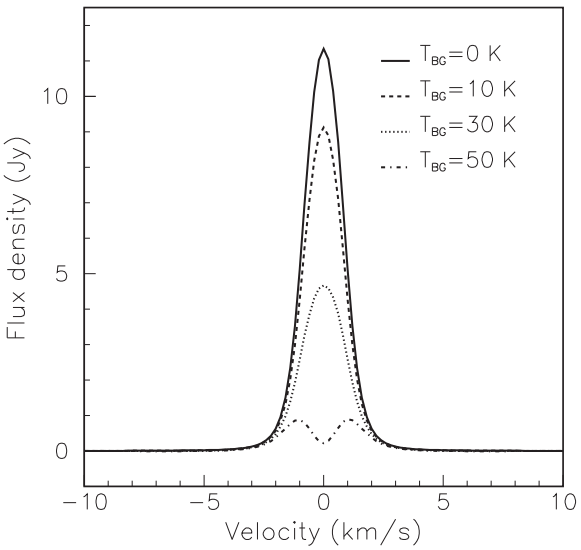

Figure 5. H I line profiles of a single detached shell (scenario 2, case D), and for various background levels (T_{BG} = 0, 10, 30, 50 K).

Table 1. Model parameters (scenario 2), $d = 200$ pc, $V_{\rm exp} = 8$ km s^{-1} and $\dot{M} = 10^{-7}$ M$_\odot$ yr^{-1}.

Case	Age (yr)	r_f(arcmin)	T_f (K)	$M_{\rm DT,\,CS}$ (M$_\odot$)
A	5×10^5	3.85	135	0.05
B	10^6	4.14	87	0.1
C	2×10^6	4.47	55	0.2
D	4×10^6	4.83	35	0.4

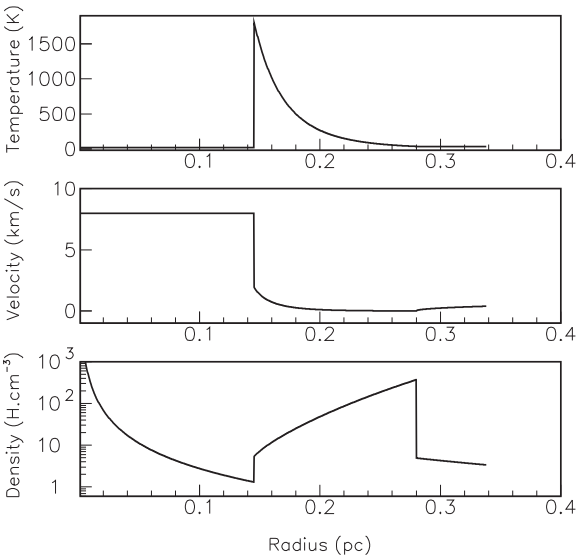

Figure 6. Density, velocity and temperature profiles for a detached shell model (scenario 2, case D).

temperature is given by $T_f \sim (3\ \mu\, m_{\rm H})/(16\ {\rm k})\ V_{\rm exp}{}^2 \sim 1800$ K (equation 6.58 in Dyson & Williams 1997) with $m_{\rm H}$ the mass of the hydrogen atom and μ the mean molecular weight. For the temperature profile inside the detached shell we use the expression 9 in Libert et al. (2007) with a temperature index, $a = -6.0$. The temperature is thus decreasing from ∼1800 K, to T_f, at the interface with ISM, r_f. The density, velocity and temperature profiles are illustrated in Fig. 6 for case D.

Self-absorption within the detached shell has a limited effect, with a reduction ranging from 1 per cent (model A) to 20 per cent (model D), as compared to the optically thin approximation (Fig. 4). However, taking into account the background introduces a much larger effect (Fig. 5).

The results depend on the adopted parameters in the model (mainly internal radius, expansion velocity and age). Smaller internal radius and expansion velocity, and/or longer age would lower the average temperature in the detached shell. This would increase the effect of self-absorption, as well as that of the background absorption. The line profiles simulated with the A and B-cases represented in Fig. 4 provide a good approximation to several observed H I line profiles (Libert et al. 2007, 2010; Matthews et al. 2013).

As an illustration, we reproduce on Fig. 7 the spatially integrated profile of Y CVn observed by Libert et al. (2007) together with a recent fit obtained by Hoai (in preparation) . For this fit, a distance of 321 pc (van Leeuwen 2007), a mass-loss rate of 1.3×10^{-7} M$_\odot$ yr^{-1}, and a duration of 7×10^5 yr have been adopted. These parameters differ from those adopted by Matthews et al.

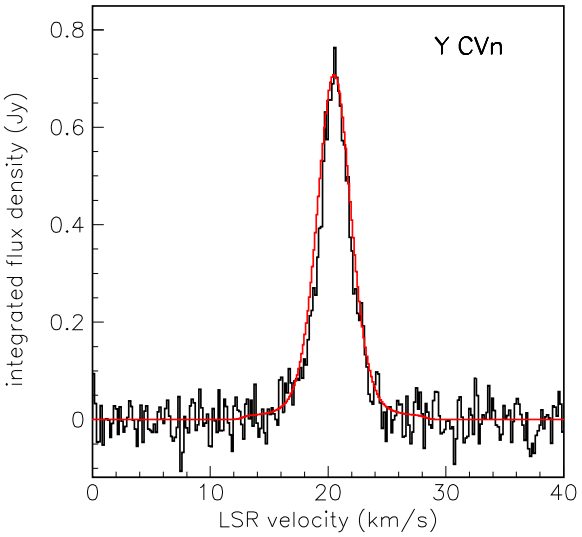

Figure 7. Y CVn integrated spectrum (Libert et al. 2007) and fit obtained by Hoai (in preparation) with scenario 2 ($d = 321$ pc, $\dot{M} = 1.3\times10^{-7}$ M$_\odot$ yr^{-1}, age $= 7\times10^5$ yr).

(2013), who assumed 1.7×10^{-7} M$_\odot$ yr^{-1} and a distance of 272 pc (Knapp et al. 2003). However, by adopting a lower mass-loss rate, and conversely, a longer duration, Hoai (in preparation) can fit the spatially resolved spectra obtained by the VLA and solve the problem faced by Matthews et al. at small radii. A difference between the mass-loss rate estimated from CO observations and that adopted in the model may have several reasons, for instance an inadequate CO/H abundance ratio.

4.3 Villaver et al. model (scenario 3)

Villaver et al. (2002) have modelled the dynamical evolution of circumstellar shells around AGB stars. The temporal variations of the stellar winds are taken from the stellar evolutionary models of Vassiliadis & Wood (1993).

For our H I simulations, we used the 1.5-M$_\odot$ circumstellar shell models of Villaver et al. (2002) at various times of the TP-AGB evolution. We selected the epochs at 5.0, 6.5 and 8.0 × 10^5 yr, which correspond to the first two thermal pulses, and then to the end of the fifth (and last) thermal pulse. The density, velocity and temperature profiles are illustrated in Fig. 8. For these models, which can reach a large size (with radii of 0.75, 1.66 and 2.5 pc, respectively), we adopt a distance of 1 kpc (implying a diameter of up to 17 arcmin).

The results are shown in Fig. 9. In this scenario, the temperature in the circumstellar environment is maintained at high values due to the interactions between the successive shells (Fig. 8). The shape of the line profile is thus dominated by thermal broadening, and does not depend much on the epoch which is considered (although the intensity of the emission depends strongly on time, together with the quantity of matter expelled by the star).

For the same reason, these results do not depend much on the background (<5 per cent for $T_{\rm BG} = 100$ K). Indeed in the models the temperature of the gas in the circumstellar shell always stays at a high level (>10^3 K, except close to the central star in the freely expanding region).

The predictions obtained with this scenario, in which wind–wind interactions are taken into account, differ clearly from those

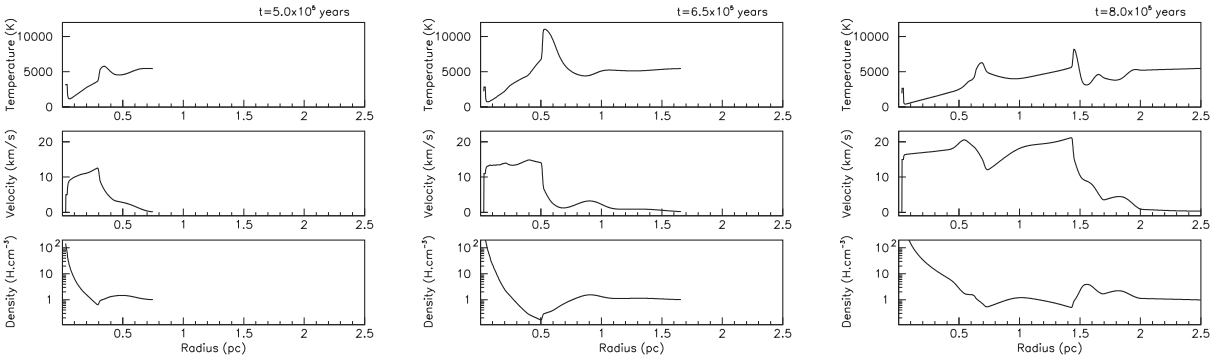

Figure 8. Density, velocity and temperature profiles for the Villaver et al. (2002) model (scenario 3) at three different epochs [5.0×10^5 yr (left), 6.5×10^5 yr (centre), 8.0×10^5 yr (right)].

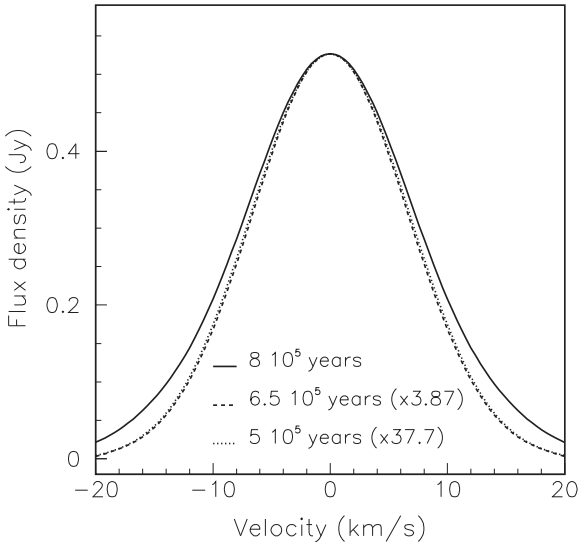

Figure 9. H I line profiles of a circumstellar shell model around a 1.5 $M_\odot$ star during the evolution on the TP-AGB phase (5.0, 6.5, 8.0 $\times$ 10^5 yr; Villaver et al. 2002), no background. The distance is set at 1000 pc. The first two profiles have been scaled by 37.7 and 3.87, respectively, in order to help the comparison between the different line profiles.

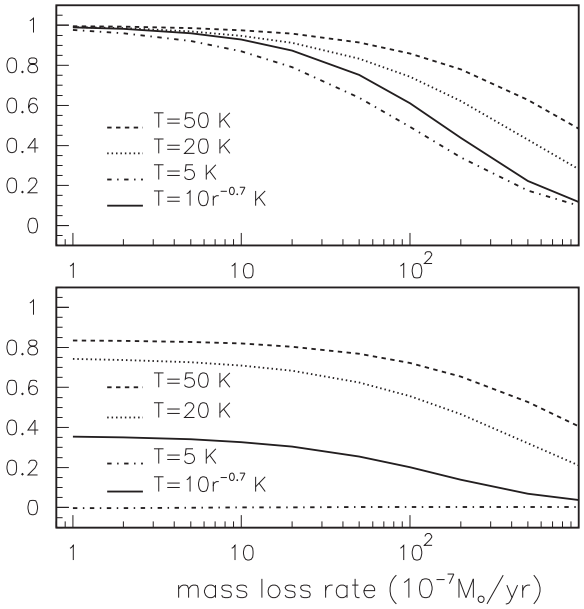

Figure 10. Ratio between the 'estimated' mass in atomic hydrogen and the real mass for the freely expanding wind case (scenario no. 1) with mass-loss rates ranging from 10^{-7} to 10^{-4} $M_\odot$ yr^{-1} (see Section 5.1) and different cases of temperature dependence (see text). Upper panel: no background. Lower panel: with a 5 K background.

obtained with the previous scenario, in which the detached shell is assumed to result from a long-duration stationary process, by a much larger width of the line profiles (full width at half-maximum, FWHM $\sim$ 16 km s^{-1}). This large width in the simulations for scenario no. 3 results mainly from the thermal broadening, and also, but to a lesser extent, from the kinematic broadening (cf. Fig. 8).

5 DISCUSSION

5.1 Optically thin approximation

If absorption can be neglected, the intensity becomes proportional to the column density of hydrogen. For a source at a distance d, the mass in atomic hydrogen ($M_{\rm H\,I}$) can be derived from the integrated flux density through the standard relation (e.g. Knapp & Bowers 1983):

$$M_{\rm H\,I} = 2.36 \times 10^{-7} d^2 \int S_{\rm H\,I} {\rm d}V,$$

in which d is expressed in pc, V in km s^{-1}, $S_{\rm H\,I}$ in Jy and $M_{\rm H\,I}$ in solar masses ($M_\odot$).

Our calculations allow us to estimate the error in the derived H I mass of circumstellar envelopes that is incurred from the assumption that the emission is optically thin and not affected by the background. As an example, in Fig. 10, we show the ratio between the estimated mass (using the standard relation) and the exact mass in atomic hydrogen. The case without background illustrates the effect of self-absorption within the circumstellar shell for different mass-loss rates. We adopt a freely expanding wind with a

temperature profile in $r^{-0.7}$ (as in Section 4.1), with r expressed in arcmin., or a constant temperature (5, 10, 20 K). The ratio clearly decreases with decreasing temperature in the circumstellar shell, increasing mass-loss rate and increasing background temperature.

In the constant temperature case with $T = 5$ K and $T_{\rm BG} = 5$ K, the line profiles should be flat (cf. radiative transfer equation in Section 3), and thus the 'estimated' masses, exactly null. Our numerical calculations agree with this prediction to better than 3×10^{-3}, for mass-loss rates up to 10^{-4} M$_\odot$ yr^{-1}.

The standard relation used for estimating the mass in atomic hydrogen should obviously be handled with caution in the case of the freely expanding wind scenario (no. 1). On the other hand, our calculations show that the deviation is much smaller for the two other scenarios (and basically negligible for scenario no. 3). This is mainly an effect of the high temperature in the detached shells resulting from the wind–wind interactions.

5.2 Spectral variations of the background

The H I absorption produced by cold galactic gas in the foreground of bright background emission may be shifted towards the velocity with highest background (cf. Levinson & Brown 1980). To illustrate this effect in the case of circumstellar shells, in Fig. 11, we show the results of our simulations for a 10^{-5} M$_\odot$ yr^{-1} freely expanding wind, as in Section 4.1, and a background temperature varying linearly between 10 K at -10 km s^{-1}, and 5 K at $+10$ km s^{-1}. The absorption is clearly shifted towards velocities with highest background. One notes also that the emission is shifted towards velocities with lowest background.

In the case of an intense and spectrally structured background, some care should be exercised when comparing the H I line centroids with the velocities determined from other lines.

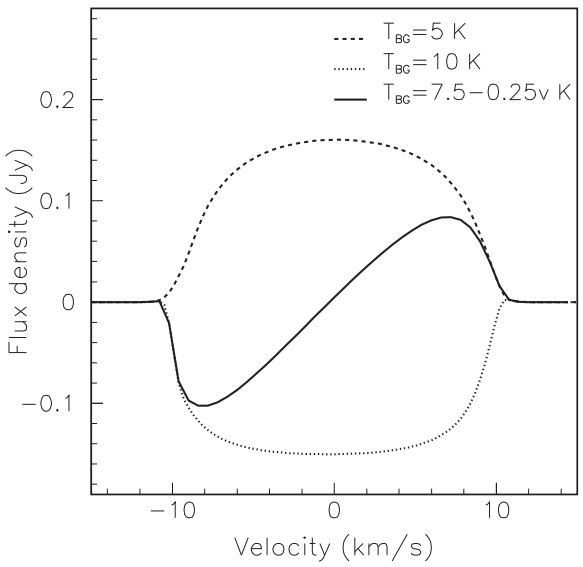

Figure 11. Effect of a background intensity varying linearly from 10 to 5 K across the line profile for a scenario 1 model with $\dot{M} = 10^{-5}$ M$_\odot$ yr^{-1}. The curves labelled '$T_{\rm BG} = 5$ K', and '$T_{\rm BG} = 10$ K', are reproduced from Fig. 3.

5.3 Comparison with observations

Freely expanding winds have been definitively detected in the H I line in only two red giants: Y CVn (Le Bertre & Gérard 2004) and Betelgeuse (Bowers & Knapp 1987). The corresponding emission is relatively weak and difficult to detect. Data obtained at high spatial resolution reveal a double-horn profile (e.g. Bowers & Knapp 1987). It is worth noting that a high-velocity expanding wind ($V_{\rm exp} \sim 35$ km s^{-1}) has also been detected around the classical Cepheid δ Cep (Matthews et al. 2012). A pedestal is suspected in a few H I line profiles that could be due the freely expanding region (Gérard & Le Bertre 2006; Matthews et al. 2013). The first scenario might also be interesting for interpreting sources in their early phase of mass-loss, or for sources, at large distance from the Galactic plane, embedded in a low-pressure ISM.

In general, sources which, up to now, have been detected in H I show quasi-Gaussian line profiles of FWHM $\sim$ 2–5 km s^{-1} (Gérard & Le Bertre 2006; Matthews et al. 2013), a property which reveals the presence of slowed-down detached shells. These profiles are well reproduced by simulations based on the scenario no. 2 presented in Section 4.2, assuming mass-loss rates of a few 10^{-7} M$_\odot$ yr^{-1}, and durations of a few 10^5 yr. In particular, for Y CVn and Betelgeuse, the main H I component has a narrow line profile ($\sim$3 km s^{-1}) and is well reproduced by this kind of simulation (Libert et al. 2007; Le Bertre et al. 2012).

Sources with large mass-loss rates ($\geq 5 \times 10^{-7}$ M$_\odot$ yr^{-1}) have rarely been detected (with the notable exceptions of IRC +10216 and AFGL 3068, see below). The simulations presented in Section 4.3 show the line profiles that sources, such as those predicted by Villaver et al. (2002), should exhibit at the end of the thermal-pulse phase, with large mass-loss rates, and with interaction with the local ISM. In these models, in which the evolution of the central star is integrated, the circumstellar envelopes result from several interacting shells, as well as from the ISM matter which has been swept-up. Shocks between successive shells maintain a high gas temperature ($\sim$4000 K).

For these models the calculated line profiles are not seriously affected by the background level, and the flux densities are large enough for allowing a detection up to a few kpc. For instance, in the GALFA-H I survey (Peek et al. 2011), the 3σ detection limit for a point source in a 1 km s^{-1} channel is $\sim$30 mJy. Saul et al. (2012) have detected many compact isolated sources in this survey. However, at the present stage, none could be associated with an evolved star (Begum et al. 2010).

Furthermore, several sources with high mass-loss rates, such as IRC + 10011 (WX Psc), IK Tau (NML Tau) or AFGL 3099 (IZ Peg) which are observed at high galactic latitude, with an expected low interstellar H I background, remain undetected (Gérard & Le Bertre 2006; Matthews et al. 2013). The simulations that we have performed based on the three different scenarios considered in this work cannot account for such a result. It seems therefore that, in sources with large mass-loss rates ($\geq 5 \times 10^{-7}$ M$_\odot$ yr^{-1}), hydrogen is generally not in atomic, but rather in molecular form.

Glassgold & Huggins (1983) have discussed the H/H$_2$ ratio in the atmospheres of red giants. They find that for stars with photospheric temperature $T_\star \geq 2500$ K, most of the hydrogen should be in atomic form, and the reverse for $T_\star \leq 2500$ K. Winters et al. (2000) find that there is an anti-correlation between $T_\star$ and the mass-loss experienced by long period variables. It seems likely that stars having a mass-loss rate larger than a few 10^{-7} M$_\odot$ yr^{-1} have also generally a low photospheric temperature, with $T_\star \leq 2500$ K, and thus a wind in which hydrogen is mostly molecular.

Recently, Matthews, Gérard & Le Bertre (2015) have reported the detection of atomic hydrogen in the circumstellar environment of IRC +10216, a prototype of a mass-losing AGB star at the end of its evolution with $\dot{M} \sim 2 \times 10^{-5}$ M$_\odot$ yr^{-1}. The observed morphology, with a complete ring of emission, is in agreement with the predictions of Villaver et al. (2002, 2012). They find that atomic hydrogen represents only a small fraction of the expected mass of the circumstellar environment (<1 per cent), supporting a composition dominated by molecular hydrogen. Unfortunately, a reliable line profile could not be extracted due to the low level of the emission and to a patchy background. The detection of H I over a spectral range ∼10 km s^{-1} suggests a line width larger than commonly observed in evolved stars, which would make it compatible with scenario no. 3. Gérard & Le Bertre (2006) have reported the possible detection of AFGL 3068, another carbon star with high mass-loss rate (∼10^{-4} M$_\odot$ yr^{-1}). In this case, also, the line width (∼30 km s^{-1}) is larger than expected for scenario no. 2, and might be better explained by scenario no. 3. Another possibility for this source which is at a large distance from the Galactic plane ($z \sim 740$ pc) would be that we are mostly detecting a freely expanding wind not slowed down by its local ISM (i.e. scenario no. 1).

If the atomic hydrogen is of atmospheric origin (a fraction of 1 per cent is expected for a star with an effective temperature of 2200 K; Glassgold & Huggins 1983), its abundance should correspondingly be scaled down in our radiative transfer simulations. The effect of the optical depth on the line profiles could be considerably reduced for such a case. For stars with lower effective temperature ($T_\star \leq 2200$ K), atomic hydrogen might also be present in the external regions of circumstellar envelopes as a result of the photodissociation of molecular hydrogen by UV photons from the ISRF (Morris & Jura 1983).

5.4 Case of a resolved source

We have concentrated our study on the prediction of spatially integrated spectra. However, circumstellar envelopes may reach a large size (∼2–3 pc; Villaver et al. 2002), and thus have a large extent over the sky. Also, interferometers provide a larger spatial resolution than single-dish antennas. It is thus interesting to examine how the line profile may vary as a function of position. As an example, in Fig. 12, we show a spectral map that would be obtained for a detached shell observed over a background with $T_{\rm BG} = 50$ K (scenario 2). The line appears mostly in emission and, as expected, delineates the detached shell. However, in the case of a high background level, the line appears also in absorption, in particular in the external part of the detached shell where the lines of sight cross regions with gas at low temperature.

Spatially resolved H I studies, with a careful subtraction of the background emission, may thus reveal spectral signatures that hold information on their physical conditions. Such signatures could help to constrain the physical properties of the gas in a region where molecules are absent or not detectable.

6 PROSPECTS

We have simulated H I 21-cm line profiles for mass-losing AGB stars expected for different scenarios assuming spherical symmetry.

However, AGB sources are moving through the ISM and their shells may be partially stripped by ram pressure (Villaver, García-Segura & Manchado 2003; Villaver, Manchado & García-Segura 2012). As a consequence of the interaction a bow-shock shape

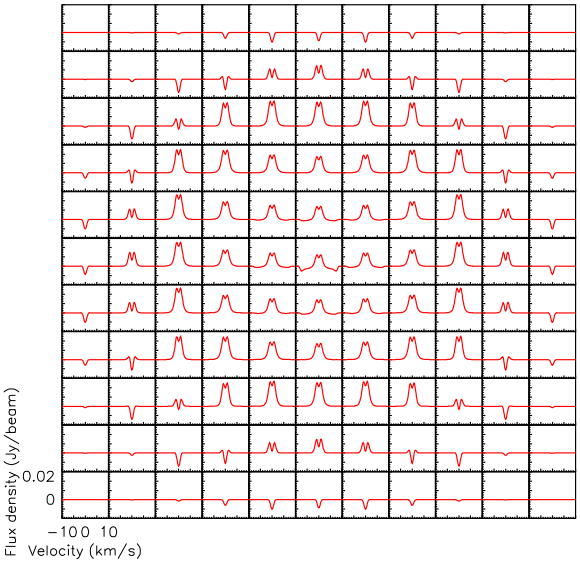

Figure 12. H I spectral map for a detached shell (case D in Table 1 with $T_{\rm BG} = 50$ K), assuming a Gaussian beam of FWHM = 1 arcmin. Steps are 1 arcmin in both directions.

appears in the direction of the movement, but also a cometary tail is formed which is fed directly from the stellar wind and from material stripped away from the bow shock. The cooling function and the temperature assumed for the wind have an important effect on the formation of the tail as shown in Villaver et al. (2012). Higher density regions formed behind the star will cool more efficiently and will collapse against the ISM pressure, allowing the formation of narrow tails.

Gérard & Le Bertre (2006) have reported shifts of the H I emission in velocity as well as in position for several sources. Matthews et al. (2008) have reported a shift in velocity for different positions along the tail of Mira (see also X Her, Matthews et al. 2011). These effects can also affect the H I line profiles, and thus the detectability. In addition, material lost by the AGB star should be spread along a tail that may reach a length of 4 pc, as in the exceptional case of Mira. On the other hand, Villaver et al. (2012) show that for sources with large mass-loss rates at the end of their evolution, dense shells could still be found close to the present star position.

We have assumed a background with a constant brightness. Of course, as explained in Section 3, this applies only to the cosmic background, and to a lesser extent to the galactic continuum emission. It does not apply to the galactic H I emission which may show spatial structures of various kinds. The resulting effect may be more complex than that simulated in Section 4. For instance, an absorption line could form preferentially at the position of a peak of galactic H I emission (a radiative transfer effect). Such a phenomenon may affect the predictions presented in Section 5.4. Therefore, a good description of the background will also be needed to model the observed line profiles. Such input may be obtained through frequency-switched observations for the galactic H I component, and through the surveys of the continuum at 21 cm which are already available (see Section 3).

It has to be noted that, in the position-switched mode of observation, the intrinsic line profile of the stellar source can also be spoiled by the patchiness of the galactic background emission (observational artefact). The main source of confusion is the

galactic H I emission which is structured spatially and spectrally. The classical position-switched mode of observation is not always efficient to correct the 21-cm spectra from the emission that is not directly associated with the star. More sophisticated methods with 2D mapping might be needed for subtracting the contaminating emission in these cases. Interferometric observations have the advantage of filtering the large-scale galactic emission. However, one should care that an intrinsic circumstellar emission is not also subtracted in this mode of observation. Also some artefacts may arise from incomplete spatial sampling of the large-scale emission, as illustrated by the case of TX Psc (Matthews et al. 2013). If feasible, an excellent u–v coverage combined with maps from a single-dish telescope providing small spacings has to be obtained. Also, for circumstellar shells angularly larger than the primary beam of the interferometer, mosaicked observations combined with single-dish maps are needed.

Another caveat is that, when the distance to the source becomes larger, the foreground ISM material may play the role of an absorbing layer of growing importance (Zuckerman et al. 1980). The circumstellar shell line profile may thus be distorted by absorption due to the foreground cold material that shares the same radial velocity range.

Sources with high mass-loss rate ($\sim 10^{-6}$–10^{-5} $M_\odot$ yr^{-1}) tend to be concentrated towards the galactic plane. They are expected to dominate the contribution of AGB stars to the replenishment of the ISM (Le Bertre et al. 2003). The recent detection of IRC + 10216 by Matthews et al. (2015) shows that atomic hydrogen should be present in these sources and that the H I line at 21 cm can be used to probe the morphology and the kinematics of stellar matter decelerated at large distance from the central star. However, as discussed above, when the background is large, a proper modelling of the line profiles will be necessary.

7 SUMMARY AND CONCLUSIONS

We have simulated H I 21-cm line profiles expected for several different scenarios representing different evolutionary stages of evolved stars, and thus corresponding to different AGB circumstellar structures. We have relaxed the optically thin hypothesis which was assumed in previous works, and included the emission from the background.

Self-absorption may be important in freely expanding circumstellar shells, as well as in some detached shells resulting from the interaction of the stellar winds with the local ISM. The H I line profile may also be affected by the background level and by the spectral profile of this background emission.

The numerical simulations that we have performed show that, under certain conditions, the observed H I 21-cm flux densities from mass-losing stars can be significantly reduced by taking into account optical depth effects and the presence of the background emission, but not to such a level such as to account for the non-detection of several sources. Therefore, one should consider that molecular hydrogen instead of atomic hydrogen likely dominates in sources with high mass-loss rates ($\geq$few 10^{-7} $M_\odot$ yr^{-1}), probably an effect of their low atmospheric temperature. Still, the recent results of Matthews et al. (2015) show that the H I line at 21 cm can be a useful probe of the outer regions of sources with low stellar effective temperature (<2500 K).

For sources with mass-loss rates $\sim 10^{-7}$ $M_\odot$ yr^{-1}, which are detected in H I, the global agreement between the observed line profiles and the simulations based on the second scenario suggests that their central stars undergo mass-loss smoothly over several 10^5 yr.

ACKNOWLEDGEMENTS

We thank Pierre Darriulat and Jan Martin Winters for their continuous support and kind encouragements. We are also grateful to N. Cox and A. J. van Marle, the organisers of the Lorentz workshop on Astrospheres (Leiden, 2013 Dec 9–13), where the ideas developed in this paper started to take shape. DTH and PTN thank the French Embassy in Hanoi and the CNRS/IN2P3 for financial support. Financial and/or material support from the Institute for Nuclear Science and Technology, Vietnam National Foundation for Science and Technology Development (NAFOSTED) under grant number 103.08-2012.34 and World Laboratory is gratefully acknowledged. LDM is supported by grant AST-1310930 from the National Science Foundation. EV acknowledges Spanish Ministerio de Economía y Competitividad funding under grant AYA2013-45347P. TL acknowledges financial support by the CNRS programmes ASA and PCMI.

REFERENCES

Begum A. et al., 2010, ApJ, 722, 395
Bowers P. F., Knapp G. R., 1987, ApJ, 315, 305
Dyson J. E., Williams D. A., 1997, The Physics of the Interstellar Medium, 2nd edn. IoP Publishing, Bristol
Gardan E., Gérard E., Le Bertre T., 2006, MNRAS, 365, 245
Gérard E., Le Bertre T., 2006, AJ, 132, 2566
Glassgold A. E., Huggins P. J., 1983, MNRAS, 203, 517
Hoai D. T., Matthews L. D., Winters J. M., Nhung P. T., Gérard E., Libert Y., Le Bertre T., 2014, A&A, 565, A54
Kalberla P. M. W., Burton W. B., Hartmann D., Arnal E. M., Bajaja E., Morras R., Pöppel W. G. L., 2005, A&A, 440, 775
Knapp G. R., Bowers P. F., 1983, ApJ, 266, 701
Knapp G. R., Morris M., 1985, ApJ, 292, 640
Knapp G. R., Pourbaix D., Platais I., Jorissen A., 2003, A&A, 403, 993
Le Bertre T., Gérard E., 2004, A&A, 419, 549
Le Bertre T., Tanaka M., Yamamura I., Murakami H., 2003, A&A, 403, 943
Le Bertre T., Matthews L. D., Gérard E., Libert Y., 2012, MNRAS, 422, 3433
Lequeux J., 2005, The Interstellar Medium, Astronomy & Astrophysics Library. Springer, Berlin
Levinson F. H., Brown R. L., 1980, ApJ, 242, 416
Libert Y., Gérard E., Le Bertre T., 2007, MNRAS, 380, 1161
Libert Y., Gérard E., Thum C., Winters J. M., Matthews L. D., Le Bertre T., 2010, A&A, 510, A14
Loup C., Forveille T., Omont A., Paul J. F., 1993, A&AS, 99, 291
Matthews L. D., Reid M. J., 2007, AJ, 133, 2291
Matthews L. D., Libert Y., Gérard E., Le Bertre T., Reid M. J., 2008, ApJ, 684, 603
Matthews L. D., Libert Y., Gérard E., Le Bertre T., Johnson M. C., Dame T. M., 2011, AJ, 141, 60
Matthews L. D., Marengo M., Evans N. R., Bono G., 2012, ApJ, 744, 53
Matthews L. D., Le Bertre T., Gérard E., Johnson M. C., 2013, AJ, 145, 97
Matthews L. D., Gérard E., Le Bertre T., 2015, MNRAS, preprint (arXiv:1502.02050)
Morris M., Jura M., 1983, ApJ, 264, 546
Morris M., Lucas R., Omont A., 1985, A&A, 142, 107
Olofsson H., 1999, in Le Bertre T., Lebre A., Waelkens C., eds, Proc. IAU Symp. 191, Asymptotic Giant Branch Stars. Astron. Soc. Pac., p. 3
Olofsson H., Bergman P., Lucas R., Eriksson K., Gustafsson B., Bieging J. H., 2000, A&A, 353, 583
Peek J. E. G., Heiles C., Douglas K. A. et al., 2011, ApJS, 194, 20
Reich W., 1982, A&AS, 48, 219

Reich P., Reich W., 1986, A&AS, 63, 205
Reich P., Testori J. C., Reich W., 2001, A&A, 376, 861
Sahai R., 1990, ApJ, 362, 652
Saul D. R., Peek J. E. G., Grcevich J. et al., 2012, ApJ, 758, 44
Schöier F. L., Olofsson H., 2001, A&A, 368, 969
Stil J. M. et al., 2006, AJ, 132, 1158
van Leeuwen F., 2007, Astrophysics and Space Science Library, Vol. 350, Hipparcos, the New Reduction of the Raw Data. Springer, Berlin
Vassiliadis E., Wood P. R., 1993, ApJ, 413, 641
Villaver E., García-Segura G., Manchado A., 2002, ApJ, 571, 880
Villaver E., García-Segura G., Manchado A., 2003, ApJ, 585, L49
Villaver E., Manchado A., García-Segura G., 2012, ApJ, 748, 94
Winters J. M., Le Bertre T., Jeong K. S., Helling C., Sedlmayr E., 2000, A&A, 361, 641
Young K., Phillips T. G., Knapp G. R., 1993, ApJ, 409, 725
Zuckerman B., Terzian Y., Silverglate P., 1980, ApJ, 241, 1014

This paper has been typeset from a TEX/LATEX file prepared by the author.

Bibliography

Adelman S.J. & Dennis J.W., 2005, BaltA, 14, 41

Alcolea J., Bujarrabal V. & Sanchez Contreras C., 1996, A&A, 312, 560

Amiri N., 2011, Developping Asymmetries in AGB Stars: Occurence, Morphology and Polarization of Circumstellar Masers, PhD thesis, Leiden

Balick B., Huarte-Espinosa M., Frank A., et al., 2013, ApJ, 772, 20

Baschek B., Scholz M. & Wehrse R., 1991, A&A, 246, 374

Bedijn P.J., 1987, A&A, 186, 136

Begum A., Stanimirović S., Peek J.E., et al., 2010, ApJ, 722, 395

Blackman E.G., Frank A., Markiel J.A., et al., 2001, Nature, 409, 485

Boothroyd A.I. & Sackmann I.-J., 1988a, ApJ, 328, 632

Boothroyd A.I. & Sackmann I.-J., 1988b, ApJ, 328, 641

Boothroyd A.I. & Sackmann I.-J., 1988c, ApJ, 328, 653

Bowen G.H. & Willson L.A., 1991, ApJ, 375, L53

Bowers P.F.& Knapp G.R., 1987, ApJ, 315, 305

Bowers P.F.& Knapp G.R., 1988, ApJ, 332, 299

Bujarrabal V. & Alcolea J., 2013, A&A, 552, A116

Bujarrabal V., Alcolea J., Van Winckel H., et al., 2013a, A&A, 557, A104

Bujarrabal V., Castro-Carrizo A., Alcolea J., et al., 2013b, A&A, 557, L11

Bujarrabal, V., Castro-Carrizo A., Alcolea J., et al., 2001, A&A, 367, 868

Bujarrabal V., 2009, FIR and sub-mm line observations of AGB and post-AGB nebulae, in Highlights of Astronomy, vol. 15, XXVIth IAU general assembly August 2009, ed. Ian F. Corbett

Bujarrabal V., Castro-Carrizo A., Alcolea J., et al., 2005, A&A, 441, 1031.

Busso M., Gallino R., Lambert D.L., et al., 1992, ApJ, 339, 218

Cami J., Yamamura I., de Jong T., et al., 2000, A&A, 360, 562

Castro-Carrizo A., Quintana-Lacaci G., Neri R., et al., 2010, A&A, 523, A59

Castro-Carrizo A., Neri R., Bujarrabal V., et al., 2012, A&A, 545, A1

Chagnon G., Mennesson B., Perrin G., et al., 2002, AJ, 124, 2821

Chiavassa A., Freytag B. & Plez B., 2013, Betelgeuse workshop 2012 proceedings, eds. P. Kervella, T. Le Bertre & G. Perrin, EAS Publications Series, 60 (2013) 145-153

Cohen M., Anderson C.M., Cowley A., et al., 1975, ApJ, 196, 179

Cohen M., Van Winckel H., Bond H.E. & Gull T.R., 2004, AJ, 127, 2362

Cox N.L.J., Kerschbaum F., van Marle A.-J, et al., 2012, A&A, 537, A35.
Dame T.M., Hartmann D. & Thaddeus P., 2001, AJ, 547, 792
De Beck E., Decin L., de Koter A., et al., 2010, A&A, 523, A18
Dennis T.J., Frank A., Blackman E.G., et al., 2009, ApJ, 707, 1485
Dermine T., Izzard R.G., Jorissen A., et al., 2013, A&A, 551, A50
Draine B.T., 2003, ARA&A, 41, 241
Dorfi E.A. & Höefner S., 1996, A&A, 313, 605
Dumm T. & Schild H., 1998, NewA, 3, 137
Dyck H.M., Benson J.A., van Belle G.T., et al., 1996, AJ, 111, 1705
Dyson J.E. & Williams D.A., 1997, The Physics of the Interstellar Medium, 2nd ed, Publisher: Bristol: Institute of Physics Publishing
Epchtein N., Le Bertre T., Lepine J.R.D, et al., 1987, A&AS, 71, 39
Ewen H.I. & Purcell E.M., 1951, Nature, 168, 356
Famaey B., Jorissen A., Luri X., et al., 2005, A&A, 430, 165
Fleischer A.J., Gauger A., Sedlmayer E., 1992, A&A, 266, 321
Fleischer A.J., Winters J.M. & Sedlmayer E., 1999, IAU Symposium, 191, 187
Freytag B. & Chiavassa A., 2013, Betelgeuse workshop 2012 proceedings, eds. P. Kervella, T. Le Bertre & G. Perrin, EAS Publications Series, 60 (2013) 137-144
Fox M.W. & Wood P.R., 1982, ApJ, 259, 198
Frankowski A. & Jorissen A., 2007, BaltA, 16, 104
Gallino R., 1988, in Evolution of peculiar red giant stars, eds. H.R. Johnson, B.Zuckerman, Cambridge UP, p.176
Gallino R., Busso M., Picchio G., et al., 1990, in From Miras to Planetary Nebulae, eds. M.O. Mennessier, A. Omont, Editions Frontières, Gif-sur-Yvette, p.329
Gardan E., Gérard E. & Le Bertre T., 2006, MNRAS, 365, 245
Gehrz R., 1989, IAU Symposium, 135, 445
Geise K.M., Mass Loss History of Evolved Stars, PhD thesis, Denver, 2011
Gérard E. & Le Bertre T., 2006, AJ, 132, 2566
Gérard E. & Le Bertre T., 2003, A&A, 397, 17
Glassgold A.E. & Huggins P.J., 1983, MNRAS, 203, 517
González D., Olofsson H., Kerschbaum F., et al., 2003, A&A, 411,123
Groenewegen M.A.T., 1993, A&A 271, 180
Gustafsson B., Edvardsson B., Eriksson K., et al., 2003, in Stellar Atmosphere Modeling, ed. I. Hubeny, D. Mihalas, & K. Werner, ASPC Proceedings, 288, 331
Habing H.J. & Olofsson H., 2004, in Asymptotic Giant Branch Stars, ed. Habing H.J. & Olofsson H., Springer-Verlag New York, p. 1
He J.H., 2007, A&A, 467, 1081
Herwig F., 2005, ARA&A, 43, 435
Hoai D.T., Matthews, L. D., Winters, J. M., et al., 2014, A&A, 565, A54
Hoai D.T., Nhung P. T., Gérard E., et al., 2015, MNRAS, 449, 2386

Höfner S. & Dorfi E.A., 1992, A&A, 265, 207
Höfner S. & Dorfi E.A., 1997, A&A, 319, 648
Howarth J.J., 2005, JBAA, 115, 334
Huarte-Spinosa M., Frank A., Blackman E.G., et al., 2012, ApJ, 757, 66
Hughes S.M.J. & Wood P.R., 1990, AJ, 99, 764
Inomata N., 2007, Publ. Astron. Soc. Japan, 59, 799
Jorissen A., van Eck S., Mayor M., et al., 1998, A&A, 332, 877
Jorissen A., Frayer D.T., Johnson H.R., et al., 1993, A&A, 271, 463
Jorissen A., 2004, in Asymptotic Giant Branch Stars, ed. Habing H.J. & Olofsson H., Springer-Verlag New York, p. 461
Jorissen A., Frankowski A., Famaey B., et al., 2009, A&A, 498, 489
Jorissen A., Mayer A., van Eck S., et al., 2011, A&A, 532, A135
Kahane C. & Jura M., 1996, A&A, 310, 952
Kalberla P.M.W., Burton W.B., Hartmann D., et al., 2005, A&A, 440, 775
Keppens R., Meliani Z., van Marle A.J., et al., 2012, Journal of Computational Physics, 231, 718
Kervella P., Montargès M., Lagadec E., et al., 2015, A&A, 578, A77
Knapp G.R. & Bowers P.F., 1983, ApJ, 266, 701
Knapp G.R. & Morris M., 1985, ApJ, 292, 640
Knapp G.R., Pourbaix D., Platais I., Jorissen A., 2003, A&A, 403, 993
Knapp G.R., Young K., Lee E., et al. 1998, ApJS, 117, 209
Koning N., Kwok S. & Steffen W., 2011, AJ, 740, 27
Kwok S., Purton C.R. & Fitzgerald P.M., 1978, ApJ, 219, L125
Kwok S., 2002, ASPC Proceedings, Ed. A.F.J. Moffat & N. St-Louis, San Francisco: Astronomical Society of the Pacific, 260, 245
Kwok S., Hrivnak B.J. & Su K.Y.L., 2000, AJ, 544, 2
Lagadec E., Verhoelst T., Mékarnia D., et al., 2011, MNRAS, 417, 32
Lagadec E. & Zijlstra A.A., 2008, 390, L59
Le Bertre T., 1997, Cool Stars Winds and Mass Loss: Observations, Lecture Notes in Physics, Springer, 497, 133
Le Bertre T. & Gérard E., 2004, A&A, 419, 549
Le Bertre T., Tanaka M., Yamamura I., Murakami H., 2003, A&A, 403, 943
Le Bertre T., Matthews L.D., Gérard E., et al., 2012, MNRAS, 422, 3433
Lebzelter T. & Hron J., 1999, A&A, 351, 533
Lebzelter T. & Hron J., 2003, A&A, 411, 533
Lequeux J., 2005, Interstellar Medium, Astronomy & Astrophysics Library, Springer-Verlag Berlin Heidelberg
Levinson F.H., & Brown R.L., 1980, ApJ, 242, 416
Libert Y., Gérard E., Thum C., et al., 2010a, A&A, 510, A14
Libert Y., Winters J.M., Le Bertre T., et al., 2010b, A&A 515, A112
Libert Y., Gérard E., Le Bertre T., et al., 2009, A&A, 500, 1131

Libert Y., Le Bertre T., Gérard E., et al., 2008, A&A, 491, 789
Libert Y., Gérard E. & Le Bertre T., 2007, MNRAS, 380, 1161
Little S.J., Little-Marenin I.R. & Bauer W.H., 1987, AJ, 94, 981
Lorenz-Martins S. & Pompeia L., 2000, MNRAS, 315, 856
Maercker M., Mohamed S., Vlemmings W.H.T., et al., 2012, Nature, 490, 232
Mamon G.A., Glassgold A.E. & Huggins P.J., 1988, AJ, 328, 797
Marengo M., 2009, PASA, 26, 365
Markwick A.J., 2000, Chemistry in Dynamically Evolving Astrophysical Regions, PhD thesis, UMIST
Matt S., Balick B., et al., 2000, ApJ, 545, 965
Matthews L.D., Libert Y., Gérard E., et al., 2008, ApJ, 684, 603
Matthews L.D., Libert Y., Gérard E., et al., 2011, AJ, 141, 60
Matthews L.D., Marengo M., Evans N.R., Bono G., 2012, ApJ, 744, 53
Matthews L.D., Le Bertre T., Gérard E. & Johnson M.C., 2013, AJ, 145, 97
Matthews L.D., Gérard E. & Le Bertre T., 2015, MNRAS, 449, 220
Matthews L.D. & Reid M.J., 2007, AJ, 133, 229
Martin D.C., Seibert M., Neill J.D., et al., 2007, Nature, 448, 780
Martínez González M.J., Asensio Ramos A., Manso Sainz R., et al., 2015, A&A, 574, 16
Mastrodemos N. & Morris M., 1999, ApJ, 523, 357
Mayer A.,Jorissen A., Kerschbaum F., et al., 2011, A&A, 531, L4
Mennesson B., Perrin G., Chagnon G., et al., 2002, ApJ, 579, 446
Men'shchikov A.B., Schertl D., Tuthill P.G., et al., 2002, A&A, 393, 867.
Morris M. & Jura M., 1983, ApJ, 264, 546
Morris M., Lucas R. & Omont A., 1985, A&A, 142, 107
Nakashima J., 2006, ApJ, 638, 1041
Neri R., Kahane C., Lucas R., et al., 1998, A&AS, 130, 1
Nguyen-Q-Rieu, Laury-Micoulaut C., Winnberg A., et al., 1979, A&A, 75, 351
Nhung P.T., Hoai D.T., Winters J.M., et al., 2015a, RAA, 15, 713
Nhung P.T., Hoai D.T., Winters J.M., et al., 2015b, A&A, 583, A64
Norris B.R.M., Tuthill P.G., Ireland M.J., et al. 2012, Nature, 484, 220
Nyman L.Å., Booth R.S., Carlstrom U., et al., 1992, A&AS, 93, 121
Olofsson H., 1999, IAU Symposium, 191, 3
Olofsson H., Bergman P., Lucas R., et al., 2000, A&A, 353, 583
Ohnaka K., 2004, A&A, 424, 1011
Paczyński B., 1970, Acta Astron., 20, 47
Paczyński B., 1975, ApJ, 202, 558
Pascoli G. & Lahoche L., 2010, PASP, 122, 1334
Peek J.E.G., Heiles C., Douglas K.A., et al., 2011, ApJS, 194, 20
Peery B.F.Jr., 1971, ApJ, 163, L1
Reich W., 1982, A&AS, 48, 219
Reich P. & Reich W., 1986, A&AS, 63, 205

Reich P., Testori J.C., Reich W., 2001, A&A, 376, 861
Percy J.R., Wilson J.B. & Henry G.W., et al., 2001, PASP, 113, 983
Percy J.R. & Desjardins A., 1996, PASP, 108, 139
Perets H.B. & Kenyon S.J., 2012, ApJ, 764, 169
Pérez-Sánchez A.F., Vlemmings W.H.T., Tafoya D., et al., 2013, MNRAS, 436, L79
Perrin G., Coudé du Foresto V., Ridgway S.T., et al., 1998, A&A 331, 619
Perryman M.A.C., Lindegren L., Kovalevsky J., et al., 1997, A&A, 323, L49
Pols O.R., 2004, Mem. S.A.It, 75, 749
Raga A.C. & Cantó J., 2008, ApJ, 865, L141
Ramstedt S., 2009a, PhD thesis, Molecules and Dust aroud AGB stars: Mass-loss rates and molecular abundances, Stockholm University
Ramstedt S., Schöier F.L., Olofsson H., et al., 2008, A&A, 487, 645
Ramstedt S., Schöier F.L., Olofsson H., 2009, A&A, 499, 515
Reimers D., 1975, Mémoires of Société Royale des Sciences de Liège, 8, 369
Rosenfield P., Marigo P., Girardi L., et al., 2014, ApJ, 790, 22.
Sabin L., Zijlstra A.A. & Greaves J.S., 2007, MNRAS, 376, 378
Sahai R., & Chronopoulos C.K., 2010, ApJ, 711, L53
Sahai R., 1990, ApJ, 362, 652
Samus N.N., Durlevich O.V., Kazarovets E.V., et al., General Catalogue of Variable Stars (Samus+ 2007-2013), VizieR On-line Data Catalog: B/gcvs
Saul D.R., Peek J.G., Grcevich J., et al., 2012, ApJ, 758, 44
Schild H., 1989, MNRAS, 240, 63
Schöier F.L. & Olofsson H., 2001, A&A, 368, 96
Scholz M., 2001, MNRAS, 321, 347
Schwarzschild M., 1975, ApJ, 195, 137
Sedlmayr E., 1994, in Lecture Notes Physics, IAU Colloquium, 428, 163
Smith V.V. & Lambert D.L., 1986, ApJ, 311, 843
Smith V.V. & Lambert D.L., 1990, ApJS, 72, 387
Soker N., 1999, AJ, 118, 2424
Soker N., 2000, A&A, 357, 557
Soker N., 2002, MNRAS, 336, 826
Speck A.K., Barlow M.J., Sylvester R.J., et al., 2000, A&AS, 146, 437
Stephenson C.B., 1984, Publ. Warner & Swasey Obs., 3, 1
Tej A., Lançon A. & Scholz M., 2003, A&A, 401, 347
Thomas J.D., 2012, Spectroscopic Analysis and Modelling of the Red Rectangle, PhD thesis, University of Toledo
Tuan Anh P., Diep P.N., et al., 2015, RAA, arXiv1503.00858, in press
Tuthill P.G., Men'shchikov A.B., Schertl D., et al., 2002, A&A, 389, 889
Ueta T., Stencel R.E., Yamamura I., et al., 2010, A&A, 514, A16
van Leeuwen F., 2007, Hipparcos, the New Reduction of the Raw Data (Springer), Astrophysics and

Space Science Library, 350
van Marle A.J., Meliani1 Z., Keppens R. & Decin L., 2011, ApJ, 734, L26
van Winckel H., 2003, ARA&A, 41, 391
van Winckel H., Lloyd Evans T., Briquet M., et al., 2009, A&A, 505, 1221
van Winckel H., Hrivnak B.J., Gorlova N., et al., 2012, A&A, 542, A53
Vassiliadis E. & Wood P.R., 1993, ApJ, 413, 641
Villaver E., García-Segura G., Manchado A., 2002, ApJ, 571, 880
Villaver E., García-Segura G., Manchado A., 2003, ApJ, 585, L49
Villaver E., Manchado A. & García-Segura G., 2012, ApJ, 748, 94
Vlemmings W.H.T., Diamond P.J. & Imai H., 2006, Nature, 440, 58
Wallerstein G. & Dominy J.F., 1988, AJ, 330, 937
Wareing C.J., Zijlstra Albert A., O'Brien T.J., 2007, ApJ, 660, L129
Whitelock P.A., 1990, PASPC, 11, 365
Willson L.A., 2007, Proceedings of the 2006 Vienna conference "Why Galaxies care about AGB stars", ed. F. Kerschbaum, C. Charbonnel & R.F. Wing, ASP Conference Series, 378, 211
Wilson W.J.& Barrett A.H., 1968, Science, 161, 778
Winters J.M., Le Bertre T., Jeong K.S., et al., 2000, A&A, 361, 641
Winters J.M., Le Bertre T., Pety J., et al., 2007, A&A, 475, 559
Winters J.M., Le Bertre T., Jeong K.S., Nyman L.Å. & Epchtein N., 2003, A&A, 409, 715.
Winters J.M., Le Bertre T., Jeong K.S., et al., 2000, A&A, 361, 641
Woitke P. & Niccolini G., 2005, A&A, 433, 1101
Woitke P., 2006, A&A, 460, L9
Wolak P., Szymczak M. & Gérard E., 2011, A&A, 537, A5
Wood P.R. & Zarro D.M., 1981, ApJ, 247, 247
Wood P.R., 1990, Pulsation and evolution of Mira variables, in From Miras to Planetary Nebulae: Which Path to Stellar Evolution?, eds. Mennessier M.O. & Omont A., Editions Frontières: Gif sur Yvette. 67
Wood P.R., 1994, Evolution of AGB stars, in Circumstellar media in the late stages of stellar evolution, eds. Clegg R.E.S, Stevens I.R. & Meikle W.P.S., Cambridge University Press
Wood P.R., Alcock C., Allsman R.A., et al., 1999, IAU Symposium, 191, 151
Young K., Phillips T.G. & Knapp G.R., 1993, AJ, 409, 725
Zuckerman B., Terzian Y., Silverglate P., 1980, ApJ, 241, 1014